Residual Stress Development due to High-Frequency Post Weld Impact Treatments for High-Strength Steels

Proefschrift

ter verkrijging van de graad van doctor
aan de Technische Universiteit Delft;
op gezag van de Rector Magnificus prof. ir. K.C.A.M. Luyben
voorzitter van het College van Promoties
in het openbaar te verdedigen op dinsdag 18 December 2014 om 15.00 uur

door

He Gao

Master of Science in Metallurgical engineering
RWTH Aachen, Germany
geboren te Liaoning, China

Dit proefschrift is goedgekeurd door de promotor:

Prof.dr. I.M. Richardson

Copromotor: Dr.ir. M.J.M. Hermans

Samenstelling promotiecommissie:

Rector Magnificus, voorzitter

Prof. dr. I.M. Richardson, Technische Universiteit Delft, promotor

dr. ir. M.J.M. Hermans, Technische Universiteit Delft, copromotor

dr. N.S. Ermolaeva, Allseas

Prof. S. Williams, Cranfield University

Prof. R.H.M. Huijsmans, Technische Universiteit Delft

Prof. dr. A.Metrikine, Technische Universiteit Delft

Prof. dr. ir. J.G. Rots, Technische Universiteit Delft

Cover designed by He Gao

Printed in The Netherlands.

CONTENTS

Lists of Symbols and Abbreviations

The lists below include the symbols and abbreviations as they are used in the present thesis. In some cases, the same symbol is used to describe two parameters. However, the explanations in the text and the context in which the symbols are used will make the meaning of all symbols unambiguous. If occasionally other symbols are used in the text, their meaning is explained clearly.

Symbol	Description	Units
A, dA	Surface area, area element;	m^2
A	Vibration amplitude	m
a, b, c	Sample dimension	m
a, b, c_f, c_r	Goldak parameters	m
A, B, C	Strengthening parameters	-
c	Heat capacity	$W\ K^{-1}$
d	Lattice spacing	m
d_0	Stress free lattice spacing	m
d_{hkl}	Lattice spacing of *hkl* lattice plane	m
$d_{0,hkl}$	Stress free lattice spacing of *hkl* lattice plane	m
E	Young's modulus	Pa
E_{hkl}	Diffraction elastic constant to Young's modulus	Pa
e_i	Energy	keV
e_{hkl}	Energy of *hkl* lattice plane	keV
$\underline{F}$	Force	N

f	Frequency	Hz
f_f, f_r	Front and rear fraction	-
H	Enthalpy	W
$\dot{H}$	Volumetric enthalpy per mass	W kg^{-1}
H_v	Vickers hardness	kgf mm^{-1}
h	Film coefficient	W m^{-2} K^{-1}
hkl	Indices for a lattice plane	-
K	Stiffness	N m^{-2}
ΔK_{th}	Fatigue crack initiation threshold	-
m	Temperature softening parameter	-
n	Positive integer	-
$p, q, t / P, Q, T$	Strain/stress combinations	-/Pa
r	Heating rate	K s^{-1}
T	Temperature	°C
T_0	Room temperature	°C
t	Time	s
t_0	Time zero	s
t	Thickness	m
Q	Heat input	W
$\dot{Q}$	Power per unit volume	W m^{-3}
$\boldsymbol{q}$	Heat flux vector	W m^{-2}
$q_{v,f}(x, y, z, t)$	Front ellipsoid heat flux	W m^{-3}
$q_{v,r}(x, y, z, t)$	Rear ellipsoid heat flux	W m^{-3}

$q_{s,c}$	Heat loss by surface conduction/convection	W m^{-2}
$q_{s,r}$	Heat loss by surface radiation	W m^{-2}
v	Travel speed	m s^{-1}
$v_{ini\,\max}$	Initial impact speed	m s^{-1}
X_1, X_2, X_3	Coordinate systems	-
x, y, z	Coordinates	m
α	Expansion coefficient	K^{-1}
ε	Strain	-
ε	Radiation emissivity	W m^{-2} K^{-4}
ε_{hkl}	Strain of *hkl* lattice plane	-
θ	Diffraction angle	°
λ	Wave length	m
λ_{hkl}	Wave length of *hkl* lattice plane	m
λ	Coefficients of thermal conductivity	W m^{-1}
ρ	Density	kg m^{-3}
η	Fraction	-
Γ	Full width half maximum	-
v	Possion's ratio	-
v_{hkl}	Possion's ratio of *hkl* lattice plane	-
$\underline{\sigma}$	Mechanical stress, vector format	Pa
σ_B	Stefan-Boltzmann constant	-
$\sigma_{ij}, i, j \in \{1, 2, 3\}$	Component of stress tensor	Pa

σ_{hkl}	Stress of *hkl* lattice plane	Pa
σ_ϕ	Applied uni-axial stress	Pa
$\underline{\tau}$	Shear stress, vector format	Pa
ϕ, ψ	Orientation angles with respect to the specimen	°
Δ_i	Channel element	-

Abbreviations	Description
1,2,3 D	One,two,three dimensional
BRSL	Block removal splitting and layering
bcc	Body centered cubic
CCT	Continuous cooling transformation
CHD	Centre hole drilling
DHD	Deep hole drilling
ETMT	Electro-thermal mechanical test
FEM	Finite element model
fcc	Face centered cubic
GMAW	Gas metal arc welding
HAZ	Heat-affect-zone
NSTC	Northern Scientific and Technological Company
PS	Plane strain
GPS	Generalised plane strain
RC	Ring core
TIG	Tungsten inert gas
XRF	X-ray fluorescence
XRD	X-ray diffraction
UIT	Ultrasonic impact treatment
VSR	Vibration stress relief

FEM Unit system

In finite element methods (FEM), it is common to use the SI-units. The following table lists the parameters needed for the calculations and their corresponding (mm, t, s)-units and conversion factors.

Parameter	SI-units	(mm, t, s)-units	conversion factors
Basis Quantities			
Dimension	m	mm	10^3
Mass	kg	t	10^{-3}
Time	s	s	1
Temperature	K	K	1
Derived Quantitates			
Force	N	N	1
Volume	m^3	mm^3	10^9
Energy	J= N m	N mm	10^3
Power	$W = J\ s^{-1} = N\ m\ s^{-1}$	$N\ mm\ s^{-1}$	10^3
Density	$kg\ m^{-3}$	$t\ mm^{-3}$	10^{-12}
Specific heat	$J\ kg^{-1}\ K^{-1}$	$N\ mm^{-1}\ t^{-1}\ K^{-1}$	10^6
Heat conductivity	$W\ m^{-1}\ K^{-1} = N\ s^{-1}\ K^{-1}$	$N^{-1}\ s^{-1}\ K^{-1}$	1
Strain	$m\ m^{-1}$	$mm\ mm^{-1}$	1
Stress	$Pa = N\ m^{-2}$	$MPa = N\ mm^{-2}$	10^{-6}

1 Introduction

1.1 Project background

Allseas Engineering bv is an engineering center of the Allseas group, a major player in the offshore pipe lay market and recently expanding the activities to the offshore heavy lift sector. Because of the necessity to design and build lifting structures and equipment of a tremendously high capacity, the demand for high-strength steels usage has been arisen. These steels are to be welded and used in a harsh offshore environment [1]. Localized heating and melting of a workpiece during welding lead to the build-up of residual stresses. When distortion is prevented due to constraints in structures or due to clamping, stress levels will be high and may exceed the yield strength [2].

In general the welded area will experience longitudinal and transverse tensile stresses, balanced by areas with stresses of a compressive nature. Due to welding, the microstructure of the weld metal and heat-affected-zone (HAZ) is different from that of the base material. In combination with construction details and weld geometry, the mechanical properties vary considerably. Furthermore, residual stresses can have a significant influence on the fatigue life of engineering components. In particular, near surface tensile stresses tend to accelerate the initiation and growth stages of the fatigue cracks, while compressive stresses close to a surface can prolong the fatigue life [3]. Post weld treatments are often carried out to mitigate or re-distribute the residual stresses, particularly at the component surface [4].

In the class of mechanical post weld treatments, most recent developments have occurred in the field of relatively novel high-frequency peening in combination with ultrasonic methods [5]. Although reported results on fatigue life are very promising, the detailed changes induced in the treated material and the mechanisms by which such changes occur are still poorly understood.

Ultrasonic impact techniques [6] make use of the combined effects of the high frequency impacts and ultrasonic oscillations in the treated material. Ultrasonic impact treatment (UIT) has been applied successfully to increase the fatigue life of parts and welded elements, to eliminate distortion caused by welding and other technological processes, to relieve residual stresses, and to increase the hardness of materials.

During welding, non-uniform plastic deformations and phase transformations take place, and residual stresses are generated as a result. The magnitude and nature of these stresses depend on the construction details and the cooling regime and may, especially in the thicker materials of interest in this study, vary

from tensile stresses to compressive stresses. When ultrasonic impact treatment is applied to a weld, in the welded areas the welding induced stresses and those due to the treatment will be superimposed resulting in a re-distribution.

The final mechanical properties of welded joints depend upon the residual stress state, and stress measurements are required in order to understand fatigue performance. Residual stress measurement techniques can be classified as destructive or non-destructive. The former is based on disturbance of the state of equilibrium of the residual stress after sectioning of the specimen, machining, layer removal or drilling. The re-distribution of the internal forces leads to local strains, which are measured to evaluate the residual stress field. The most usual methods are hole drilling, ring core and sectioning [7]. The non-destructive methods are based on the relationship between the physical and crystallographic parameters and the prevailing stress state. The methods most often employed are X-ray and neutron diffraction [8, 9] using the lattice spacing as a strain gauge. Ultrasonic techniques are also available and are based on variations in the velocity of ultrasonic wave propagation in the materials under the action of mechanical stresses [10, 11].

Due to the beneficial compressive stress introduced by the post weld impact treatment, the crack growth threshold of the workpiece is increased and thus fatigue resistance is enhanced [12]. Introduction of ultrasonic waves may lead to a stress relaxation in the as-welded component, which is considered to be helpful for extending of the fatigue performance.

1.2 Research objective

The primary aim of this project is to understand the mechanisms involved in post weld ultrasonic impact treatments, how these affect the residual stress states in the welded area and what influences these have on the development of the microstructure.

This project is divided into two parts: part A focuses on the characterization of microstructure and part B on the characterization of residual stress states before and after post weld treatments by means of experimental and numerical methods. This work is based on part B, the objectives of which are listed as follows:

- Characterization of the base material.
- Multi-pass welding of high strength steel.
- Application of ultrasonic impact treatment to the multi-pass welds.
- Residual stress measurements in the multi-pass and ultrasonic impact treated welds.

- Temperature measurement and validation of the multiple welding thermal cycles.

- Simulation of transient stress and strain relevant to the HAZ in multi-pass welds.

- Understanding of stress evolution in the multi-pass welds on a pass-by pass basis.

- Interpretation of stress relaxation due to the ultrasonic impact treatment.

- Fatigue improvement due to the post weld ultrasonic impact treatment.

1.3 Definitions and conventions

Fig. 1-1 shows the coordinate system used throughout this work. The welding direction is defined as the longitudinal X direction. The in-plane Y and Z directions are defined as the transverse and through thickness directions.
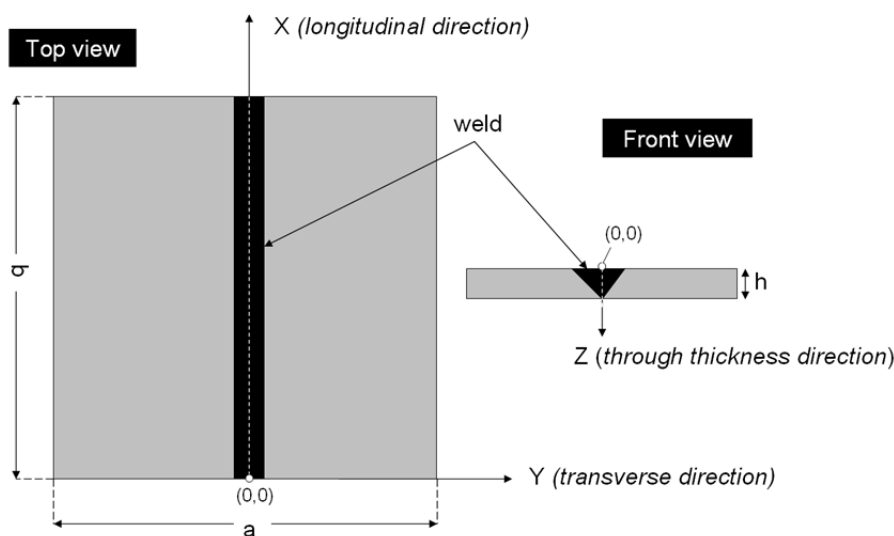
Fig. 1-1: The coordination system in welding.

1.4 Thesis outline

In this thesis several topics relevant to this project are discussed.

In chapter 2, some conventional post weld treatments aimed at improving the fatigue strength of a welded workpiece are firstly introduced, followed by a detailed discussion of a novel post weld technique, 'ultrasonic impact treatment' (UIT). Secondly, residual stress basics, such as definition, origin and

classification, are described. Thirdly, two main classifications of residual stress measurements are specified; *i.e.* destructive or non-destructive. After comparison, synchrotron X-ray diffraction in combination with the centre hole drilling method were selected for this study to characterise the through-thickness residual stresses due to welding and post weld treatments.

High strength steel S690QL1 (Fe-0.16C-0.2Si-0.87Mn-0.33Cr-0.21Mo (wt.%)) was used in this study. A summary of materials is given in chapter 3. Temperature dependent thermal properties were calculated based on the material chemical composition. Temperature dependent mechanical properties were obtained from high temperature tensile testing and free dilatation at different cooling rates.

In chapter 4, the welding arrangement and transient temperature measurements are presented. Six pass welds were made on a 16 mm thick steel section. Two dimensional (2D) shell and three dimensional (3D) solid finite element (FE) models were constructed and validated by comparing the measured and predicted time-temperature profiles. A sensitivity of the model with respect to the input parameters and model constructions is discussed.

Transient stress measurement during welding is difficult to achieve. A transient force and strain investigation relevant to the weld heat-affected-zone (HAZ) in the six pass weld is shown in chapter 5. Electro-thermal mechanical testing (ETMT) was performed to represent the top and bottom surface in the HAZ with similar thermal cycles and constraining conditions during multi-pass welding. Material responses during the multiple thermal cycles, such as thermal expansion, elasto-plastic deformation, and volume changes due to phase transformations are described.

Stress measurements and validation on a pass-by-pass basis are presented in chapter 6. Depth resolved stress measurements in two orthogonal directions were carried out using energy dispersive synchrotron X-ray diffraction. Information concerning stress build-up and evolution with multiple thermal cycles was obtained. The stresses predicted from the FE model are compared with the measured results.

Stress relaxation due to the post weld ultrasonic impact treatment is shown in chapter 7. Different treating parameters, such as travel speed, treating angle, number of treatment passes and temperature of the workpiece prior the treatment, provide different residual stress distributions, which influence the distortion of the workpiece after unclamping. Residual stresses immediately under the treated surface were measured using the centre hole drilling method. Fatigue tests were performed on the specimen to access the effects of welding and ultrasonic impact treatment.

A general discussion for an improvement of temperature dependent material properties and an indication of how to model the UIT process is given in

chapter 8.

In chapter 9, conclusions from this work are drawn and recommendations for future development are presented.

2 Background

Post weld treatments are normally recommended to improve the fatigue strength of a welded workpiece. In this chapter, some conventional post weld treatments are firstly introduced, and followed by a detailed discussion of a novel technique 'ultrasonic impact treatment' (UIT). Secondly, residual stress basics, such as definition, origin and classification, are described. Thirdly, two main classifications residual stress measurements are specified; *i.e.* destructive or non-destructive. After comparison, synchrotron X-ray diffraction in combination with the centre hole drilling method were selected for this study to characterise the through-thickness residual stresses due to welding and post weld treatments.

2.1 Conventional post weld fatigue life extension techniques

The welded joints normally have a low fatigue strength compared to the base material, which is due to the presence of notches and high tensile residual stresses. Notches occur because of the geometry of the joint and weld imperfections such as undercut and slag inclusions. Tensile residual stresses arise from the contraction of the weld metal during cooling and solidification.

In many applications, *e.g.* high capacity lifting construction, there is a tendency to pursue an increase in the performance to weight ratio by applying high strength steels. Improvement of the fatigue strength of welded joints by application of different post weld treatments has therefore received considerable attention lately [13].

Conventional post weld treatment techniques include grinding, air hammer peening, shot peening, needle peening and tungsten inert gas (TIG) re-melting. Depending on function philosophies, these methods can be divided into two main groups as shown in Fig. 2-1: (i) improvement of weld geometry; (ii) residual stress reduction [14].

Machining and re-melting methods can well improve the weld toe profile and reduce stress concentration effects. However, tensile residual stresses remain due to the heat produced in the treatment operation. Mechanical techniques can both improve the weld toe profile and induce beneficial compressive stresses at weld toes.

A very common, reliable and mature technique to reduce residual stresses is by applying a heat treatment. This technique does not influence the weld geometry.

The workpiece is heated to a temperature range causing plastic deformation and held at this temperature for a certain time. Thermal stress relaxation will take place. The cooling rate of the treatment should be slow in order to avoid non-equilibrium phase transformations, which would again introduce stresses. However, this method is limited by high energy consumption and costs. In the next sections some alternative techniques are briefly explained.
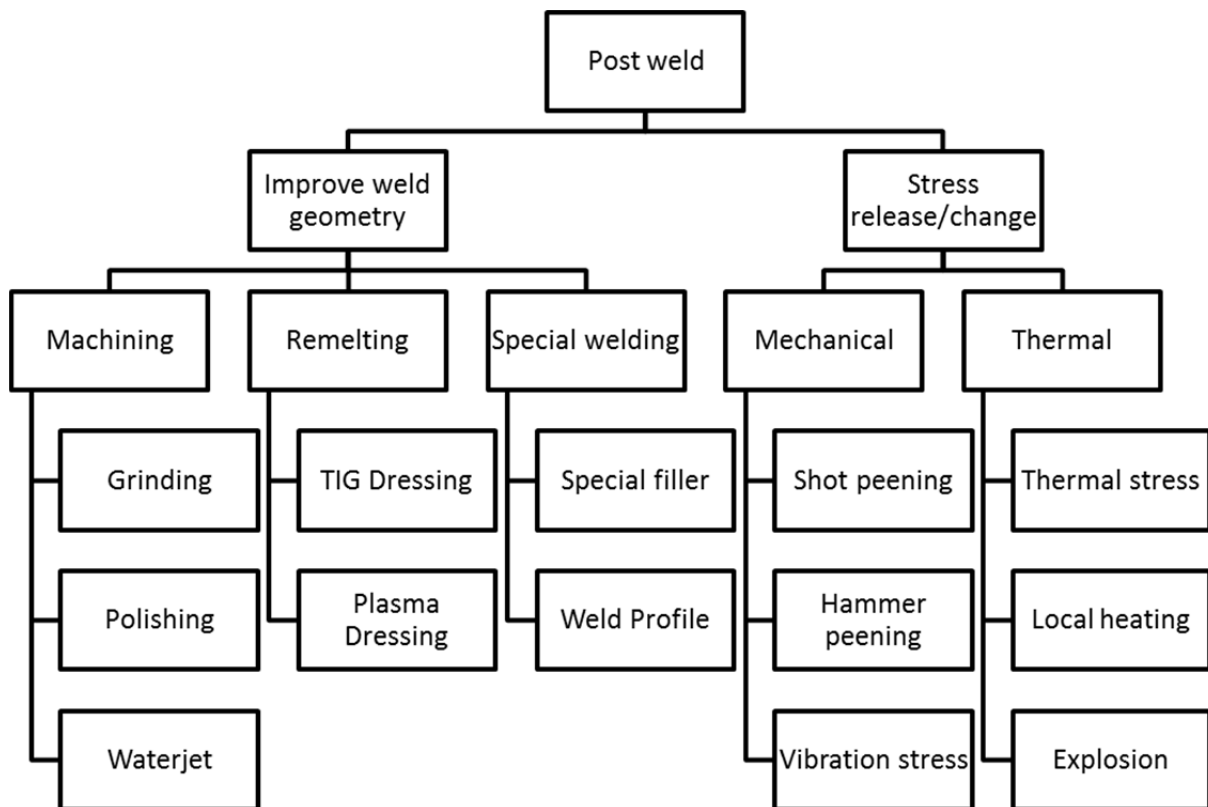
Fig. 2-1: Different post weld fatigue life extension methods [14].

2.1.1 Burr grinding

A significant improvement in fatigue strength of welded constructions can be achieved by burr grinding. Burr grinding [15] aims to remove small crack-like defects at the weld toe, thereby introducing a significant crack initiation delay. A secondary benefit in terms of fatigue performance is achieved by reducing the notch stress concentration at the weld toe, *i.e.*, weld geometry. Burr grinding is most successful when applied to basic weld detail types, such as transversely loaded full penetration T-joints, cruciform joints and butt welds. However, burr grinding introduces groove marks in the direction transverse to the weld which may serve as crack initiation sites. It is not recommended as a treatment for welded joints that are loaded in a direction parallel to the weld.

2.1.2 Tungsten inert gas (TIG) dressing

The TIG dressing [16] improvement technique also aims at removing small

crack-like defects and reducing the notch stress concentration at the weld toe. An improvement in fatigue strength is achieved by means of re-melting. As a result, the weld should be thoroughly de-slagged and wire brushed to remove scale and any oxide layers prior the treatment. If necessary, light grinding may be used to obtain a clean surface. The heat input during TIG dressing is normally less than that used for welding the joint. TIG dressing leads to the formation of a new heat-affected-zone, which can result in unacceptable softening in higher strength steels.

2.1.3 Hammer peening

Hammer peening [17] is applied by plastically deforming the surface with a hammer. This method introduces large residual compressive stresses, which can penetrate into the plate thickness, up to a few millimetres. In cases where surface cracks are repaired by grinding and welding, there may be occasions when crack tips are not fully removed. In those cases, cracks will re-initiate and propagate relatively soon after the repair. By applying the hammer peening treatment, compressive residual stresses are introduced, which can impede the re-initiation of the cracks and therefore greatly extend the fatigue life. The hammer peening treatment requires reasonably accurate positioning of the tool over the weld toe in order to deform metal of both the weld and the parent materials. The resulting groove must be smooth and free from individual indentations.

2.1.4 Shot peening

Shot peening [4] is also used to produce a compressive residual stress layer and to modify mechanical properties of metals. The process works by impacting a surface with 'shots' (round metallic, glass or ceramic particles) with a force sufficient to create plastic deformation. Peening a surface means spreading it plastically and causing changes in the mechanical properties of the surface. These plastic deformations induce residual compressive stresses in the peened surface along with tensile stress in the interior. The surface compressive stresses increase resistance to fatigue and also to some forms of corrosion. The tensile stresses deep in the part are not as problematic as tensile stresses at the surface, because cracks are less likely to start in the interior.

2.1.5 Laser peening

Laser peening [18] is a process in which metal is peened by using a powerful laser. In this process, the surface of the material is covered with a thin layer of opaque material (such as black paint) and over this layer a thick layer of transparent material (such as water) is placed. The laser beam passes through the transparent material and causes a thin layer of the opaque material to vaporize. The rapidly expanding gas is confined by the transparent overlay and creates very high pressures. The surface pressure propagates into the metallic

substrate as a shock wave. With the help of the shock waves, laser peening produces a layer of residual compressive stresses at the surface that penetrates deeper than that attainable from conventional shot peening treatments. The primary benefit of laser peening is a deep compressive layer with minimal cold working, which increases the component resistance to failure mechanisms. This technique is often used to improve fatigue resistance of highly stressed critical turbine engine components [19], but it is not cost effective for general applications.

2.1.6 Vibration stress relief

Vibration stress relief (VSR) [20] is a method using mechanical and other methods to vibrate the workpiece, which may result in releasing the residual stresses. This method has developed rapidly in recent years due to its low investment costs, short production cycle and low energy consumption. Although VSR has been extensively used for more than 40 years, the mechanism of VSR is still under investigation. Quantitative evaluation of the effectiveness of VSR is an essential problem.

2.2 Ultrasonic impact treatment

Ultrasonic impact treatment (UIT) is a novel technique that makes use of mechanical impacts with a high frequency component at the weld toe to improve the final mechanical properties of a weld [21]. Weich *et al.* [22] found that post weld UIT improves the shape of the weld toe; *i.e.* the weld toe radii become more uniform. UIT also introduces compressive stresses at the surface at least up to a depth of 1 to 1.5 mm, which can reach values up to the yield strength. The fatigue life the workpiece is prolonged by this technique.

Compared with the conventional post weld treatment techniques, ultrasonic impact treatment has significant benefits in terms of light weight tooling, low noise, high efficiency, low cost and energy consumption [23, 24]. When applying to welded joints, the UIT changes the crack nucleating mechanism from surface cracking at the weld toe to subsurface. Micro-defects are eliminated and residual compressive stresses are introduced at the weld toe, which results in an extended fatigue life of the welded joint [25].

2.2.1 Background history

The ultrasonic impact treatment technique was originally developed by Statnikov and a team of scientists and engineers in the Soviet Union in the 1970s. It was initially used in submarine manufacturing to strengthen the hulls of nuclear submarines. The technique was further developed at the Northern Scientific and Technological Company (NSTC) in Russia. Over the past few

years, UIT has been developed and expanded by Applied Ultrasonics and introduced for commercial and operational applications. Nowadays, UIT is applied for welding renovation in various industries including bridge construction, offshore structures, crane construction, aerospace, power station and railways [26, 27].

The development of the method in the late 1990s and early 2000s resulted in the current commercial Esonix system [21], which is employed in the present study. The Esonix system controls the quality, properties and characteristics of the surface, modifies material properties in the treatment area, improves the fatigue and corrosion resistance, as well as the resistance to abrasion and contact failures, reduces residual stresses and deformations, and stabilizes and improves static quality and reliability characteristics in mechanical engineering [28-31].
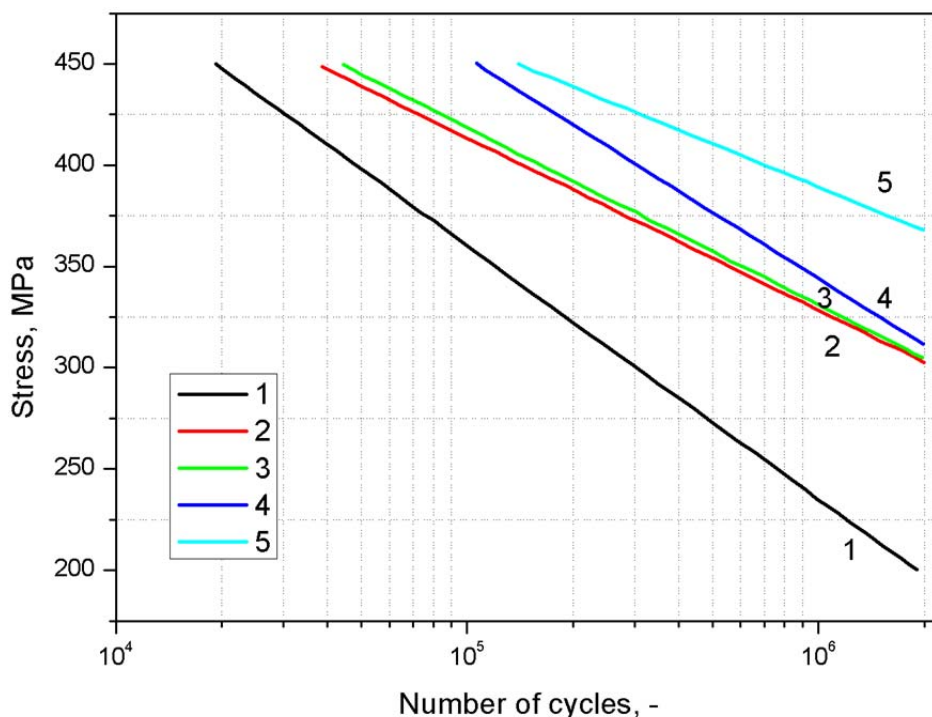
Fig. 2-2: Fatigue curves for welded joints in steel Weldox 420 in the as-welded and improved conditions: 1 – as-welded, 2 – hammer peened, 3 – shot peened, 4 – TIG dressed, 5 – UIT treated using indenters of diameter 3 mm [28].

Since plastic deformation is one of effects accompanying this method, interest in UIT has resulted in analogies between UIT and other conventional plastic deformation treatment methods such as shot peening, hammer peening and ultrasonic peening. UIT is the most effective method to improve the fatigue performance compared with the other post weld treatments. A summary of the results reported by Statnikov [28] is shown in Fig. 2-2.

2.2.2 System and the principle

The ultrasonic impact treating method is based on conversion of harmonic oscillations of an ultrasonic transducer into impact impulses. The UIT equipment comprises an ultrasonic generator and a peening device. The ultrasonic frequencies of 27, 36, 44 and 55 kHz can be generated by means of the ultrasonic generator. Inside of the peening device, electrical energy can be converted into a mechanical vibration by means of the magenetostrictive transducer. A waveguide is installed to enlarge the vibration amplitude from several micrometres to several tens of micrometres. In order to effectively transfer the energy from the waveguide to the workpiece, some free-floating pins are installed at the end of the waveguide. Before the treatment, a movable mass is withdrawn from the surface to store some impact energy into the spring. During the treatment, the pins can cyclically impact the surface of the workpiece with a relatively low impact frequency (around 50 to 100 Hz) and produce a compressive plastic deformed zone below the surface as shown in Fig. 2-3. When the pins are in contact with the treated surface, ultrasonic energy can be conducted into the workpiece. The material and the size of the pins can be adjusted according to the requirements of the treatment [32, 33].
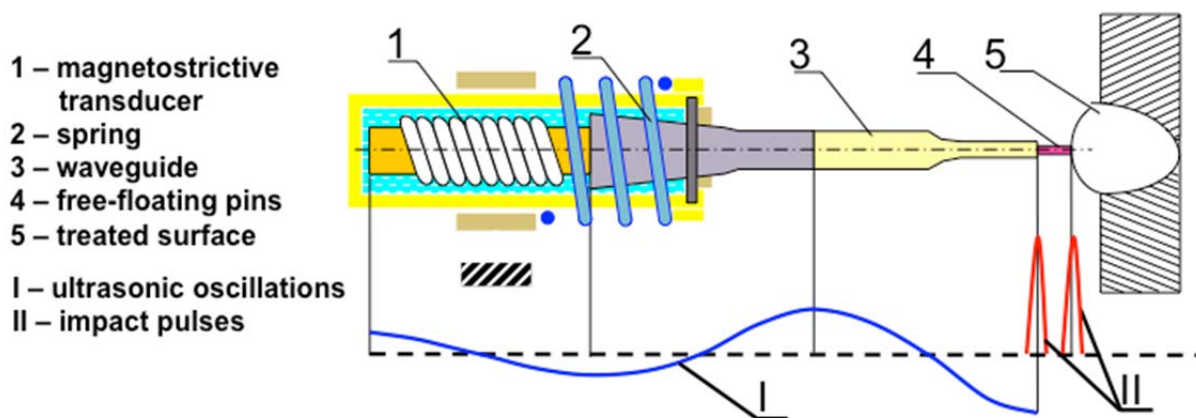
Fig. 2-3: Schematic diagram of UIT peening device [33].

The pins are recommended to place perpendicularly to the surface of the workpiece. As a result, the impact of the pins can be carried out under a load provided by the weight of the tool. When applying at the weld toe, the pins are suggested to keep an angle from the normal and transverse directions, thereby simultaneously treating the weld metal and the heat-affected-zone as shown in Fig. 2-4 [34]. The recommended angle is between 30 to 60 degree.

Fig. 2-4: Application of UIT with multiple indenters at the toe of a weld [34].

2.2.3 Influencing parameters for UIT

Esonix UIT provides four levels of ultrasonic frequency. With different frequencies, the sizes of the tools are different as shown in Fig. 2-5. The frequency in combination with the power determines the vibration amplitude. With the same frequency, it can be expected that, a higher power has a more pronounced effect on the treated material as shown in Fig. 2-6. Tensile testing of an aluminium single crystal with the application of ultrasound shows that the specimen becomes much softer when the power is increased.

Fig. 2-5: Range of high-power hand tools [21].
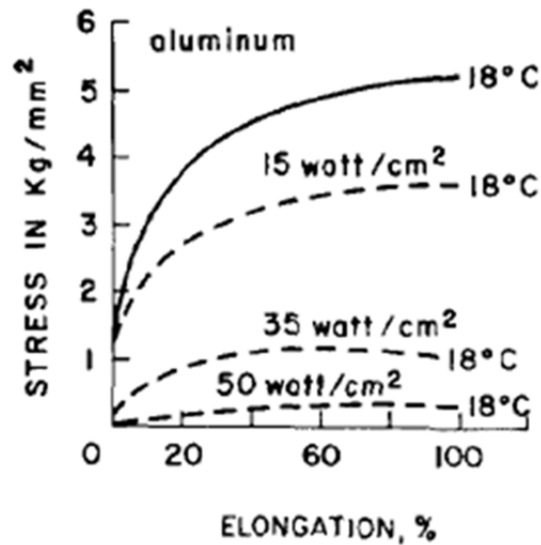
Fig. 2-6: Stress-elongation for aluminium single crystals with ultrasound [35].

For different treated materials, the extent of the treated areas can be different. Fig. 2-7 and Fig. 2-8 represent the indentation area on ultrasonic-free impacting upon an aluminium specimen and a steel specimen. The indentation area becomes larger when increasing the initial pressure. For the aluminium specimen, similar indentation areas are observed with the three cases described. The needle indenters have identical diameter of 6.35 mm but different length of 25 mm and 9.2 mm, respectively. However, the top radius of the needle indenter is not specified. The indentation areas with different needle lengths do not show significant difference. To achieve the same indentation area, ball indenter should have a diameter of 8 mm. For the steel specimen, the indentation area is smaller than that of the aluminium specimen under the same treating conditions, as the hardness of steel is higher than aluminium.
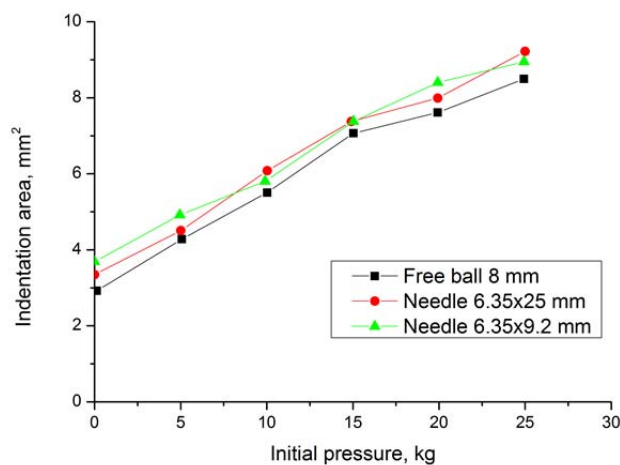
Fig. 2-7: Ultrasonic-free impacting on aluminium alloy [21].
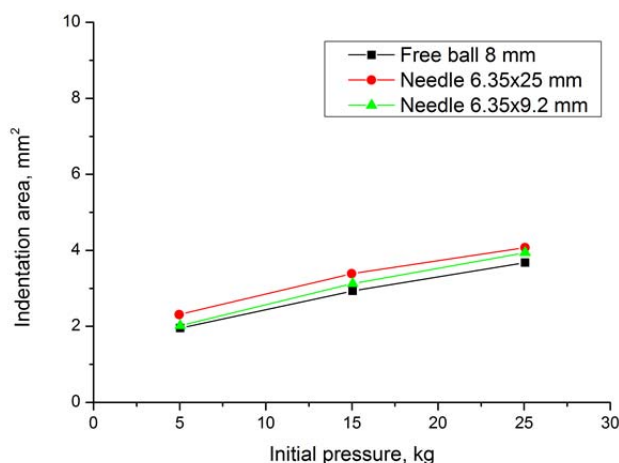
Fig. 2-8: Ultrasonic-free impacting on steel [21].

Fig. 2-9 shows indentation area of ultrasonic and ultrasonic-free impacting upon an aluminium specimen using needle indenter diameter of 6.35 mm and length of 25 mm. When ultrasound is imposed during the impact (vibration amplitude 50 μm), the specimen becomes much softer and the indentation area becomes larger than that without ultrasound. It has to be noticed that Statnikov did not mention how to switch on/off the ultrasound during the treatment. It could be just a comparison of a pneumatic impact and ultrasonic impact with the same initial conditions.
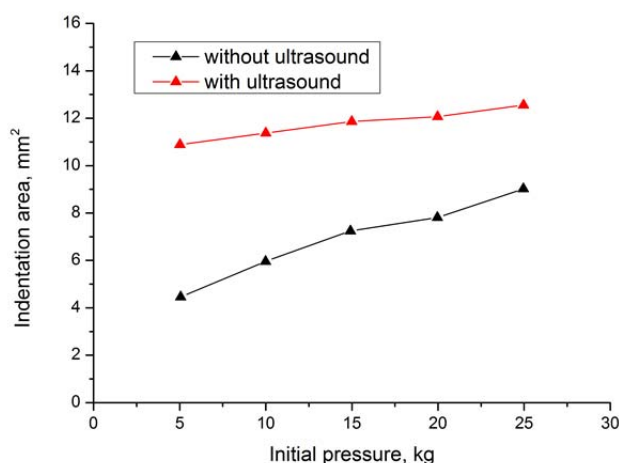
Fig. 2-9: Indentation area with ultrasonic and ultrasonic-free impact [21].

The geometry of the indenter is also one of the important parameters. Fig. 2-10 shows the micro-hardness distribution across the thickness of an aluminium specimen upon impacting by different indenters (vibrational amplitude 50 μm). The ultrasonic impact by a needle indenter increased the micro-hardness of the aluminium specimens from HV_{20} 38 to HV_{20} 72 kgf/mm^2, while impacting by a ball indenter gave a hardness up to HV_{20} 58 kgf/mm^2. In the former case the depth of hardening is 0.4 mm, and in the latter case 0.3 mm. This might

because the needle indenter has high displacement stability on the treated area, while the ball indenter has unlimited freedom of displacement in any direction.
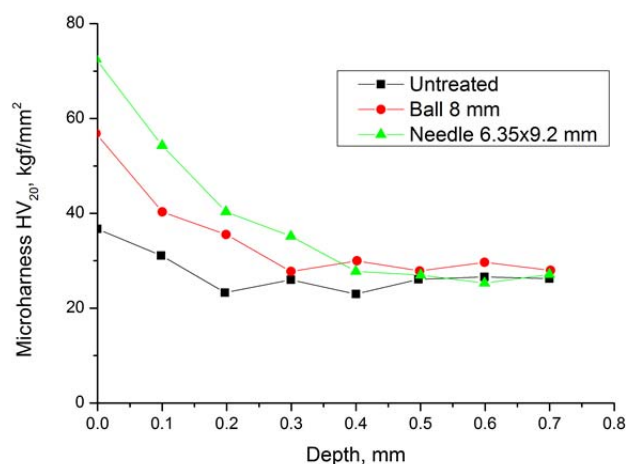
Fig. 2-10: Micro-hardness change due to UIT [21].

2.2.4 Impact control

Statnikov [26] reports general control parameters for the ultrasonic impact treatment. The UIT tool should be fixed at right angles to the surface to be treated and pressed against it with an axial force of 20 to 40 N (2 to 4 kg). This force is suggested to be created by the weight of the tool itself. Generally, the operating frequency of the ultrasonic generator is 27 kHz, and current is 10 to 14 A. The vibration amplitude of the output end of the waveguide is in the order of 25 to 40 μm, which is automatically controlled by the setting of the output power in the range of 600 to 1200 W. A 3 mm diameter of impact pins (indenters) is recommended. When treating the welds, which are easily accessible, 3 to 4 pins are used in a row. The average travel speed is suggested to be between 0.3 to 1.5 m min^{-1} (5 to 15 mm s^{-1}).

2.2.5 Effects of UIT on material properties and behaviour

The effect of UIT on the material is schematically shown in Fig. 2-11, which demonstrates the zones of physical action on a welded joint in a cross-sectional view of the surface layer of the treated metal. The UIT process is accompanied by quick local heating of the material at the ultrasonic impact point and quick heat removal from this area. However, the temperature in this region is not yet known. In addition, intense plastic deformation occurs in this area. The combination of the above conditions produces a material with new properties that appears on metallographic pictures as a 'white layer', which is not apt to etching as shown in Fig. 2-12. This material is characterized by high contact strength and corrosion resistance [36]. In the 'plastic deformation zone', the effect of cyclic endurance, compensation of the deformation and corrosion-fatigue strength can be improved. In the 'Impulse relaxation zone',

the residual stress and strain can be reduced by up to 70% of the initial state. In the 'Ultrasound relaxation zone', the residual stress and strain can also be reduced by up to 50% of the initial state.

Zones	EFFECT
"White layer"	Wear-resistance, corrosion resistance
Plastic deformation	Cyclic endurance, compensation of deformation, corrosion-fatigue strength
Impulse relaxation	Reduction in residual welded stress and strain of up to 70% of the initial state
Ultrasound relaxation	Reduction in residual welded stress and strain of up to 50% of the initial state
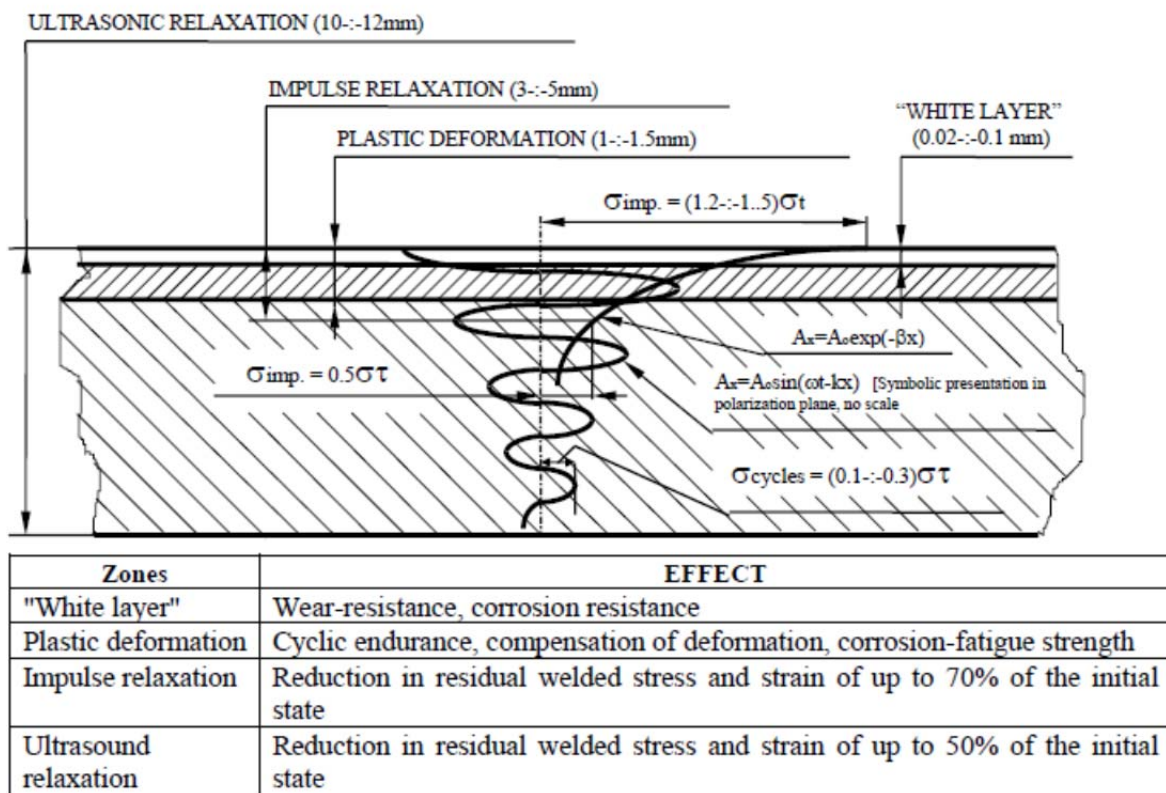
Fig. 2-11: UIT action physical zones [21].
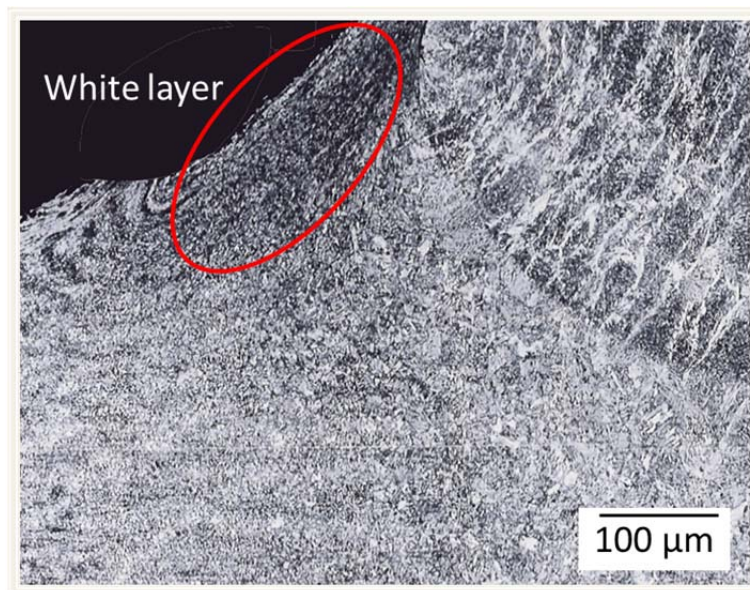
Fig. 2-12: White layer in the UIT zone [21].

The treatments can influence the fatigue life of the workpiece. Most publications in the literature only indicate the number of cycles to failure.

Weich *et al.* [22] carried out a more detailed study and reported that the improvement is mainly caused by an extension of the crack initiation and propagation phase in the surface layers. This conclusion is not unexpected. Thermal imaging facilitates analysis of the early crack initiation behaviour. The results show that after UIT, several small cracks occur. Except for the final crack which leads to rupture, these cracks grow slowly up to a depth of 1.5 to 2 mm shown in Fig. 2-13. In this surface layer compressive residual stresses are produced by UIT, which leads to a reduced crack propagation velocity.
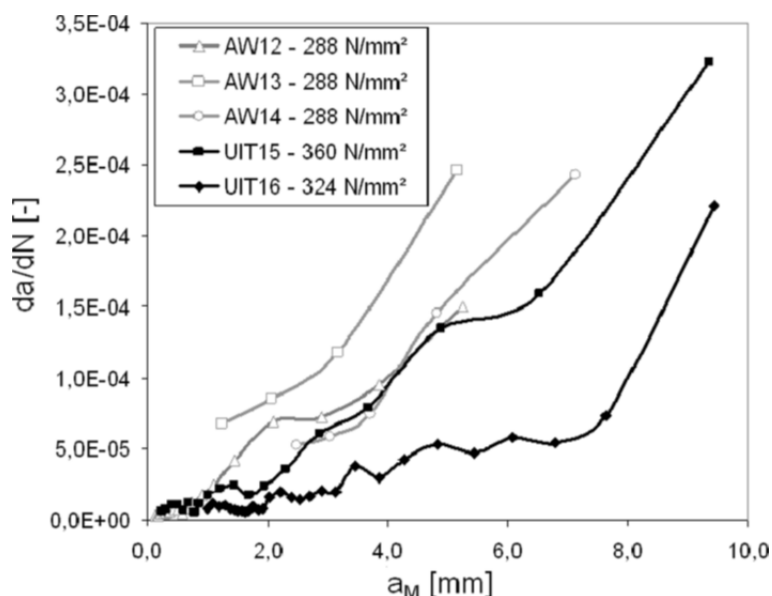
Fig. 2-13: Increase of the change of the crack size (da) depending on the medium crack depth [22], (AW: as-welded condition, 12 to 16: number of samples, stress range is given behind).

2.3 Residual stress basics

2.3.1 Definitions of stresses

A material object of cross section, *A*, which could be a structure, a component, a specimen, a volume element within a test piece *etc.*, subjected to a force $\underline{F}$ experiences a stress $\underline{\sigma}$ that is equal to the force divided by the surface area over which it is acting,

$$\underline{\sigma} = \frac{\underline{F}}{A}.$$

$\hspace{10cm}$ (2-1)

A distinction is made between normal stresses $\underline{\sigma}$ generated by forces normal to the cross section under consideration, and shear stresses $\underline{\tau}$ generated by forces parallel to the observation plane. Fig. 2-14 illustrates this.
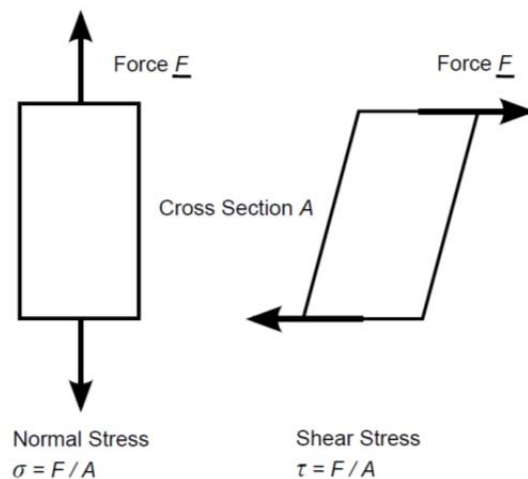
Fig. 2-14: Normal and shear stresses.

In three-dimensional space, a second rank tensor is obtained, describing the stress state at the location of interest within an object:

$$\sigma_{ij} = \begin{pmatrix} \sigma_{11} & \sigma_{12} & \sigma_{13} \\ \sigma_{21} & \sigma_{22} & \sigma_{23} \\ \sigma_{31} & \sigma_{32} & \sigma_{33} \end{pmatrix}.$$

(2-2)

Indices 11, 22, and 33 represent normal stresses, while the other combinations are used for the shear components. Fig. 2-15 illustrates the situation. A force $\underline{F}$ = (F_1, F_2, F_3) defined in co-ordinate system (X_1, X_2, X_3) acting on a small cubical volume element at the location of interest, gives rise to a stress state at this location that can be described by the stress tensor in Equation (2-2).
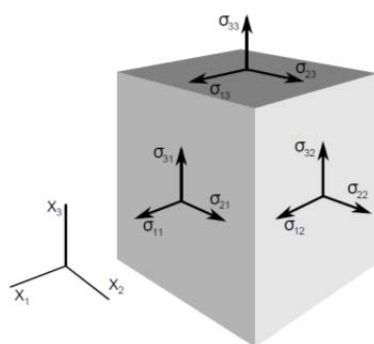
Fig. 2-15: Components of the stress tensor σ in co-ordinate system (X_1;X_2;X_3) [37].

The normal stresses are distinguished as tensile or compressive, depending on whether the force causes the object to expand (tensile stress) or to contract (compressive stress) at the location of interest. Tensile stresses are quantified by positive numbers, while negative values describe compressive stresses.

19

2.3.2 Origin of residual stress

Residual stresses can be considered as internal stresses, which maintain a balance within the materials after external forces are removed [38]. During the processing of metals, such as casting, pressing, welding, cutting, heat treatment and assembly, different levels of residual stresses can be generated within the workpiece. These stresses influence the mechanical behaviour of the materials. Compressive residual stresses distributed at the surface, may improve the fatigue strength, increase the resistance to stress corrosion and thus prolong the life of parts and components; whereas tensile residual stresses at the surface reduce the fatigue life time, the resistance to stress corrosion, the dimensional accuracy, and may even lead to unexpected deformation, cracking and other incidents of early failure.

The origin of residual stresses can be illustrated as follows [37],

a. Elastic misfits

Residual stresses can be introduced by elastic misfits, and they are a function of both stiffness and misfits. Fig. 2-16 shows a parallel bar structure. Bar A is slighter shorter than bar B. When attaching bar A with the upper frame, all the bars are deformed in the elastic region. Bar A is under tension and bar B is under compression. Assuming K_A and K_B are the stiffness of bars A and B, α is the ratio of K_B/K_A. The displacement of bar A and B varies when α is different. Peg-in-a-hole and shrink fitting can be examples for residual stresses caused by elastic misfits.
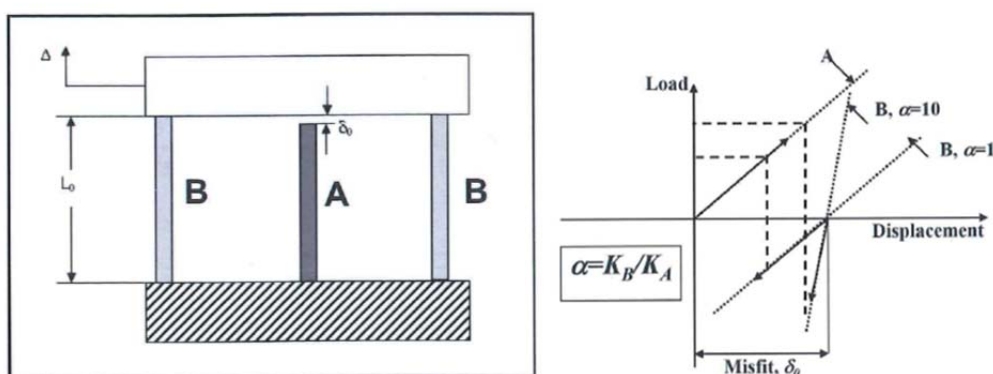
Fig. 2-16: Elastic misfit bar model [39].

b. Elastic-plastic misfits

Plastic deformation occurs in ductile materials when loaded beyond their elastic limit. This type of deformation is in general irreversible; *i.e.* the material does not return to its original shape once the load is removed. Elastic deformation can be recovered after removal of the load.

c. Temperature gradients

During surface coating, quenching or welding process, surface regions normally cool faster than the interior of the material. In extreme cases the thermal gradients can be sufficiently large to cause plastic deformation. In quenching processes this effect is further enhanced, mostly aiming at the introduction of beneficial compressive surface residual stresses.

d. Phase transformation

Residual stresses can be generated during the phase transformation of low alloy steels from a body centred cubic (bcc) to a face centred cubic (fcc) structure at high temperatures and vice versa, which corresponds to a rapid change of the specific volume of the crystallographic cell.

e. Composite materials

Composite and multi-phase materials are functional materials making use of a combination of the attractive features of their constituents. Different material properties (coefficients of thermal expansion) can lead to a shape mismatch and residual stresses are generated.

2.3.3 Classification of residual stress

Residual stresses are classified based on the length scale into three groups as shown in Fig. 2-17.

Type I: This type deals with residual macro-stresses. The length scale in this category should be large enough to cover all phases presented in the material and contain a sufficient number of crystallites. Releasing of this type of stress causes macroscopic shape change of the material. The main focus of this study is on this type of residual stresses.

Type II: This type is referred to meso-stresses. These stresses act between adjacent grains. Releasing of this type of stress causes macroscopic distortions. As an example, if there is a deformation gradient (or temperature gradient) between grains in a material, this type of residual stresses will be generated.

Type III: Similar to type II, this type of stress deals with micro-stresses. They act on the inter-atomic level. For example, different impurities of atomic lattice can generate such stresses. Releasing of this type of stress does not cause macroscopic distortion.
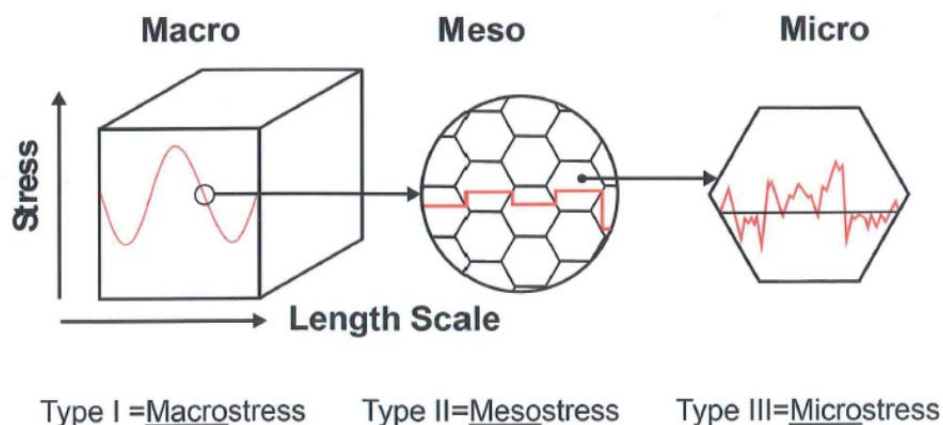
Fig. 2-17: Classification of residual stresses [39].

2.4 Residual stress measurement techniques

Techniques to measure the residual stresses within the materials can be classified as either destructive or non-destructive [40], see Fig. 2-18. Destructive methods, such as centre hole drilling, ring core and deep hole drilling are partially destroy the tested specimen. Block removal splitting and layering (BRSL), slotting and contour mapping require complete destruction of the tested specimen.

Centre hole drilling (CHD) is mainly used for close surface less than 2 mm measurement. The diameter of the hole is around 1 to 2 mm with a depth resolution of 0.1 mm. The ring core method can achieve deeper measurements to 5 mm below the surface; however the diameter of the ring is relatively large (10 mm). With the same depth resolution, the mean stresses are measured representing a larger area. Deep hole drilling (DHD) can reach a thickness of 750 mm with a very good spatial resolution; however the set-up is not readily accessible and is expensive. All three semi-invasive methods can provide incremental in plane stress information, *i.e.* two principal stresses and one shear stress as a function of thickness. The specimen can be reused at the position far away from the previous measurement. BRSL can reach a measurement depth of 250 mm. However, this method can only provide two principle stresses. Contour mapping only provides one stress component, where a mapping of the cross section can be obtained. The specimen of the latter two methods cannot be reused. Detailed information can be found in Table 2-1.
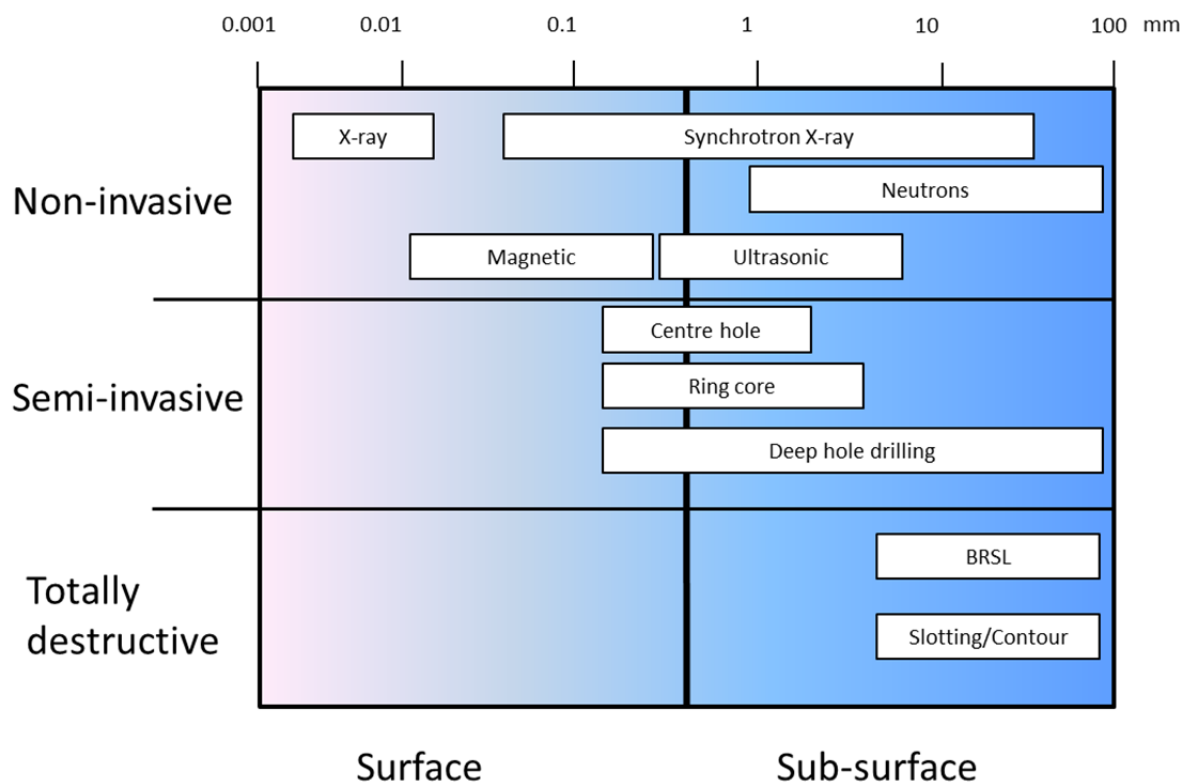
Fig. 2-18: Residual stress measurement techniques.

Table 2-1: Destructive residual stress measurement.

CHD	Ring core	DHD	BRSL	Contour
t < 2 mm	t < 5 mm	t < 750 mm	t < 250	t < 75 mm
$\sigma_{xx}(z)$	$\sigma_{xx}(z)$	$\sigma_{xx}(z)$	$\sigma_{xx}(z)$	$\sigma_{xx}(y, z)$
$\sigma_{yy}(z)$	$\sigma_{yy}(z)$	$\sigma_{yy}(z)$	$\sigma_{yy}(z)$	
$\sigma_{xy}(z)$	$\sigma_{xy}(z)$	$\sigma_{xy}(z)$		

For non-destructive method, lab X-ray diffraction is used in the surface stress measurement (several micrometres). Synchrotron X-ray diffraction can penetrate thicker steel plates. Some of the synchrotron radiation facilities can provide very high energy flux, which can extend stress measurements to depths of several centimetres. The exposure time for each measurement is short (several minutes), and this method is useful to construct a through-thickness stress map. Neutron diffraction is often used for the stress measurements on large dimension specimens; however the exposure time for each measurement is relatively long (half hour).

2.4.1 Destructive methods

The destructive techniques are based on disturbing of the state of equilibrium of the residual stresses due to sectioning of the workpiece, machining, layer removal or drilling. The re-distribution of the internal forces leads to local strains, which can be measured to evaluate the residual stress field.

a. Centre hole drilling

The most common method is centre hole drilling (CHD). The centre hole drilling method (ASTM Standard E837) [41, 42] relies on stress relaxation, when a hole is drilled into the centre of a rosette strain gauge, as shown in Fig. 2-19(a) type A. When the material is removed by drilling, the gauges monitor the extent of the strain relief and the direction, and magnitude of the principal stresses can be calculated. The principle of the measurement is based on the influence of stress on the electrical conductance and resistance of the strain gauge material. An electrical conductor will become narrower and longer when it is stretched within the limits of its elasticity. This change increases its electrical resistance. Conversely, a conductor will broaden and shorten under compressive forces thereby decreasing its electrical resistance. Therefore, it is essential that the strain gauge is tightly connected to the surface of the workpiece. As the surface of a weld is not flat in general, different types of strain gauges are required. A common strain gauge applied near welds is depicted in Fig. 2-19(a) type B.
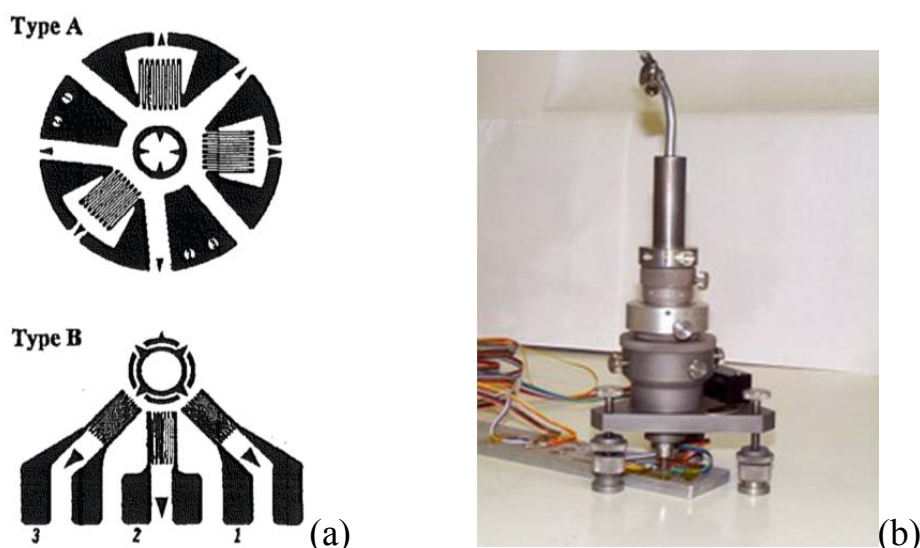
Fig. 2-19: (a) Strain gauges, (b) centre hole drilling equipment [42].

A special high speed air turbine drill, as shown in Fig. 2-19(b), is first located over the rosette centre and then used to remove material to a controlled depth. At each depth increment, the strain relief at each of the gauges is measured and converted into stress. Upon subsequent material removal the stress distribution as a function of depth can be obtained. In other words, during intermittent hole

drilling, the strains are measured at the surface, from which a stress profile in the thickness direction can be calculated. The centre hole drilling method is used in those situations where the residual stress is relatively uniform over the drilling depth.

Beaney [43] estimates the error in stress measurements by hole drilling in steel to be around 8%. When the stresses are greater than 60% of the yield strength, the level of error increases due to local plasticity of the hole.

b. Ring core method

The ring core (RC) method [44] involves cutting an annular groove into a component and the resulting surface strain relaxation within the central core is measured at predetermined depth increments using a strain gauge rosette, see Fig. 2-20. The surface strain relaxation is then decomposed into residual stresses for each depth increment using numerically determined influence coefficients. Typically, depths are limited to 5 mm for a standard 14 mm diameter core.
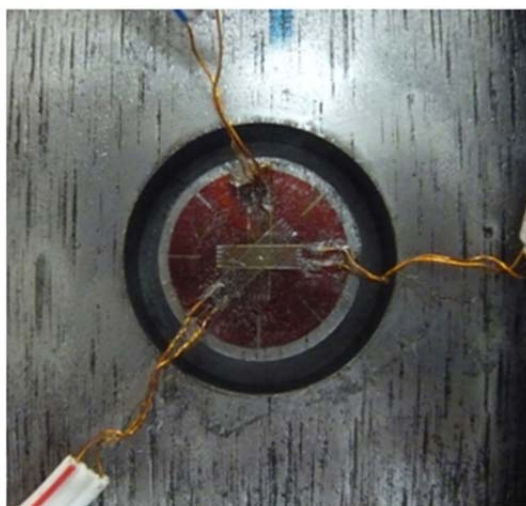
Fig. 2-20: Ring core method [39].

The ring core method offers the following advantages over the hole drilling method. The strain signal produced in the ring core method is nominally an order of magnitude greater than in hole drilling because the strains are more fully relaxed under the strain gauge rosettes. Hole drilling can only be used to quantify the residual stresses that are less than nominally half of the yield strength of the material [45]. This is due to the stress intensity factor around the hole that is introduced inside the monitoring strain gauge grids. Using the ring core method, material around the strain gauge grid is removed, which does not produce a stress intensity factor under the active strain gauge grid. Stress can be measured accurately up to the yield strength. The ring core method is less sensitive to errors involved in placement of the cutting tool relative to the strain gauge since the strain relaxation is uniform. The depth of the measurement can

reach 5 mm from the surface, however, the measured in-plane stresses are averaged over a relatively large area compared to hole drilling.

c. Deep hole drilling

Deep hole drilling (DHD) [46] involves the machining of holes with a relatively large depth to diameter ratio. The technique involves drilling a reference hole through the component and accurately measuring its diameter before and after stress release by trepanning coaxially around it. The differences between the measured diameters before and after stress release enable the original residual stresses to be calculated using elasticity theory. Fig. 2-21 shows a schematic of the 4 main steps involved during the DHD process.

The advantages of deep hole drilling are listed as follows: semi-destructive enables repeated residual stress measurements at many different stages in component life; residual stresses can be measured at depths up to 750mm; laboratory or 'on-site' measurements; through-thickness bi-axial residual stress distribution measured (*e.g.* σ_{xx}, σ_{yy} and τ_{xy}), including stress gradients; high magnitude residual stresses can be measured (*i.e.* can take account of plasticity); applicable to both simple and complex component shapes; applicable to a wide range of materials, both metallic and non-metallic; and fast process in relation to the quantity of stress information produced. However, DHD is not suitable for measurements in thin sheet (less than 6 mm), and it is much more expensive than centre hole drilling and ring core method.
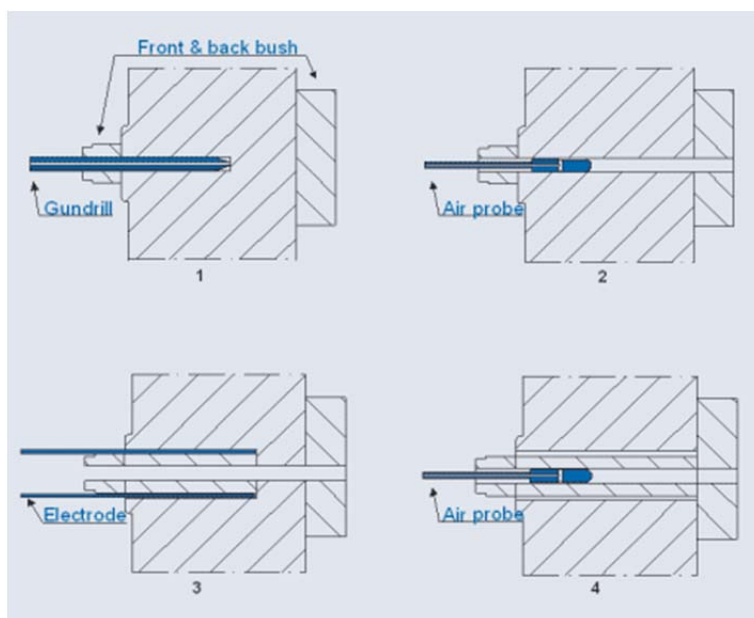
Fig. 2-21: Schematic pictures of the 4 main steps involved during the DHD process [39].

d. Contour method

The contour method [47] allows for high-resolution one dimensional (1D)

stress mapping across the entire cross sections of test pieces. It is applied in three basic steps. First, the component is cut by electro-discharge machining (EDM) into two pieces along the cross-section, where the measurement is taken. Then the deflections caused by residual stresses are measured across the cut surface by means of a co-ordinate measurement machine. Finally, by analytical or numerical methods, the residual stress field is derived that would force the cut surface back into the shape it had before cutting, namely flat, see Fig. 2-22. A high resolution map of the stresses normal to the cut is obtained. However, this method provides only a uni-axial residual stress measurement, and cannot easily be applied on components with complex shapes.
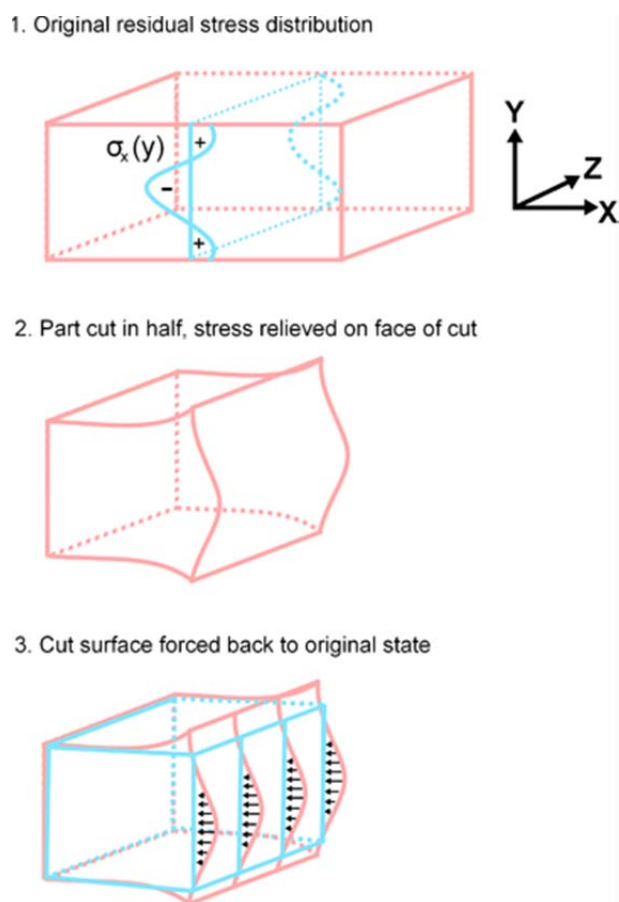
Fig. 2-22: An illustration of the principal used to calculate residual stresses from the cut surface distortions [39].

2.4.2 Non-destructive methods

The non-destructive techniques to measure residual stresses include diffraction methods, ultrasonic wave velocity and magneto-acoustic emission [48] *etc.*.

a. Diffraction methods

The residual stress measurement techniques of both X-ray diffraction and

neutron diffraction use the distance between crystallographic planes as a strain gauge. The elastic deformations cause changes in the spacing of the lattice planes from their stress free value to a new value that corresponds to the magnitude of the residual stress. The atoms in a crystalline sample are arranged periodically in a lattice. An incident beam with a specific wavelength will be scattered by the lattice. The interference between the reflected rays will be destructive for most directions, but it will be constructive when Bragg's law is fulfilled. As an illustration Fig. 2-23 shows the diffraction pattern of a 440C steel [49]. This is a quenched and tempered martensitic steel and diffraction peaks of several ferrite planes and carbides are indicated.
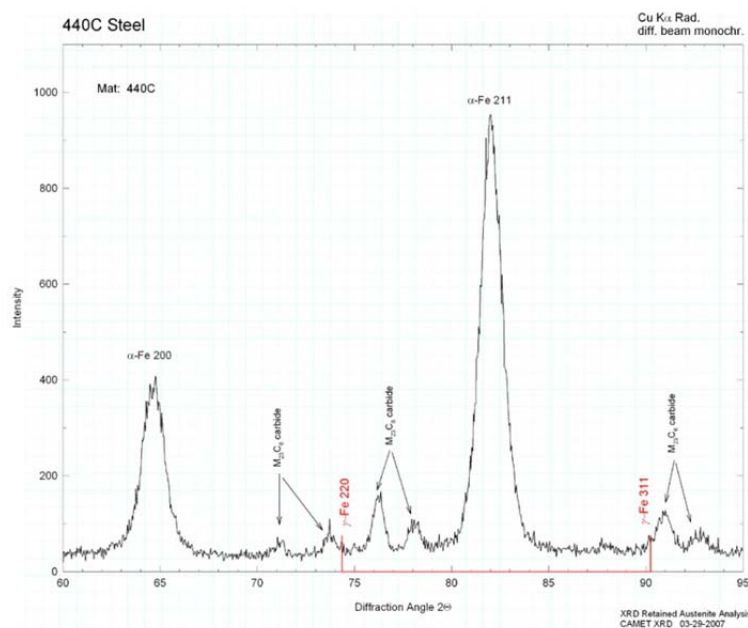
Fig. 2-23: X-ray diffraction pattern, intensity as a function of diffraction angle, of 440C alloy steel [49].

For a specific X-ray wavelength, the diffraction angle, *2θ*, is measured experimentally and the lattice spacing is calculated using Bragg's law [50]

$$2d_{hkl}\sin\theta = n\lambda \text{ ,}$$

(2-3)

where d_{hkl} is the distance between the lattice-planes, θ is the angle between the X-ray and the surface, also known as diffraction angle or Bragg angle (Fig. 2-24), λ is the wavelength of the X-ray and *n* is the integer determined by the order given. At an angle θ, the constructive interference of the waves will cause a peak in the diffraction pattern; this peak position can be related to the *d*-spacing through Bragg's equation.

28
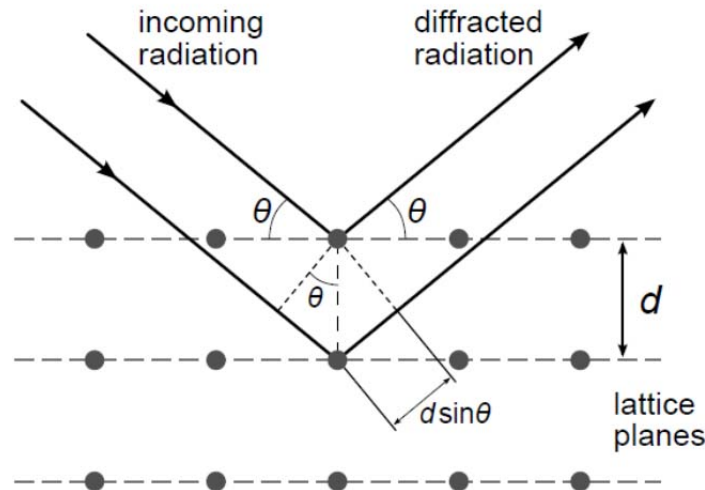
Fig. 2-24: Diffraction of X-ray on a set of lattice planes with inter-planar spacing d_{hkl} [8].
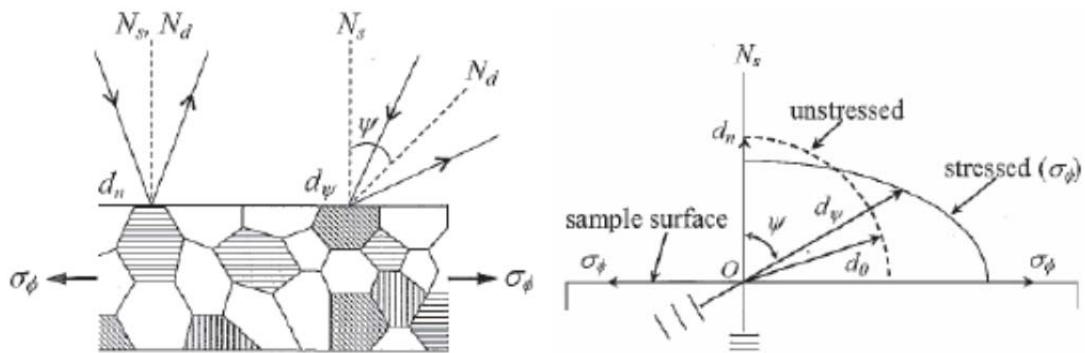
(a)   (b)

Fig. 2-25: Principle of strain measurement, with (a) diffraction on grains, and (b) a vector diagram of the lattice spacing in varying directions. N_s is the normal to the surface, N_d is the normal to the diffraction planes, σ_ϕ is the applied uni-axial stress, ψ is the angle between N_s and N_d and d is the lattice spacing [8].

Consider a piece of material that is uni-axially stressed in the direction ϕ (σ_ϕ), as schematically shown in Fig. 2-25(a), where N_s is the direction normal to the surface and N_d is the direction normal to the diffraction planes [8]. The strain in the direction normal to the surface ε can then be written as

$$\varepsilon = \frac{d_n - d_0}{d_0},$$
(2-4)

where d_n is the lattice spacing of the grains that have their lattice planes oriented parallel to the direction ϕ and d_0 is the stress free lattice spacing. Assuming that the material is isotropic, Hooke's law can be used to calculate

the stress

$$\sigma_\phi = \frac{E(d_n - d_0)}{v \cdot d_0},$$ (2-5)

in which E is the Young's modulus and v is the Poisson's ratio. Only the grains with their lattice planes oriented perpendicular to N_d will contribute to the diffraction.

For an applied stress σ_ϕ, the lattice spacing will depend on the orientation of the diffracting lattice planes. For the case depicted in Fig. 2-25, the lattice spacing of the grains with their lattice planes oriented parallel to σ_ϕ will become smaller than d_0, while those with their lattice planes oriented perpendicular to σ_ϕ will become larger. In other words the lattice spacing is a function of the measurement direction ϕ, as schematically shown in Fig. 2-25(b). This relation is very useful for the determination of multi-axial stresses and forms the basis of $sin^2\Psi$-method. For a bi-axial stress situation, the stress in an arbitrary direction can be found by using the same principle as explained in detail by Cullity [8].

The errors in the determination of stresses by means of XRD are dependent on several factors. The instrumental factors are in general well known for the specific equipment. These include alignment, centre of rotation and background noise issues. Diffraction angles (2θ) must be obtained precisely, within 0.01°. With respect to the determination of d_0, the chemical composition of the material is of crucial importance. The residual stress can be altered based on the change of chemical composition, for instance decarburization [51].

Besides the chemical composition, microstructural effects influence the XRD pattern. The grain size (*i.e.* the number of grains which may diffract), stacking faults, anisotropy, twinning and texture are issues that must be considered. In addition, the presence of strains in the specimen may lead to a shift and broadening of the XRD peaks. This is shown schematically in Fig. 2-26.
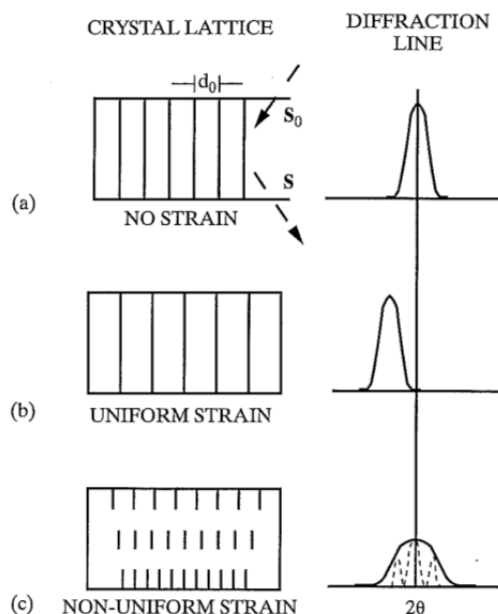
Fig. 2-26: Effect of uniform and non-uniform strains (left side) on diffraction peak position and width (right side). (a) shows the unstrained sample, (b) shows uniform strain and (c) shows non-uniform strain within the volume sampled by the X-ray beam [8].

Several X-ray sources for diffraction experiments are available. Laboratory X-ray diffraction is a method to evaluate very shallow surface stresses, as the penetration depth of X-rays usually does not exceed 30 to 40 μm. Delft University of Technology can provide such a facility to measure the residual stresses using the $sin^2 \Psi$-method. The beam size could be varied by the beam slits, and a size of 0.5×2 mm^2 is recommended by Van der Aa [52].

Energy dispersive synchrotron X-ray diffraction is a versatile and powerful tool for materials research providing a full X-ray spectrum at a single diffraction angle. The combination of high flux, spectral information and excellent beam definition offers the prospect of a high spatial resolution with short counting times, opening up a whole new range of possible applications ranging from basic materials engineering to dynamic *in situ* measurements. Synchrotron X-rays have a higher energy and will penetrate deeper compared with Laboratory X-rays. The photon energy range can reach 300 keV, which together with the high flux allows penetration depths of several centimetres in most engineering materials [53].

The physical principle of neutron diffraction is identical to the X-ray diffraction method, but allows stress measurements throughout plate thickness up to 50 mm in steel and 100 mm in aluminium [54]. Neutron diffraction utilizes approximately 10^3 greater penetrating power than laboratory X-rays. This makes it possible to measure through-thickness stress profiles [55]. However, the diffracting volume cannot be reduced beyond a certain limit, otherwise

counting times become extremely long or counting statistics will be poor.

b. Velocity of ultrasonic propagation

The velocity of ultrasonic propagation [7, 56] in an isotropic elastic body is proportional to the stress intensity in the workpiece. Within metal component, longitudinal ultrasonic waves have a different propagation velocity due to the non-linear relationship between strain and displacement, from which the residual stress can be calculated. If the ultrasonic power is large enough, the ultrasonic waves can penetrate any thickness of the workpiece, so that it can be used to measure three-dimensional residual stresses in components. It is fast and is simple to set-up, but the method is still in the experimental stage and is not widely used. To apply this technique at a weld or an impact treated weld will be difficult as stress gradients are large, changes in microstructure occur depending on the thermal cycle and texture and anisotropic effects due the treatment will make a calibration difficult.

c. Magneto-acoustic emission

Magneto-acoustic emission [7, 56] is a method based on the principle that, the residual stress in a workpiece will obstruct the movement of magnetic domain. This method is also referred to Barkhausen noise measurement. When a ferromagnetic material is magnetized, sudden discontinuous movement of the magnetic domain will produce elastic waves. These waves can be monitored by acoustic emission equipment [57]. Nowadays, the MAE method is widely used to measure the residual stress of ferromagnetic material. The method is fast and can be applied without contact, which is advantageous. However, the results are affected by many factors. This technique is very material sensitive, and thus careful calibration is required. In addition, it is required to apply an external magnetic field, which may result in inhomogeneous magnetization, high energy consumption, remanence and magnetic pollution.

2.5 Concluding remarks

High strength steels are increasingly used for heavily loaded constructions. After welding, the generated residual tensile stresses are harmful for the fatigue life of the workpiece. Post weld treatments are therefore suggested. Ultrasonic impact treatment (UIT) is a novel technique applied to the toe of welded joints, which improves the weld geometry, introduces beneficial compressive stresses at the surface, and re-distributes or releases the residual stresses in the welded workpiece. As a result, the reliability of the welded joint is improved in terms of extending the fatigue life.

A large number of techniques is available to measure residual stresses, each of these have advantages and disadvantages. The selection of appropriate

techniques should be based on the spatial resolution required and the location where alteration of the stresses are expected. For destructive methods, incremental centre hole drilling is adopted for close surface (2 mm below) stress measurement with a very high spatial resolution. The ring core method can provide a deeper measurement with a depth of 5 mm, while the in-plane stress is averaged over a large area. Deep hole drilling is suitable for stress measurements of very thick sections (up to 750 mm). The contour method can provide a stress map of an entire cross section, however only one stress component is measured. For non-destructive methods, laboratory XRD can be used to measure stresses near the surface up to 0.05 mm. Magneto-acoustic emission and ultrasonic propagation can cover the range between 0.3 mm to 1 mm. For deeper penetration, synchrotron XRD and neutron diffraction are recommended for a depth of several tens of millimetres. In this study, the stress build-up and re-distribution due to deposition of a weld bead, and the stress relaxation due to post weld ultrasonic impact treatment are of the interests over the entire plate, and synchrotron XRD is therefore selected as the most appropriate method to represent the bulk stresses. However due to the elongated gauge length in synchrotron XRD, stresses at positions located within 1 mm from the surface cannot be obtained. Underneath the weld toe, a compressive region is generated due to the mechanical impact, centre hole drilling method can be used in combination with synchrotron XRD to obtain a full stress profile through thickness.

3 Materials

During welding, the material from the weld zone to the base material behaves differently due to local heating, and the temperature dependent material properties are therefore of importance to understand the material responses and construct reliable numerical welding models. Thermal properties at elevated temperatures, such as density, thermal conductivity and specific heat are dependent on the chemical composition of the material. Mechanical properties at elevated temperatures can be different due to different pre-processing procedures. High temperature tensile testing and free dilatation testing can be applied to obtain the Young's modulus, yield stress and expansion properties.

3.1 High strength steels

High strength steels (HSS) have a high yield and tensile strength, and are therefore extensively used in high load bearing body structures, such as jacket structures, bridges, buildings and cranes.

Fig. 3-1 shows the steel development of several strength classes over the last decades. The steels are classified according to the yield strength in combination with the manufacturing route. Different manufacturing strategies are applied to obtain the steels, *i.e.* normalizing (N), thermo-mechanically rolling (M) and quenching and tempering (Q). The temperature cycle of the processes are schematically presented in Fig. 3-2.

The conventional fine grained normalized construction steels (N-type) with a yield strength up to 460 MPa are manufactured by heating the steel to 920 °C, followed by air cooling. The solid state phase transformations during this cycle invoke grain refinement. An alternative procedure for obtaining high strength is thermo-mechanically rolling, and a yield strength ranging from 355 to 700 MPa can be achieved. The steels are rolled at relatively low temperatures and have excellent toughness and weldability properties. An even higher yield strength ranging from 690 to 1100 MPa can be obtained by quenching and tempering process.
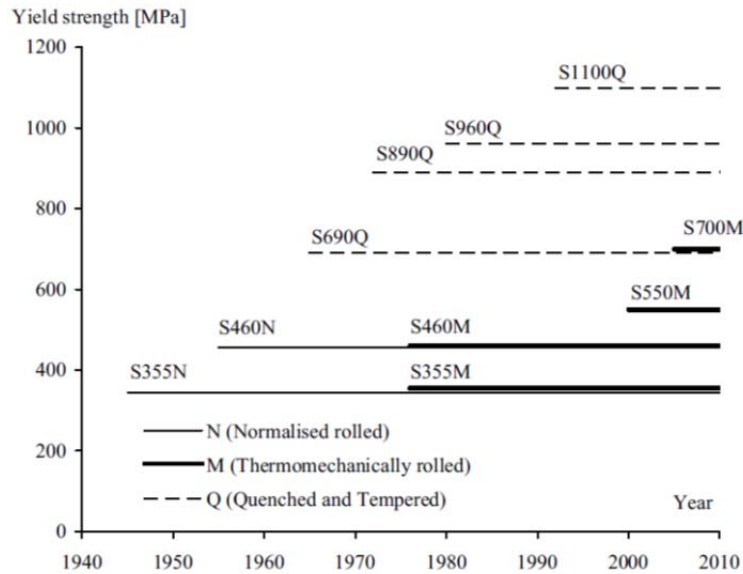
Fig. 3-1: Development of high strength steel grades [58].

Quenched and tempered steels are firstly austenitised, *i.e.* heated above the Ac_3 temperature, after which they are rapidly cooled transforming the austenite to martensite. For increased toughness properties the steels are often micro-alloyed with nickel (Ni), chromium (Cr) and molybdenum (Mo) [59], to guarantee weldability. In the final step, a tempering process heats the steel up to a temperature below the Ac_1 temperature, after which air cooling is applied. In this study a quenched and tempered steel S690QL1 was selected. A small number of experiments were also carried out on S700M.
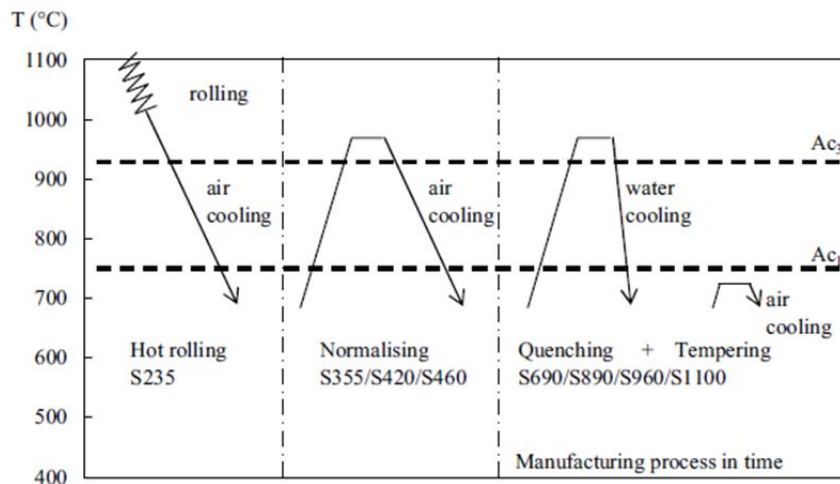
Fig. 3-2: Temperature-time dependence in the manufacturing of rolled steel [58].

3.2 Material chemical compositions

The steel used in this study is a high strength quenched and tempered structural

36

steel, S690QL1. This steel [60] has good bending properties and a good weldability is reported [61].

The chemical composition of S690QL1 steel according to the EN 10025-6 standard [62] is given in Table 3-1. The values indicate the maximum amount of each of the alloying elements in the ladle. Depending on the thickness of the product and the manufacturing conditions, the manufacturer may add one or several alloying elements up to the maximum values in order to obtain the specified properties. The chemical composition of the as-received plates, meet the requirement of the S690 standard.

Table 3-1: Maximum permissible alloy content of S690QL1 steels according to EN 10025-6 standards [62] in wt.%, Fe balance.

%	C	Si	Mn	P	S	Al	B	Cr
Maximum	0.2	0.8	1.7	0.02	0.01	-	0.005	1.5
	Cu	Mo	N	Nb	Ni	Ti	V	Zr
Maximum	0.5	0.7	0.015	0.06	2.0	0.05	0.12	0.15

The chemical composition of the as-received plates was analysed using the X-ray fluorescence (XRF) [63] technique and LECO furnace induction [64] for the carbon and sulphur analysis [65]. The XRF analyses were performed on 4 different samples with a Philips PW2400[TM]WD-XRF spectrometer. Data evaluation was done with UniQuant[®] 5.0 software. The results obtained (see Table 3-2) were averaged and found to be within acceptable range of the ladle composition.

Table 3-2: Chemical composition of S690QL1 steels obtained by XRF and LECO analysis in wt.%, Fe balance.

%	C	Si	Mn	P	S	Al	B	Cr
Average	0.16	-	0.86	0.04	0.0007	-	-	0.32
	Cu	Mo	N	Nb	Ni	Ti	V	Zr
Average	0.015	0.18	-	0.03	0.075	0.006	-	-

A Böhler UNION NiMoCr filler wire with a diameter of 1.2 mm was used for

welding. According to AWS A5.28 (Specification for Low-Alloy Steel Electrodes and Rods for Gas Shielded Arc Welding) specification [66], the electrode is classified as an ER100S-G wire [67] with a chemical composition as given in Table 3-3.

Table 3-3: Chemical composition for ER100S-G filler wire in wt.%, Fe balance.

%	C	Si	Mn	Ni	Mo	Cr	Ti
Average	0.08	0.6	1.7	1.5	0.5	0.2	-

3.3 Characterization of S690QL1

3.3.1 Base material properties

The microstructure of the steel consists of tempered martensite in a ferritic matrix with an average grain size around 30 μm, see Fig. 3-3. Tensile tests were performed to obtain the yield strength and Young's modulus of the as-received material. The yield strength of the base material is 830 MPa and Young's modulus is 210 GPa. The hardness is $HV_{0.5}$ 292 fkg/mm^2.
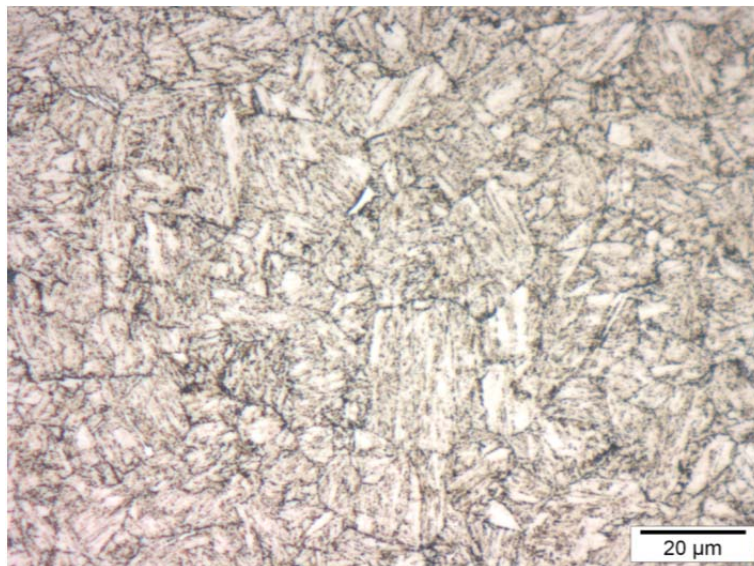
Fig. 3-3: Microstructure of base material [65].

3.3.2 Solid state phase transformation behaviour

A Bähr thermoanalysis DIL805 dilatometer was employed to study the solid state phase transformation behaviour and to obtain the temperature dependent thermal expansion of S690QL1 [68, 69]. For the free dilatation tests, samples were machined with a dimension of $2 \times 2 \times 10$ mm^3 and a thermocouple was

discharged spot welded on the middle of each specimen to enable continuous controlling and monitoring of the temperature during testing. Experiments were carried out in a vacuum of 10^{-5} torr and cooling of the specimens was achieved by controlling the flow rate of high purity argon gas. All the specimens were first heated to 1000 °C with a heating rate of 10 K s^{-1}, soaked at that temperature for 5 min, and then cooled to room temperature using different cooling rates of 1, 5, 10, 20, 50 and 100 K s^{-1}.

The change in length as a function of temperature for different cooling rates is shown in Fig. 3-4. From this data the thermal expansion of the ferritic phase in the heating regime and of the austenite during the cooling cycle can be derived. Furthermore, transformation start and finish temperatures can be obtained in combination with the dilatation involved in the transformations.

In the heating stage, a reduction in length due to austenisation starts at around 720 °C, and the transformation is completed at around 850 °C. In the cooling stage, different phases are formed as a result of the different cooling rates employed. Table 3-4 shows the start and finish temperature of phase transformation for different cooling rates.
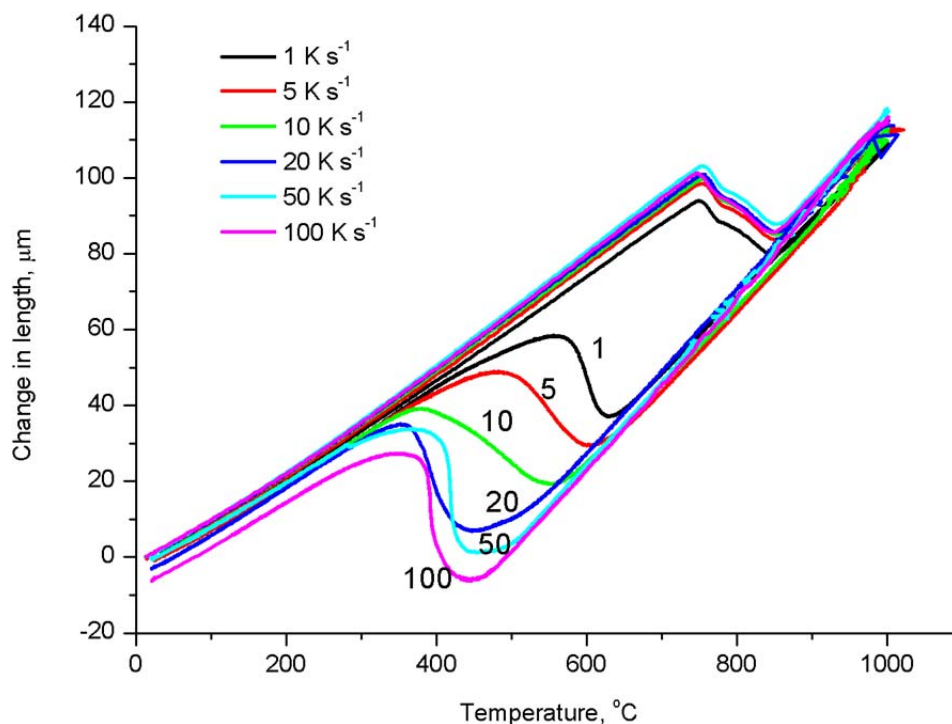
Fig. 3-4: Change in length in free dilation as function of the temperature for different cooling rates.

Table 3-4: Start and finish temperature of phase transformation with different cooling rates.

Cooling rate (K s^{-1})	Start temperature (°C)	Finish temperature (°C)
1	620	580
5	600	500
10	570	400
20	430	380
50	430	400
100	430	390

The samples were cut along the middle cross section, where the thermocouple was attached, polished and etched with 5% Nital solvent for 5 seconds. Optical microscopy reveals that with a cooling rate of 100 K s^{-1}, an almost fully martensitic microstructure is found. A cooling rate of 20 K s^{-1}, results in the presence of a combination of ferrite, bainite and martensite, whereas with a cooling rate of 10 K s^{-1}, ferrite and bainite are formed. At a cooling rate of 1 K s^{-1}, ferrite and pearlite are observed. The microstructures obtained with the different cooling rates are shown in Fig. 3-5.

(a)   (b)

(c)   (d)
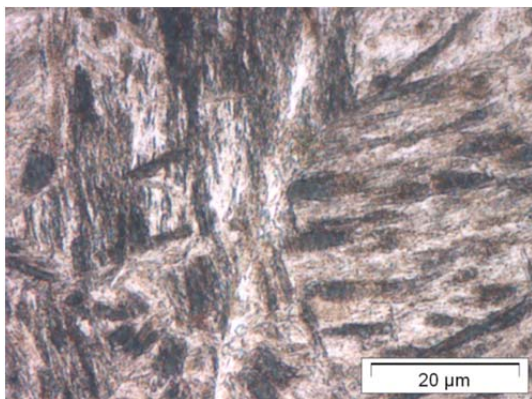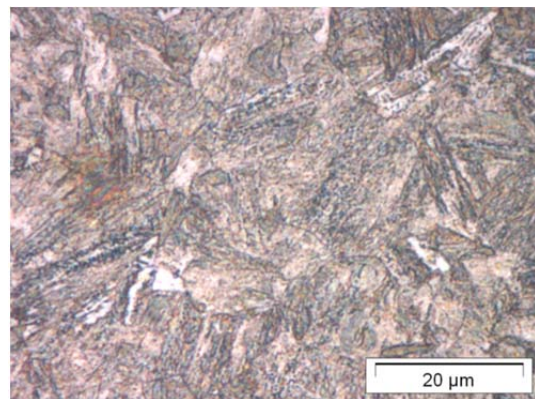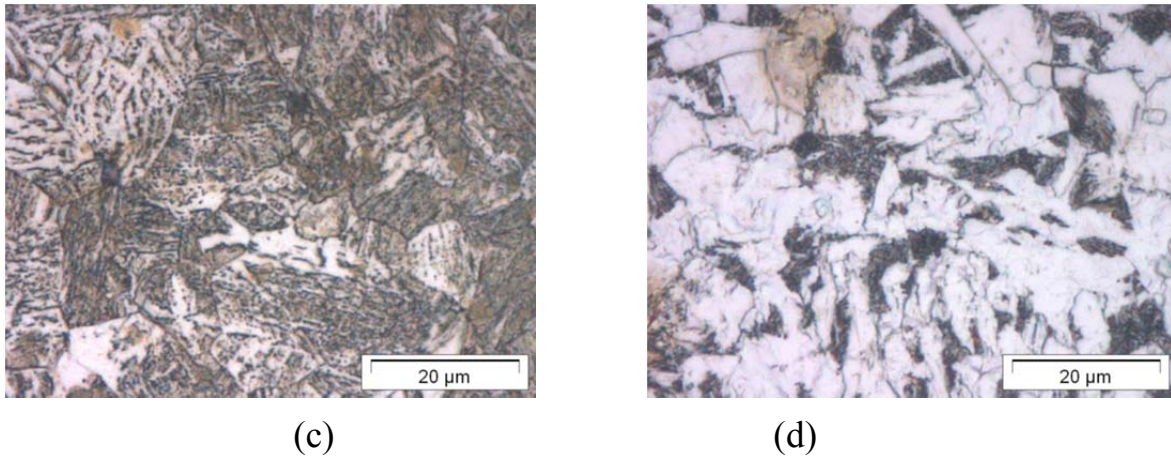
Fig. 3-5: Cross-sectional microstructure of dilatation samples with different cooling rates, (a) 100 K s^{-1}, (b) 20 K s^{-1}, (c) 10 K s^{-1}, (d) 1 K s^{-1}.

The Vicker hardness of the above mentioned samples subjected to different cooling rates was measured at two positions with an indentation load of 0.3 kg and averaged, with the similar method from Jiang [70]. Vickers hardness is around 210 fkg/mm^2 for the cooling rate of 1 K s^{-1}. With increasing cooling rates the hardness increases. When the cooling rate is larger than 20 K s^{-1}, the Vicker hardness remains more or less constant and is over HV$_{0.3}$ 400 fkg/mm^2, see Fig. 3-6.
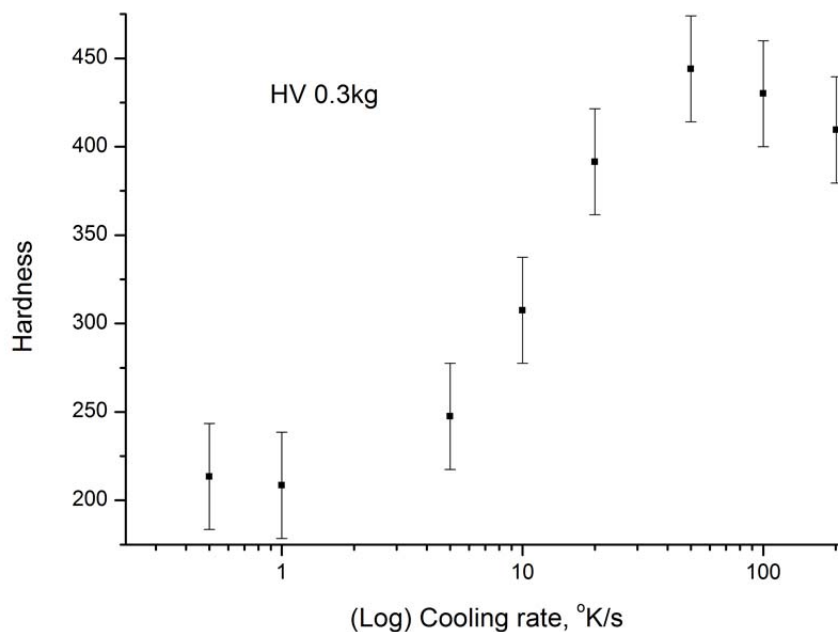
Fig. 3-6: Vicker hardness as a function of cooling rate.

3.3.3 Tensile tests at elevated temperatures

Tensile testing at elevated temperatures [71] was carried out in a 25 kN MTS servo-hydraulic tensile machine capable of imposing independent temperature

and strain profiles on a test specimen, with the similar method from Dutta [72]. Testing was carried at six temperatures, namely 300, 400, 500, 600, 800 and 1000 °C until the engineering strain reached 6%. Each test was repeated three times and the results were averaged to improve the measurement statistics. For temperatures above 500 °C, tests were performed at two different strain rates: 2.5×10^{-3} and 2.5×10^{-4} s^{-1}. The strain rates were kept constant during the entire tensile test. The results are shown in Fig. 3-7.
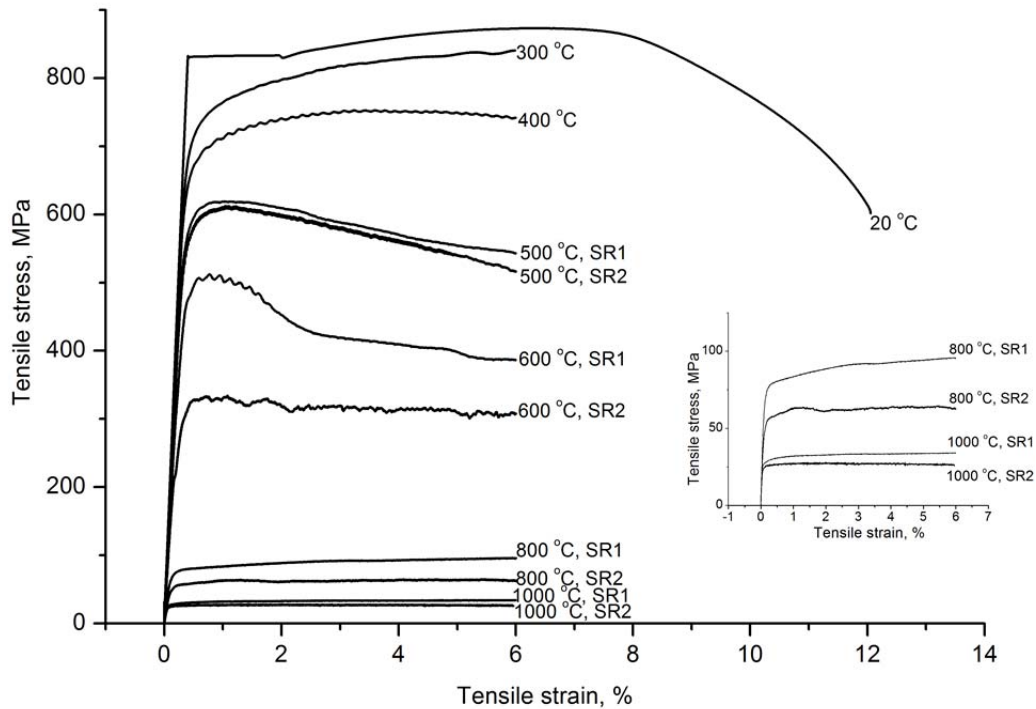
Fig. 3-7: High temperature tensile tests with two strain rates, SR1: 2.5 × 10^{-3} s^{-1}, SR2: 2.5 × 10^{-4} s^{-1}.

The Young's modulus and yield stress of S690QL1 at elevated temperatures were derived from the high temperature tensile test and are shown in Fig. 3-8. Decreasing tendencies of these mechanical properties are observed when temperature is increased.
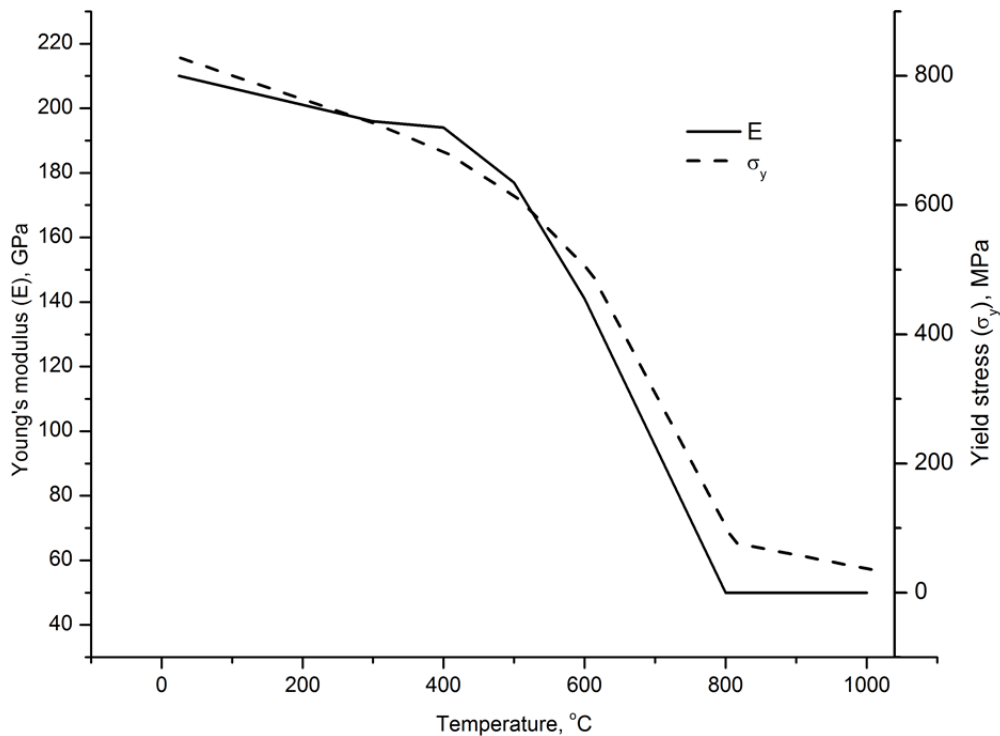
Fig. 3-8: Young's modulus and yield stress as a function of temperature.

3.4 Calculated material properties of S690QL1

JMatPro[®] is a cross-platform program [73], which calculates a wide range of material properties based on the chemical composition of alloys and is particularly aimed at multi-phase alloys used in industrial practice.

From the equilibrium phase diagram the solidus and liquidus temperatures are determined to be 1462 to 1509 °C, respectively. From calculation, Ac_1 and Ac_3 temperatures are 711 °C and 845 °C, respectively, which are similar to the values obtained from the dilatation measurement, see Fig. 3-4. A continuous cooling transformation (CCT) diagram of S690QL1 is given in Fig. 3-9. The starting temperature of the phase transformation is defined when 1% of the material is transformed, whereas the finish temperature is selected when the transformation is completed for 99%. The data on transformation start and finish temperature during cooling obtained by the free dilatation experiments are in good agreement with these calculations.
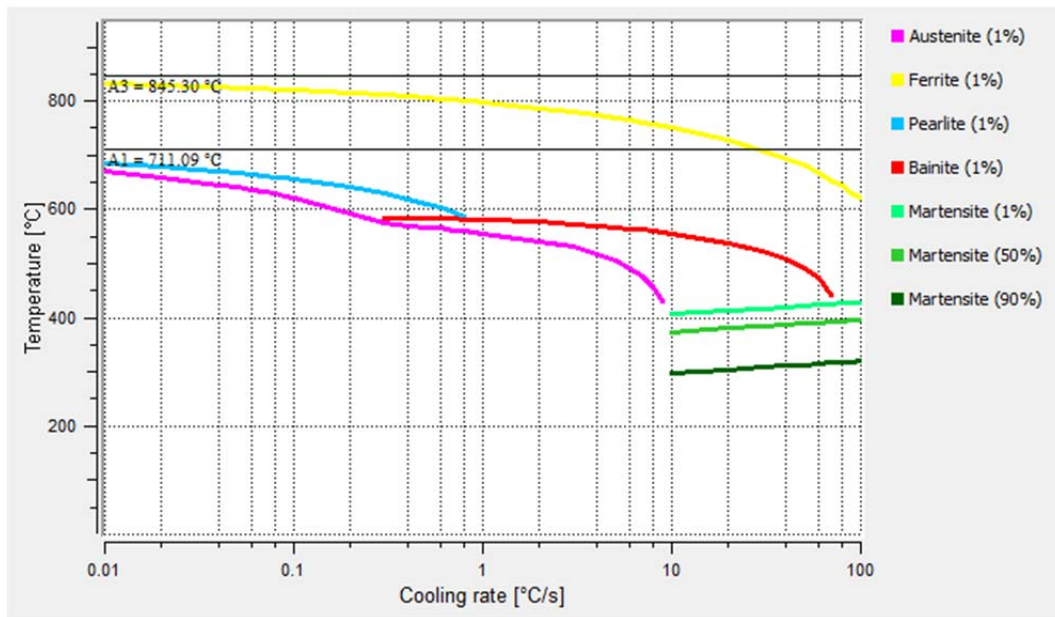
Fig. 3-9: CCT diagram of S690QL1 calculated by use of JMatPro®.

Temperature-dependent thermo-physical properties of S690QL1, *i.e.* thermal conductivity, specific heat, and density, were calculated and are shown in Fig. 3-10. They were assumed to be the same for both parent and weld materials used in the transient thermal analysis.
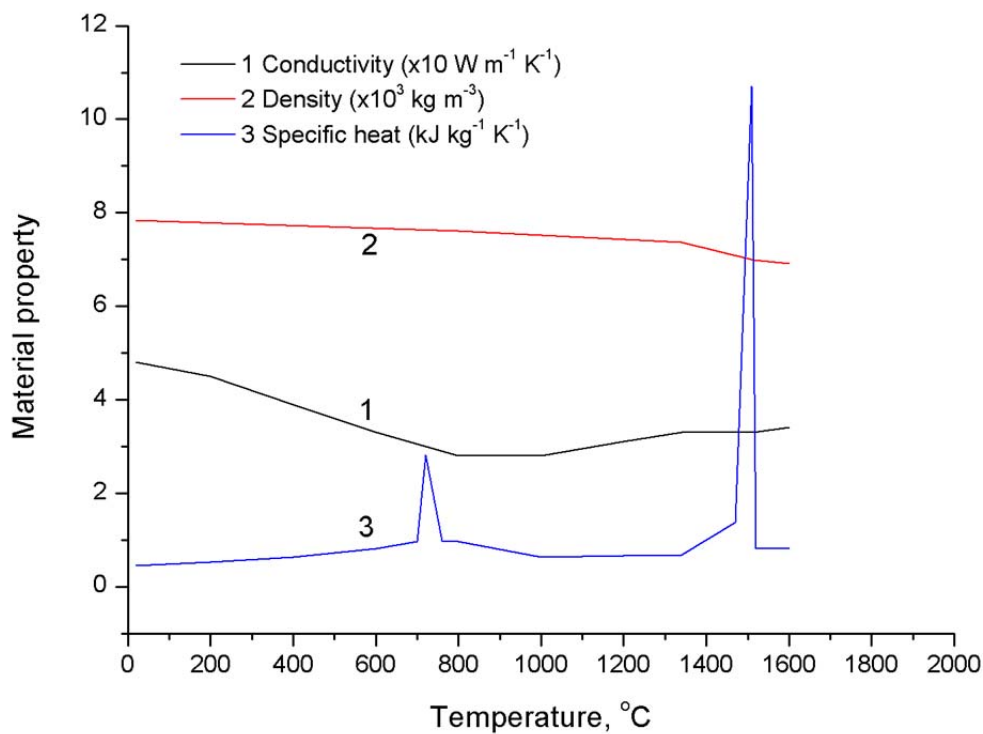
Fig. 3-10: Thermal properties of S690QL1 as a function of the temperature.

3.5 S700MC

In this study, the as-received S690QL1 has a thickness of 16 mm. At least six weld passes are required to fully cover the weld gap for such thickness. A step-by-step welding strategy was arranged to optimise the welding parameters and get a better understanding of weld stress development in multi-pass welding. S700MC with a thickness of 4 mm and 8 mm was chosen for single and two pass welds, respectively. S690QL1 with a thickness of 16 mm was welded in six passes. S700MC [74] is a thermo-mechanically controlled rolled advanced high strength steel (yield stress of 711 MPa). The chemical composition from the steel provider is listed in Table 3-5.

Table 3-5: Chemical composition in wt.% of S700MC with for 4 mm and 8 mm steel plates, Fe balance [75].

%	C	Si	Mn	P	S	Al	B	Cr
Average	0.049	0.109	1.934	0.009	0.001	0.041	0.0001	0.017
	Cu	Mo	N	Nb	Ni	Ti	V	Sn
Average	0.011	0.004	0.0049	0.068	0.019	0.121	0.007	0.001

Temperature-dependent thermal and mechanical properties of S700MC, *i.e.* elastic modulus, Poisson's ratio, coefficient of thermal expansion, and yield stress were obtained from calculation using JMatPro and are shown in Fig. 3-11.
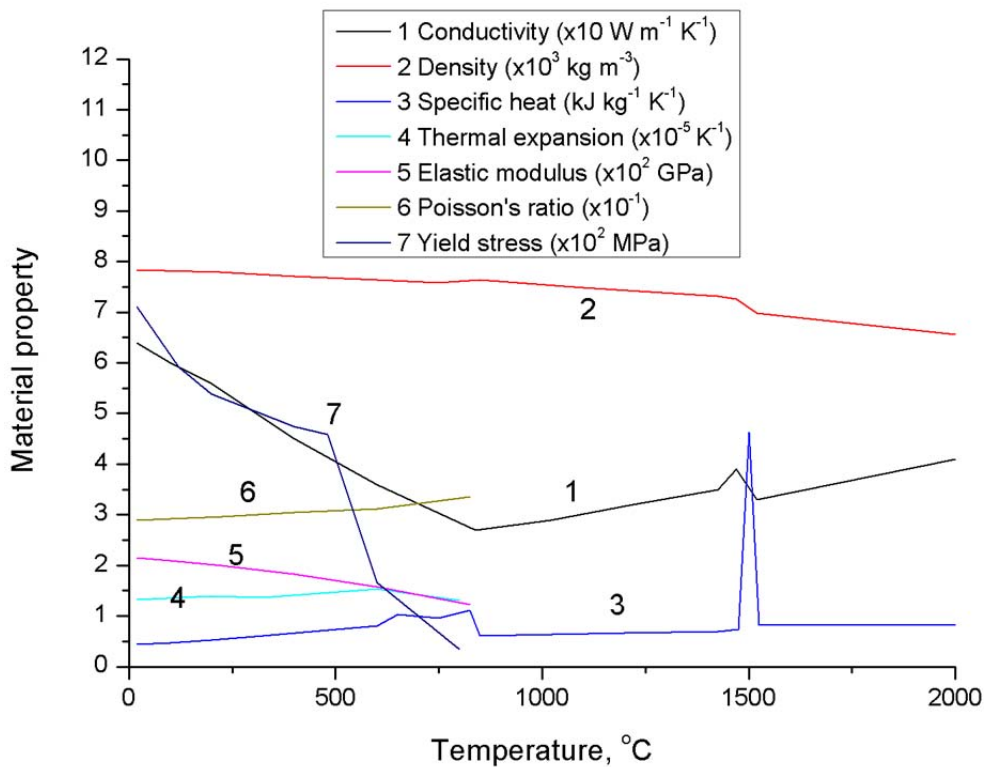
Fig. 3-11: Thermal and mechanical properties of S700MC as a function of the temperature.

3.6 Concluding remarks

In this chapter, an overview is given on the materials used in this study. High strength quenched and tempered steel S690QL1 with a thickness of 16 mm was selected for multi-pass welding experiments. Thermo-mechanical rolled S700MC steel with thicknesses of 4 and 8 mm will be applied to obtain the optimized welding parameters in the first two passes. The properties provided in this chapter are used in the developed thermal mechanical models to obtain the stress distribution in the welded plates.

The chemical composition of S690QL1 is determined and is in agreement with the EN 10025-6 standard. Thermal physical properties at elevated temperatres were calculated by means of JMatPro® based on the chemical composition. Free dilatation was performed with several cooling rates to obtain the thermal expansion coefficients and the volume changes due to solid state phase transformations. Hardness as a function of temperature for several cooling rates was measured. Tensile testing at elevated temperatures was carried out to determine the temperature dependency of the flow curves.

4 Transient welding temperature[a]

The temperature cycle during welding has an important effect on the material characteristics of weld and parent metal, residual stress state and dimension of the welded construction [76-78]. To form a weld in a steel section using a filler material, the parent metal and filler metal experience heating, melting and solidification in a localized zone created by a transient heat source. The heat source causes a highly non-uniform temperature distribution across the joint and the parent metal. In this chapter, the experimental arrangement for single pass and multi-pass welding are presented, and detailed parameters for welding of high strength steels are given. This is followed by an introduction of the theoretical background of heat flow during welding, and a description of constructed two dimensional shell and three dimensional solid finite element thermal models. These thermal models are validated with experimental measured time-temperature profiles and weld pool geometries. Sensitivity of the thermal models with respect to the input parameters and model construction are described.

4.1 Welding approach

4.1.1 Welding arc

Normally gases are poor conductors of electricity, as they contain no free charge carriers needed for the current flow. However, when sufficient energy is supplied to the gas, the atoms or molecules will ionize, generating free electrons and ions and making conduction possible. Under practical arc welding condition, the distance between the electrodes is usually small (between 0.1 and 1 cm). One of the electrodes is rod-shaped, the other one is usually flat (workpiece), in which case the arc is almost always bell-shaped (Fig. 4-1).
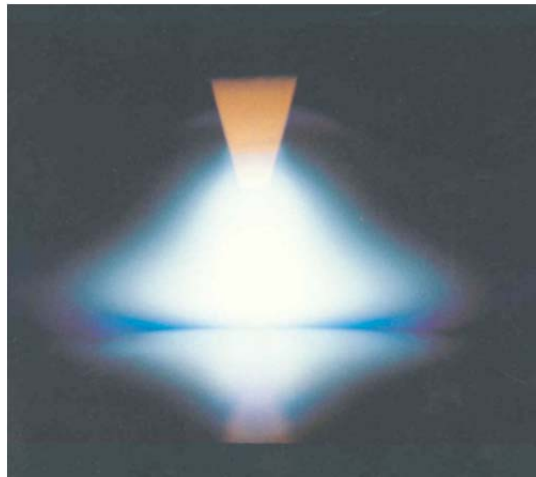
Fig. 4-1: Bell-shaped arc [79].

4.1.2 Gas metal arc welding

The principle of gas metal arc welding (GMAW) is shown in Fig. 4-2. In this process, a consumable electrode is used in the form of a continuously fed wire. The wire can be either solid metal, or may consist of a thin metal tube filled with powder (flux-cored wire). Use of flux-cored wire has the advantage that the chemical composition of the weld metal can easily be controlled. The current is transferred to the electrode at the contact tube.

In GMAW different shielding gases may be employed, depending on the metal to be welded. Usually an inert gas (argon, helium or an argon-helium mixture) in combination with small amounts of oxygen and/or CO_2 are used for welding of steel. These oxidising additions stabilise the arc and improve the flow characteristics of the liquid weld metal.
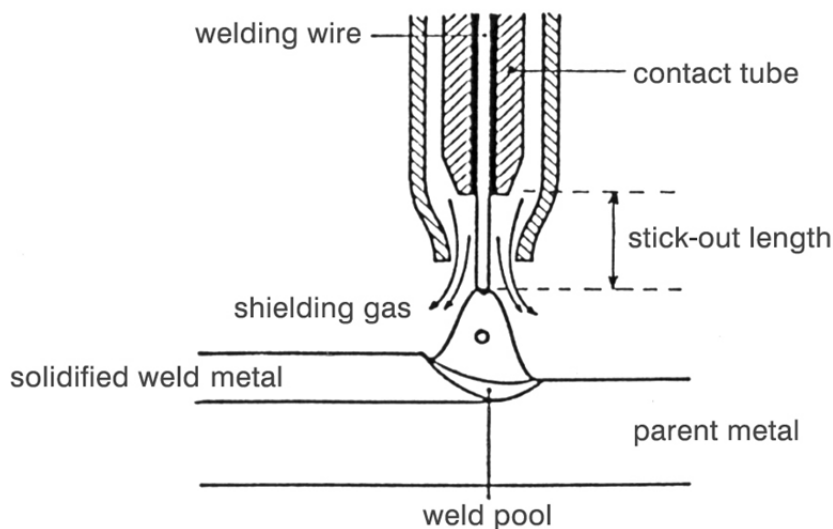
Fig. 4-2: Gas metal arc welding [79].

In GMAW, a distinction must be made between short-circuit arc welding and open-arc welding, see Fig. 4-3. In the case of short-circuit arc welding, periodic short-circuiting occurs between the electrode and the workpiece. Metal

transport takes place during the short-circuiting period, while the arc is extinguished. Short-circuit arc welding is operated at relatively low values of voltage and current. Because of the relatively small heat input the short-circuit arc welding process is particularly suited for welding thin (sheet) materials and the root weld in multi-pass welding. Application of short-circuit arc welding is limited by the risk of lack of fusion due to the low heat input and by the occurrence of spattering.

In the case of open-arc welding, metals are transferred as distinct droplets when the voltage is increased. At relatively low current, droplets are in the form of large globules. When the current exceeds a transition value, metal transport changes from larger globules through small droplets to a vaporized stream at the highest energies [80]. Since this spray transfer variation of the GMAW process requires higher voltage and current than short circuit transfer, and as a result of the higher heat input and larger weld pool area, it is generally used only on workpiece of thicknesses above about 8 mm [80]. Also, because of the large weld pool, it is usually limited to flat and horizontal welding position, but is sometimes also used for vertical-down welds. Spray transfer is generally not practical for root pass welds.
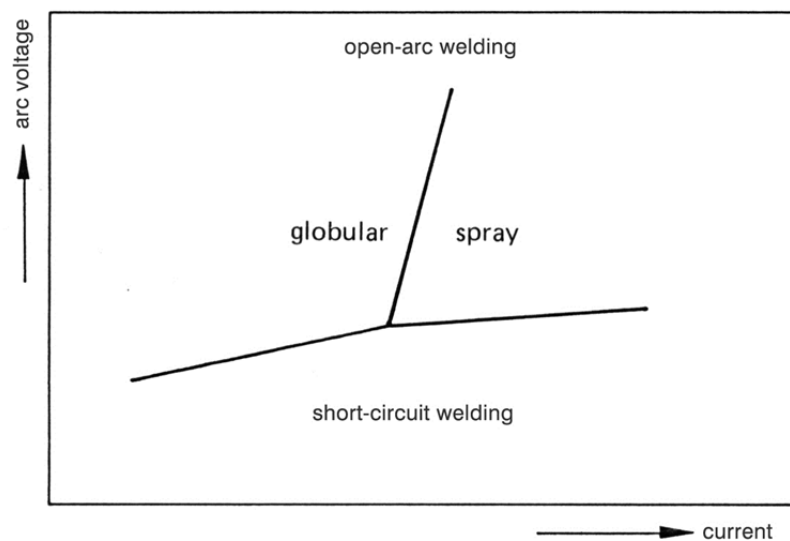
Fig. 4-3: Distinction between short-circuit arc welding and open-arc welding [79].

4.1.3 Welding experiment

Welding experiments in this work were performed using GMAW on S700MC and S690QL1 high strength steels, with the similar method from Chen and Coules [81, 82]. The experimental welding arrangement is shown in Fig. 4-4, where XYZ directions are defined. The plate moves along the X-axis underneath a stationary welding torch. In multi-pass welding, the torch position

has to be adjusted after each weld, and the welding torch can be positioned along the Y- and Z-axes for this purpose.

A clamping system with five vertical hydraulic clamps (AMF 6958SU-16) on each side of the workpiece was used [83, 84]. An air operated hydraulic pump (AMF 6904-20) applied pressure. The maximum oil pressure allowed at the clamp is 150 bar which corresponds to an effective clamping force of 4.8 kN (490 kg). In this work, the clamps were released when the temperature of the welded plate reached room temperature. The welding power source used for GMAW process was a Cloos Quinto Profi 503. The power generator was used in combination with controller and wire feed unit.
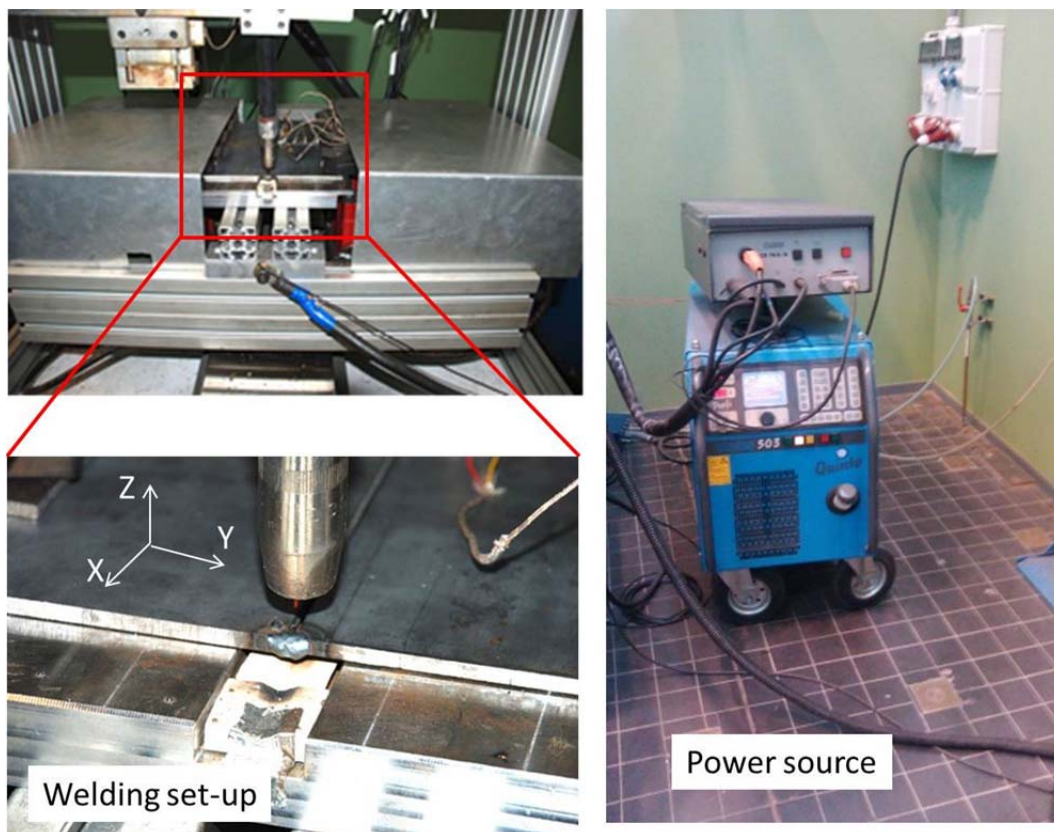
Fig. 4-4: Experimental welding arrangement.

The workpiece consisted of two steel plates with a length of 260 mm and a width of 100 mm. Three thicknesses (4, 8 and 16 mm) of plate were selected. The plates were milled along the long edge to form a 60 degree V-groove. According to the step-by-step welding strategy, a single and a two pass weld were applied to fully cover the weld groove in 4 and 8 mm thick S700MC steel, respectively. S690QL1 with a thickness of 16 mm was welded in six passes. These were first tack-welded in order to keep a constant weld gap of 0.5 mm. Ceramic bricks were placed beneath the joint centre line to preserve heat during welding and to prevent the molten filler metal adhering to the backing plate. The single pass weld and the first pass in the multi-pass welds were carried out in a short-circuiting metal transfer mode. With the selected welding conditions,

full penetration was obtained. In the subsequent welding passes the filler metal was deposited in a spay transfer mode, which required a higher welding current and arc voltage. In comparison to the short-circuiting metal transfer mode, the heat input associated with spray arc welding enlarges both the molten weld pool and the heat affected zone [84]. During welding, the current and voltage were monitored at a sample rate of two Hertz. An Ar (75%) - CO_2 (15%) gas shielding with a flow rate of 15 l min^{-1} was employed. The contact tube to the workpiece distance was 9 mm, and the shielding cup diameter was 10 mm. The torch had a leading angle relative to the Z-axis of 10° in XZ plane. The welding parameters for different thicknesses are listed in Table 4-1.

Table 4-1: Welding parameters of high strength steels for different thicknesses.

Thickness	Pass	Voltage (V)	Current (A)	Welding speed (mm s^{-1})	Wire feed rate (m min^{-1})
4 mm	1	20	196	5.0	5.7
8 mm	1	25	200	4.5	5.7
	2	30	300	9.0	11.0
16 mm	1	23.5	220	4.5	6.2
	2-6	31	305	8.5	11.0

The inter-pass temperature should be maintained at between 150 to 200 °C for high strength steel S690QL as indicated by Willms [85]. In this experiment, due to the complexity of the arrangement and the time required to reposition the welding torch, the inter-pass temperature was kept to 150 °C.

To obtain the temporal and spatial temperature cycles at specific locations on the plate during welding, K-type thermocouples were spot-welded in the middle of the plate on the reverse surface along the Y direction at distances of 2, 5, 10, 20, 30, 50 and 70 mm from the weld centre line. The accarucy of the measurement is ±1 °C. The uncertainty in positioning of the thermocouples is 0.25 mm, and the temperature error close to the weld centre line is estimated to be ±20 °C. A Yokogawa DL series transient recorder was used to collect the thermocouple voltage signal, which was converted into temperature. The experimentally obtained time-temperature data is used to validate thermal finite element models.

4.2 Welding thermal field

The thermal analysis includes the heat flow in the electrode, the weld pool, the arc and the solid workpiece. The complexity of the transport phenomena in gas metal arc welding process [81, 86, 87] is shown schematically in Fig. 4-5. The drag forces, electromagnetic forces, impact forces, plasma forces, electromagnetic surface tension and buoyancy forces are generated in the arc and weld pool. The heat generation and transfer from the arc to the workpiece are also complex. From an experimental point of view it is difficult to measure the temperature distribution within the weld pool and the arc, whereas from a numerical perspective it is difficult to model explicitly. In order to reduce this complexity, all phenomena at the electrode and in the arc are generally included in an expression of a volume heat flux entering the workpiece [88, 89]. Furthermore, fluid flow in the weld pool, re-distributing the heat, is not modelled in an explicit way, but also included in the distribution of the heat flux.
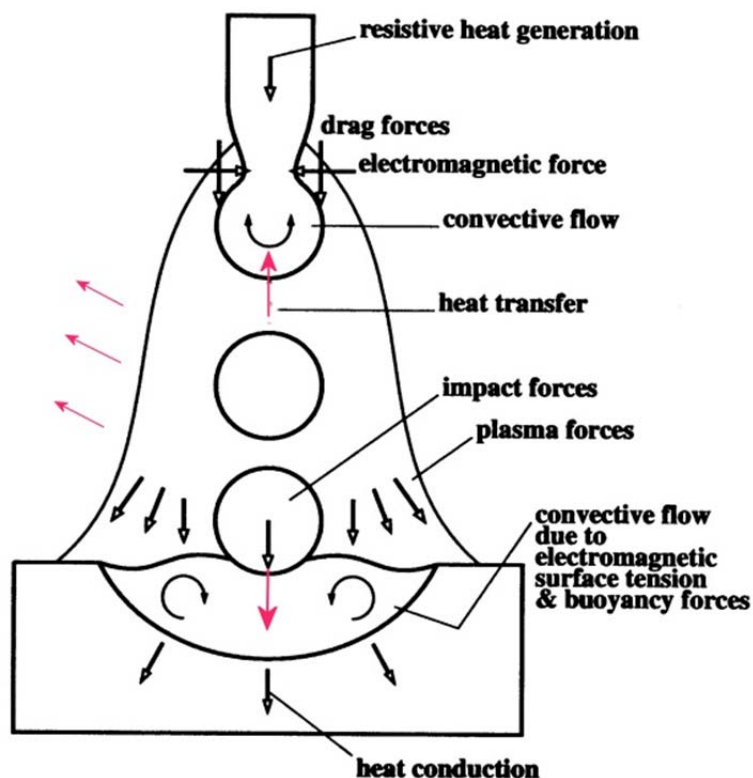
Fig. 4-5: Schematic presentation of the transport phenomena in the gas metal arc welding process [90].

Thermal analysis can be classified into three main parts: heat input and heat losses, and heat transportation. The heat source of the welding process (*i.e.* the arc) generates a heat flux into the workpiece. This energy is distributed within

the workpiece according to the Fourier's law of isotropic heat conduction. The heat losses out of the workpiece are governed by heat conduction, convection and radiation at the surfaces. This heat balance is presented schematically in Fig. 4-6.
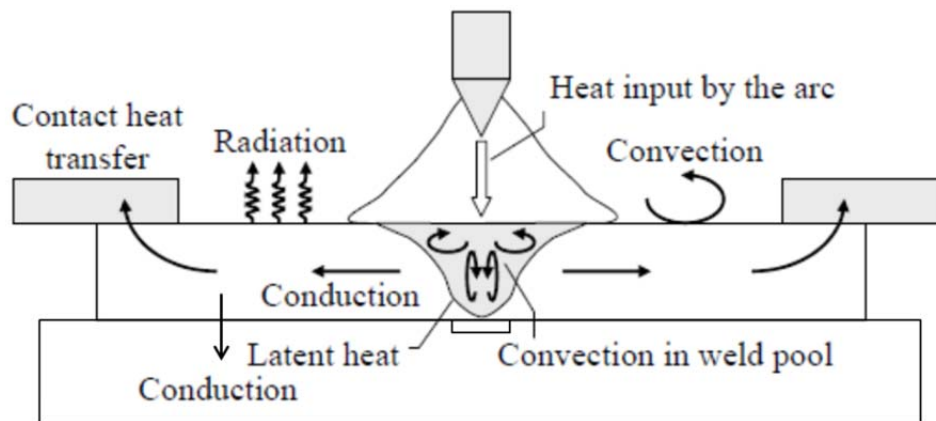
Fig. 4-6: Heat balance of the plate during welding.

Computational simulation based on the finite element method (FEM) is a very useful tool to predict welding distortion and residual stress levels in an early stage of product design and welding procedure development [91-93]. To apply FEM using solid mechanics to model the welding process, an accurate simulation of the welding heat source is required to produce reliable heat inputs. Accurate temperature distributions can be achieved by applying this heat input together with suitable initial and boundary conditions. The temperature distribution determines material properties, welding distortion and residual stresses of the welded structure.

Based on a circular disc heat source model with a Gaussian distribution of the heat flux on the surface of the workpiece [94], Goldak *et al.* [88] developed a double ellipsoidal power density distribution of the heat source, which can be used to simulate different types of welding processes with shallow or deep penetration. For gas metal arc welding, Goldak's double-ellipsoid heat flux distribution representing the welding heat source is generally adopted. As shown in Fig. 4-7, the heat flux distribution combines two different ellipses. The double-ellipsoid heat fluxes, $q_{v,f}(x,y,z,t)$ and $q_{v,r}(x,y,z,t)$, describe the heat flux distribution in the front and rear section of the heat source respectively and can be expressed as [88]

$$q_{v,f}\left(x,y,z,t\right)=\frac{6\sqrt{3}Qf_f}{abc_f\pi\sqrt{\pi}}e^{-3\left(\frac{x^2}{a^2}+\frac{y^2}{b^2}+\frac{(z-vt)^2}{c_f^2}\right)}$$

(4-1)

,

$$q_{v,r}(x,y,z,t) = \frac{6\sqrt{3}Qf_r}{abc_r\pi\sqrt{\pi}} e^{-3\left(\frac{x^2}{a^2}+\frac{y^2}{b^2}+\frac{(z-vt)^2}{c_r^2}\right)}$$

(4-2)

,

where f_f and f_r are the fractional factors of the heat deposited in the front and rear sections, Q is the heat input. The constants, a, b, c_f and c_r, as shown in Fig. 4-7, are heat source parameters that define the size and shape of the ellipses and thus the heat source distribution.
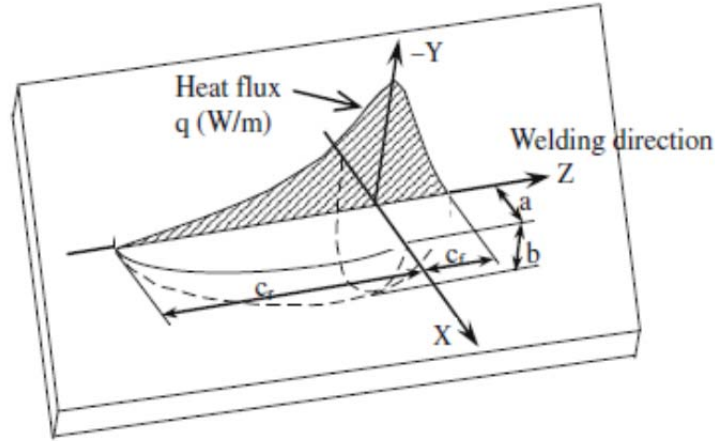
Fig. 4-7: Goldak's double-ellipsoid heat flux distribution [88].

To calculate the distribution and magnitude of the heat source, the heat source parameters are determined through an almost linear relationship between the weld pool geometry and the heat input as suggested by Wahab *et al.* [95] and Wang *et al.* [96]. Values of welding process parameters, such as the welding power can be determined experimentally by measuring the welding current and arc voltage. The power in combination with the welding speed v, and the efficiency of the process determines the heat input per unit length. These welding parameters determine the weld pool shape and thereby affect the dimensional heat source parameters.

Once the heat has entered the material, heat dissipation leads to a certain temperature distribution. During and after welding, the heat dissipation and heat loss occur *via* conduction, convection and radiation, and the workpiece will finally return to its original homogeneous temperature. The heat loss by surface conduction and convection $q_{s,c}$ can be defined as

$$q_{s,c} = h(T - T_0)$$

(4-3)

,

where h is a constant film coefficient, T_0 is room temperature; T is the temperature at the surface. The heat loss due to surface radiation $q_{s,r}$ is defined as

$$q_{s,r} = \varepsilon\sigma_B(T^4 - T_0^4)$$

(4-4)

,

where ε is the radiation emissivity and σ_B is the Stefan-Boltzmann constant.

The energy balance over the workpiece expresses the change in stored energy leading to

$$\rho \dot{H} = \dot{Q} - \nabla q \tag{4-5}$$

where ρ is the mass density, $\dot{H}$ is the volumetric enthalpy and $\dot{Q}$ is the power per unit volume. Fourier's law of isotropic heat conduction gives

$$q = -\lambda \nabla T \tag{4-6}$$

where q is the heat flux vector, λ is a matrix of coefficients of thermal conductivity. The coefficient of thermal conductivity depends on the chemical composition, microstructure and temperature. The enthalpy is related to the temperature by the heat capacity c:

$$c = \frac{dH}{dT} \tag{4-7}$$

The combination of the above equations leads to the classical heat conduction equation:

$$\rho \frac{dH}{dT} \dot{T} = \dot{Q} + \nabla(\lambda \nabla T) \tag{4-8}$$

The initial temperature of the workpiece is defined as room temperature. The heat losses due to clamp and backing contacts, heat convection and radiation to the environment are modelled as boundary conditions.

4.3 Modelling approach

4.3.1 Heat source and heat loss

Based on Goldak's equations, a user subroutine was written using FORTRAN® to calculate the position and time-dependent volumetric heat flux distributions. The subroutine was embedded into ABAQUS/Standard®. This volumetric heat flux was then assigned to related elements, while the heat source is passing by. The heat source parameters to simulate single and multi-pass welding are obtained from the dimension of the weld pool [88], and given in Table 4-2.

The schematic picture of the heat losses is shown in Fig. 4-6. At the top and side surfaces, a uniform convection coefficient and emissivity were used. The surface heat transfer coefficient of 10 W m^{-2} K^{-1} was assumed to include convection, based on the surface heat transfer predictions by Van der Aa [97]. Surface radiation was included for out-of-plane heat transfer with an emissivity of 0.9 [98]. At the rear surface, heat transfer coefficients due to conduction were defined in three regions: up to 5 mm from weld centre line: 5 W m^{-2} K^{-1}

(ceramic bricks were placed underneath and the heat disspation is expected to be slow); from 5 to 30 mm: 30 W m^{-2} K^{-1} and from 30 to 100 mm: 50 W m^{-2} K^{-1} (the dimension of the backing plate is larger than the welded plate and the heat disspation far away from the weld centre is expected to be fast). These values are suggested by Pazooki [99].Thermal material properties given in chapter 3 were included in the model. Heat conduction does not occur across lines of symmetry. The initial temperature was assumed constant at room temperature 28 °C.

Table 4-2: Geometrical heat source parameters for the Goldak model for plate thicknesses of 4, 8 and 16 mm.

Plate thickness Pass number	a (mm)	b (mm)	c_f (mm)	c_r (mm)
4 mm	3	5	3	6
8 mm pass 1	3.75	6.5	3.75	7.5
8 mm pass 2	3.5	6	3.5	7
16 mm pass 1	3.75	6.5	3.75	7.5
16 mm pass 2-6	3.5	6	3.5	7

4.3.2 Two-dimensional model

A two dimensional (2D) shell model was constructed to represent the full cross-sectional plane. A three dimensional (3D) double ellipsoid heat source passes this cross-sectional plane. The generated heat due to the heat source is transferred within the plane according to the heat conduction equation 4-8. Heat losses were modelled *via* the surface film and radiation equations 4-3 and 4-4, respectively. A homogenous solid section was defined and assigned to the plane to represent a typical cross-section during welding. Longitudinal heat transfer was assumed not to occur, as the 3D double ellipsoid heat source already accounts for the thermal gradient in this direction. The element type selected was a 4-node linear heat transfer quadrilateral (DC2D4) with linear geometrical order. The mesh is denser close to the weld centre. The minimal mesh size in the weld centre is 1 × 1 mm^2, near the edge of the plate the size is 8 × 1 mm^2. Fig. 4-8 shows the meshes for the three plate thicknesses. For a heat transfer analysis, the number of the nodes is identical with the number of the model variables, as only one variable (temperature) was defined. Four nodes are

defined per element. Information with respect to the model is presented in Table 4-3. The computational (CPU) time dramatically increased with the increasing number of the layers and is included in the table.
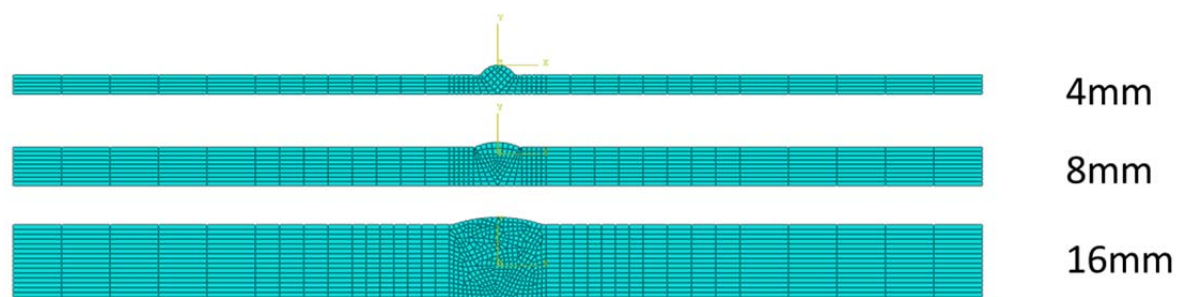
Fig. 4-8: Cross sectional geometry and mesh for the different plate thicknesses.

Table 4-3: 2D shell model information of different plate thicknesses.

Plate thickness (mm)	Number of passes	Nodes	Elements	Variables	CPU time (s)
4	1	286	234	286	86
8	2	490	434	490	4546
16	6	1000	939	1000	62810

4.3.3 Three-dimensional model

The plates were also modelled as 3D solid deformable bodies. Perpendicular to the welding direction, transition elements are used at a certain distance from the weld centre line to enlarge the element size. An 8-node linear heat transfer brick (DC3D8) was defined for the element type with a linear geometrical order. The minimal mesh size in the weld centre is $2 \times 1 \times 1$ mm^3, near the edge of the plate the size is $8 \times 8 \times 1$ mm^3. For symmetrical welding situations, *i.e.* the 4 mm thick plate with a single weld pass and the 8 mm thick plate with two weld passes, only half the cross section was modelled. The six weld passes in 16 mm thick plate was modelled over the full cross section due to the asymmetrical nature. To save computational time, one sixth of the plate length (48 mm) was modelled. A steady state is reached after 5 s after weld starts. Fig. 4-9 shows the dimensions and model specifics of the plates. The 3D solid model information for different plate thickness is given in Table 4-4.
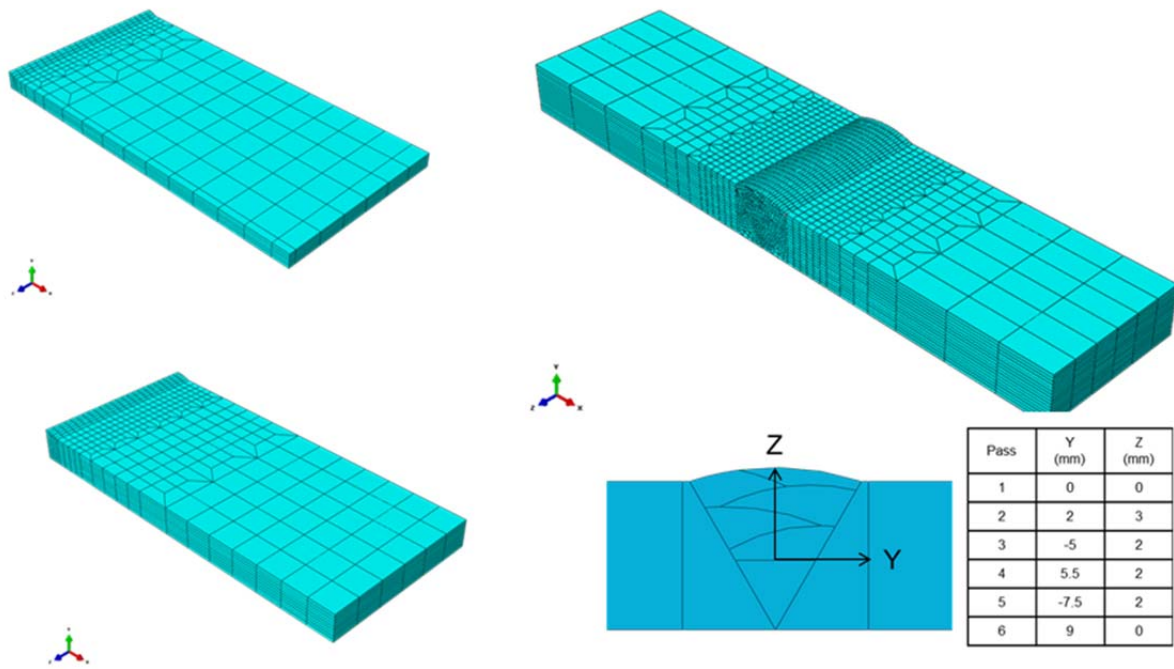
Fig. 4-9: Geometry and mesh of the plates with different thicknesses.

Table 4-4: 3D solid model information of different plate thicknesses.

Plate thickness (mm)	Number of passes	Nodes	Elements	Variables	CPU time (s)
4	1	1482	1080	1482	33178
8	2	3980	3240	3980	17598
16	6	19296	17472	19296	1769549

4.3.4 Time rescale and filler metal

In a single pass weld, the simulated welding time is the same as the total time of experiment, as there is only one thermal cycle. In a multi-pass weld, due to the length reduction in the model, the simulated welding has to be rescaled when the subsequent welding step starts. The chemical compostion of the filler metal is slightly different from the base material (chapter 3.2). However, the material property of the filler metal is difficult to obtain experimentally, particularly due to dilution by the plate material; the same properties as the base material were assigned. Some error may result and this has to be bourne in mind when interpreting the results of the model.

58

4.3.5 Model summary

For the single pass welding of the 4 mm thick plate, the filler elements are all presented in the initial pre-welding condition. The heat input and welding speed are given in Table 4-1, and the heat losses are described in chapter 4.3.1. The centre of the heat source is applied on top of the weld bead and the dimension of the heat source, derived from measurements made on deposited weld beads shown in Table 4-2. Fluid flow is not condisered in the model. The fusion boundary is defined by the filler elements reaching the melting temperature. For the two pass welding of the 8 mm thick plate, the filler elements of the subsequent step are de-activated in the first welding step, and only activated when the second welding step starts ('following the element birth and death' technique). The second pass has a higher heat input than the root pass and is symmetrically deposited. The heat losses remain the same as for the root pass. The heat source is applied on top of the second weld bead. Six passes are required to cover the weld gap of the 16 mm thick plate. The successive weld passes are asymmetrically deposited and thus the heat source has to be re-positioned. The movement of the heat source obtained from the movement of the welding torch in the experiment is given in Fig. 4-9. These displacements were applied in the weld. The weld layer dimension was obtained from the macros of the welds after each weld pass.

4.4 Results and validation

4.4.1 Single pass weld

Fig. 4-10 shows the transient temperature on the rear surface of the plate at different positions; 3, 10, 30 and 50 mm from the weld centre line. At these four reference points the transient temperature during welding and cooling stages are shown. The dashed lines show the experimental results with a sample rate of two Hertz. The numerical results at the same positions are included in the same charts as the solid lines. Results from the 2D shell model and the 3D solid model are presented in Fig. 4-10(a) and Fig. 4-10(b), respectively. Different regions in the workpiece reach the peak temperature at different times due to the heat transfer from the weld centre to the base materials. When the closest attached thermocouple shows a peak temperature, the positions in the transversal directions are still at a lower temperature. After a few seconds, the position where the second thermocouple is attached reaches its peak temperature, this is also valid for thermocouple positions further away from the fusion line. Compared with the experimental results, the four thermal cycles, including the peak temperatures, are well predicted both from 2D shell and 3D solid thermal models, while the shell model takes much less computational time.
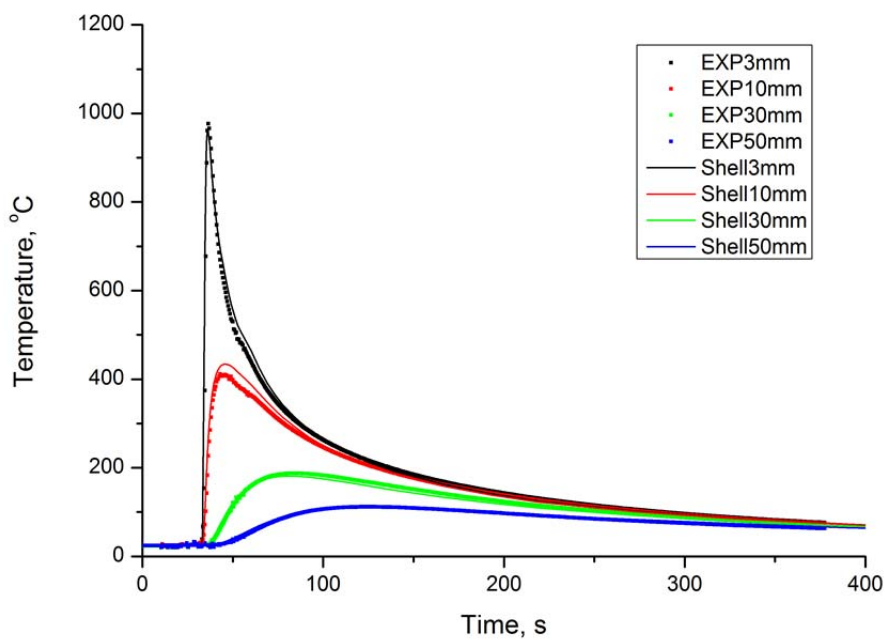
(a)
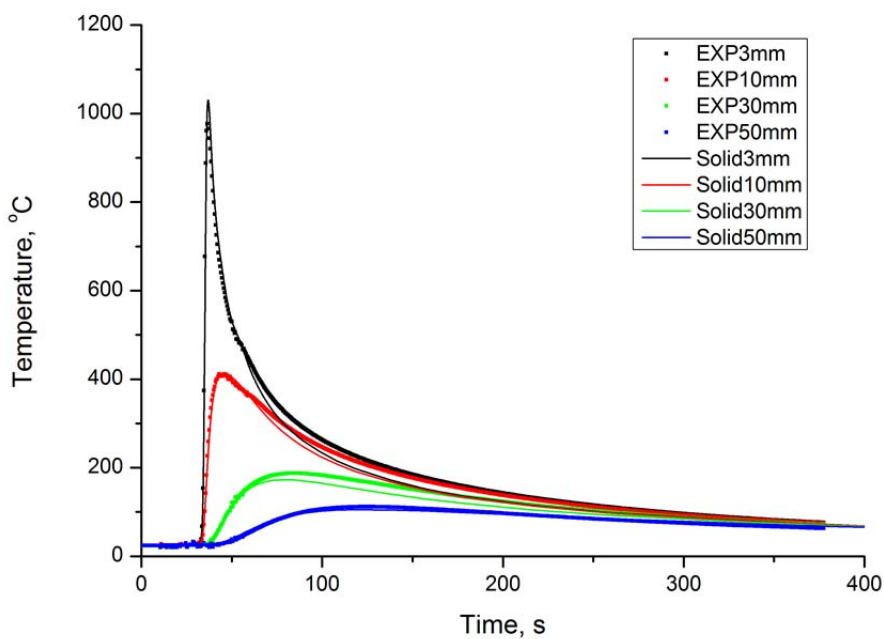
(b)

Fig. 4-10: Experimental and calculated temperature on the rear surface of the plate as a function of time for (a) the 2D shell model and (b) the 3D solid model for a single pass weld.

4.4.2 Two pass weld

Fig. 4-11 shows the transient temperature on the rear surface of the plate at different positions; 5, 10, 20 and 50 mm from the weld centre line. At these four

reference points the transient temperature during the welding and cooling stages for the two weld passes are shown. The dashed lines show the experimental results with a sample rate of one Hertz. The numerical results at the same positions are included in the same figures represented by the solid lines. Results from the shell model are presented in Fig. 4-11(a), whereas the solid model results are shown in Fig. 4-11(b). The thermal cycles and the peak temperatures of the experimental measurements and the numerical simulations at the four positions are in good agreement. The inter-pass temperature between the two passes is validated. In the cooling stage of the first pass, below 400 °C the predicted temperature deceases slightly faster than experiment (deviation within 30 °C). In the second pass, when the plate is preheated from the first pass, this mismatch disappears.
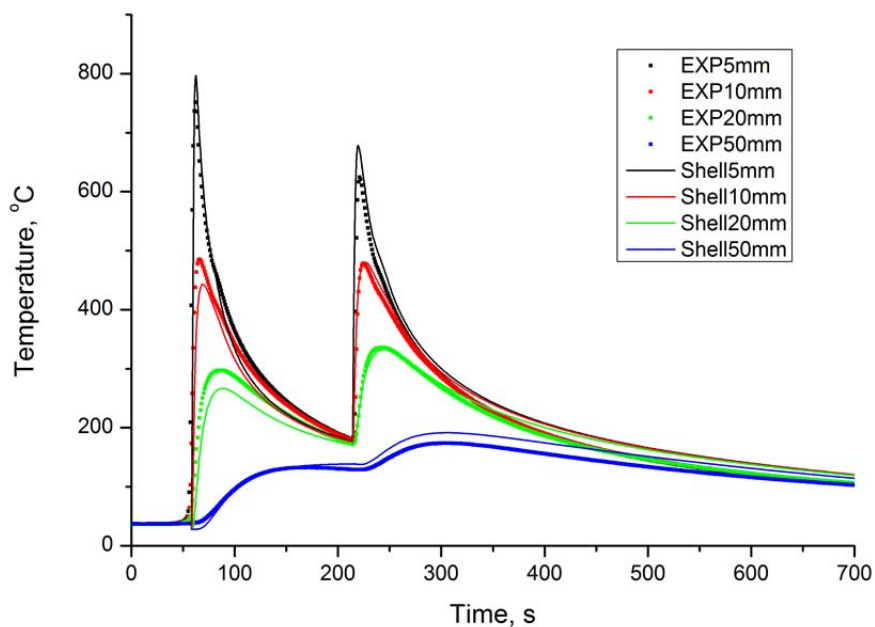
(a)
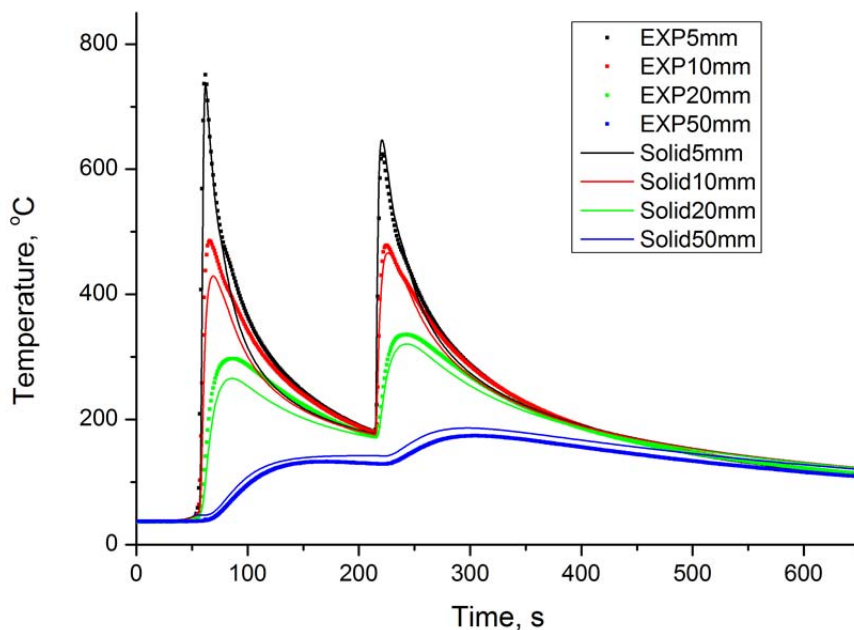
(b)

Fig. 4-11: Experimental and calculated temperature on the rear surface of the plate as a function of time for (a) the 2D shell model and (b) the 3D solid model for a two pass weld.

4.4.3 Six pass weld

Fig. 4-12 shows the transient temperature on the rear surface of the plate at different positions; 3, 10, 30 and 50 mm from the weld centre line. At these four reference points the transient temperature during the welding and cooling stages of the six thermal cycles are shown. The dashed lines show the experimental results with a sample rate of one Hertz. The numerical results at the same positions are included in the same charts as solid lines. Results from the shell model are presented in Fig. 4-12(a), and from the solid model in Fig. 4-12(b). The thermal cycles and the peak temperatures of experimental measurements and numerical simulations are in good agreement. The five inter-pass temperatures between the six passes are validated with the measured results. It should be emphasised that at the position 3 and 10 mm from weld centre line, the model provides a good prediction of the thermal behaviour in the heat-affected-zone. As stresses are concentrated in this region and stress re-distribution will take place during each weld pass, accurate time-temperature profiles are essential for stress analysis.
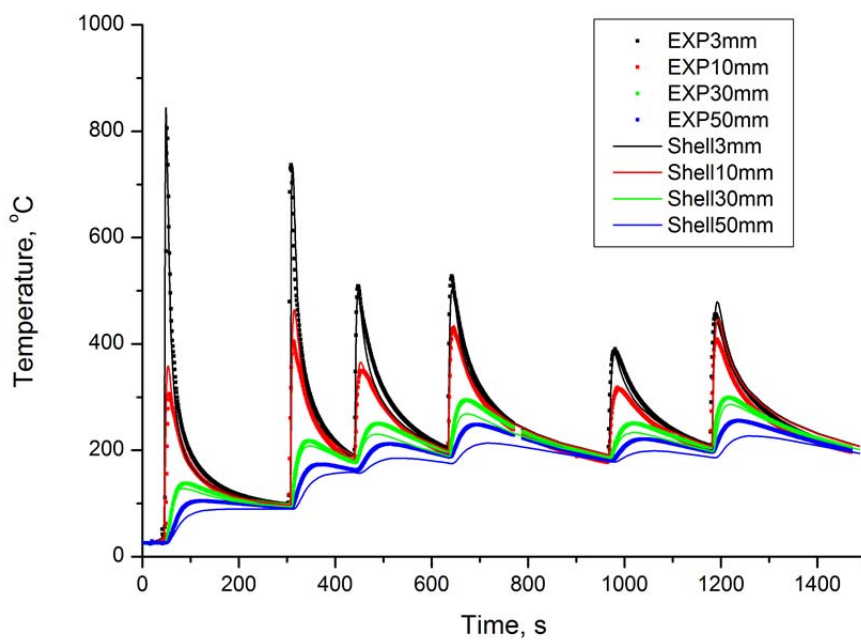
(a)
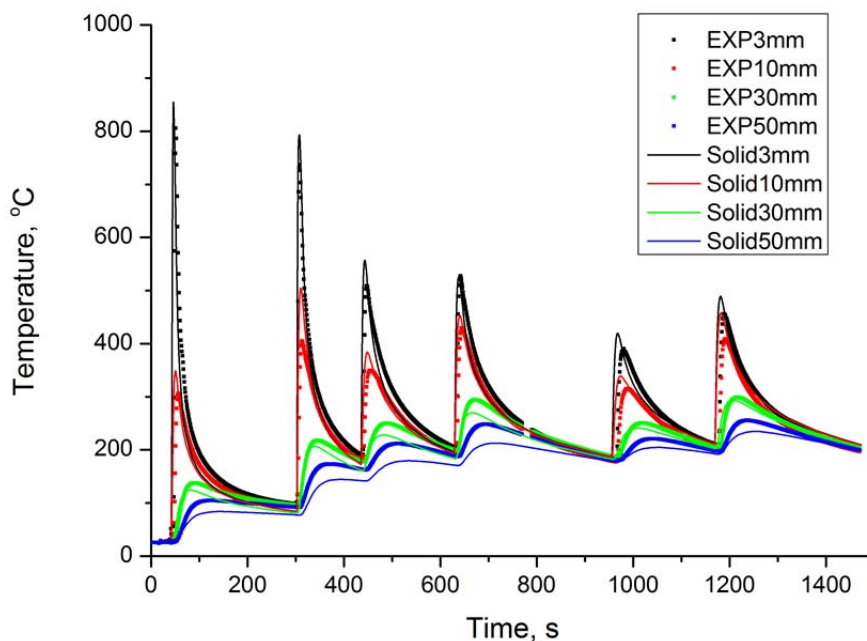
(b)

Fig. 4-12: Experimental and calculated temperature on the rear surface of the plate as a function of time for (a) the 2D shell model and (b) the 3D solid model for a six pass weld.

4.4.4 Heat-affected-zone

Local heating during welding produces a heat flow in and around the welded area. The material will locally melt and after solidification a joint is created.

The region surrounding the weld metal is affected by the weld thermal cycle and is known as the heat-affected-zone (HAZ). The mechanical properties of the weld metal and the HAZ are related to their microstructures, and depend on the initial chemical composition of the material and the thermal history. The knowledge of the weld thermal cycle in the heat-affected-zone and in the weld pool can help to prevent problems concerning cracking. The peak temperature reached in a specific region in combination with the heating and cooling rates determine the microstructural development. The heat flows from the fusion region defining isothermal planes perpendicular to the direction of the heat flow, as represented in Fig. 4-13, where different regions can be identified:

1. Weld metal: This region experienced melting and subsequent solidification of the weld pool. When no consumable electrode or filler wire is used, it consists of molten base metal. In the case that a consumable material is used, it will consist of a mixture of base metal and consumable. This zone resembles an as-cast microstructure.

2. Coarse grained HAZ (CGHAZ): The coarse grained HAZ is adjacent to the fusion boundary of the weld. This area has been exposed to high peak temperatures just below the solidius of the steel. At these temperatures grain growth takes place, which can be observed from large prior austenite grains.

3. Fine grained HAZ (FGHAZ): Since the peak temperature in this region is slightly above the temperature at which the first austenite appears (Ac_3), austenite grain growth is limited. Due to nucleation process of new phases during the ferrite to austenite and the austenite to ferrite/bainite/martensite transformation, grain refinement is obtained.

4. Intercritical HAZ (ICHAZ): The base metal is subjected to peak temperatures between the austenisation temperature (Ac_3) and the eutectoid temperature (Ac_1), where ferrite and austenite coexist. The carbon starts partitioning to austenite. This region has a duplex microstructure defined by abutting lath colonies and a small volume fraction of equiaxed grains.

5. Subcritical HAZ: The last region before reaching the unaffected base metal has been exposed to temperatures below the eutectoid temperature. In case that the weld thermal cycle is long enough, spherodized microstructures can be found, formed from initial cementite plates. Additionally, martensite might be tempered.
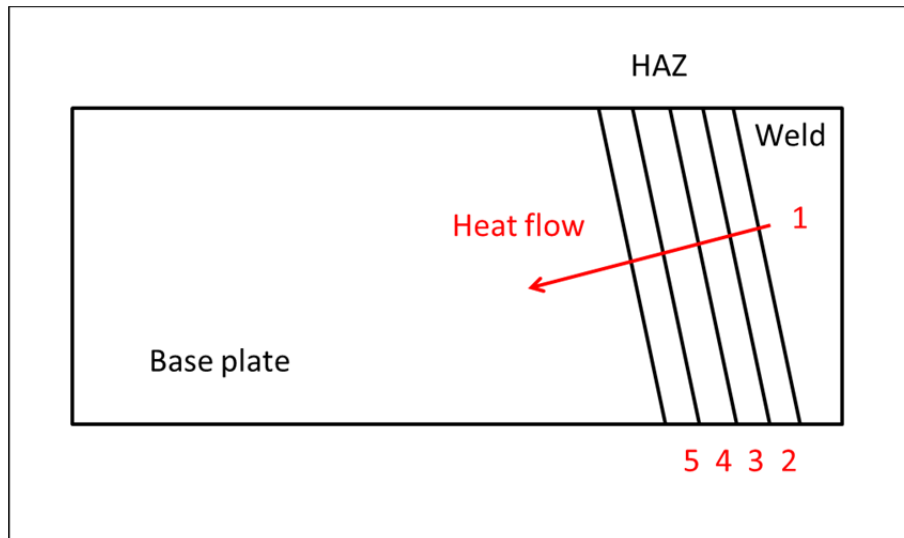
Fig. 4-13: Schematic representation of the heat-affected-zone in an arc weld.

The cross sectional macrograph of the six pass weld is shown in Fig. 4-14(a). The sample was ground, polished and etched with 5% Nital for five seconds. The fusion line of the weld metal can be easily observed from the microstructure. The successive welding passes partially re-melt the previously deposited layers. The coarse grain heat-affected-zone (CGHAZ), fine grain heat-affected-zone (FGHAZ) and intercritical heat-affected zone (ICHAZ) are found successively greater distance from the fusion line. The white band indicates the ICHAZ with temperatures between the Ac_1 (720 °C) and Ac_3 (850 °C) temperatures. The boundary between the base metal and ICHAZ is the Ac_1 temperature.

(a)
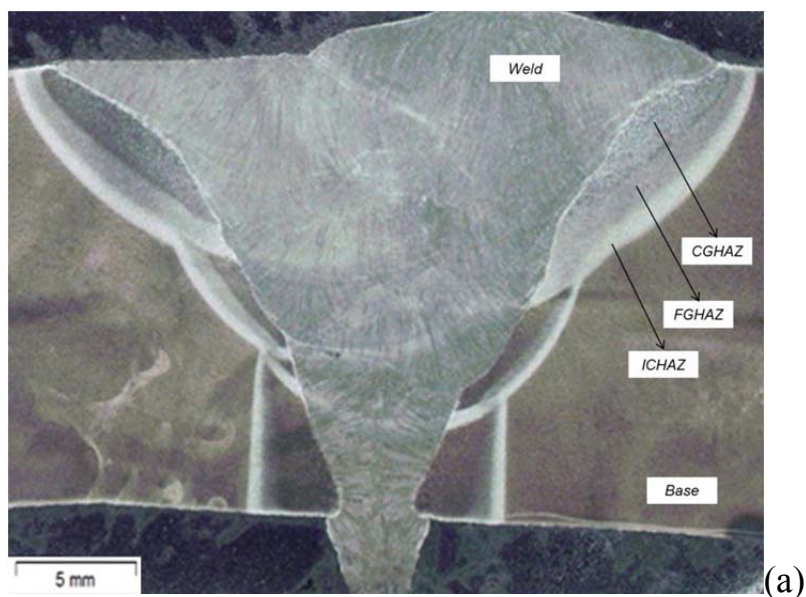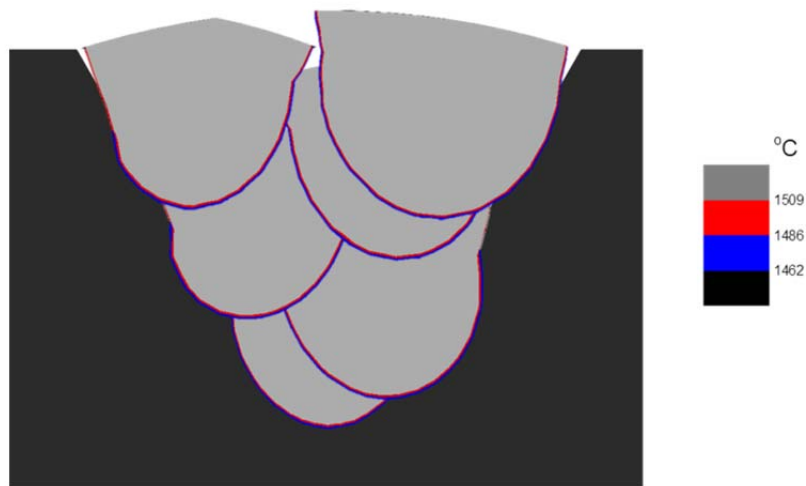
(b)

Fig. 4-14: (a) Measured weld pool and heat affected zone, (b) predicted molten region.

Fig. 4-14(b) shows the predicted molten region of the six pass weld when the weld pool is the largest during welding. The solidus and liquidus temperature of the material are 1462 °C and 1509 °C, respectively. In the first weld pass, the predicted molten region in the root is not as deep as that from the measured location of the fusion line, as flow motion was not considered in this FE model. In the experiment, the molten filler metal firstly filled the weld gap and then solidified. However, in the simulation the filler elements in the first pass were already present before welding. The temperatures of the elements increased due to the applied heat source. Those elements experienced peak temperature higher than the melting point were considered to melt. This is not a problem from the second to the fourth weld pass onward, as there was already a deposited weld bead from the previous pass. In the last two passes, when the groove was fully covered, a small amount of the filler metal from the reinforcement can flow to the base material before fully solidified. In the simulation, there are some small gaps between the predicted molten region and the groove in the base materials. Weld metal was considered to be here, however the peak temperature of those elements in the model was low than the melting point. This is also due to the limitation of the solid structure model, which cannot consider the fluid flow.

Overall, by comparing the depth and width of each weld cross section, it appears that the experimental and numerical results are in good agreement. Validation of the thermal models by measured temperature cycles combined with information from the weld pool geometry enhanced the reliability of the thermal model of the welding process. This is essential for stress prediction

using sequentially coupled thermal mechanical models.

4.5 Discussion

The time-temperature profiles of the single pass weld are well validated by the numerical model. The two pass and six pass model are not as good as the single pass model, as the complexity of the model is increased by the successive thermal cycles, weld bead geometry and asymmetrical deposition.

As introduced in chapter 4.2, thermal analysis is mainly affected by the heat input and heat losses. The heat input is determined from the input energy voltage (U), current (I) and efficiency (η), dimension of the heat source (a, b, c_f, c_r, f_f, f_r), and the welding speed (v). The heat loss is determined from the heat film coefficient (h) and the sink temperature (T_0). In this section, the sensitivity of the thermal FE model is tested with those mentioned parameters.

A 2D shell model of a single pass weld was used for the tests. The reference parameters are listed in Table 4-5. Keeping the same input energy, welding speed and heat loss condition, when the dimension of the heat source (a, b, c) is doubled individually, the peak temperatures are reduced by 10%, 28% and 12% compared to the reference model, respectively. When the fraction of the heat source is changed into a combination of 0.6 and 1.4, the peak temperatures are changed within 1%. When only the welding speed is doubled, the peak temperature is reduced by 20% and the temperature gradient along the transverse direction becomes steep. When only the efficiency of the input energy is reduced by 50%, the peak temperature is reduced by 20%. When only the film coefficient or the sink temperature is doubled, the peak temperature is reduced within 5%.

Table 4-5: Parameters for sensitivity tests.

U (W)	I (A)	η	a (mm)	b (mm)	c_f (mm)
20	196	0.75	3	5	3

c_r (mm)	f_f	f_r	v (m s^{-1})	h (W m^{-2} K^{-1})	T_0 (°C)
6	0.7	1.3	4.5	10	20

Apart from the input parameters, the simulated results may also be affected by the model construction, *i.e.* geometrical order, mesh size and integration type. High geometrical order of the elements is normally used in stress analysis when a few model variables have to be considered, while the thermal model only has one variable (temperature), it does not give a difference. The integration method is coped with the geometrical order to determine the number of the integration points. When there are at least four integration points used to calculate the temperature at one node, thermal analysis will be reliable. When the mesh size is smaller than 2 mm in the weld region, it does not influence the calculation of the temperature distribution.

4.6 Concluding remarks

Welding of high strength steels in three different thicknesses 4 mm with single pass, 8 mm with two passes and 16 mm with six passes was carried out. Optimised welding parameters, such as voltage, wire feed rate, travel speed and repositioning of the torch, were obtained. Transient temperatures at several distances from the weld centre line were measured by thermocouples. The step by step investigation on single pass, two pass and six pass welds helps to define appropriate dimensions for the heat input (Goldak parameters) and heat output (heat loss parameters), which were applied to the finite element models. The heat input was thus derived from measurement of deposited weld beads, whereas the heat losses were obtain from published literature without further adjustment. 2D shell and 3D solid models were used to predict the transient temperature during welding. The temperature validations of single, two and six pass welding were well achieved. The predicted time-temperature profiles have a deviation within 30 °C compared with the measured results in both the HAZ and the base material. The 2D shell model was much more time efficient than the 3D solid model (30 times faster). The geometry of the weld pool and heat-affected-zones were discussed for further validation. Sensitivity of the thermal models with respect to the input parameters and model construction were described.

5 **Transient thermal mechanical behaviour**[b]

Stress evolution during welding, especially in multi-pass welds, is rarely studied, as it is difficult to measure. In this chapter, transient force and the strain measurements were carried out during thermal cycling using an electro-thermal mechanical testing (ETMT) machine [100]. Idealised time-temperature profiles were employed representing multiple weld thermal cycles at two specific locations in the heat-affected-zone. Three mechanical boundary conditions are considered: (i) free dilatation tests, which provide *in-situ* strain data, (ii) completely constrained, and (iii) combined tests of free dilatation in the heating stage and complete constraint in the cooling stage. These tests were performed to represent realistic welding conditions.

5.1 Approach of transient weld stress measurement

In welding, the workpiece experiences rapid heating, inducing localised melting and relatively fast cooling. Due to the applied thermal cycle the original microstructure of steel is altered and at the same time, substantial residual stresses are induced [38, 101], which may increase the driving force for fracture and reduce the fatigue life of the component. For thick-section materials, welding is generally performed in multiple passes [91, 102-104]. Each successive thermal cycle will cause local re-melting, thermal expansion and contraction, plastic deformation, solid state phase transformations, grain growth or refinement, recrystallization and recovery [105, 106], all of which contribute to a complicated and evolving stress state.

In this respect the constraining conditions enforced on the workpiece during welding are of importance [83, 84, 107]. These constraints are the result of the entire construction, clamping and the solidified weld metal. In a typical butt welding case, the material in the heat-affected-zone is free to expand in the heating stage, and constrained in the cooling stage due to the constraints of solidification of the weld metal. In multi-pass welding, the material located at the top surface is constrained in the cooling stage of the last pass, while the material located at the bottom surface is constrained directly after the first pass.

Thermal mechanical finite element (FE) models can be used to predict the temperature history and the stress evolution of the workpiece [86, 88, 92]. Transient temperature measurements during welding by means of thermocouples are generally used to validate the thermal models. Furthermore, the modelling results can be verified by the position of the fusion line or by specific microstructural formation such as for instance the position of the fine-grained heat-affected-zone. Information concerning the stress or strain development is however more difficult to obtain, especially during multi-pass welding. Strain measurements by means of strain gauges [82, 108] or by digital image correlation [109, 110] only capture surface strains and are restricted by practical considerations to temperatures lower than about 400 °C, as the temperature resistance of any adhesive or paint limit their applicability. However during welding, induced stresses at the weld toe and in the coarse grained heat-affected-zone, where temperatures in excess of 1000 °C are encountered, cannot be measured by either of the techniques mentioned above. In addition, for thicker sections, stress gradients are expected over the thickness in the weld region, thus only surface strain measurements are not sufficient to understand the stress build-up and re-distribution due to multiple thermal cycles. Synchrotron X-ray or neutron diffraction techniques [111, 112] can be employed to measure stresses in thick sections; however, these techniques are not readily accessible and are generally conducted after welding.

Transient stresses have been evaluated by Satoh *et al*. [113] for round bar test specimens subjected to thermal cycles typically occurring in the heat-affected-zone of a weld. In these tests, the localised heating of the gauge length induces a non-uniform temperature distribution, and stress gradients due to plastic deformation can be expected along the sample length. Shirzadi *et al*. [114] modified the Satoh tests by bonding of two pieces of non-transforming nickel superalloy to the test materials. A homogeneous temperature and stress distribution within the tested material were achieved. However, both Satoh and Shirzadi applied a completely constrained boundary condition to the sample, while at the position of the weld HAZ, the constraints are much more complicated, *e.g.* free dilatation in the heating stage and complete constraint in the cooling stage in a single pass weld.

5.2 Electro-thermal mechanical test

Six pass welds were made on V-grooved 16 mm thick high strength steel S690QL1 plate by means of gas metal arc welding. Detailed welding conditions can be found in chapter 4. In the first weld pass, the filler metal was deposited in the centre of the weld groove. In subsequent weld passes, the torch was repositioned in order to fully cover the groove, overlapping the previous

solidified layers.

Based on the temperature measurements, two positions in the heat-affected-zone, which experience a peak temperature of approximately 1000 °C, were selected (10 mm at the top surface and 2 mm at the bottom surface from the weld centre line) as shown in Fig. 5-1(a). The time-temperature profiles of these two positions are shown in Fig. 5-1(b) and Fig. 5-1(c). At the top surface, the temperature gradually increases and a maximum is found when the final pass is made. The peak temperature profile does not show a monotonic increase due to the repositioning of the torch. The bottom surface experiences the highest temperature during the first pass. For consecutive passes the peak temperature gradually drops.

(a)

(b)   (c)
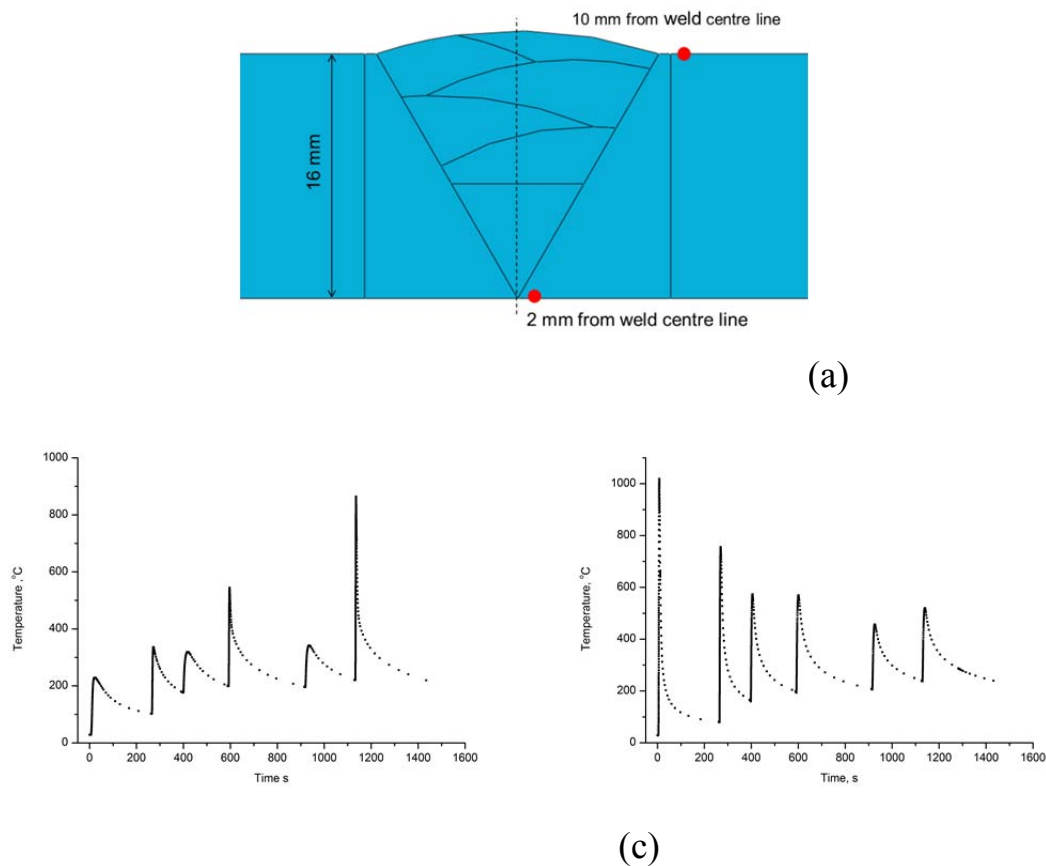
Fig. 5-1: (a) Schematic cross-sectional representation of the weld passes, (b) the temperature profiles of 10 mm at the top surface and (c) the temperature profiles of 2 mm at the bottom surface.

For the electro-thermal mechanical test (ETMT), rectangular S690QL1 samples were manufactured with dimensions of $1 \times 1 \times 16$ mm^3. The sample was placed in the middle of the chamber and was heated by a controlled current. The heating rate is simulated as a constant value of 10 K s^{-1}. The cooling rate is obtained from the temperature difference over a period of five seconds after cooling started. The idealised temperatures were allowed to fall to the inter-pass

temperature before the following heating stage. Thus time was not conserved; *i.e.* the idealised experiment is shorter than the real weld. The idealised time-temperature profiles at the top surface 10 mm and at the bottom surface 2 mm from the weld centre line are shown in Fig. 5-2(a-b). The samples are subjected to these two temperature profiles.
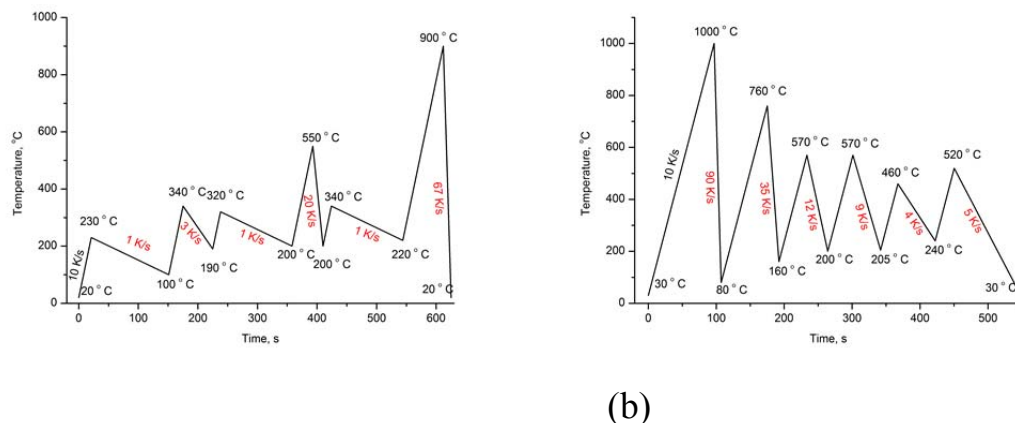
(a)   (b)

Fig. 5-2: Idealised time-temperature profiles (a) at the top surface 10 mm and (b) at the bottom surface 2 mm from the weld centre line.

An R-type thermocouple was attached at the middle of the sample to measure the temperature. The sample experiences a thermal gradient, as the clamps are water-cooled (Fig. 5-3(a-b)). The temperature distribution over the sample length as a function of time $T(x,r,t)$ can be represented by the following equation [115],

$$T(x,r,t) = T_0 + rt\left(1 - \left(\frac{x}{a/2}\right)^2\right)$$

(5-1)

where x is distance from the centre of the sample, T_0 is room temperature, r indicates the heating rate, and t represents the heating time. The length, width and thickness of the sample are defined as a, b and c, respectively. The temperature over the sample length for different peak temperatures is shown in Fig. 5-3(c). The temperature gradient over the thickness and width of the sample is neglected. A sensor attached to the sample is used to record the change in position and load. Three kinds of tests using the ETMT machine were arranged to investigate the thermal-mechanical behaviour as a results of multiple thermal cycles: (i) A free dilatation test. The machine is in load control mode. The sample is free to expand, and the force is zero during the entire process. The change in length due to expansions and contractions can be obtained, which provides information on the strain in the sample. (ii) A completely constrained test. The machine is in position control mode. The sample is unable to expand, and thus the strain is zero during the entire test. In

72

this configuration, the reaction force due to expansions and contractions can be obtained. (iii) A combined free dilatation and completely constrained test. The machine is switched between position and load control modes. The sample is free to expand in the heating stage and completely constrained in the cooling stage. The specimen representing the top surface of the six pass weld is free to expand in the first five thermal cycles and the heating stage of the last weld pass, while it is completely constrained in the last cooling stage, representing the solidified adjacent weld metal. The specimen representing the bottom surface of the six pass weld is only free to expand in the first heating stage, while it is completely constrained in the first cooling stage and the following five thermal cycles, symbolising the presence of solidified weld metal.
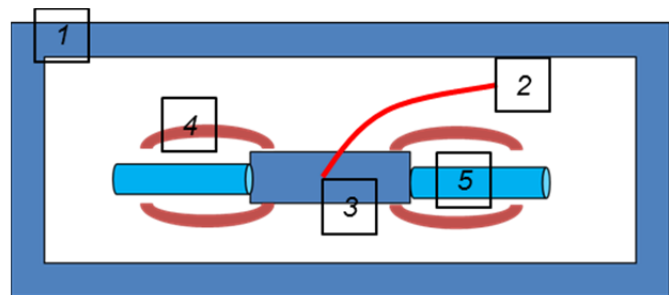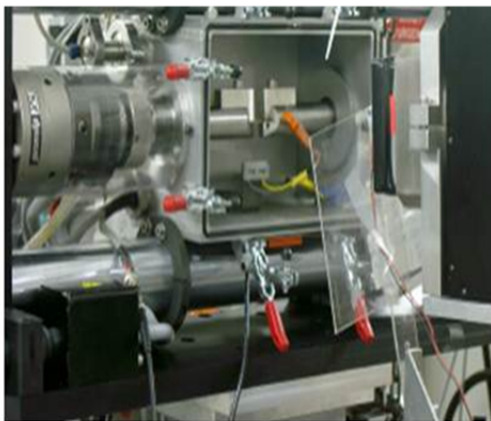
1: Chamber, 2: R-thermocouple, 3: Sample
4: Clamp, 5: Sensor

(a)   (b)
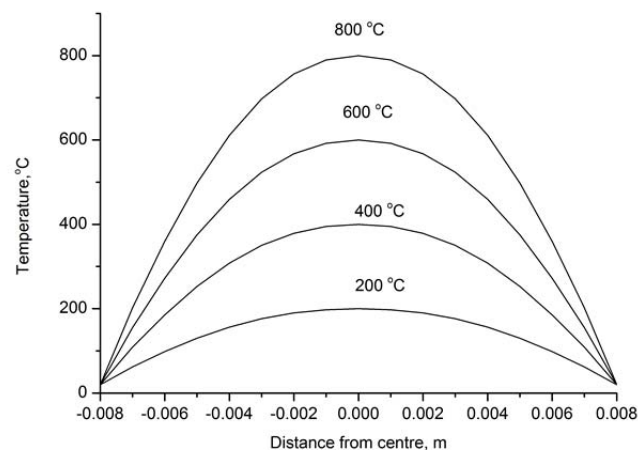
(c)

Fig. 5-3: (a) ETMT machine, (b) schematic representation of the ETMT and (c) temperature over the sample length.

5.3 Finite element thermal mechanical model

A 3D FE thermal mechanical shell model was constructed using ABAQUS software® to predict the transient force and strain during multiple thermal cycles. The dimension of the shell part is 16×1 mm². The seed size is 0.25 mm. The shell plane is set in the middle of a continuum entity. There are four nodes in one shell element (S4R element type). Totally 325 nodes and 256 elements are defined in the model. The temperature at each node is pre-defined as a field. The temperature in the middle of the sample follows the idealised time-temperature profiles shown in Fig. 5-3(c), while the temperature distribution over the sample length given by equation 5-1 was implemented as a user defined temperature subroutine in the model.

As a boundary condition of the free dilatation test, the sample was symmetrically constrained in the centre. In the completely constrained test, the sample was constrained at the two ends to disable the horizontal displacement. In the case of the combined test, the sample was free to expand in the heating stages, and then horizontally constrained after either the first or the sixth cooling cycle.

Volume changes as a result of phase transformations were coupled with the thermal expansion. Data from high temperature tensile tests provided the temperature dependent Young's modulus and yield stress. The measured flow stress curves were applied to model the hardening behaviour of the steel. These material properties can be found in chapter 3.

5.4 Results and validation

5.4.1 Temperature

Transient temperatures at the centre of the specimen, representing the top and bottom surface of a welded plate, both from the experimental measurements and the numerical calculations are shown in Fig. 5-4(a-b), respectively. The peak and inter-pass temperatures of the six thermal cycles show good agreement between the experimental and numerical results.

(a)   (b)
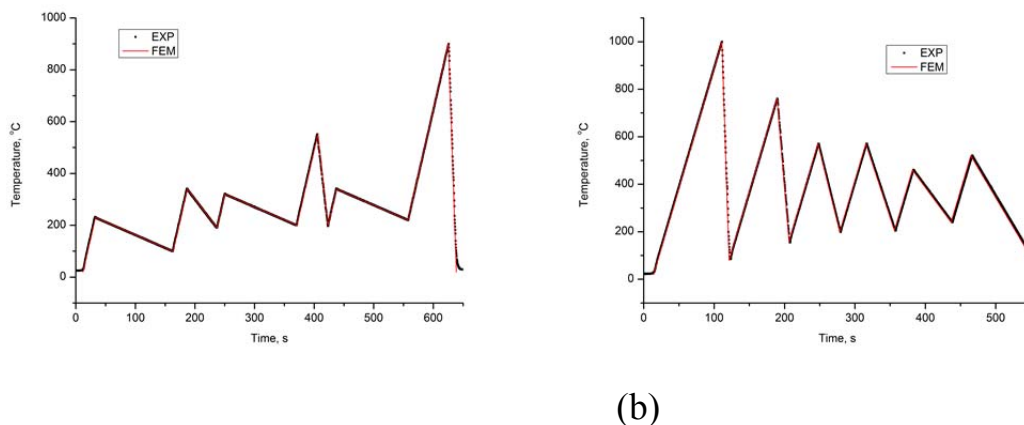
Fig. 5-4: Transient temperature results representing the centre of (a) the top surface and (b) the bottom surface.

5.4.2 Strain and force evolution

For the free dilatation test, the sample is free to expand and no stress can be generated. In the heating stages, thermal expansion leads to an increase of strain, while in the cooling stages, the strain decreases due to contraction. The transient measured (EXP) and calculated (FEM) strains representing the top surface subjected to six thermal cycles are compared in Fig. 5-5(a). The transient differences between the experimental and numerical results are also shown in this figure. As the time increment in the experiment and model are not identical, both curves are interpolated to plot the transient differences. In the first five thermal cycles, the sample is deformed in the elastic region. In principal after completely cooling, each sample should return to its original length. However, because successive inter-pass temperatures increase from 100 to 220 °C, the strain is accumulated. The differences between the experimental and numerical results are less than a strain of 0.0003. In the heating stage of the last thermal cycle, the strain increases, levels off and increases again. The initial increase due to thermal expansion of the ferritic phase is affected by the ferrite to austenite phase transformation, starting from around 720 °C (Ac_1). The volume reduction during the phase transition suspends the increase of strain. After completion of the transformation at around 845 °C (Ac_3), the strain increases again due to the thermal expansion of austenite. In the cooling stage, at a cooling rate of 67 K s^{-1}, austenite transforms into martensite when the temperature is below the martensite start temperature at around 430 °C. This transformation involves a volume increase. Compared with the results of the ETM test, the model predicts the thermal expansion and contraction considering phase transformations with a standard deviation error of 5.5 $\times 10^{-4}$.

The results of the sample representing the bottom surface are shown in Fig. 5-5(b). During the first thermal cycle, the sample experiences the highest peak temperature and phase transformations take place both in the heating and cooling stages. The start and finish time of the transformations obtained from

75

the experiment and the simulation are in good agreement. The predicted expansion rate is larger than that measured from the experiment, which leads to an overestimation of 0.001 strain. After the first thermal cycle, this deviation accumulates and remains unchanged in the rest of the process. In the second thermal cycle, the peak temperature is between the Ac_1 and Ac_3 temperatures. As only the central part of the specimen reaches the intercritical temperature, a small fraction of the material is subjected to phase transformations. This effect is still visible in the graph by the smoothing of the strain peak and is found to result in a mismatch in the strain around 0.002. In the following thermal cycles, the deviation of the strain is within 0.001. The thermal mechanical behaviour representing the bottom surface of six pass welds is predicted with a standard deviation error of 4.9×10^{-4}.

For the completely constrained test, the sample is unable to expand and no strain can be generated. In the heating stages, the sample is completely constrained at the two ends and thus under compression, while in the cooling stages, the compressive stresses are partially released depending on the inter-pass temperature. Fig. 5-6 shows the results of the transient force for the specimen representing the top surface. In the first three thermal cycles, the difference between the experimental and simulated results on the force is less than 50 N. Sharp peaks in the force are generated due to elastic deformation. In the fourth thermal cycle, as the sample is plastically deformed, a smooth peak is generated and the force becomes tensile in nature upon cooling. In the last thermal cycle, when the sample is cooled rapidly, martensite is formed. Due to the related volumetric change, the force has an apparent drop after which it increases again as a result of thermal contraction. In general, a good agreement exists between the measurements and the calculations. In the first five thermal cycles, the force difference is less than 50 N. In the last thermal cycle, after plastic deformation takes place, the force decreases until the end of the heating stage. The tensile force is overestimated by approximately 350 N in the last cooling stage. This can be due to the inaccurate elasto-plastic properties at high temperatures defined in the model during final cooling. The sample is plastically deformed more readily in the experiment, while in the simulation, a higher tensile peak is found.
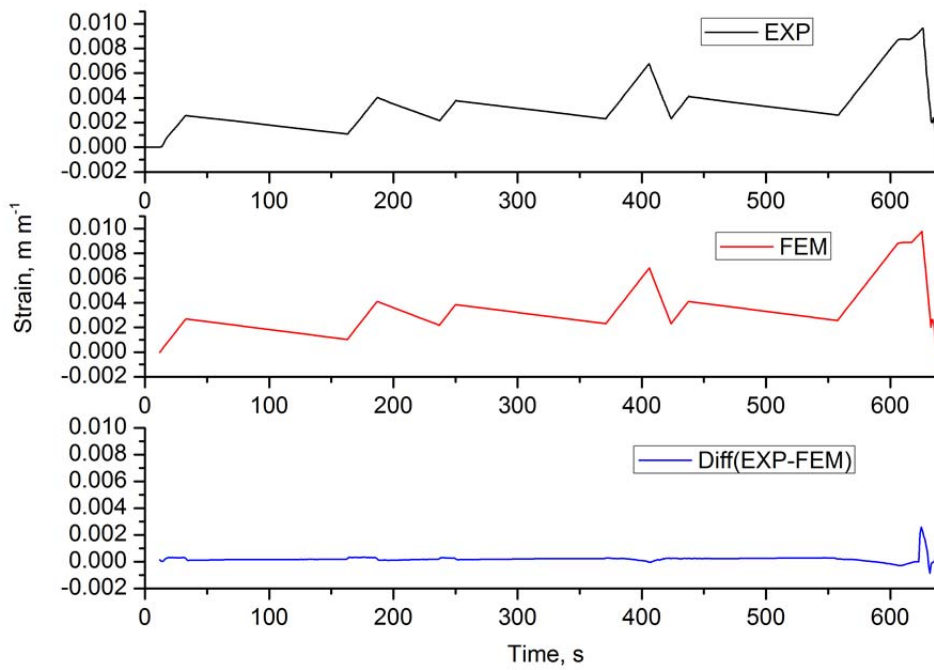
(a)
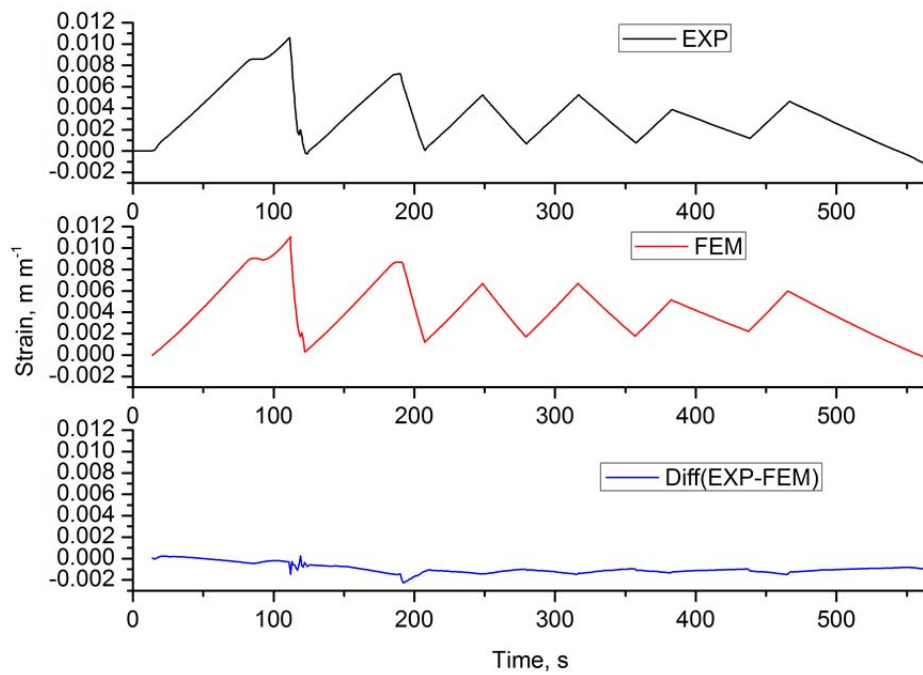
(b)

Fig. 5-5: Transient strain results representing (a) the top surface, (b) the bottom surface.
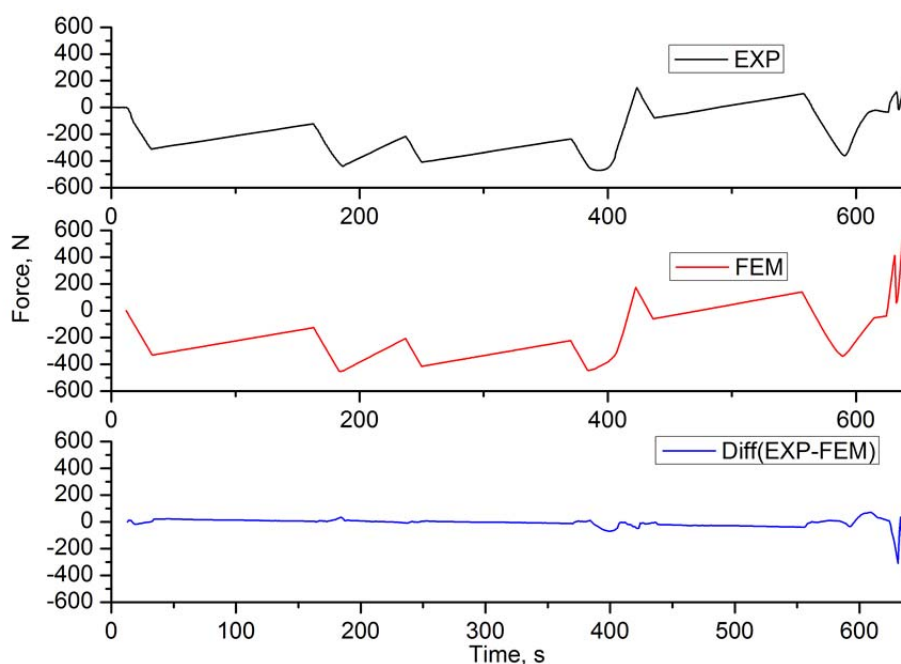
Fig. 5-6: Transient force results representing the top surface.

Combined free dilatation and constraint tests were performed to represent more realistic multi-pass welding conditions. Results from these tests for the samples representing the top and bottom surfaces are shown in Fig. 5-7(a-b), respectively. The primary axis on the left indicates the force, while the secondary axis on the right indicates the strain. For the top surface specimen, the first part of the experiment (*i.e.* the first five thermal cycles and the sixth heating stage) shows the same behaviour as in the free dilatation test. The sample is free to expand, whereas the force remains zero. The strain evolution is obtained and compared with the numerical results, showing a good agreement. In the last cooling stage, the sample is completely constrained. A tensile force is introduced in the sample due to thermal contraction. At the onset of the martensitic phase transformation a drop in force is observed as a result of the volumetric increase involved. In this stage of testing, the strain remains constant until the end of the measurement.

The sample representing the bottom surface is in load control only during the first heating stage, the remainder of experiment is carried out in position control. For this test, the experimental and numerical results of the transient strain and force are also compared. The strain increases until the end of the first heating stage and remains unchanged for the remainder of the test. The force is fluctuating from the first cooling stage. The strain evolutions of the combined dilatation and constraint test are reasonably well predicted by the model at both top and bottom surfaces. The simulated force evolution is in good agreement with experimental results at low temperatures, but is overestimated by 250 N at high temperatures (beyond Ac_1).

78
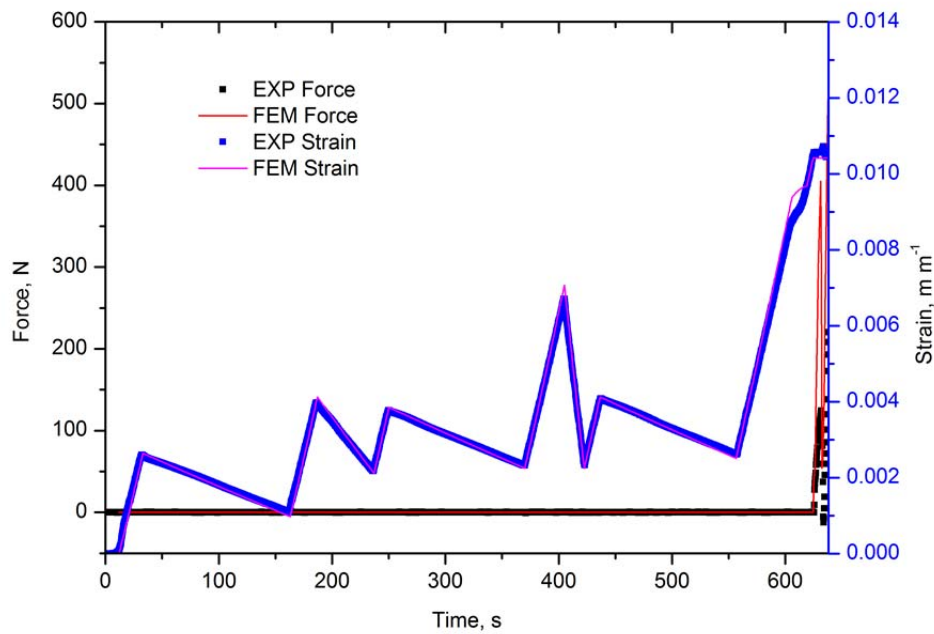
(a)
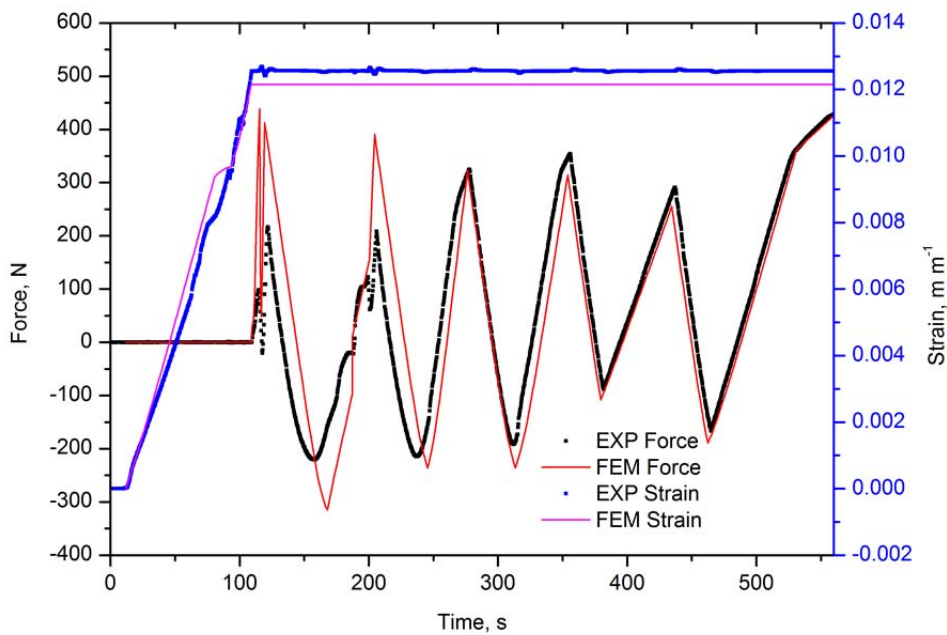
(b)

Fig. 5-7: Combined dilatation and constraint test results representing (a) the top surface and (b) the bottom surface.

5.5 Discussion

In welding, the workpiece is non-uniformly heated by the heat source. In

general temperature gradients encountered in the workpiece are steep. The peak temperatures and cooling rates depend on position and time. The strain and stress evolution is governed by thermal expansion and contraction, the occurrence of phase transformations in combination with the constraints applied. In multi-pass welding the consecutive thermal cycles will alter the material properties as repeated phase transformations and the effects of annealing, grain growth and refinement *etc.* are imposed.

In the modelling of strains and stresses in welding all relevant phenomena, ranging from an accurate description of the heat source to the application of boundary conditions for the constraints, should be included. The first step is the prediction of reliable temperature data. Gao *et al.* [116] describe methods to model temperature fields in multi-pass welding. Secondly, in welding, the workpiece is constrained by the application of clamps or by constraints of the construction. However, in the neighbourhood of the weld groove, constraints may vary in multi-pass welding due to the presence of deposited material during each pass. A third issue is to incorporate appropriate temperature dependent mechanical properties. In general, data on Young's modulus and yield strength obtained from tensile testing at elevated temperature is used.

The use of ETM testing permits simplification of the complex situation under welding conditions, as boundary conditions are well defined. Therefore, modelling of the ETM testing enables identification of the factors that introduce errors in the prediction. It should be kept in mind that the samples in ETM test experience a thermal gradient. However, this situation also occurs during welding and does not impose a major problem as in the models the temperature at each element is determined and mechanical properties according to this temperature are assigned.

In welding models the constraints are introduced to the plate by mechanical boundary conditions at the edges. The elements situated at the groove are able to move towards the imaginary centre of the plate. The freedom is automatically rejected when the elements become activated and are appointed certain mechanical properties. In ETM testing, well defined constraints can be applied and the effects on force and strain development can be studied. In this work free dilatation, a completely constrained condition and a combination of both have been investigated. In the models the constraints employed in ETM testing are introduced, and thus also well defined.

In the strain and stress models describing the ETM testing, the input of temperature dependant properties is required. In this work mechanical properties are obtained from tensile testing at elevated temperatures and the thermal expansion is extracted from dilatometry studies, see chapter 3.

High temperature tensile tests provide useful information for the elasto-plastic deformation of the material at different temperatures. However, this data does

not represent the state of the material after a thermal cycle involving a high peak temperature and fast cooling rates. The mechanical properties obtained from tensile testing may be appropriate for temperatures up to Ac_1, but for temperatures in excess of this value, the occurrence of grain growth and phase transformations may alter the mechanical properties significantly. In addition thermal expansion coefficients may be influenced by thermal cycling too.

Improvements in the models can be achieved by using material properties obtained from modified high temperature tensile tests, where the tensile samples are firstly heated above the Ac_3 temperature and then cooled at a controlled rate to the testing temperature. The evolution of the expansion coefficients during multiple thermal cycles, especially at high temperatures, may also improve the accuracy of the models.

5.6 Concluding remarks

In this chapter, ETM tests were performed to represent two specific positions of weld HAZ. The thermal cycles applied were obtained from the temperature measurements of six pass weld. The mechanical boundary conditions applied were defined as a free dilatation, completely constrained conditions and a combination of those two. The results from the FE model show a good agreement with the experimental data. A better understanding of the strain and force development as a result of the thermal expansion, volume change due to phase transformation and temperature dependent plastic deformation during multi-pass welding has been obtained.

6 Residual welding stress[cd]

In multi-pass welding, each successive thermal cycle will introduce local melting, solid state phase transformations, grain growth, grain refinement, recrystallization and recovery, all of which lead to a complicated stress state. Most stress measurements performed on multi-pass welds only show the final residual stress state [92, 107, 117]. Information concerning stress development receives little attention. When in numerical simulations, stresses are not validated after each weld pass, errors in the predicted final stress state may accumulate, leading to poor accuracy, particularly after a large number of passes. Even if a good agreement is found between numerical solutions and the final residual stress measurements, this does not imply that the finite element (FE) model gives an appropriate representation of the stress evolution. In this chapter stress evolution of a six pass weld is discussed on a pass-by-pass basis. Depth resolved strain measurements in two orthogonal directions were carried out after each weld pass using energy dispersive synchrotron X-ray diffraction. The residual stresses were calculated using the biaxial Hooke's law. A sequentially thermal-mechanical coupled model was constructed for stress analysis. The residual stresses were validated on a pass-by-pass basis, which improves the reliability of the FE models constructed. Based on the models, cross-sectional stress distributions are presented after each pass, revealing the weld stress development in multi-pass welds.

6.1 Research background of residual welding stress

Thermal mechanical tests with appropriate welding thermal cycles and constraining conditions are used to investigate the stress development, *e.g.* tests of Satoh [118], Shirzadi [114] and Gao [119] introduced in chapter 5. However, these tests are only applied to the specimen representing the top and bottom

---

surfaces of a multi-pass welded plate with known time-temperature profiles. Furthermore, the mechanical boundary conditions are defined as either free dilatation or fully constrained, while in real welding situations, the constraints are more gradually generated during solidification and subsequent cooling. These tests were used for the purpose of model validation and can only give an indication of the stress development during multi-pass welding at specific positions. Therefore, pass-by-pass stress measurements are valuable for the development of numerical simulations, providing data to validate the calculated stress distribution after each weld pass. This will lead to more accurate and reliable predictions of multi-pass weld residual stress fields.

6.1.1 Stress formation during welding

The welding process causes a highly non-uniform heating of the parts being joined. Areas of the workpiece close to the welding arc are heated to temperatures close to the melting temperature of the material, and are subsequently cooled, conducting the heat further to the bulk of the workpiece. For an applied thermal change (ΔT) on an isotropic material, the accompanying thermal strain ($\Delta\varepsilon^{th}$) is defined by the linear thermal expansion coefficient (α)

$$\Delta\varepsilon^{th} = \alpha\Delta T .$$ (6-1)
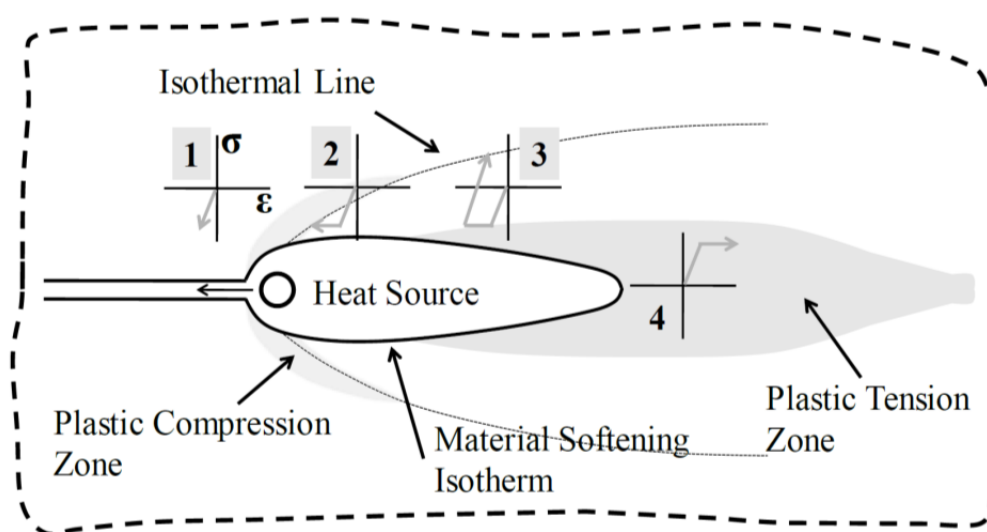
Fig. 6-1: Stress zones generated during welding [120].

Fig. 6-1 shows schematically the stress zones generated during welding. Points 1, 2, and 3 are situated along a horizontal line next to the weld seam and hence, they represent the consecutive stress development at a point lying at a distance from the weld line. Firstly, the material is exposed to elastic compression (Point 1) due to the constrained expansion of the heated material. Plastic compression takes place when stresses exceed the yield stress (Point 2). In the cooling stage when the heat source has passed by, elastic stresses are unloaded (Point 3).

84

Point 4 represents the area where filler material is added to the weld groove and is only subjected to tensioning since the material was not present prior to welding.

Due to heating, the material in front of the weld is compressed plastically. The material in the weld pool looses all strength upon melting. During subsequent cooling, the material contracts, and thus the solidified material in the fusion zone is subjected to tensile stresses.

6.1.2 Three bar model

The longitudinal stress development during welding can be illustrated by a one dimensional three-bar model presented in Fig. 6-2, which represents the situation of a butt weld in a thin rectangular plate.
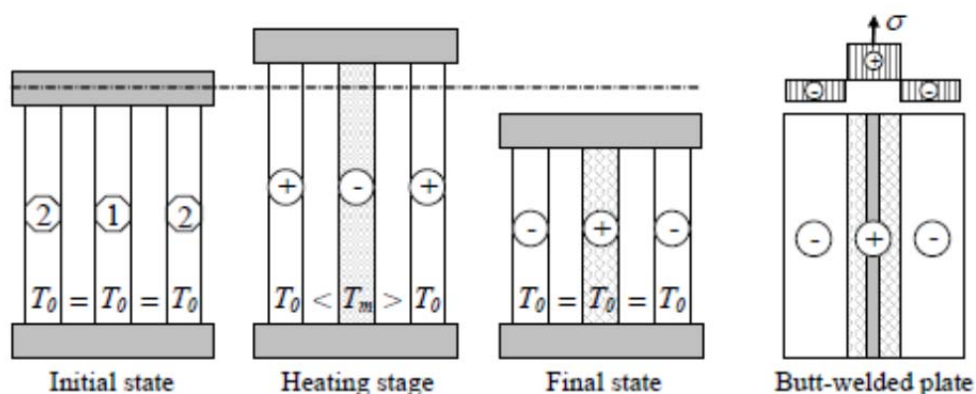
Fig. 6-2: Three-bar system constrained by rigid bases under an applied temperature cycle and the analogy with a butt-welded plate.

The middle bar represents the weld and heat-affected-zone, and the outer bars represent the cold base material. These three bars have equal length (l) and cross sections, which are linked at the top and bottom sides by two rigid transverse bars. Due to this transverse linking, all bars are forced to have the same length at any instance in time. In addition, the system should be balanced at all times, which can be expressed as

$$\sigma_1 = 2\sigma_2. \qquad (6\text{-}2)$$

where the subscripts 1 and 2 represent the middle bar and the outer bars respectively.

In the initial state, all bars are at room temperature (T_0). Subsequently, the middle bar is heated to a temperature T_m below the melting point, while the outer bars remain at temperature T_0. Upon heating, the middle bar expands as

$$\frac{\Delta l}{l} = \alpha \Delta T \qquad (6\text{-}3)$$

.

The expansion of the middle bar is restrained by the two outer bars, causing compressive stresses in the middle bar, and tensile stresses in the outer bars. Due to the boundary condition that all bars must have the same length at all times and the stresses must be in equilibrium, the following equation must be satisfied

$$\frac{\sigma_1}{E(T)} + \alpha \Delta T + \frac{\sigma_2}{E(T_0)} = 0 , \tag{6-4}$$

in which $E(T_0)$ is the Young's modulus at room temperature, and $E(T)$ the Young's modulus at temperature T. This leads to the following expression for the stress development in the middle bar

$$\sigma_1 = -\alpha \Delta T \frac{2E(T_0)}{1+(2E(T_0)/E(T))} . \tag{6-5}$$

Temperature dependent material properties (high strength steel S690QL1) were appointed to this three bar model. The stress development in the middle and outer bars, for an applied temperature cycle of heating and cooling to bar 1, is given in Fig. 6-3. The temperature in the middle bar increases from 25 to 1400 °C in 5 s, and decreases again to 25 °C in another 5 s. The expansion rate is assumed to be 1.6×10^{-5} K^{-1}. In the heating stage, the expansion of the middle bar is constrained, which is as a result under compression. Upon cooling, the whole process is reversed: tensile stresses develop in the middle bar due to the constrained contraction, and balancing tensile stresses develop in the outer bars. In the final stage, after the full cycle of heating and cooling, the middle bar experiences a tensile stress below the materials yield stress, while the outer bars are in a balancing compressive stress state. In analogy with a real weld it can be expected that close to the weld, tensile residual stresses are present. With increasing distance from the fusion line the stresses gradually decrease, eventually becoming compressive nature [120].

The stresses mentioned in the three bar model is in elastic region. When the temperature is increased, the yield point of material decreases. At around 750 °C, when the internal stresses exceed the yield point, plastic deformation will take place. Similar principle for the stress evolution in the cooling stage, see Fig. 6-4.
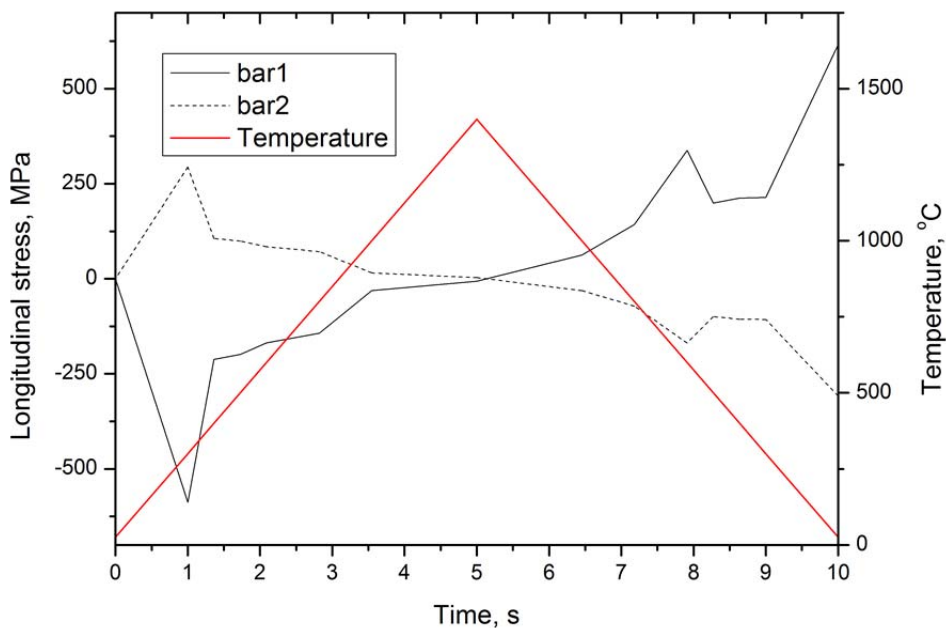
Fig. 6-3: *Thermal load (temperature) on bar 1 and resulting longitudinal stress development in bars 1 and 2 as a* function of time.
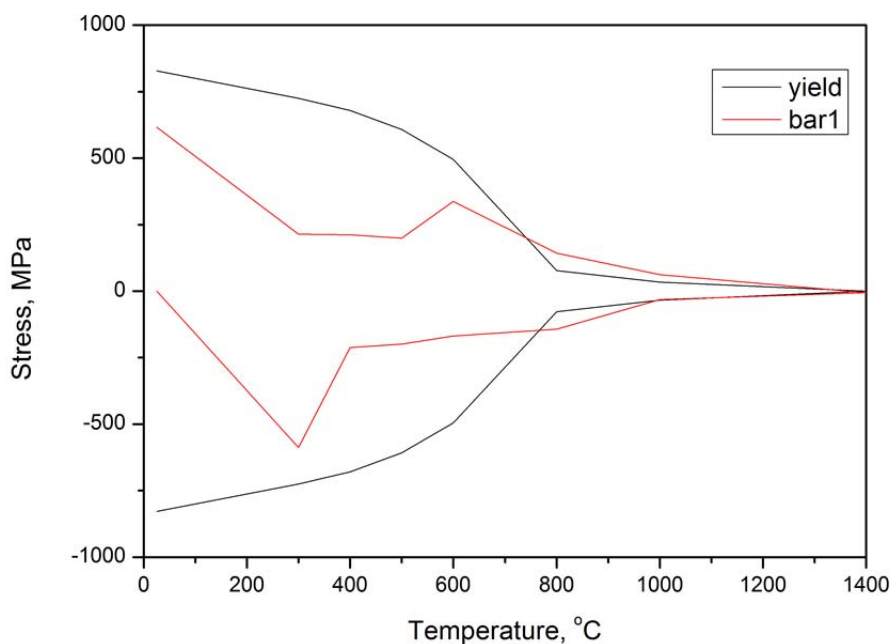
Fig. 6-4: *Longitudinal stress development in bar 1 and material yield strength as a function of temperature.*

6.1.3 Solid-liquid transformation

The equivalent plastic strain (PEEQ) in a material is a scalar variable that is

used to represent the material's inelastic deformation. $PEEQ_i$ is equal to the sum of $PEEQ_{i-1}$ and $\Delta PEEQ$. $\Delta PEEQ$ is a function of all the plastic strain components ΔPE_{ij}. When temperature of the material point exceeds $T_{melting,}$ $PEEQ_i$ is overwritten by the minimum value between ($PEEQ_{i-1}+\Delta PEEQ$) and zero. When PEEQ is zero, stress will not build-up representing the liquid stage. However, all the plastic strain components PE_{ij} are still recorded by the model. If the temperature of the material point falls below the melting temperature, the model will firstly update $PEEQ_{i-1}$ from the last step (zero in this case), $\Delta PEEQ$ is calculated from the recorded ΔPE_{ij}. An example of a bar model is given explaining the equivalent plastic strain reset, see Fig. 6-5, T_{max} and $T_{melting}$ are 2000 °C and 1462 °C, respectively.
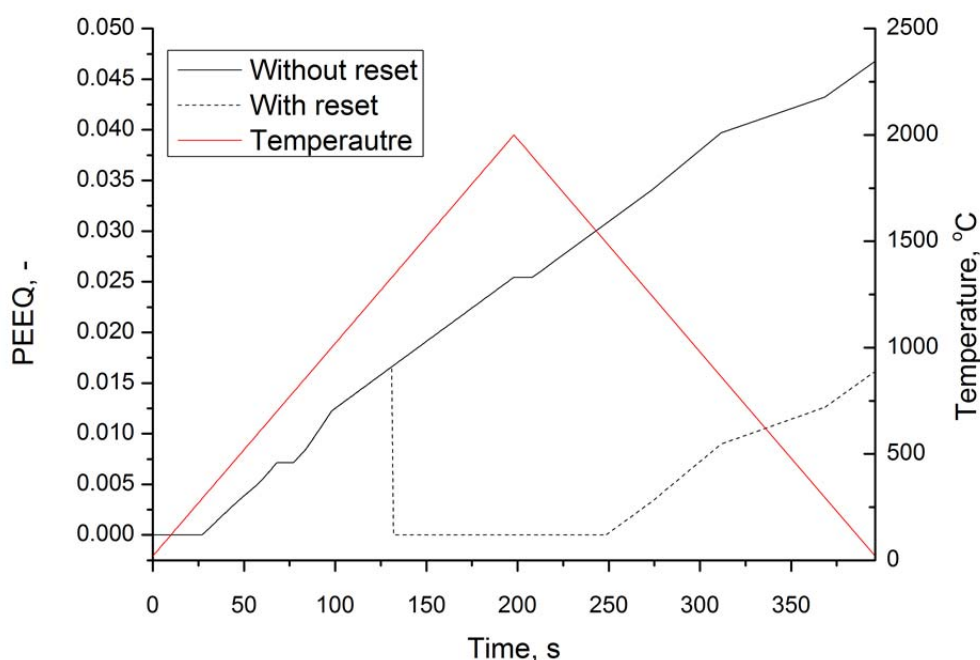
Fig. 6-5: Equivalent plastic strain reset on one bar model.

6.1.4 Solid-solid transformation

Most materials are not only subjected to solid-liquid transformation, but also experience solid-solid phase transformations both during heating and cooling [121]. There are two ways to implement the solid state phase transformation into finite element models, *i.e.* explicitly or implicitly.

For the explicit method, the evolution of different phases is obtained from the continuous cooling transformation (CCT) diagram. Depending on the cooling rate, steel might transform into one or more phases: martensite (M), bainite (B), ferrite (F) or perlite (P).

The boundaries of the domains where these phases grow as functions of the temperature *T* and the time *t* can be modelled with polygons. There are

algorithms to determine whether a point (T,t) is within the domain or not. In the present work, a simplified method has been implemented using an inverse parabolic approach for each phase domain:

$$T(t) = \pm a\sqrt{t-t_0} + T_0, t > t_0 \tag{6-6}$$

$$T(t) = \min(T, T_{up}) \tag{6-7}$$

$$T(t) = \max(T, T_{low}) \tag{6-8}$$

where a, t_0, T_0, T_{low}, T_{up} are a scaling factor, the start time for the transition, an offset temperature, the lower temperature limit and the upper temperature limit for the phase, respectively. If the current state (T,t) is within the domain of any phase, this phase grows.

LeBlond [122] equation is applied for the diffusion-controlled solid-solid phase transformations on cooling, *i.e.* austenite→ferrite or austenite→perlite/bainite. For a constant temperature change rate, this equation can be integrated analytically to

$$P_i(T,t) = P_i^{EQ}(T)\left(1 - \exp\left(\frac{-t}{\tau}\right)\right). \tag{6-9}$$

where τ is a phase growth parameter. For any phase except austenite, the equilibrium fraction of phase i is set to the current fraction of phase i plus the austenite phase fraction: $P_i^{EQ} = P_i + P_{austenite}$. For austenite above the A_{c3} temperature, the equilibrium phase fraction is set to $P_{austenite}^{EQ} = 1$.

The diffusionless solid-solid phase transformations from austenite to martensite can be described by the time-independent Koistinen-Marburger equation [123]

$$P_M(T,t) = P_i^{EQ}\left(1 - \exp\left(-b(M_s - T)\right)\right). \tag{6-10}$$

Here, P_i^{EQ} is the initial austenite fraction at the start of the martensite transition and b is a martensite growth parameter. The total phase volume V, the phase volume change ΔV and the incremental phase strain $\Delta\varepsilon_{ph}$ is determined using a linear mixing rule involving the fraction P_i of each phase i:

$$V = \sum_{i=1}^{nPhases} V_i P_i \tag{6-11}$$

$$\Delta V = \sum_{i=1}^{nPhases} V_i \Delta P_i \tag{6-12}$$

$$\Delta\varepsilon = \frac{1}{3}\frac{\Delta V}{V_{Start}}. \tag{6-13}$$

The initial phase volume V_{Start} is determined by the initial phase fractions.
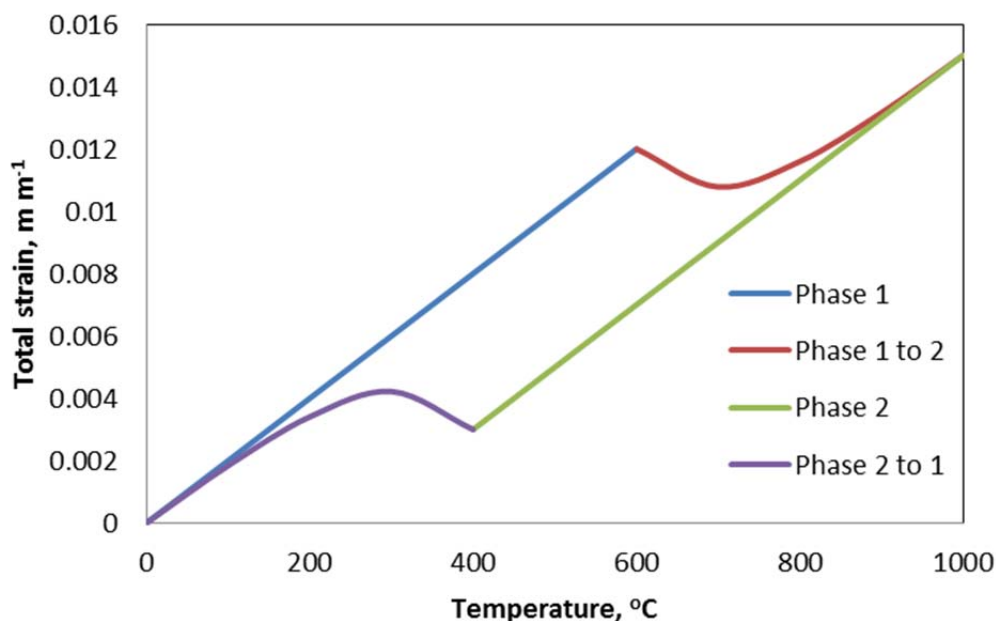
(a)
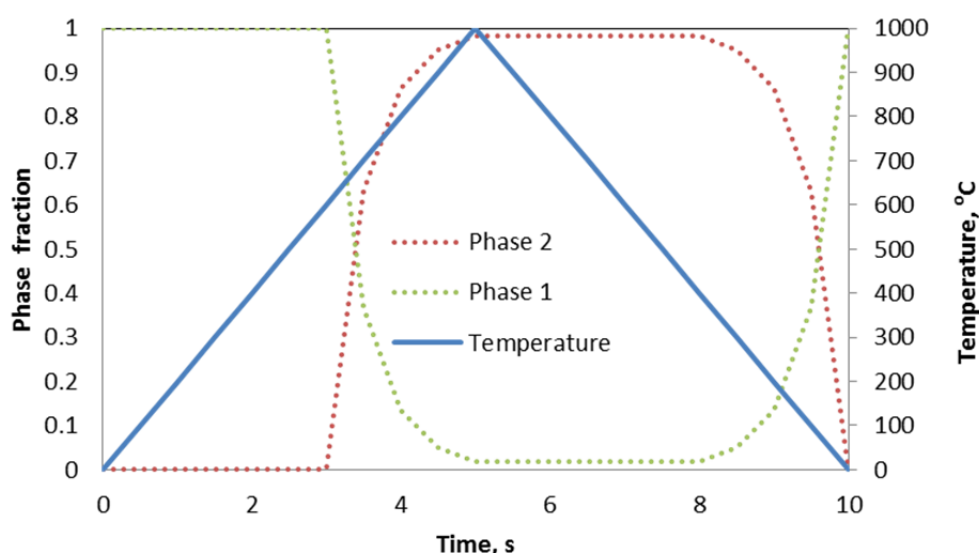
(b)

Fig. 6-6: (a) Strain change, (b) phase change due to one thermal cycle.

Fig. 6-6 shows an example of a computed dilatometer curve for an arbitrary two-phase material. The material is heated up to 1000 °C with subsequent cooling to room temperature. Phase 1 grows below 600 °C, phase 2 above 400 °C. It is assumed that both phases show diffusion-controlled growth with a common growth constant of 0.5 s [124]. The coefficient of thermal expansion is set to $2\times10^{-5}\,\text{K}^{-1}$. The volume change from phase 1 to 2 is set to 1.5% leading to a maximum phase strain of 0.5% (which is one third of the volume change). Unfortunately, the difficulty to obtain appropriate temperature dependent material data of individual phases and the volume changes due to different phase transitions are a limitation of the explicit method.

The advantage of implicit method is not necessary to consider the fraction of the phase. The expansion coefficients at different cooling rates can be experimentally determined by the free dilatation tests. These material responses can be appointed at different locations in the weld component based on cooling rate. The transverse expansion during welding is illustrated using a transverse three bar model. The right-side edge of the bar is constrained to represent the clamping condition. A heat source applied at the left-side edge represents the area exposed to welding arc. The selected peak temperatures of bar 1, 2 and 3 are 1000, 800 and 500 °C, respectively, see Fig. 6-7. Bar 3 represents the base material of the welded plate, where no phase transformations occur. Linear thermal expansion and contraction takes place in this region. When the peak temperature is in the intercritical region (between Ac_1 and Ac_3), which is selected for bar 2, a volume change due to the phase transformation occurs. In combination with the thermal expansion, a slope change of the expansion curve is observed in the heating stage. The dilatation tests with a peak temperature in this region are lacking, and thus an assumption is made: if the peak temperature is below the Ac_3 temperature, the contraction follows the heating curve from the dilation test in the opposite direction. When the peak temperature is higher than Ac_3 which occurs for bar 1, austenite is formed. The expansive contribution from bar 2 is included. In this bar, the contraction during cooling follows the dilatation curves according to different cooling rates. A volume increase due to phase transformation is observed as can be seen in the figure at approximately 150 s.

(a)

(b)

(c)
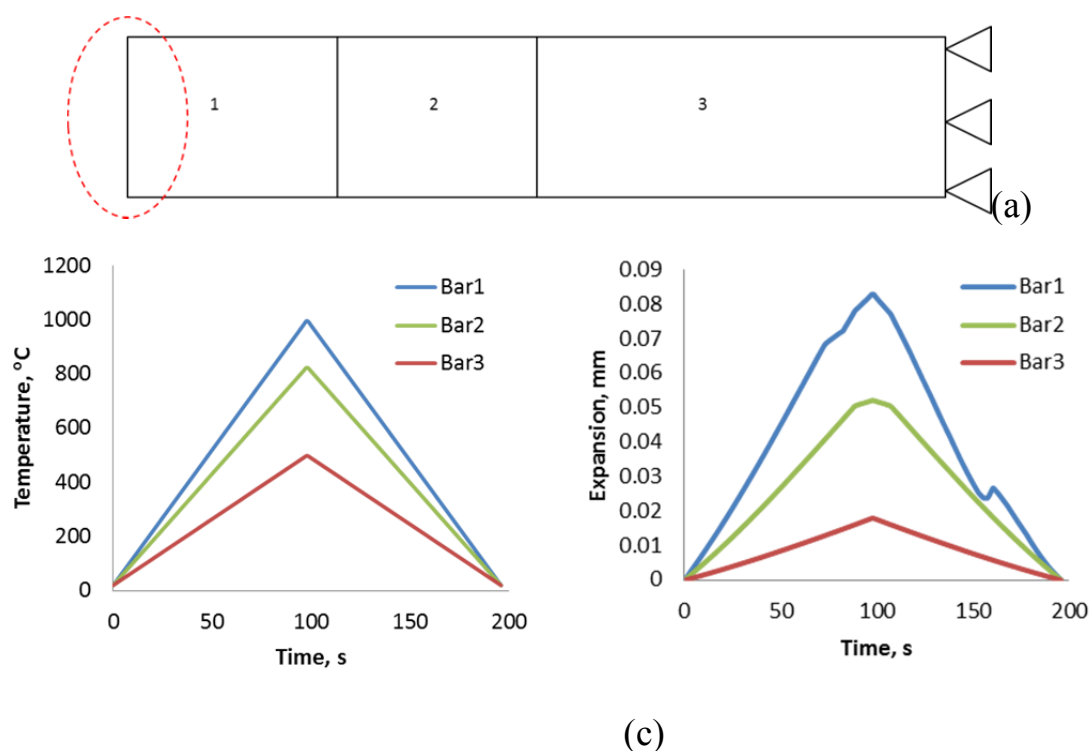
Fig. 6-7: (a) Transverse expansion during welding represented by the three-bar model, (b) applied temperature and (c) resultant expansion.

91

6.2 Experimental approach

6.2.1 Six pass welds preparation

Details of the welding arrangement and procedures followed were presented in chapter 4.2. Six steel plates with a thickness of 16 mm were prepared for stress measurement each with an increasing number of passes from 1 to 6. The welded workpiece were constrained by clamps until they had completely cooled down to room temperature.

6.2.2 Synchrotron X-ray diffraction

The experimental arrangement of the energy dispersive synchrotron X-ray diffraction measurements in European Synchrotron Radiation Facility (ESRF), Grenoble, France, is shown in Fig. 6-8. The incident-beam geometry was defined by a pair of vertical and horizontal slits with a size of 100×100 μm^2. The diffracted beam size was defined by two sets of static slits, one close to the sample with a horizontal gap of 100 μm and another slit close to the detector with a horizontal gap of 400 μm. The vertical beam geometry was defined by the vertical gap of the incident slits only. Between the slits, the beam travelled through a copper tube shielded with lead. Additional slabs of lead were mounted around the detector window to prevent the entry of background radiation. Strains in two orthogonal directions are measured (perpendicular to the incident beam). Two liquid-nitrogen-cooled germanium single-crystal detectors with 4096 channels were placed at a 2θ position of approximately 5°. In this configuration a gauge volume of $0.1 \times 0.1 \times 2$ mm^3 is obtained with a gauge length of 2 mm. The exposure time for each position was 150 s. The detectors were calibrated using a barium radioactive source with a known spectral emission, which was fitted with a second-order polynomial,

$$e_i = a_1 + a_2\Delta_i + a_3\Delta_i^2 \tag{6-14}$$

to convert each channel element Δ_i to an energy e_i. The calibrated conversion constants a_1, a_2, a_3, in the transverse direction (perpendicular to the weld seam) are 0.07504, 0.05731, and -3.253×10^{-8} respectively and in the longitudinal direction (parallel to the weld seam) the constants are 0.03357, 0.05853 and -3.448×10^{-8}. This resulted in a detector resolution (channel width) in the transverse direction of 0.05731 keV and in the longitudinal direction of 0.05853 keV. The small second-order conversion coefficients indicate that the conversion is almost linear.
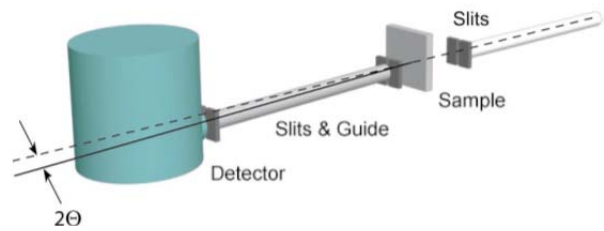
(a)   (b)

Fig. 6-8: (a) Energy dispersive diffraction arrangement [125], (b) schematic representation of the set-up.

6.2.3 Data processing and analysis

Fig. 6-9(a) shows one of the diffraction pattern measured at the underside of the six pass welded plate (90 mm from the weld centre line and 2 mm from the bottom surface), located in the base material showing four peaks of the bcc planes ({200}, {211}, {220}, {310}). Fig. 6-9(b) shows one of the diffraction patterns of the six pass welded plate (2 mm from the weld centre line and 2 mm from the bottom surface), located in the heat-affected zone close to the fusion line (see the inset picture). This position experiences a peak temperature of around 1000 °C and a cooling rate of around 67 K s^{-1}. Apart from the four bcc peaks, three fcc peaks of retained austenite ({220}, {311}, {222}) are observed.
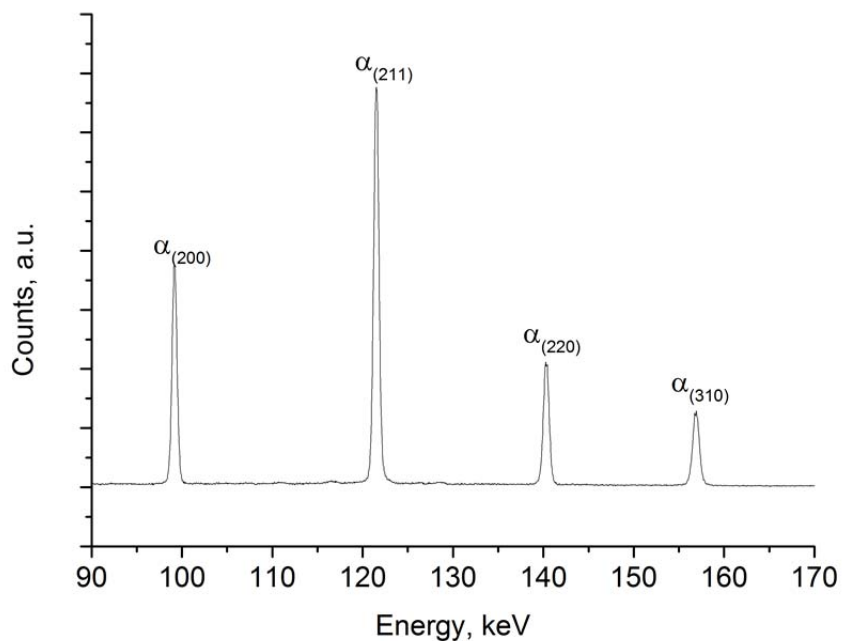
(a)
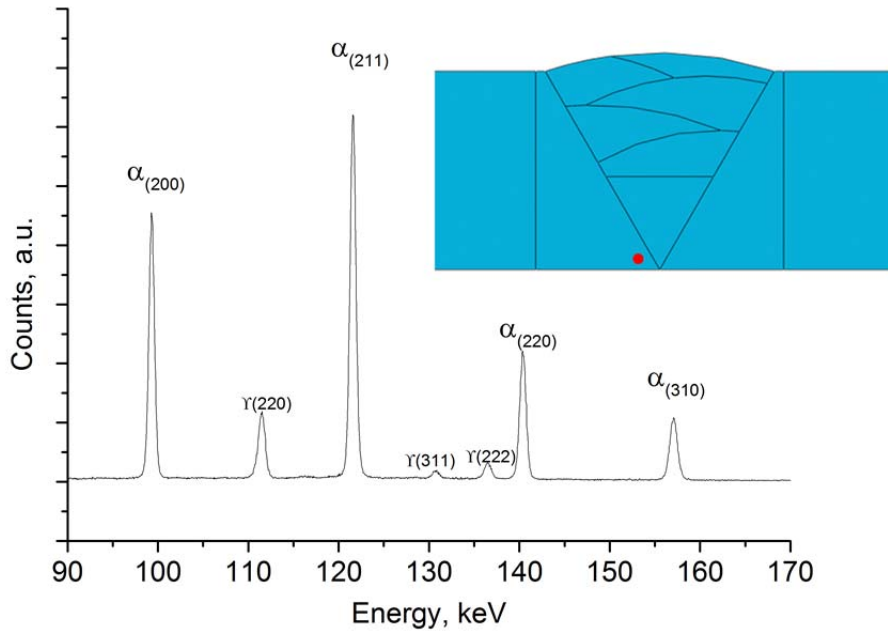
(b)

Fig. 6-9: Energy dispersive patterns (a) in the base material, (b) close to the fusion line.

A pseudo-Voigt approximation, consisting of a weighted sum of a Gaussian and a Lorenzian contribution, is used to determine the centre position of the peak. It is described as

$$Voigt_{pseudo} = (1-\eta)Gauss(\Gamma) + \eta Lorenz(\Gamma),$$ (6-15)

where η is the mixing factor of Gaussian and Lorenzian contribution, and Γ is the full width at half maximum (FWHM) [126]. Fig. 6-10 shows the peak fitting for the {200} bcc plane. The height of the base is 48.62 counts, the height of the peak is 3758.14 counts, the position of the peak is 99.17 keV, the half width at half maximum of the diffracted peak is 0.26 keV and the fraction of the Lorenzian contribution is 0.16. The residual between the experimental measurements and the fitted profile is plotted below the fitted diffraction curve. The strain uncertainty induced by the fitting procedure used is below the order of 10^{-6}.

`
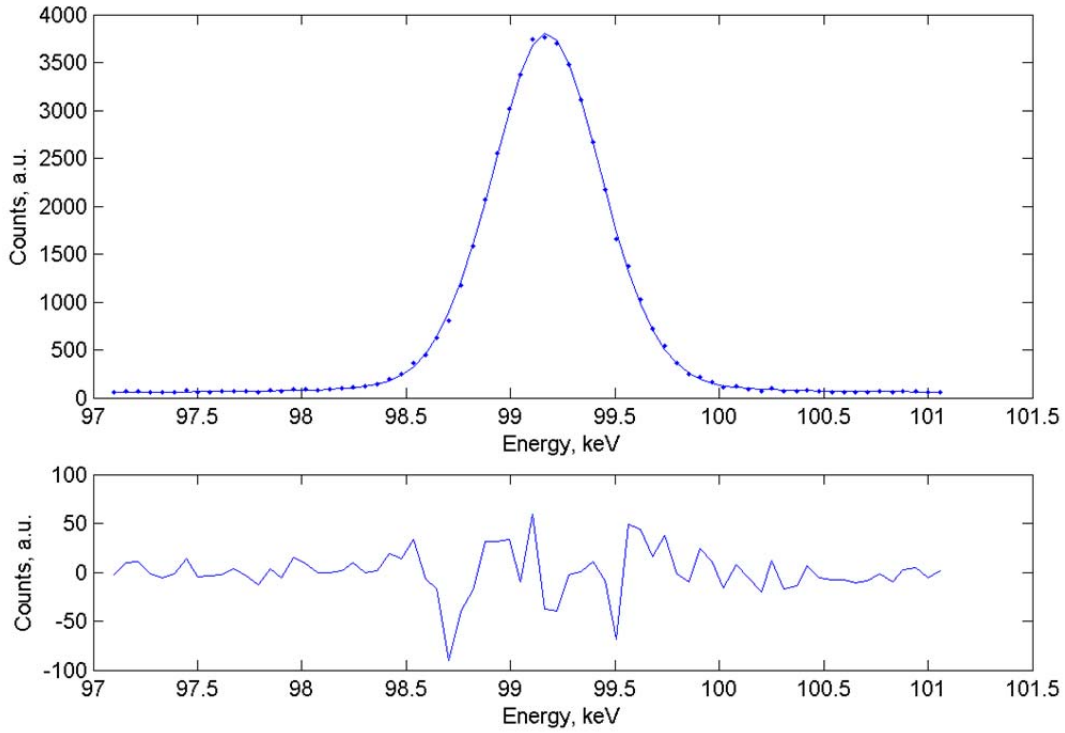
Fig. 6-10:Pseudo-Voigt fitting and residuals of a {200} bcc plane.

Iron powder was used to estimate the variation in the peak energy due to the combined influence of the instrument uncertainty and the fitting procedure. The peak energy was determined in duplicate for the four bcc planes. A strain uncertainty induced by reproduced measurement is below the order of 10^{-4}.

From Bragg's law, for a fixed diffraction angle θ, the d spacing of a plane can be obtained *via* the wavelength λ, which is inverse proportional to the measured energy e_{hkl},

$$d_{hkl} = \frac{\lambda_{hkl}}{2\sin\theta} = \frac{hc}{2e_{hkl}\sin\theta},$$

(6-16)

where c is the speed of light and h is the Planck constant. The relative strain ε can be derived from the difference between the measured energy e_{hkl} and the energy $e_{0,hkl}$ for the stress free state,

$$\varepsilon_{hkl} = \frac{d_{hkl} - d_{0,hkl}}{d_{0,hkl}} = \frac{e_{0,hkl} - e_{hkl}}{e_{hkl}}.$$

(6-17)

The planar stress σ_i is calculated by the biaxial Hooke's law,

$$\sigma_{i,hkl} = \frac{E_{khl}}{1 - v_{hkl}^2}(\varepsilon_{i,hkl} + v_{khl}\varepsilon_{j,hkl}),$$ (6-18)

where i and j are two orthogonal directions and using the diffraction elastic constant E_{hkl} and Poisson's ratio v_{hkl} of the individual planes, which were determined by Dutta *et al.* and are given in Table 6-1 [127].

Table 6-1: Diffraction elastic constants and Poisson's ratios for individual bcc planes [127].

Plane	{200}	{211}	{220}	{310}
E (GPa)	169.3	221.5	218.2	220.0
v	0.295	0.227	0.239	0.230

6.2.4 Stress free sample

A stress free sample was electro-discharged machined from the middle of the six pass welded plate with a thickness of 2 mm. In addition combing was done with several vertical slits at positions of 5, 20 and 50 mm from the weld centre line to release the strains even further, as shown in Fig. 6-11(a-b). The slit depth and width are 10 and 1 mm, respectively.

Plate size: L=250mm, W=200mm, T=16mm
Sample size: 2mm x 200mm x16mm

(a)

Position from the centre a = 5 mm, b = 20 mm, c = 50 mm
Cut depth d = 10 mm, cut width: around 1mm
Plate dimension: T = 16 mm, W = 200 mm
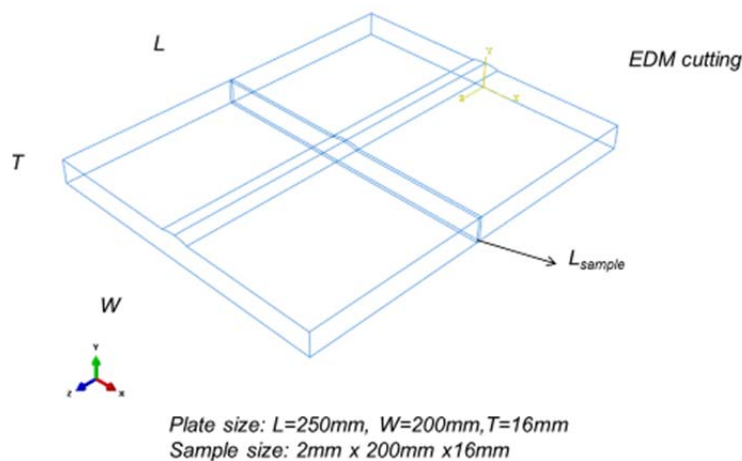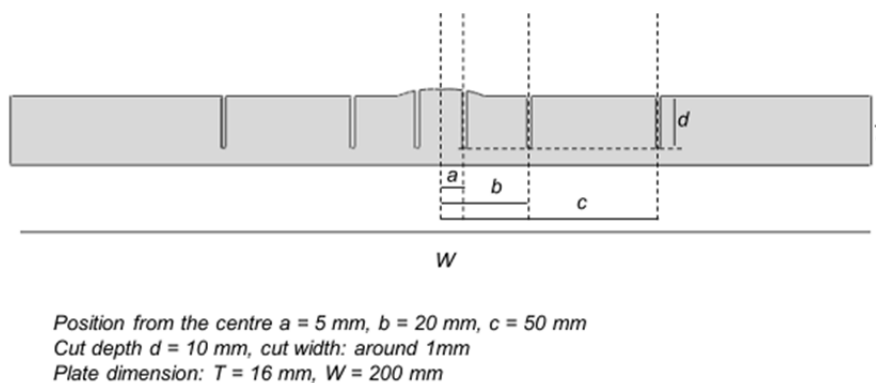
(b)

Fig. 6-11: (a) Location of the stress free sample, (b) cross section of the stress free sample indicating the location and dimensions of the combing slits.

6.2.5 Measurement positions

In total 114 positions were measured in the stress free and the six pass weld as shown in Fig. 6-12. The dots indicate the measurement locations. The solid lines indicate the position of the V-groove. In the weld region, ranging from -20 to +20 mm from the weld centre line, the measurement density is relatively high, specifically at the weld root and weld toe where the stress concentration factor is expected to be high [128]. In the thickness direction seven measurements were performed. In the base metal, the measurement density is reduced and comprises of nine measurements. The experimental results will be presented in contour plots. It should be noted that the centre of the gauge volume is plotted. As the gauge volume has a length of 2 mm, the data extends to 1 mm below the plate top and bottom surfaces. For the first five weld passes, the weld gap is gradually filled by the filler metal. Measurements were only carried out along line a, b and c.
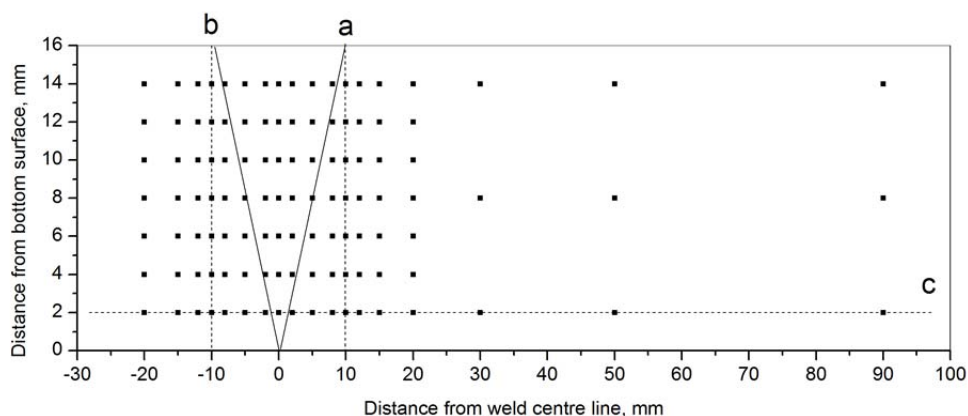
Fig. 6-12: Measurement position map of six pass weld.

6.3 Modelling approach

6.3.1 Simulation of welding

The multi-pass welding simulation began with two dimensional (2D) finite element (FE) models. In 1989, Free and Goff [129] used 2D plane strain elements for residual stress simulation in welded plates. Butt welding of the metal plate was simplified by assuming symmetry along the longitudinal (welding direction) through thickness plane, and hence the time of calculation was reduced. Assuming a plane strain (PS) condition, the weld metal was deposited instantaneously by modelling a typical transverse cross-section. Plane strain elements were defined in one plane, and all loading and deformation were also restricted to this plane. This strategy of modelling is normally used for bodies that are very long relative to their lateral dimensions [130], which is applicable to many welding applications. Webster *et al.* [131] has demonstrated that there is a minimal longitudinal variation in distortion for continuous weldments with heat inputs maintained constant throughout the weld length, and the limiting assumption of instantaneous welding appears to be reasonable. However, the use of plane strain elements resulted in higher stress predictions, as these elements cannot accommodate any thermal expansion in the longitudinal direction.

Generalised plane strain (GPS) models [132] define two planes that can move with respect to each other. By defining one reference point, the introduced strain in the longitudinal direction of the model varies linearly with respect to the position in the planes [130]. Generalised plane strain elements are typically used to model a section of a long structure that is free to expand axially or is subjected to axial loading.

By modelling a typical cross-section, the results tend to represent the residual stress distribution under certain 2D assumptions. Although these models yield useful information, the thermal and stress-strain responses of all weldments under a moving heat source are transient and three dimensional (3D) in nature [89, 133]. Thus, 3D modelling is of great importance in reflecting the reality of the residual stress distribution, especially for complex geometries where no geometric simplification can be assumed; however, the computational time can be long.

6.3.2 Model comparison

A comparison of the three models introduced was made on the basis of a single pass weld to investigate the efficiency and accuracy. A 2D shell deformable plane was built with CPE8RT (8-node plane strain thermally coupled quadrilateral with reduced integration) elements and CPEG8RT (8-node generalised plane strain thermally coupled quadrilateral with reduced integration) elements [130], and a 3D solid deformable body was built with

C3D20RT (20-node thermally coupled brick with reduced integration) elements. The geometric order of the element is quadratic, which requires fewer elements than a linear order for the same number of integration points or provides more integration points for the same number of elements. The plane strain (PS) and generalised plane strain (GPS) models have the same mesh and thus the same number of elements. Reduced integration was performed for the thermal mechanical analysis. The temperature and displacement at the nodes were fully coupled. Table 6-2 shows a comparison of the 3D solid, 2D PS and 2D GPS models. If the calculation time for the PS model is assumed to be 1, the time for the GPS model is 2.63, and the time for the 3D model is 127.

Table 6-2: Comparison of 3D solid, 2D PS and 2D GPS models.

	2D PS	2D GPS	3D solid
Fractional size of plate	1	1	1/6
Number of Elements	252	252	1086
Element family	Couple T-D	Couple T-D	Couple T-D
Element type	CPE8RT	CPEG8RT	C3D20RT
Geometric order	Quadratic	Quadratic	Quadratic
Nodes	1371	1372	5495
Degrees of Freedom	3	3	4
Variables	2018	2821	17967
Wall-clock time (s)	413	1090	52237
Time factor	1	2.63	127

Fig. 6-13 shows the transient stress comparison at the top surface in the transverse direction 30 mm from the weld centre line for the 2D PS, GPS and 3D solid models. 'Slong' indicates the longitudinal stress and 'Strans' the transverse stress. It can be expected that the longitudinal stress peak (550 MPa) predicted by the 2D PS model is overestimated due to the longitudinal constraint. The longitudinal stress peak (380 MPa) predicted by the 2D GPS model is smaller due to the free longitudinal expansion. The longitudinal stress predicted by the 3D solid model (470 MPa) lies between the predictions of the 2D PS and GPS models. The peak stress from the 2D PS model is 1.2 times

larger than that from the 3D solid model, while the peak stress from the 2D GPS model is 0.8 times smaller than that from the 3D solid model. The longitudinal stresses predicted by the 2D PS and 3D solid models follow the same trend during cooling, while the longitudinal stress predicted by the 2D GPS model decreases more slowly. The final longitudinal stress state at this position is in compression, and the stress difference between the three models lies within 50 MPa. The transverse stresses follow the same trend during the thermal cycles, and the final stress difference between the three models lies within 70 MPa.
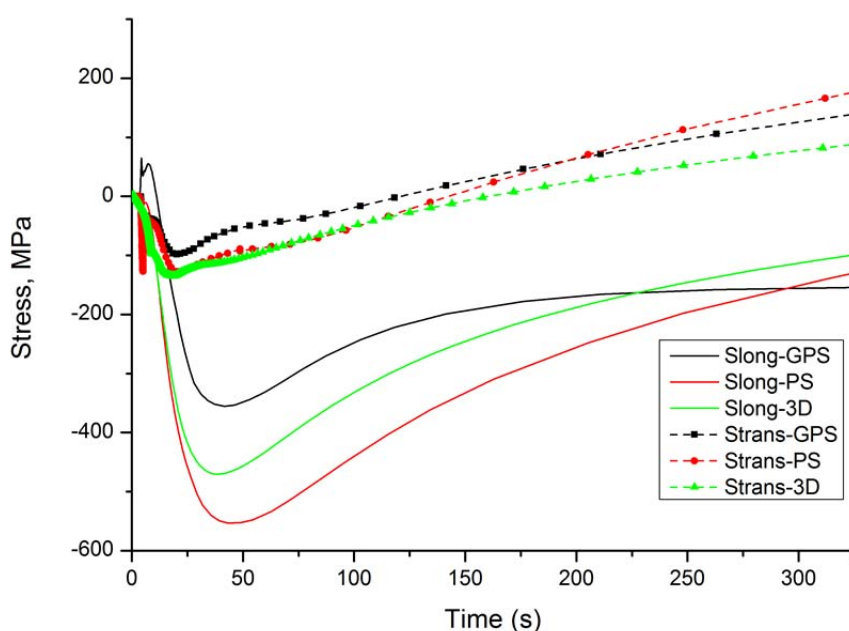
Fig. 6-13: In-situ stress prediction at the top surface of the plate 30 mm from the weld centre line of a single pass weld using the PS,GPS and solid models.

6.3.3 Model construction

Structural modelling was performed to calculate the thermal mechanical behaviour of the samples during welding. The computational domain of the models was limited to the sample, which means that the clamping system and welding heat source were not modelled explicitly. Fluid flow phenomena were not taken into account.

The constructed thermal model was presented in Chapter 4.3. This model was extended and coupled with the mechanical analysis enabling the prediction of the welding distortions and material residual stresses. The deformation of the workpiece after welding was resulted from the localized thermal expansion and contraction in combination with plastic deformation at elevated temperatures.

The effect of phase transformations on welding stresses and strains were included by the implicit method introduced in chapter 6.1.

A 2D shell generalized plane strain model was used to investigate the stress evolution of the multi-pass welds, see Fig. 6-14. The geometric order of the element is quadratic. The element type is CPEG8RT. The transient temperature obtained from the thermal model was imported into each stress analysis. The assembly of the model is kept the same as the thermal model. Thermal and mechanical material properties were assigned to the workpiece. The initial temperature of the workpiece was defined as room temperature. Mechanical boundary conditions were modelled by constraining certain nodes. Underneath the positions of the clamps, the vertical displacement is constrained; two bottom corners were also constrained to prevent horizontal and vertical displacement. These constraints are removed after unclamping. Equivalent plastic strain was reset to zero when the elements reached a temperature higher than the solidius temperature. The model change technique was used to activate the filler metal material, as stated in chapter 4.3.
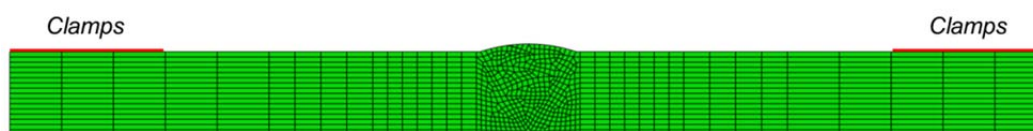
Fig. 6-14: 2D GPS model of six pass weld.

6.4 Results and validation

6.4.1 Stress free analysis

From the experimental results, contour maps have been composed showing energy, strain and stress distributions. The scales from the minimum to the maximum are divided into 8 increments. Fig. 6-15(a) shows the peak energy distributions of the stress free and the six pass welded plates for the {200} bcc plane.

In the stress free sample, peak energy between 99.17 to 99.25 keV (light green) is observed in majority regions of the workpiece. In the weld zone, a dark green region with a peak energy between 99.10 and 99.17 keV and a yellow region with a peak energy between 99.25 to 99.32 keV are found. In the six pass welded plate, the energy varies from 98.89 keV in the weld centre to 99.46 keV at the edge of the plate. Compared with the energy distribution in the as-welded

plate, the variation in energies in the stress free sample is relatively small (a factor of 10).

(a)

(b)
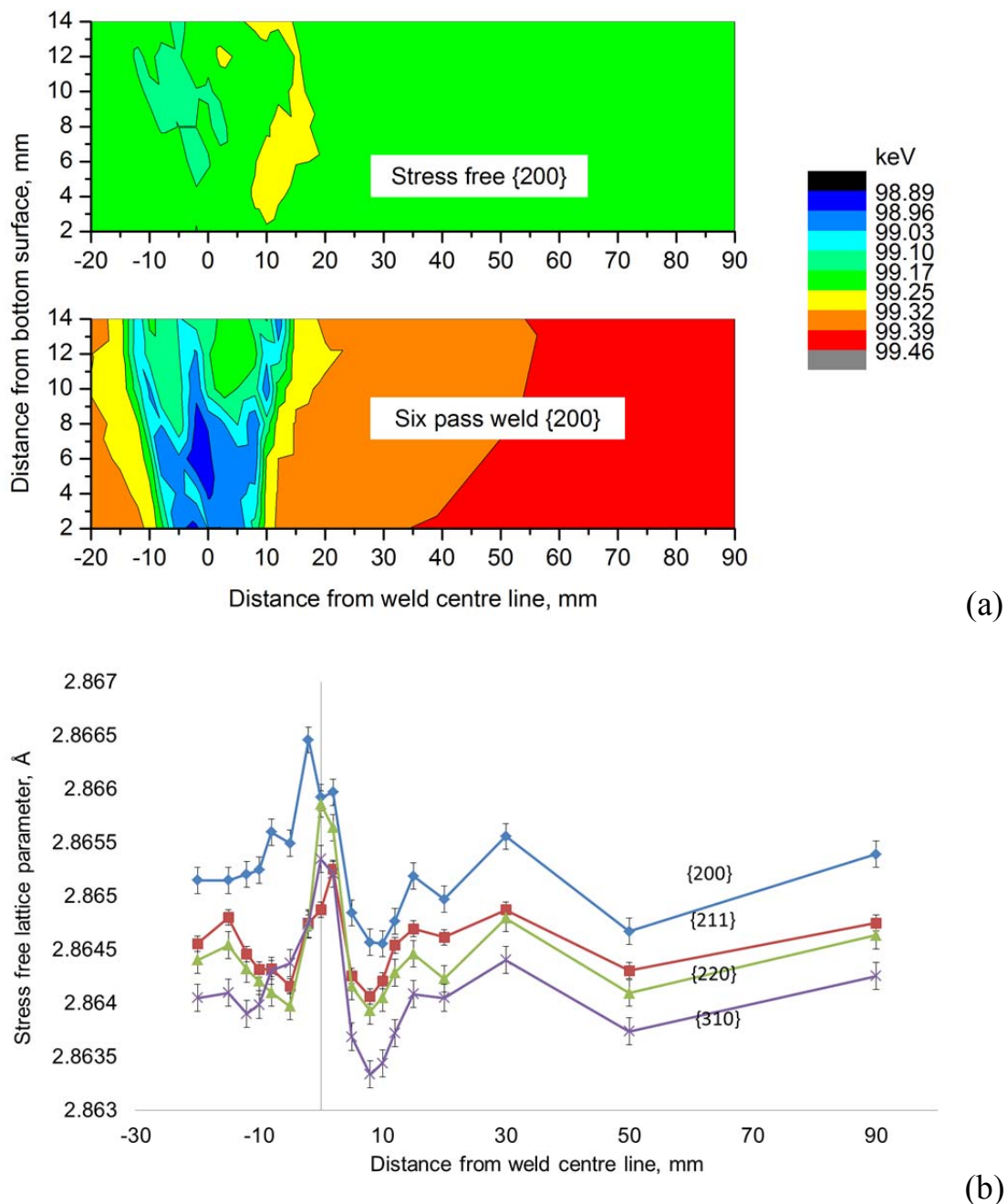
Fig. 6-15: (a) Peak energy distributions of a stress free and an as-welded condition of {200} bcc planes and (b) stress free lattice parameters for four bcc planes at 2 mm from the bottom surface as a function of distance from the weld centre line.

The calculated stress free lattice parameters of the four bcc planes ({200}, {211}, {220}, {310}) at 2 mm from the bottom surface as a function of distance from the weld centre line are shown in Fig. 6-15(b). The stress free lattice parameters vary from the edge to the centre [134]. A decreasing tendency

of the lattice parameters is observed from {200} to {310}. Stress free lattice parameters of each plane were selected for calculating the strain at related positions.

The lattice parameter variation can be explained by: (i) the alteration of the base metal microstructure in the weld metal and heat affected zones due to the weld thermal cycles. Solid state phase transformation, recrystallization and tempering may take place, affecting the lattice parameter; (ii) the elastic strains in the sample were not completely released. A tendency in lattice parameter as a function of distance to the weld centre line shows similarities to that of a welded specimen, *i.e.* a larger lattice parameter in the weld area which is loaded in tension and a smaller lattice parameter in regions experiencing compressive loads. This is supported by the fact that the lattice parameter of the four planes do not coincide. If the stress was completely released, the lattice parameters of the four planes should be the same. However, the strain is calculated by the shift of energy, which is a relative value to the energy $e_{0,hkl}$ of the stress free sample.

6.4.2 Stress map of six pass weld

The transverse strain maps (*i.e.* strains perpendicular to the weld seam) of the four bcc planes ({200}, {211}, {220}, {310}) of the as-welded plate are shown in Fig. 6-16.The strain distributions of these four planes show similar trends. The {200} bcc plane is subjected to the highest deformation compared with the other three planes due to the lower elastic modulus of this plane and is thereby easier to deform [127]. Negative strains from -0.0015 to -0.0011 are present close to the weld root. Underneath the weld toes, the strains are also negative in nature ranging from -0.0011 to -0.0007. Below the last weld bead, positive strains from 0.0007 to 0.0015 are observed. Far away from the weld centre and in the base metal, the strains are relative small.
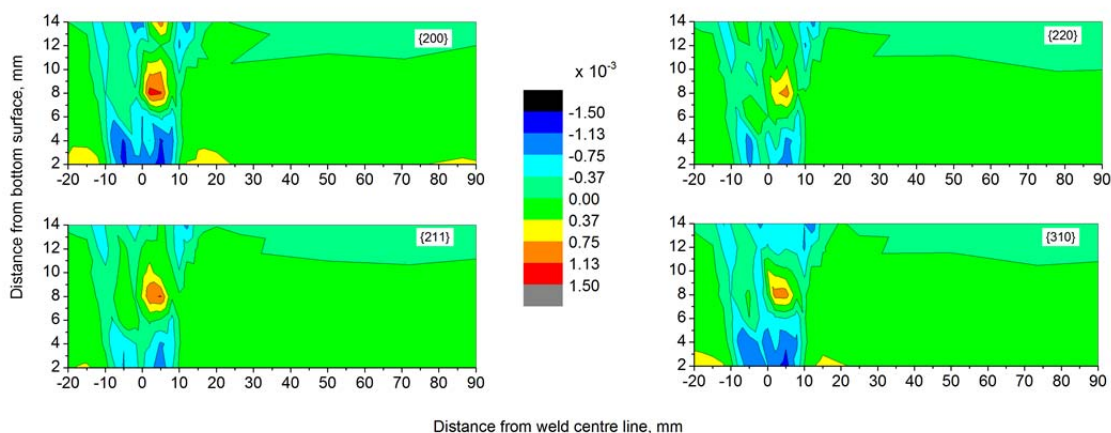
Fig. 6-16: Transverse strain maps of {200}, {211}, {220}, {310} bcc planes in the as-welded condition.

Fig. 6-17(a) shows the comparison with transverse and longitudinal strain of {211} plane. The longitudinal strain in the weld centre is tensile in nature reaching a value of 0.0026 and is coloured with orange. The strain concentrated along the fusion line of the final weld and beneath the joint of the weld reinforcement is reaching a value of 0.0019 and is coloured with yellow. A strain reaching a value of 0.0033 is found in the middle of the weld zone and is coloured with red. It can be observed that the longitudinal strain is much larger than the transverse strain.
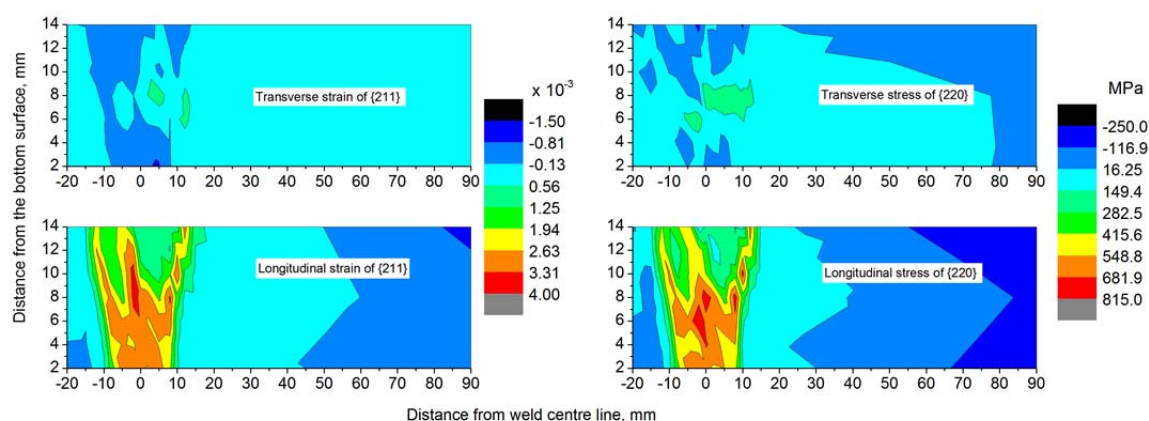
(a)   (b)

Fig. 6-17: Transverse and longitudinal (a) strain map of {211} plane, (b) stress map of {220} plane.

Considering the diffraction elastic constants and Poisson's ratios of individual planes, the transverse stress of {220} plane is calculated and shown in Fig. 6-17(b). Underneath the last weld bead, tensile residual stresses around 415 MPa are generated. Close to the weld root residual stresses are compressive in nature of around 116 MPa. The longitudinal stresses of {220} plane shows that tensile stresses with a maximum of 815 MPa are found in the middle of the weld zone. Stresses underneath the joint of the weld reinforcement, along the fusion line are of the order 548 MPa. In the weld zone the stresses are typically around 681 MPa [135].

6.4.3 Stress field validation of six pass weld

Fig. 6-18 shows the measured and predicted transverse stress distribution of the six pass weld. The measured stresses are averaged from four bcc planes. The results are compared over a rectangular grid of 40×12 mm^2. The predicted stresses close to the bottom surface show a good agreement with the experimental results. In the middle of the weld, the predicted maximum tensile stress is under-estimated by 100 MPa. This deviation may be generated from the d_0 measurement. Some residual stresses may still remain at this region in the stress free sample. The d_0 can be under-estimated, which in turn leads to a shift

of the stress.

The stress distributions over the measured and simulated cross section show a strong resemblance. The tensile region present under the last weld bead, predicted by the model is supported by the experimental measurements (region 1). The less tensile regions 2 and 3 generated due to the third and the fifth weld pass are also found in the measured results. In regions 4 and 5, close to the weld root, concentrated compressive stresses are observed, while in regions 6 and 7, tensile stresses are present both in the measured and simulated results.
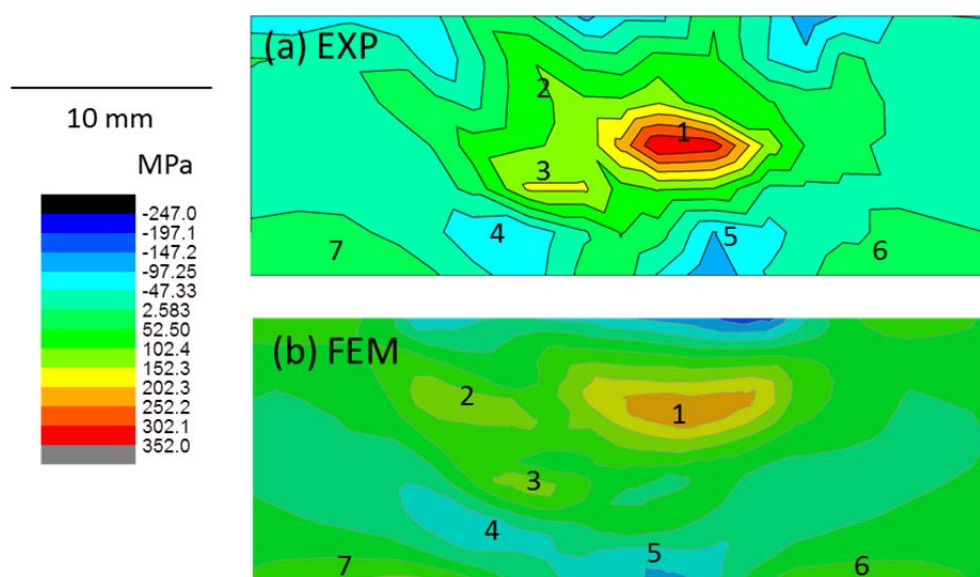
Fig. 6-18: Transverse stress maps over the weld cross section (a) experimental results and (b) simulated results.

6.4.4 *Ex-situ* weld strain development

Transverse strains are measured at 10 mm from the weld centre line along line 'a', as indicated in Fig. 6-19(a). The results as a function of the distance from the bottom surface along this line after weld pass 1 to 6 are presented in Fig. 6-19(b). For the interpretation of the results it should be kept in mind that the transverse location where filler metal is deposited is altered for each pass.
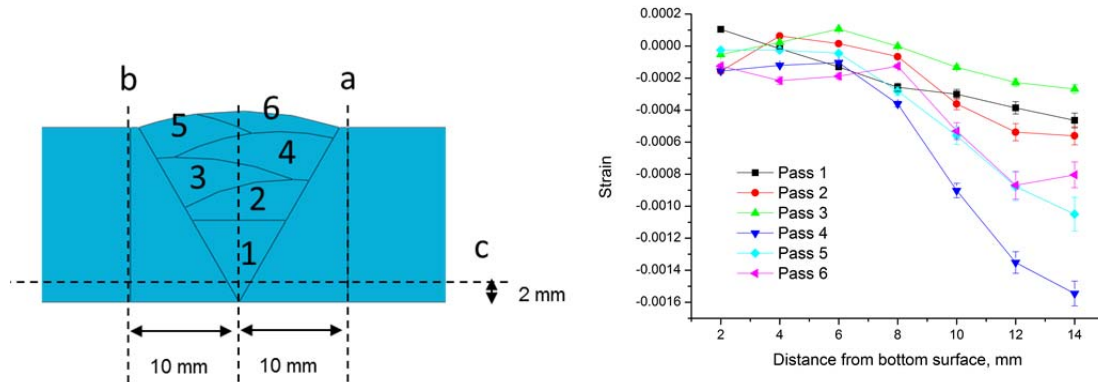
(a)   (b)

Fig. 6-19: (a) Schematic representation of six pass weld, (b) measured transverse weld strain as a function of distance to the bottom surface at 10 mm from the weld centre line along line 'a' after weld pass 1 to 6.
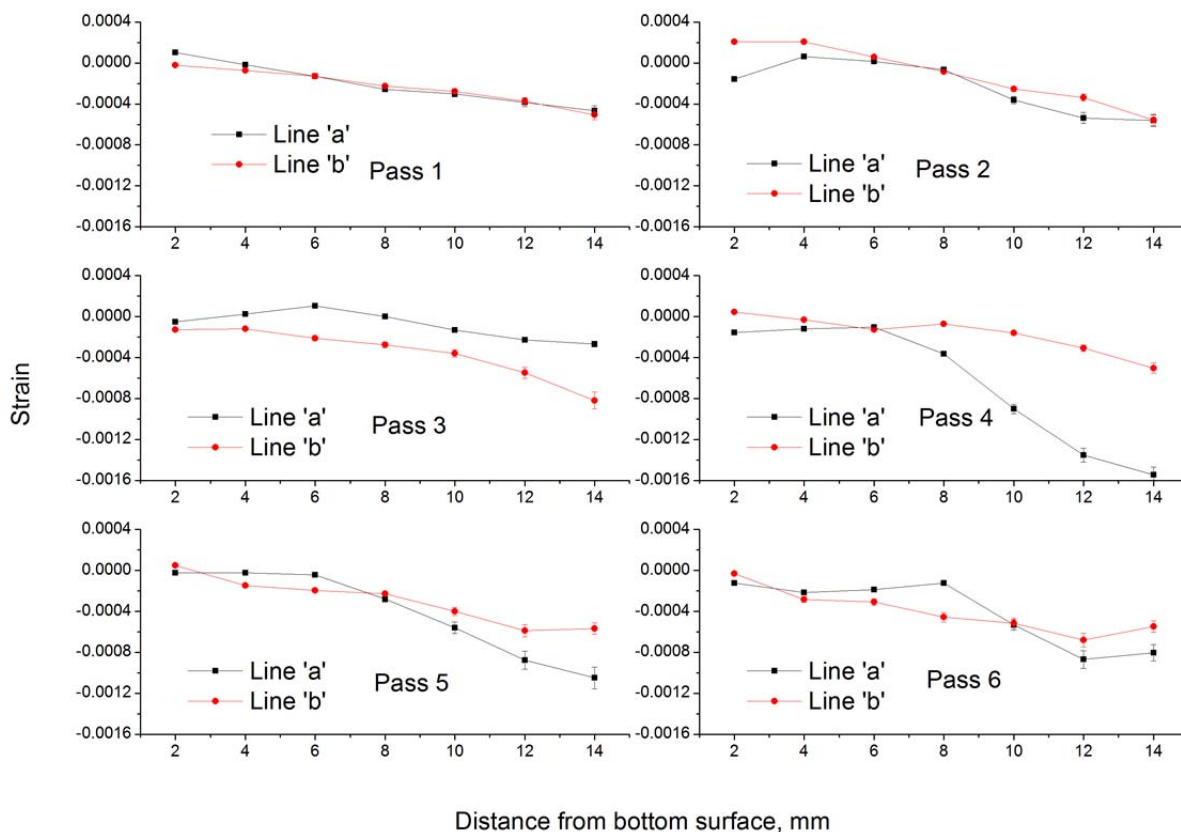
Fig. 6-20: Comparison of measured transverse strain along line 'a' and 'b' after weld pass 1 to 6.

The first weld pass is deposited in the centre of the groove and fills the groove

up to 7 mm from the bottom surface. The strain along line 'a' close to the bottom surface is positive. A decreasing tendency of strain is observed from the bottom to the top surface. For the second pass, the heat source is repositioned to the top right hand side of the first pass, *i.e.* the heat source is closer to line 'a' and the material in asymmetrically deposited, extending to 10 mm from the bottom surface. The strain close to the bottom surface is smaller than that in the previous step, while an increasing tendency of the strain is observed from 4 to 10 mm from the bottom surface due to the deposition of the second weld layer. The third pass is made on the top left hand side of the second pass, and the heat source is repositioned away from line 'a'. The strain level along line 'a' is changed towards positive. After the fourth pass, the deposited material fills the groove up to 14 mm from the bottom surface on the right hand side of the weld groove. The strain becomes more negative at the top surface of the plate. When the weld nears completion after the fifth pass the measured strain is less negative at the top surface. A similar trend can be seen when the final pass is made. Fig. 6-20 shows the comparison of measured transverse strains along line 'a' and 'b' after weld pass 1 to 6. Line 'b' is also 10 mm from the weld centre line on the opposite side of the weld to line 'a'. The first pass is symmetrically deposited and the measured strains along line 'a' and 'b' are similar. The repositioning of the heat source dictates which side of the groove becomes more strained. This confirms the trends described before, indicating that the position of the heat source and the degree to which the groove is filled affect the strain levels. The last weld pass covers the entire weld groove. A smooth weld toe is formed, which leads to a reduction of strain at the top surface.

6.4.5 Pass-by-pass stress validation

In Fig. 6-19(a), line 'c' is located 2 mm from the bottom surface perpendicular to the weld seam. The transverse stresses along line 'c' after weld passes 1 to 6 are plotted in Fig. 6-21. The dots indicate the experimental measurements and the solid lines indicate the simulated results. In the first weld pass, the shrinkage of the weld metal is counteracted by the constraints from the base material, which leads to tensile stresses in the fusion zone. At 5 mm from the weld centre line, the stresses become compressive. At 10 mm from the weld centre line, both the model and experiments show a maximum tensile stress. Up to 20 mm from the weld centre line, a decreasing tendency is observed. From 20 mm, the predicted stress remains unchanged to the edge of the specimen, while the measured stress gradually decreases. In successive weld passes, similar phenomena are found; however an asymmetrical stress distribution is observed due to the repositioning of the heat source. Overall, the model has a reasonable accuracy when predicting the stress build-up.
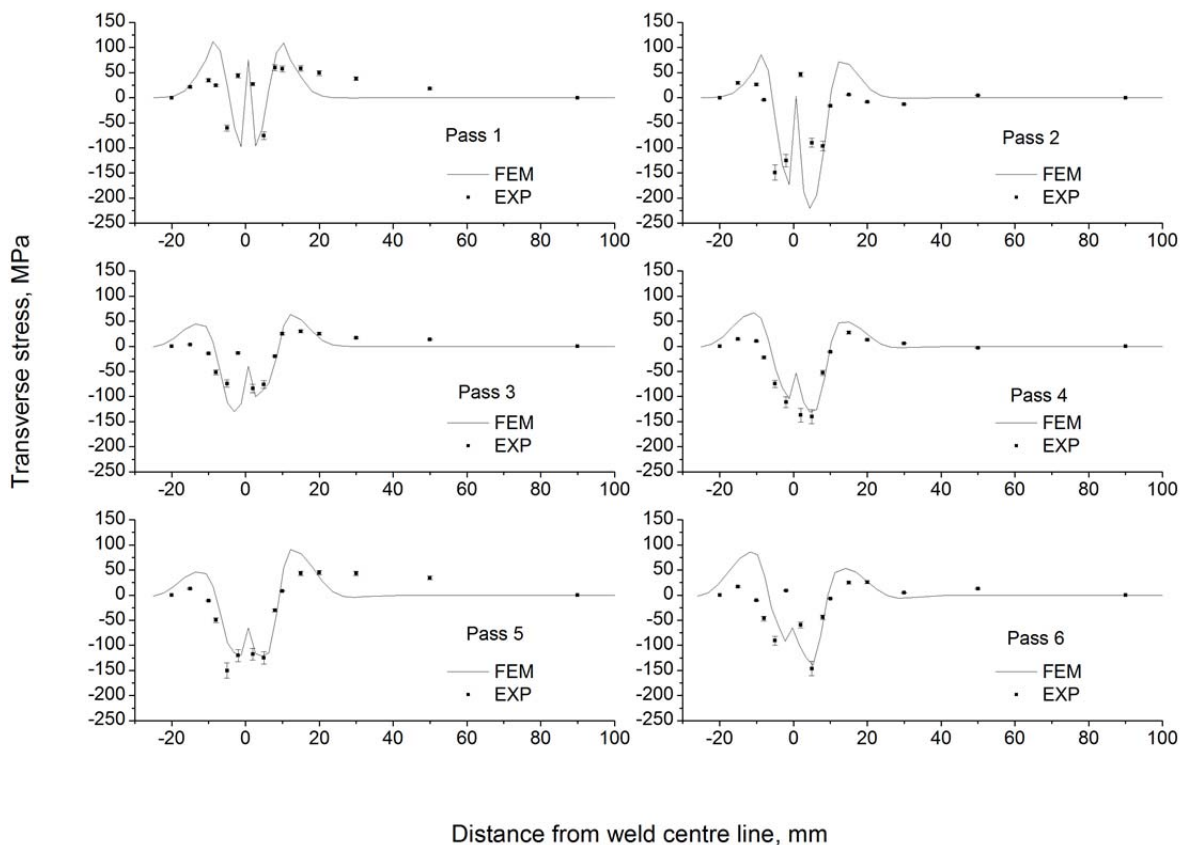
Fig. 6-21: Transverse stress validation 2 mm from bottom surface perpendicular to the weld seam after weld passes 1 to 6.

6.5 Discussion

Fatigue problems of welded components normally arise under transverse loading, *e.g. pipes*. Transverse tensile stresses within the workpiece are critical for crack initiation and propagation. Therefore, the focus in this work is on the transverse stress distribution. A better understanding of the stress build-up and re-distribution in the weld specimen is invaluable for improving multi-pass welding techniques.

The simulated transverse stress distributions after each weld pass with and without clamping are shown in Fig. 6-22. It can be seen that during the fabrication of a six pass weld, the tensile and compressive regions shift and unclamping also has a re-distributing effect on the stresses.

During the first weld pass, the filler material is symmetrically deposited in the weld groove, while the workpiece is constrained by the clamping device. Tensile stresses are generated in the weld bead counteracting the transverse

shrinkage. Due to the V-shape of the deposited weld bead, the upper part of the weld has a larger contraction than the lower part, which leads to a compressive region in the root area. At the top surface of the weld bead, the material has more freedom during cooling, and thus a maximum tensile stress is present below the weld bead surface. Tensile stresses concentrate at the groove-weld bead interface due to geometrical effects. After unclamping, the elastic stresses within the workpiece are partially released, which leads to a distortion of the workpiece and re-distribution of stresses. Near the top surface of the weld bead the stress becomes compressive. The previously present tensile zone becomes smaller in size and shifts towards the bottom surface. Due to the distortion at the bottom surface, two tensile regions are generated to maintain stress equilibrium.
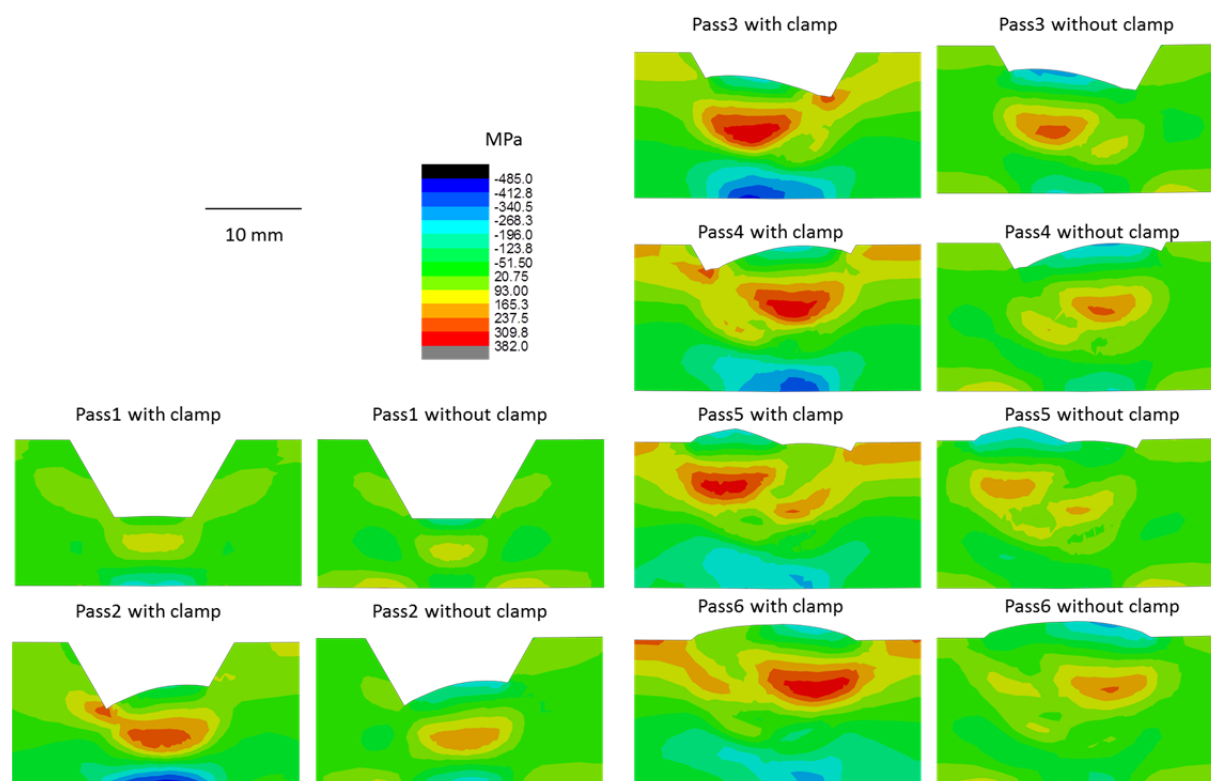
Fig. 6-22: Transverse stress developments from 1 to 6 pass with and without clamps.

The heat source is repositioned after each weld pass. Additional heat is introduced in the subsequent passes, partially re-melting the previous weld bead. The remaining solid root heats up but has a constraining effect on the workpiece. The compression close to the weld root will build-up as the contraction in subsequent passes is opposed by the root area. With an increasing number of passes, the level of the compressive stress reduces as the heat source moves upward and the area supporting the shrinkage becomes larger. With each deposited pass, the tensile zone moves upward and is concentrated underneath

the location of the heat source. After completion of the weld, the stresses at the weld toe will be reduced as the transition of weld metal to base metal becomes smoother, and geometrical effects become smaller.

Some limitations of this work have to be mentioned. Experimentally it is difficult to measure the *in-situ* stress during welding in the synchrotron X-ray beam. The solution addressed here is a compromise, where *ex-situ* stresses are measured after the completion of each pass. The welded samples with different number of passes were prepared in advance. Therefore, the stress development mentioned in this work is not on the same plate, but on six plates with identical welding arrangements (automated welding set-up with the same welding parameters). As the investigation of stress development is aimed at a six pass welded section, the penetration of the beam flux is limited by the sample thickness. The workpiece attached to the backing plate and clamps cannot be measured in transmission mode, the stresses were therefore measured in the unclamped condition.

For the models, to compare with the measured stress in the unclamped condition, the predicted stress fields at each inter-pass temperature were stored. In an additional analysing step the evolution of these stress fields during further cooling to the room temperature followed by unclamping was calculated. To study the stress development for subsequent passes, the analysis was restarted at the inter-pass temperature.

The fluid flow is not considered. The heat distribution is incorporated by the elliptical heat flux model of Goldak. The equivalent plastic strain of an element is reset to zero when the temperature exceeds the solidus temperature, ensuring that no stresses are built up in the liquid metal.

The effects of solid state phase transformation of the quenched and tempered base metal on the stress development are modelled based on the free dilatation tests. If the peak temperature of an element remains lower than the Ac_1 temperature, the thermal expansion and contraction follows the dilatation curve of tempered martensite. If the peak temperature of an element exceeds the Ac_3 temperature, the volumetric change of the phase transformation is included, while during cooling thermal contraction follows the dilatation path of austenite. Depending on the cooling rates bainite, martensite or a mixture of these phases will be formed. The starting point of the transformation is determined from the dilatation curves. It should be mentioned that the dilatation curves are measured for a single peak temperature of 1000 °C. In a real weld, the variation in peak temperature is between Ac_3 and the liquidus, affecting the grain size and thus the transformation behaviour. In a relatively small region of a weld, the peak temperature is in the intercritical region (around 1 mm wide), where tempered martensite and austenite co-exist. In the model, elements in the intercritical region during cooling follow the dilatation path of the heating cycle, *i.e.* the austenite transforms directly into tempered martensite. This implies that the

volumetric change due to the phase transformation is released at a high temperature, which can induce a minor error. The mechanical material properties assigned in the model might have a larger effect on the calculated stress state. Tensile tests of the quenched and tempered base metal were carried out only at elevated temperatures, and these properties are also applied to the model in the cooling stage. However, during the cooling cycle of welding the austenitic phase is metastable up to the martensite start temperature, whereas in the model, properties of tempered martensite are still applied.

6.6 Concluding remarks

In this chapter, research background of residual welding stress is firstly introduced, and it was noticed that knowledge in terms of stress development during multi-pass welding is lacking. Stress measurement on a pass-by-pass basis is critical to understanding the stress evolution with multiple thermal cycles, and also to increase the reliability of the numerical models with several intermediate validations. The validation of the stresses aslo supports that the definition of the parameters in the thermal model is appropriate.

During welding, non-homogenous temperature distribution leads to non-homogenous plastic deformation. A three-bar model is then given to discuss the longitudinal stress evolution due to thermal loading. Tension in the weld and compression in the base material are generated in the workpiece to maintain the stress equilibrium. The material in the weld pool losses all strength upon melting. When the peak temperature exceeds the material melting temperature, the equivalent plastic strain is reset. When the temperature falls below the melting temperature, the stress starts to build-up again.

Phase transformations take place in the subsequent cooling step and can be modelled with two methods. For the explicit method, the evolution of different phases is obtained from a CCT diagram. For the implicit method, the expansion coefficients at different cooling rates are experimentally determined by free dilatation tests. The advantage of this method is that the fraction of the phase is not necessary to be considered. The thermal mechanical material responses at different cooling rates can represent different locations in the weld component.

A sequentially coupled model was used for stress analysis. The FE 2D shell plane strain (PS), 2D shell generalised plane strain (GPS) and 3D solid models were constructed and compared. The PS model constrains the longitudinal expansion, which in turn overestimates the longitudinal stress. The GPS model frees the longitudinal expansion, and the longitudinal stress is the lowest. The 3D solid model predicts stresses in between those of the PS and GPS models. The final stress states predicted by all three models are within 70 MPa. The transverse stress of the three models shows similar trends. The calculation time

of the GPS model is 2.6 times more than the PS model, and the 3D solid model is 127 times more than the PS model. Therefore, if only the transverse stress is of concern, the PS model is good enough for the prediction. The GPS model provides the longitudinal expansion with reasonable calculation time. The 3D solid model can give more reliable results while consuming much time. A 2D shell generalised plane strain model is selected for the stress validation.

Energy dispersive synchrotron X-ray diffraction is an appropriate way to measure the depth resolved strain with reasonable exposure time, especially for thick sections. Based on pass-by-pass measurements, stress alternation due to repositioning of the welding torch after each pass is well studied. The cross sectional stress distribution of the six pass weld is obtained. Transverse compressive stresses are observed close to the weld root, and transverse tensile stresses are present under the last bead welded. Longitudinal tensile stress is found in the weld and along the fusion boundary. The maximum stress in longitudinal direction is around two times larger than that in transverse direction. The predicted residual stresses show a good agreement with the experimental results. An interpretation of the stress development in multi-pass welds is finally obtained based on the validated FE model.

7 Ultrasonic impact treatment[ef]

Ultrasonic impact treatment was applied at the toes of multi-pass welds. Different treating parameters, such as travel speed, treating angle, number of treatment passes and temperature condition prior the treatment, were performed. Stress relaxation through thickness was observed *via* synchrotron X-ray diffraction measurements. Compressive residual stresses were introduced under the treated surface and measured by means of the centre hole drilling method. Fatigue tests were performed on the samples subjected to the same thermal cycles as those in the HAZ of multi-pass welds. Some samples were subjected to an ultrasonic impact treatment. The alternations of stress states, weld geometries and microstructures, which assist in extending the fatigue life, were studied.

7.1 Experimental approach

7.1.1 Ultrasonic impact treatment equipment

Ultrasonic impact treatment (UIT) is a novel technology combining ultrasonic vibration and mechanical impact to improve the fatigue properties of a workpiece [5, 6, 12, 27, 32, 35, 136]. The application of UIT improves the properties of welded and base material structures by introducing compressive residual stress, changing weld toe geometry, and modifying microstructures, which assists in extending the fatigue life of the manufactured components.

Esonix UIT equipment [30, 34] consisting of a generator and a peening tool was used to perform the post weld treatment (Fig. 7-1). The generator provides power (1.2 kW) at a working frequency of 27 kHz. The ultrasonic vibration amplitude is measured to be 28 µm at the tip of the waveguide in unloaded condition. The waveguide has a contact area of 20×10 mm^2. The mechanical peening frequency is measured to be 50 Hz. The peening head contains 4 pins

in a row, and each of the pins has a diameter of 3 mm and a head radius of 1.5 mm. The force applied by the peening tool to the metal surface was dependent the self-weight of the tool, and was measured to be 30 N.

Fig. 7-1: UIT generator and peening tool [30].

The impact frequency of the peening tool was measured by a CMOS high speed camera (Phantom V5) with a Nikon 70-300 mm optical lens. The recording frequency is 3000 frames per second (fps). A number of recorded frames with a UIT travel speed of 5 mm s^{-1} are shown in Fig. 7-2. At frame 333, the pins are in contact with the treated surface. At frame 363, the pins are at the farthest position from the treated surface, whereas at frame 393, the pins are again just in contact with the treated surface. At frame 396, the pins are about to leave the treated surface. According to the recorded frames from the high speed camera, one indentation cycle is 0.02 s; and the contact time between the pins and the treated surface is 0.001 s. The error is in the order of half a frame (±0.00015 s).
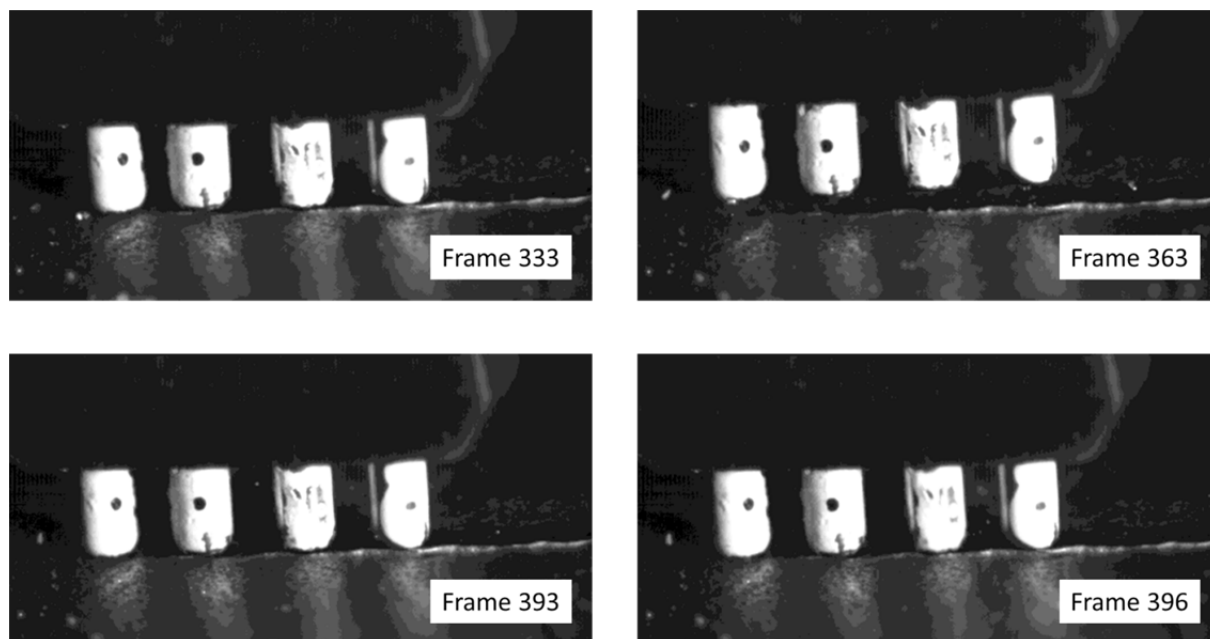
Fig. 7-2: Mechanical impact recorded from high speed camera.

7.1.2 Post weld ultrasonic impact treatment

The ultrasonic impact treatment comprises the combined effect of ultrasonic waves and mechanical impacts. To study the effects of ultrasonic wave induced stress relaxation in the surface, initial testing was carried out during which only the ultrasonic transducer was coupled to the six pass weld. The transducer was stationary and located at the weld toe in the middle of the plate and was operating for five minutes, as shown schematically in Fig. 7-3(a). The contact area is the dimension of the transducer as 20×10 mm^2. Comparison of the stress distribution in the six pass weld and ultrasonically treated weld will be shown in chapter 7.2.
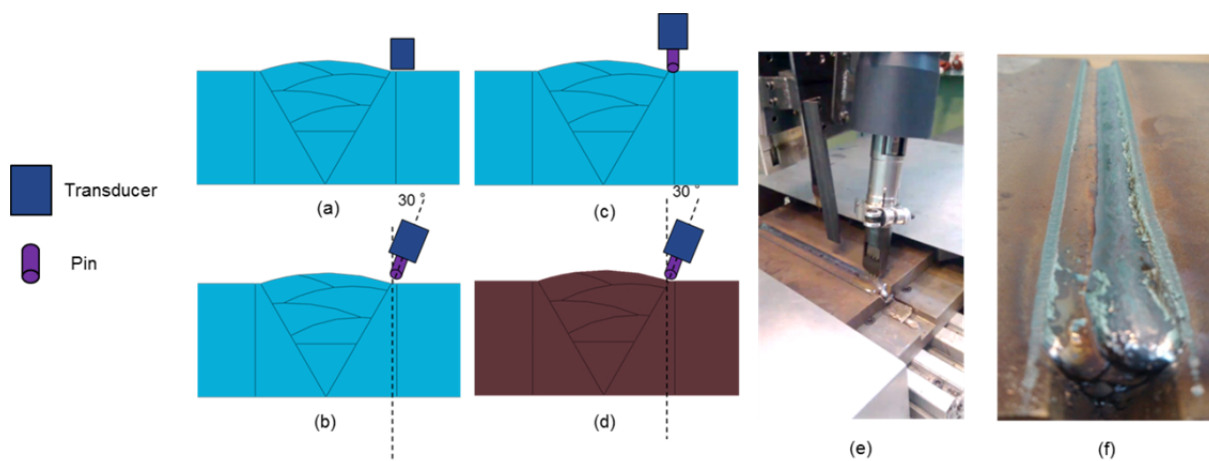
Fig. 7-3: Ultrasonic impact treatment with different treating parameters.

Table 7-1: Samples with different UIT conditions.

Sample	Angle (°)	Speed (mm s^{-1})	Cold/Warm	Pass
0	Six pass weld			
i	Ultrasound	0	C	N.A.
1	30	5	C	1
2	30	5	C	5
3	30	10	C	1
4	30	10	C	5
5	0	10	C	1
6	30	10	W	1

Impact treated samples were made with the UIT tool mechanically mounted behind the welding torch with an adjustable angle (±30° from the normal direction in the cross-sectional plane). Ultrasonic impact treatments were applied to both weld toes of the six pass welded plate with different treating parameters. Treating angles of 0 and 30°, travel speeds of 5 and 10 mm s^{-1}, numbers of treatment passes of 1 and 5, and warm and cold conditions prior the treatment were selected. The warm condition is defined as the temperature directly after the welding. Considering the time for adjusting the UIT tool, the temperature on the weld bead was measured by a thermocouple and was around 100 °C when the treatment started. The cold condition is defined as room temperature (after more than 4 hours cooling). Schematic pictures of the different UIT conditions are shown in Fig. 7-3(b-d). All the treatments were made under constrained conditions. After treatment, the constraints to the workpiece were removed. Fig. 7-3(e) shows the experimental arrangement, and Fig. 7-3(f) shows the ultrasonic impact treated six pass weld.

Table 7-1 lists of different UIT conditions applied to the samples. Sample 0 is the six pass weld regarded to be a reference. Sample i is the six pass weld only treated with ultrasound. Sample 1 is the ultrasonic impact treated weld with a treating angle of 30°, travel speed of 5 mm s^{-1}, one treating pass in cold condition, which is considered as a base line UIT condition. From sample 2 to 6, the UIT conditions have different treating angles, travel speeds, numbers of treating passes or temperature conditions as described in the table.

7.2 Results

7.2.1 Stress relaxation

Residual stresses in ultrasonic impact treated welds were measured at ESRF comparable to the experiments described in chapter 6.2. The measurement scheme is as shown in Fig. 7-4, where the dots indicate the measurement locations. The solid lines indicate the position of the V-groove, and for the measurement points along the dashed lines (a, b and c) the full width at half maximum (FWHM) of the diffracted peaks were evaluated. In the specimen which was treated only by ultrasound, the number of measurements was reduced and limited to the area ranging from 0 to +20 mm from the weld centre line, as indicated by the red box. It should be noted that the centre of the gauge volume is plotted. As the gauge volume has a length of 2 mm, the data extends to 1 mm below the plate top and above the plate bottom surfaces.

116
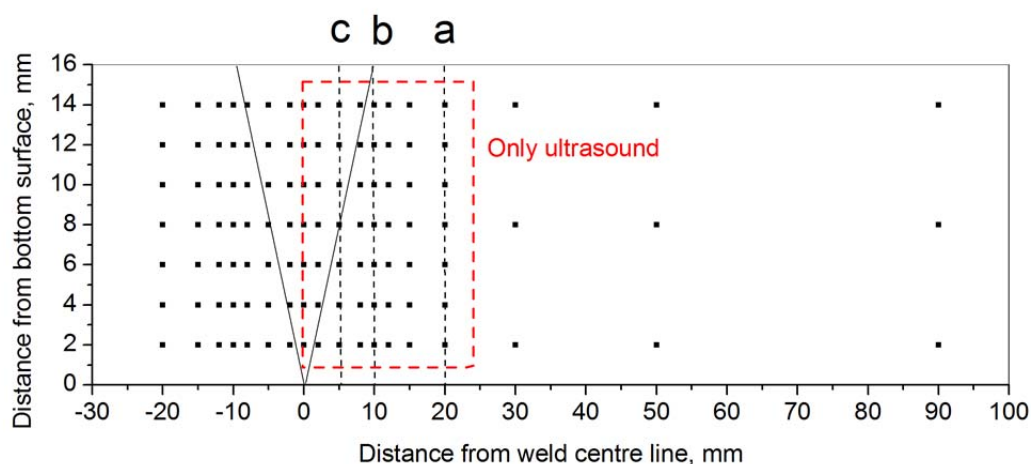
Fig. 7-4: Measurement position map of ultrasonic impact treated welds.

As the {200} bcc plane is the most deformable plane, the stress changes due to the post weld treatments can be easily observed [127]. Therefore, the behaviour of this plane is selected to investigate the effects of different treatments. The transverse strain and stress of the {200} bcc plane of the six pass welded (sample 0) and the post weld ultrasonically treated (sample i) specimen are compared. The regions ranging from 0 to +20 mm from the weld centre line are shown in Fig. 7-5. The highly strained region in the middle of the ultrasound treated plate (red area) completely disappeared, and the less strained regions (orange and yellow areas) are reduced by 85% and 25%, respectively. The regions close to the weld root with negative strains seem to become more homogeneous. In the transverse stress maps similar distributions are obtained and the differences are due to the contribution of the longitudinal strain, as indicated by the biaxial Hook's law (introduced in chapter 6.2). The maximum tensile stress underneath the final weld bead of the six pass welded plate is 460 MPa, while the ultrasonically treated plate has a maximum stress level of 396 MPa. The surrounding less stressed regions (orange and yellow areas) are enlarged.

117
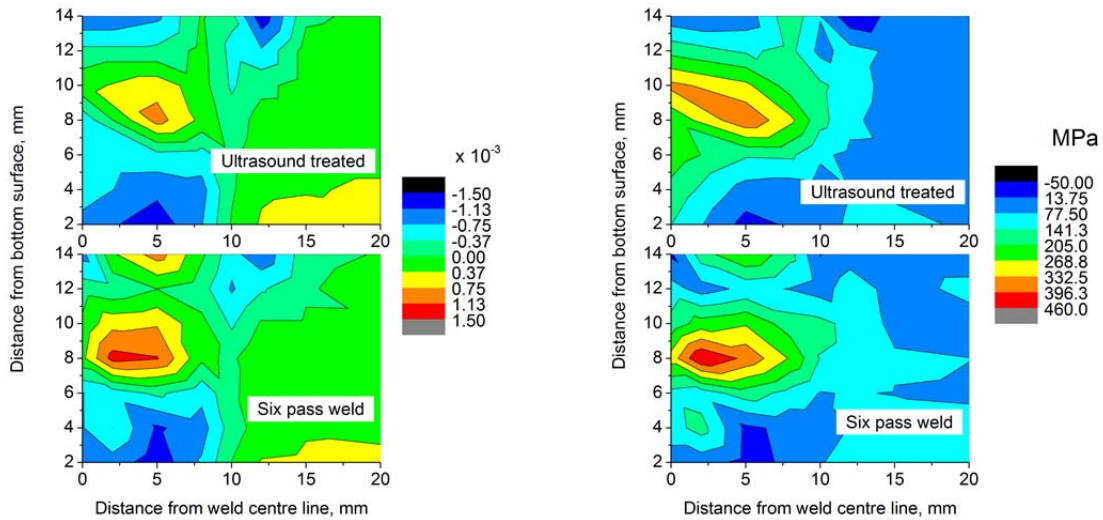
(a)   (b)

Fig. 7-5: Transverse (a) strain, (b) stress map in {200} bcc plane of six pass welded (sample 0) and ultrasonically treated plates (sample i).

The transverse strain maps of the {200} bcc plane of the six pass welded (sample 0) and post weld ultrasonic impact treated (sample 1) specimen are shown in Fig. 7-6(a) for the regions ranging from -20 to 20 mm from the weld centre line. The distribution of blue areas with negative strains close to the weld root in the six pass welded plate fluctuates, while after the ultrasonic impact treatment, the strains of the regions become more smoothly distributed. The highly strained red area disappears, the orange area diminishes, and the yellow area becomes narrower. The strains at the weld toes are reduced.
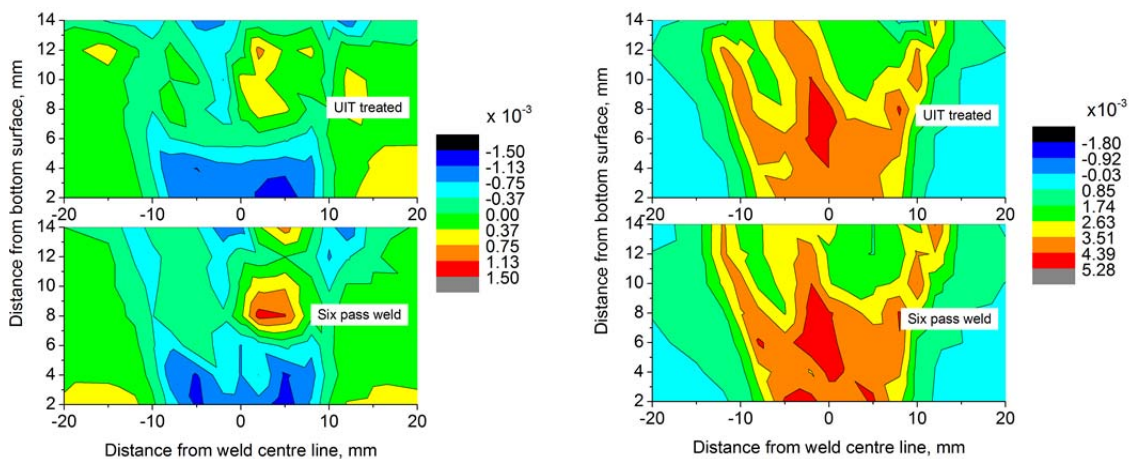
(a)   (b)

Fig. 7-6: (a) Transverse strain maps, (b) longitudinal strain maps of the six pass welded (sample 0) and ultrasonic impact treated plates (sample 1).

The longitudinal strain maps of the bcc planes of the six pass welded and the post weld ultrasonic impact treated conditions are shown in Fig. 7-6(b). A yellow area with positive strains between 0.0026 to 0.0035 is present along the heat-affected-zone. The red area with positive strains ranging from 0.0044 to 0.0053 is present in the middle of the plate. After the ultrasonic impact treatment, the red area close to the weld root disappears. The red area in the middle of the plate is reduced in size by approximately 20%. The yellow and orange areas underneath the weld toes are reduced in size.

The transverse stress maps of the six pass welded and the post weld ultrasonic impact treated conditions are shown in Fig. 7-7(a). The maximum tensile stress in the middle of the plate is reduced from 460 MPa to 330 MPa after the ultrasonic impact treatment is applied. The highly stressed red and orange areas disappear. The yellow area is reduced by approximately 60%.

The longitudinal stress maps of the six pass welded and the post weld ultrasonic impact treated conditions are shown in Fig. 7-7(b). The stress distributions show the same trend as the strain distributions. After the treatment, the tensile stresses close to the weld root and weld toes were reduced. The maximum tensile stress present in the middle of the plate is 950 MPa. Compared with the six pass welded plate, the red high stress area is reduced by approximately 40%.
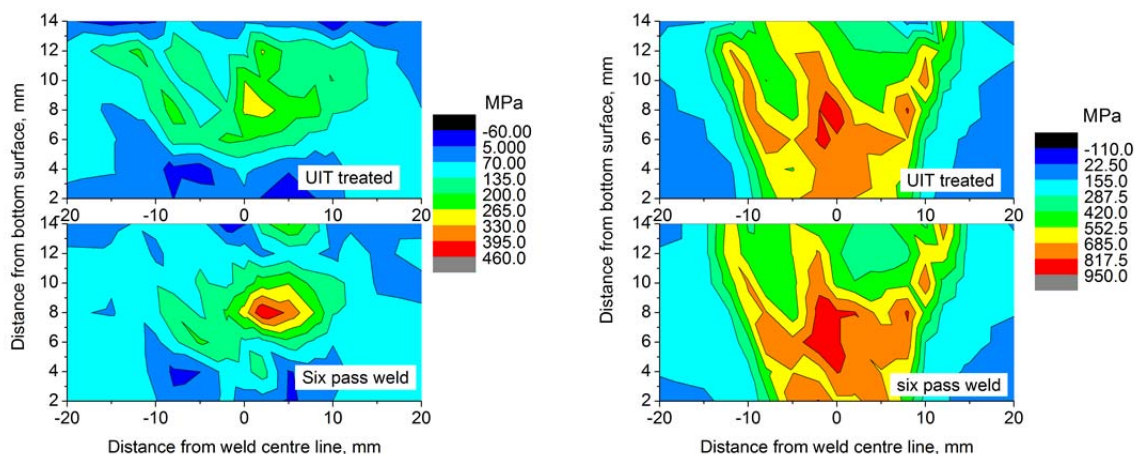
(a) (b)

Fig. 7-7: (a) Transverse stress maps, (b) longitudinal stress maps of the six pass welded (sample 0) and the ultrasonic impact treated plates (sample 1).

7.2.2 Full width half maximum

Thermal loading and plastic deformation during welding and ultrasonic impact treatment can introduce lattice defects in the material, which can lead to a peak broadening of the diffraction pattern [137]. Fig. 7-8(a) shows the full width at half maximum (FWHM) of the energy dispersive diffraction patterns along the

depth at the position of 5, 10 and 20 mm from the weld centre line, coinciding with the lines a, b and c, respectively, as indicated in Fig. 7-4. The solid lines indicate the FWHM of the fitted diffraction peaks of the six pass weld. In the base metal a constant FWHM is observed as a function of distance from the bottom surface (along line a). Under the weld toe along line b, the FWHM is comparable to the unaffected base metal near the bottom surface, but increases significantly by 55% when approaching the top surface. Along line c, an increasing tendency of the FWHM is also observed as a function of the distance to the bottom surface. In the weld metal the diffraction peak become broader compared to the base metal. However, the FWHM does not reach the levels encountered at the weld toe.

The dash lines in Fig. 7-8(a) indicate the FWHM after the ultrasound treatment is applied to the weld. Along line a, the FWHM is almost constant and similar to that of the base metal in the six pass welded plate. Along line b, an increase of the FWHM is observed near the top surface. However, compared to the as-welded plate, the FWHM at the top surface is reduced by 6%. Along line c, an increasing FWHM is found with increasing distance from the bottom surface. Compared to the same position in the as-welded specimen, below 4 mm from the bottom surface no peak broadening is found. A decreases of 6% in width is observed close to the top surface.

(a)   (b)
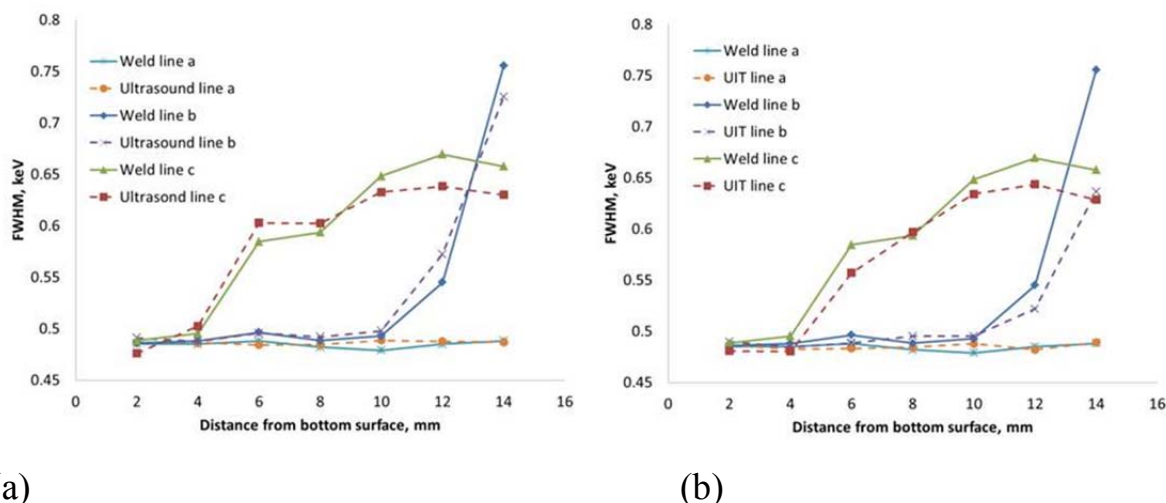
Fig. 7-8: Full width at half maximum of the diffraction peaks of (a) the six pass weld (sample 0) and the ultrasound treated weld (sample i), (b) the six pass weld and the ultrasonic impact treated weld (sample 1), at 5 (line c), 10 (line b) and 20 (line a) mm from the weld centre line, the peak with fitting errors is in the order of 10^{-6} (described in chapter 6.2.3).

Fig. 7-8(b) shows a comparison of the full width at half maximum of the six pass weld to the ultrasonic impact treated weld. The solid lines again indicate the FWHM of the six pass weld and the dash lines represent the FWHM of the

ultrasonic impact treated weld. Along line a, representing the base metal, the FWHM of the treated sample is similar to the as-welded condition. Along line b, the FWHM increases when approaching the top surface. However, compared to the as-welded condition the width is reduced by 24% at the top surface underneath the impact area. Alone line c, the FWHM of the ultrasonic impact treated condition is approximately 6% smaller close to the top surface compared to the as-welded condition and remains consistently lower over the entire depth.

7.2.3 Stress distribution due to different UIT parameters

Fig. 7-9 shows the transverse stress maps of the {200} bcc plane in the as-welded and different ultrasonic impact treated plates. After six pass welding, tensile stresses are present in the middle of the sample 0 and compressive stresses are concentrated close to the weld root. Comparing sample 1 (UIT, speed 5 mm s^{-1}, 1 pass, 30° angle and cold condition) with sample 0, compressive stresses are introduced under the weld toe due to the impact. The maximum tensile stress in the middle of the weld is significant reduced by approximately 250 MPa. The tensile regions (red and orange area) completely disappear. Close to the weld root, the compressive stresses are re-distributed to maintain the stress equilibrium in the workpiece. Sample 2 is treated with 5 passes, while the rest of the parameters are the same as for sample 1. Compared with sample 0, stress relaxation and re-distribution are both observed. Compared with sample 1, the compressive stresses under the weld toe are increased due to multiple impact passes. As a result, the tensile stresses relaxation through the thickness is not as good as single impact. The compressive regions close to the weld root are expanded.

When the plate is treated with a travel speed of 10 mm s^{-1}, the compressive stresses under the weld toe are not as high as in sample 1 due to the smaller treating time. The maximum tensile stress in the middle of sample 3 remains the same as that in sample 0, while the concentrated tensile region becomes narrower compared with sample 0. Compressive stresses close to the weld root are re-distributed accordingly. If the high travel speed is maintained, but the number of treating passes is increased, reduction of the tensile region in the middle of sample 4 becomes effective again. The effectiveness of stress relaxation is better than that in sample 3, and is as good as found for sample 1.

When the plate is treated at an angle of 0°, the impact is vertical to the weld toe. Compared with sample 1, more compressive stresses are built-up under the weld toe. The tensile region in the middle of sample 5 becomes more narrow compared with that in sample 0, while the magnitude of the stress in the weld remains the same. The re-distribution of the compressive stresses close to the weld root can still be observed. When the plate is treated in a warm condition, additional compressive stresses are measured under the weld toe. The

maximum tensile stress in sample 6 is reduced by 160 MPa compared to sample 0.
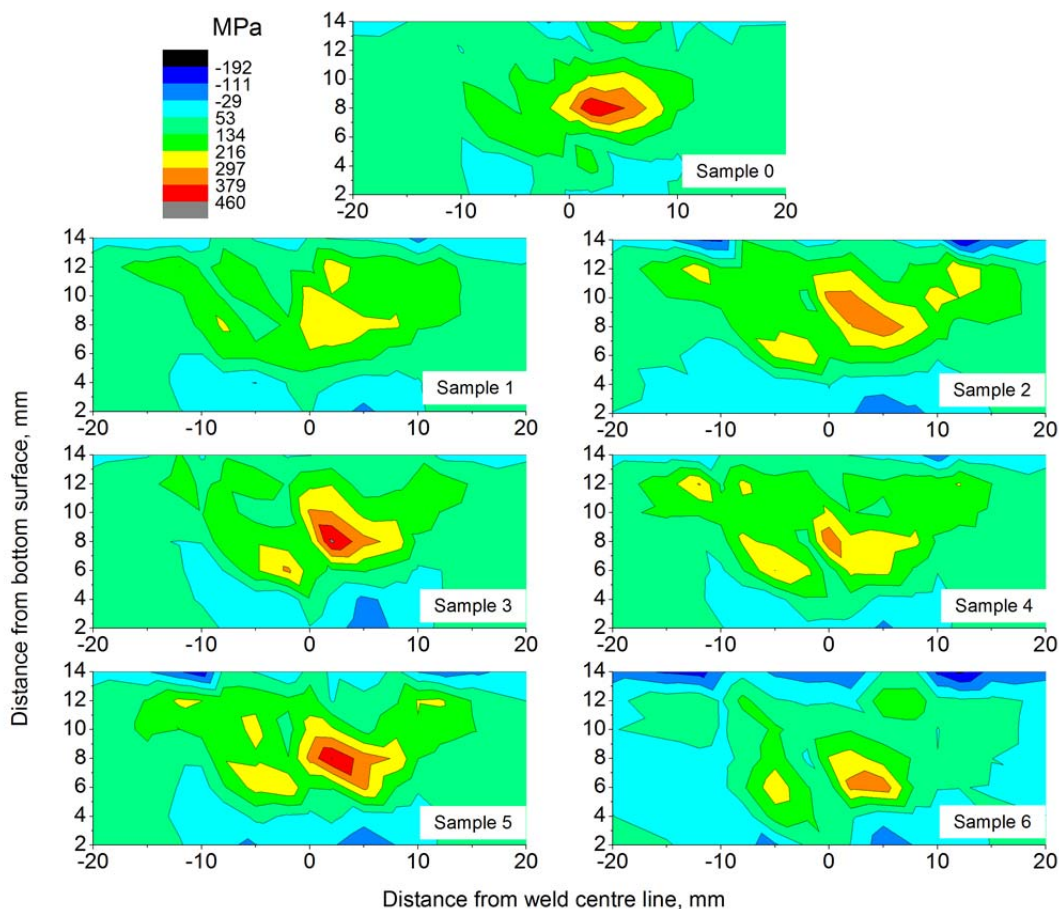
Fig. 7-9: Transverse stress of {200} bcc plane in the as-welded and ultrasonic impact treated plates.

Stresses induced by welding are stored within the workpiece. After unclamping, elastic stresses in the workpiece are released. The samples distort differently for different post weld treatment conditions. The maximum distance between the distorted edge and the horizontal plane is defined as *d*. The distortion distance of the six pass weld is 3.14 mm, which can be considered as a reference for the post weld treatments. After the treatment (UIT, speed 5 mm s^{-1}, 1 pass, 30° angle and cold condition), the distortion distance of sample 1 is 2.71 mm, which is a 13% reduction compared to the reference. When the sample is treated with 5 passes, a 19% reduction of distortion distance is observed. Doubling the travelling speed (sample 3) leads to a reduction in distortion distance by 5%. When the traveling speed is doubled and the treatment is carried out with 5 treating passes (sample 4), the distortion distance is 10% less with respect to the reference. When the treating angle is 0° from the normal direction, the stress reduction in the weld is less effective than that when the treating angle is 30°. The distortion distance of sample 5 only shows a 2% reduction. When the workpiece is treated in a warm condition, the stress in the

weld significantly decreases and the distortion distance of sample 6 is reduced by 23%. A summary of the distortion results is provided in Table 7-2.

Table 7-2: Distortion of workpiece with different treating conditions.

	Sample	d (mm)	Reduction (%)
	0	3.14	reference
	1	2.71	13
	2	2.53	19
	3	2.98	5
	4	2.81	10
	5	3.07	2
	6	2.40	23

7.2.4 Stress at the weld toe

Centre hole drilling (CHD) is an appropriate method to obtain the near surface stress. The CHD technique is performed by measuring the surface strains caused by the relief of residual stresses during the incremental machining of a shallow hole in a component. The principle is that the removal of the stressed material results in the material surrounding the hole readjusting its stress state to attain residual stress equilibrium [138, 139].

The basic experimental procedure is described as follows [140]: prepare (*e.g.* smooth and degrease) the component surface at the measurement location; bond a CHD strain gauge rosette to the component; align the CHD machine with the strain gauge; drill the central hole in a series of increments; measure the hole depth and record the strain gauge readings for each increment drilled; analyse the depth and strain gauge data to calculate the residual stress distribution.

RESTAN (Residual Stress Analyser)-MTS3000, developed and produced by SINT Technology, was used for the CHD stress measurement, see Fig. 7-10. The tests were conducted in accordance with the ASTM E837-13 standard [141]. Strain gauge type B RY61-1.5/120R and adhesive for ferrite steel Z70 were selected. Spider 8 data acquisition equipment was used to record the strain change. The diameter of the drill (D_0) was 1.52 mm and the diameter of the

gauge circle (*D*) was 5.12 mm. The depth of the hole (*H*) was 1 mm made in with 10 equal steps.

(a)   (b)
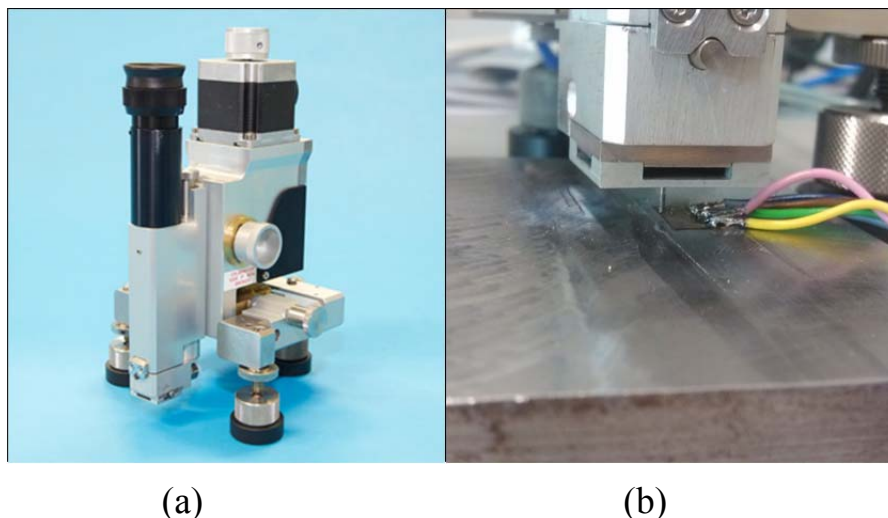
Fig. 7-10: (a) RESTAN MTS3000, (b) hole drilling arrangement.

Before the measurement, the as-welded and UIT treated plates were prepared in the following way to obtain a flat and smooth surface, see Fig. 7-11. As the measurements were located at the weld toe, some material from the weld cap had to be removed to position the strain gauge. The indentation groove with UIT sample 1 is about 0.15 mm from the surface. For comparison purposes, 0.2 mm from both plate surfaces was milled to obtain a flat measurement surface. The strain gauge was place 10 mm from the weld centre line.

(a)   (b)
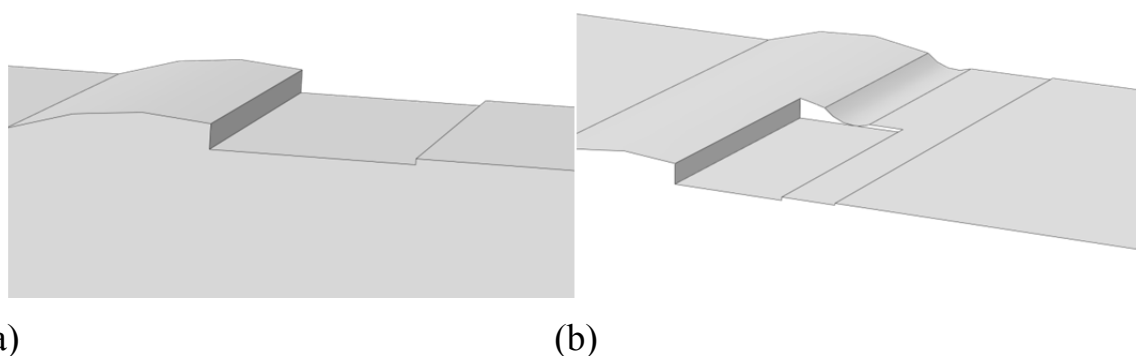
Fig. 7-11: Preparation of the hole drilling plates, (a) as-welded, (b) UIT treated plates.

Residual stresses from centre hole drilling are derived from the measured strains according to ASTM E837 [41]. The following combination strains are determined from the measured strains ε_1, ε_2, ε_3,

$$p = (\varepsilon_3 + \varepsilon_1)/2,$$ (7-1)

$$q = (\varepsilon_3 - \varepsilon_1)/2,$$ (7-2)

$$t = (\varepsilon_3 + \varepsilon_1 - 2\varepsilon_2)/2.$$ (7-3)

The three corresponding combination stresses P, Q and T are then given by

$$P = \frac{\sigma_y + \sigma_x}{2} = -\frac{Ep}{a(1+\nu)} \, ,$$

(7-4)

$$Q = \frac{\sigma_y - \sigma_x}{2} = -\frac{Eq}{b} \, ,$$

(7-5)

$$T = \tau_{xy} = -\frac{Et}{b} \, .$$

(7-6)

The incremental coefficient a is a ratio of the hole depth to the diameter of the gauge circle and b is a ratio of the diameter of the drill and gauge circle [41]. E and ν are the bulk elastic modulus and Poisson's ratio, respectively.
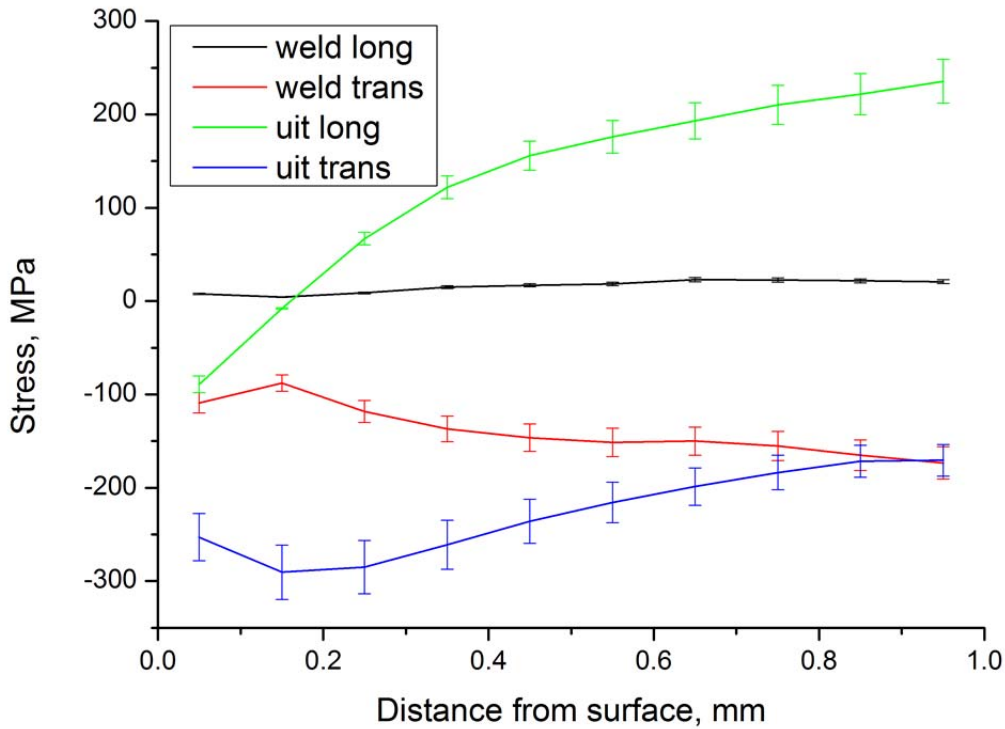
Fig. 7-12: Near surface residual stress obtained from CHD in as-welded and UIT treated plates under the weld toe.

Residual stresses in the as-welded and UIT treated plates as a function of distance from the treated surface are shown in Fig. 7-12. After welding, the longitudinal residual stress is low in magnitude and tensile in nature up to 1 mm below the surface. The transverse residual stress is compressive and has a decreasing tendency from -109 to -173 MPa. After the treatment, the longitudinal and transverse residual stresses become more compressive (-89 and -252 MPa) at the surface. Up to 1 mm below the surface, the longitudinal stresses has an increasing tendency from -89 to 235 MPa, while the transverse

residual stress first decreases to -290 MPa and then increases to -170 MPa. Stresses in a reference plate without heat treatment and UIT are below 25 MPa.

Fig. 7-13 shows the through-thickness transverse stresses in as-welded and UIT treated plates under the weld toe. The near surface stresses are combined with the subsurface synchrotron XRD measured stresses. It should be noticed that the synchrotron XRD results have an elongated gauge length along the thickness due to the arrangement of XRD measurements in transmission mode. Thus, for instance the measured position closest to the top surface already represents an averaged stress state from 1 to 3 mm below the surface. In general, the results from the hole drilling measurements converge with those from synchrotron XRD. After the treatment, more compressive stresses were observed close to the treated surface. At 1 mm below the surface, the residual stresses in the six pass weld and UIT treated weld are similar in magnitude (-170 MPa). At position from 3 to 10 mm below the surface, the stresses in the UIT treated weld become more tensile compared to the six pass weld, as the stresses have to be equilibrium.
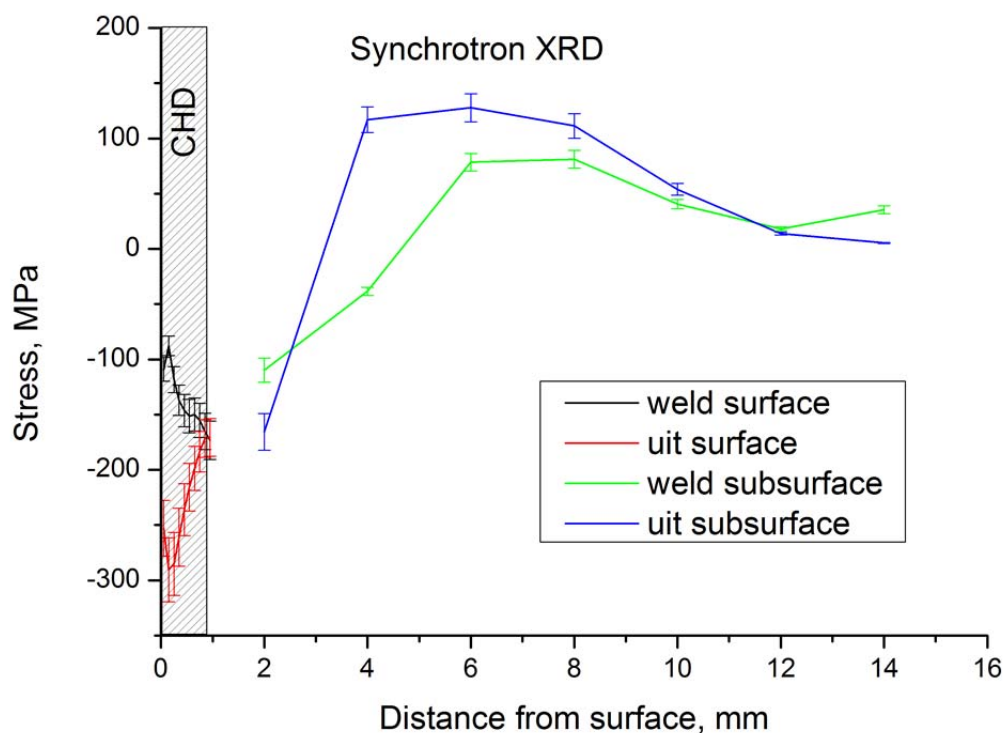
Fig. 7-13: Through-thickness transverse stresses in as-welded and UIT treated plates under the weld toe.

7.3 Fatigue performance[g]

The welded joints normally have a low fatigue strength compared to the base material, which is due to the presence of notches and high tensile residual stresses. Therefore, post weld ultrasonic impact treatments were applied to improve the fatigue performance of the workpiece. The mechanism of the fatigue extension due to changing of stress states, weld geometries and microstructures are discussed.

In the current study, the fatigue tests are difficult to perform directly on either the welded workpiece or the post weld treated workpiece due to the large dimension ($260 \times 200 \times 16$ mm^3). However, machining of the workpiece to a suitable dimension in order to fit into standard fatigue testing equipment will release the welding induced stresses, and the stress relaxation due to the post weld treatment cannot be studied. To reduce the complexity of a real weld, fatigue samples were prepared in a way to consider the aspects of welding and ultrasonic impact treatment.

7.3.1 Sample preparation

Rectangular test specimens were electro-discharged machined (EDM) from the as-received plate S690QL1. The sample dimensions were 80 mm long, 8 mm thick and 16 mm wide. An EDM notch was introduced at the middle of the sample to avoid crack initiation at the corners.

The fatigue tests were firstly applied to as-received base material (Sample 1). In order to study the effect of microstructure changes as a result of weld thermal cycles, samples representing the fine grained heat-affected-zone (FGHAZ) and coarse grained heat-affected-zone (CGHAZ) were prepared by means of a physical welding simulation. The peak temperatures of 900 °C and 1200 °C were applied to create these specific microstructures. Sample 3, 4, 7, 8, 9 and 10 were subjected to thermal cycles of the fine or coarse grained heat-affected-zone. An ultrasonic impact treatment was applied to the as-received material (sample 5 and 6) and the heat treated material (sample 7, 8, 9 and 10). To study only the geometrical effect on the fatigue performance without introduction of compressive stresses, a groove was machined on sample 2, 3 and 4 with dimensions similar to the UIT groove. An overview of the fatigue tests are given in Table 7-3, and a schematic picture of different fatigue samples is shown in Fig. 7-14.

For the HAZ simulation, the Gleeble 1500 physical simulator was employed

---

[g] This work was with the help of J.F. Rodriguez as a Master study in TU Delft, Fatigue crack growth in high-strength steel weld microstructures after UIT, TUDelft, Master thesis (2014).

with a resolution of ± 1 °C, a control accuracy of ± 1 °C and a measurement accuracy of 1% of the actual temperature in addition to the accuracy of the thermocouple wire (0.75% of the actual temperature). The maximum error in the temperature during thermal cycling is estimated to be ±20 °C according to the Gleeble 1500 user manual [142]. A fatigue testing machine MTS 350 kN was used for the experiments. The parameters of the fatigue experiments were (i) a stress range of 495 MPa, (ii) a maximum stress of 550 MPa and (iii) a testing frequency of 40 Hz. The samples are pre-loaded at a load level of 1 kN before starting the fatigue experiments.

Table 7-3: Overview of the fatigue tests.

Sample	UIT Passes	Description
1	0	Base S690QL1
2	0	Base S690QL1 with artificial groove
3	0	Fine Grained HAZ S690QL1 with artificial groove
4	0	Coarse Grained HAZ S690QL1 with artificial groove
5	3	Base S690QL1
6	5	Base S690QL1
7	3	Fine Grained HAZ S690QL1
8	5	Fine Grained HAZ S690QL1
9	3	Coarse Grained HAZ S690QL1
10	5	Coarse Grained HAZ S690QL1
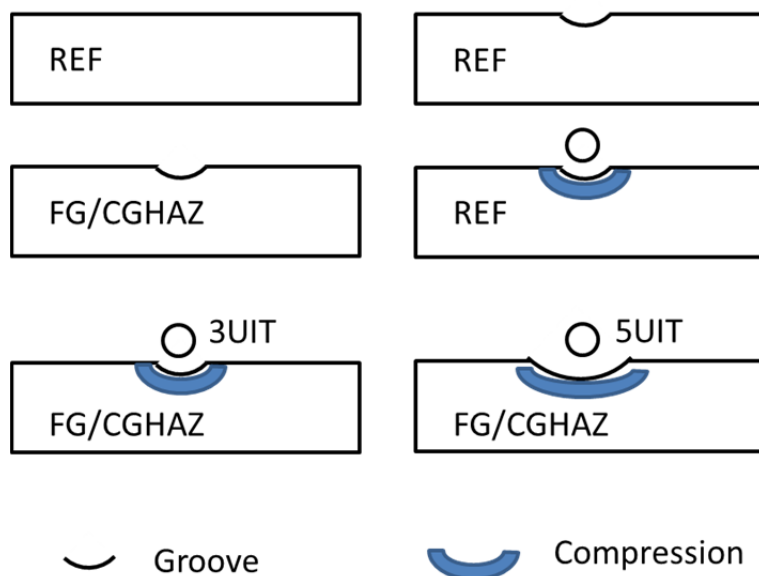
Fig. 7-14: Schematic picture of different fatigue samples.

7.3.2 Fatigue results

The results of fatigue tests are summarized in Table 7-4. For each tested condition, three samples were used to increase the reliability of the measurements, and the results were averaged. $FAT_{95\%}$ is the stress range at a 95% survival probability with 2×10^6 fatigue cycles. A bigger $FAT_{95\%}$ indicates a better fatigue performance. When no crack growth is detected after 2×10^6 cycles the test was considered to be a run-out.

Result of sample 1 indicates the fatigue class of the as-received material (218 MPa). Introduction of the groove on the as received material (sample 2) reduces the fatigue class (185 MPa). Samples 5 and 6 represent the UIT on the as received material with 3 and 5 passes. The fatigue class of these samples is significantly improved. Sample 5 (723 MPa) with 3 passes seems to provide a better result than sample 6 with 5 passes (511 MPa). After the heat treatments, sample 3 with a groove on the fine grained heat-affected-zone and sample 4 with a groove on coarse grained heat-affected-zone show similar results to sample 2 (groove on the as received material), which is not as good as sample 1 (the as received material). Sample 4 (188 MPa) provides slightly better result than sample 3 (184 MPa). Sample 7 and 8 with 3 and 5 passes UIT on fine grained heat-affected-zone (347 MPa and 322 MPa) improves the fatigue class compared to the base material. Sample 9 and 10 with 3 and 5 passes UIT on coarse grained HAZ samples result in run-outs of the fatigue tests.

Table 7-4: Fatigue class of the tested series.

Sample	FAT$_{95\%}$ (MPa)	STD (MPa)
1	218	3
2	185	6
3	184	6
4	188	2
5	723	157
6	511	86
7	347	15
8	322	19
9	>550	-
10	>550	-

7.4 Discussion

Stress measurements of six pass weld were shown in chapter 6. Tensile stresses were concentrated under the last weld bead, while compressive stresses were observed close to the weld root to maintain the stress equilibrium. In this chapter, stress distribution after ultrasonic treatment and ultrasonic impact treatments were compared with the as-welded condition.

Statnikov stated that ultrasonic waves affect the residual stress to a depth up to 12 mm, resulting in a reduction of residual stresses up to 50% [21]. However, this statement was based on studies related to ultrasonic impact treated surfaces, where the effects of ultrasound are super-imposed on mechanical impacts. Due to these combined effects, it is very difficult to understand the role of ultrasound. In this work, the measured stress maps of the as-welded and ultrasonically treated plates show that ultrasound waves lead to a re-distribution of the residual stresses over the entire thickness (in this case 16 mm), see Fig. 7-5. The maximum stress in the workpiece decreases due to ultrasonic induced material softening, and the stresses in the surrounded region are re-distributed to maintain the stress equilibrium. Experiments from Shalvandi [143] show that, the mechanical properties of the material become softer both in the elastic and plastic regions with increasing ultrasonic intensity, see Fig. 7-15.

Dutta *et al.* [144] applied ultrasound to the specimen while tensile testing and found the dislocation density and the fraction of low-angle grain boundaries decrease significantly, accompanied by preferential grain rotation. The

softening effect of the ultrasound is found to drive recovery associated with a significant reduction in subgrain formation during deformation.
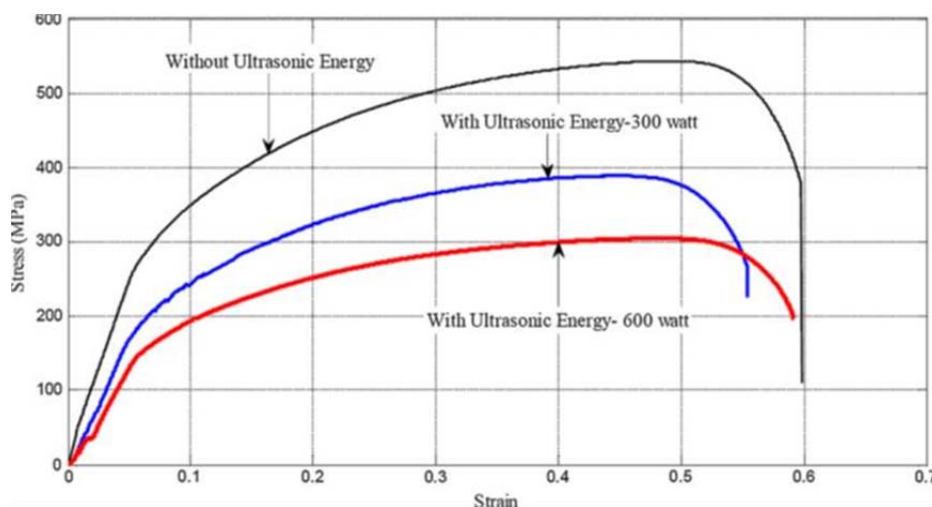
Fig. 7-15: Stress-strain curves of typical tensile specimen with and without ultrasonic vibration [143].

After the ultrasonic impact treatment, compressive stresses are introduced under the treated surface. The maximum tensile stress underneath the last weld bead is reduced by approximately 28% compared to the as-welded condition for the described treating parameters. The mechanical impacts on the treated surface effectively transport the ultrasonic waves into the workpiece, which contributes to stress reduction up to a depth of 6 to 8 mm below the top surface (this is the highly stressed region in the weld). The stresses in the surrounded regions are re-distributed to maintain the stress equilibrium. It is confirmed that material softening effects due to the application of ultrasound are more pronounced when deformation takes place.

FWHM of the diffraction pattern gives an indication of the lattice defects. After welding, the lattice defects under the weld toe are 55% higher than in the base material. After ultrasonic treatment, the lattice defects under the weld toe are reduced by 6% compared to the as-welded condition. The errors generated from peak fitting are in the order of 10^{-6} keV. The deviation of repeated measurements is within 0.01 keV. After ultrasonic impact treatment, a reduction of lattice defects by 24% is observed due to the mechanical impacts applied at the weld toe. In the weld zone under the top surface (alone line c), only ultrasound affects this region, and the reduction of the lattice defects in the ultrasonic treated and ultrasonic impact treated welds are similar (about 6%).

Lower travel speed and more treating passes increase the contact time per unit length between the pins and the treated surface, which contributes to the effectiveness of stress relaxation. When UIT is vertically applied at the weld toe, more compressive stresses can be introduced under the weld toe compared to

that with a treating angle, while the stress relaxation in the weld is less effective. When the workpiece is treated in a warm condition directly after welding, additional compressive stresses are introduced under the weld toe as the materials are much softer and easily deformed. More tensile stresses are required under this compressive region to compensate the compressive stresses, which leads to a more uniform distribution of the tensile stresses in the weld. The stress states of the workpiece can be correlated with the distortion after unclamping. Compared with the as-welded condition, different treating conditions reduce the distortion by 2 to 23%. Introduction of beneficial compressive stresses under the weld toe and homogenisation of through-thickness tensile stresses both contribute to the reduction of welding distortion [145].

Synchrotron XRD can provide stress maps of the workpiece. However, it is not adapted to show the stress distribution close to the surface, where UIT takes place. Close surface stress measurement techniques were compared in chapter 2, and the centre hole drilling method selected was used in this work. In combination with synchrotron XRD measurement, the through-thickness stresses are obtained. Due to the mechanical impact, compressive stresses are locally introduced at the weld toe. Through the thickness, stresses are more tensile in nature under the compressive region compared with the as welded condition to maintain the stress equilibrium. It has to be noticed that the gauge length along the thickness from hole drilling and synchrotron XRD methods are different. Moreover, when calculating the stresses, bulk Young's modulus was used for hole drilling results, while diffraction elastic constants were used for synchrotron XRD results.

Fatigue tests are difficult to directly perform on either a welded workpiece or a post weld treated workpiece due to the large dimension [23, 24]. If the welded or treated workpiece are cut or machined to a suitable size, the residual stresses will be released. In order to reduce the complexity of a real weld, the fatigue tests were performed on the samples subjected to the same thermal cycles as those in the HAZ of multi-pass welds. Some samples were subjected to an ultrasonic impact treatment. The alternations of stress states, weld geometries and microstructures, which assist in extending the fatigue life, were studied. Results show that UIT is an effective method to extend the fatigue life compared to the as-welded condition.

Compared fatigue sample 1 with 2, introduction of a groove on the as-received material reduces the fatigue performance due to the geometrical discontinuity. Compared fatigue sample 5 and 6 with 2, UIT on the as-received material improves the fatigue performance. Although the indentation groove is a factor that may reduce the fatigue, due to the beneficial compressive stresses introduced at the surface, the fatigue performance is improved overall. A decrease in fatigue performance is observed with the increase in the number of

UIT passes. This trend is observed in all series. Although more treating passes can provide more compressive stresses, it can also invoke more damages on the surface. Sample 3 (FGHAZ-Groove) and sample 4 (CGHAZ-Groove) show similar fatigue performance as sample 2, but not as well as sample 1. The heat treatment does not influence the fatigue performance too much when a groove is already present without any local compressive stresses (*i.e.* a pre-machined groove). When UIT is applied on the FGHAZ (sample 7 and 8) and CGHAZ (sample 9 and 10), better fatigue performances are obtained.

Sample 9 and 10 (3 and 5 passes UIT on CGHAZ) did not present crack initiation. It can be explained that higher martensite content in CGHAZ causes approximately a linear increase in the threshold stress intensity range due to the increase of hardness. Murakami *et al.* [146] developed an expression for defining the threshold stress intensity range function of hardness and the area of the defect,

$$\Delta K_{th} = 3.3 \cdot 10^{-3}(H_v + 120)(\sqrt[6]{area})^{\frac{1}{3}},$$

(7-7)

where the fatigue crack initiation threshold is a function of the crack area in μm^2 and the Vickers hardness H_v in kgf/mm^2.

Some limitations of this study should be mentioned. It is not feasible to weld or treat the workpiece at the beamline, and thus seven as-welded plates were prepared with identical welding conditions. The post weld treatments were then applied to six of these as-welded plates. As the ultrasonic transducer has a flat surface, it is difficult to move the transducer along the weld toe. In order to study the effect of solely applying ultrasound, as a proof of principle, a compromise had to be made for a stationary treatment. From the study of Shalvandi [143], ultrasonic induced material softening is observed during deformation. When ultrasound is applied without any impact, no deformation will take place under the treated surface. Residual stresses may not be affected. The treating time is therefore selected to be 5 min to magnify the effects of ultrasound, which is longer than the real time of UIT application (1 min). It is confirmed that ultrasound can re-distribute the stresses when they are already present in the workpiece even without any deformation. The statistics due to the small number of fatigue tests in each condition can be improved, but a trend in the fatigue improvement due to ultrasonic impact treatment is observed.

7.5 Concluding remarks

Ultrasonic impact treatment is an effective method to introduce beneficial compressive stresses under the treated surface (measured by hole drilling method), and release and re-distribute the residual stresses through the

thickness of the workpiece (measured by synchrotron XRD method). Ultrasonic induced material softening is more pronounced when deformation takes place, which leads to a more uniform stress re-distribution in the weld.

After welding, diffraction peak broadening is observed under the weld toe due to the increase of lattice defects. Ultrasonic impact treatment significantly reduces the lattice defects by 24% under the treated surface.

Lower travel speed and more treating passes contribute to the effectiveness of the stress relaxation. When applying UIT at the weld toe, stress relaxation is more effective with the pins at angle from the normal and transverse directions, thereby simultaneously treating the weld metal and the heat-affected-zone. The tensile residual stresses in the weld are observed to be more uniformly re-distributed. When the workpiece is treated in a warm condition directly after welding, besides the stress relaxation in the subsurface, additional compressive stresses are introduced under the weld toe.

Ultrasonic impact treatment is an effective way to extend the fatigue life of a workpiece. Grooves reduce the fatigue life of a component if the stress concentration factor is increased. An indentation groove created by UIT may reduce the fatigue life, however due to the beneficial compressive stresses introduced at the surface, the overall fatigue performance is improved. Martensite formation due to the thermal cycles can increase the hardness of the material, which contributes to an extension of the fatigue performance. Compressive stresses at the weld toe are beneficial, but more treating passes may lead to more damage of the surface.

8 General discussion

The final stress state of a welded component is determined by the thermal cycle of the welding process and the associated microstructural evolution. The thermal cycle can be accurately simulated by defining appropriate heat input and heat loss conditions, and a sensitivity test of these parameters is given in chapter 4.5. The temperature dependent material properties are essential to predict the material responses and therefore obtain a physically realistic numerical model.

With the known chemical composition of the materials, the thermal properties can be appropriately obtained. The welding thermal fields predicted with the FE model were validated with experimental results. The time-temperature profiles at different locations and fusion boundaries are in good agreement. The mechanical properties defined in the welding models are normally obtained from thermal mechanical tests at elevated temperatures. However, the welding thermal cycles include both heating and cooling stages. During the cooling stage, different peak temperatures and cooling rates may generate different phases, which can affect the subsequent mechanical properties. The properties in the heating stage therefore might not be valid in the cooling stage. Moreover, multiple thermal cycles might alter the mechanical properties even further. If such changes are not taken into account, the predicted results from the model can deviate from the experimentally obtained results.

The stresses in a six pass weld were validated on a pass-by-pass basis. Based on the stress measurements, post weld ultrasonic impact treatment led to a stress relaxation in the six pass weld. However, a comprehensive UIT FE model is not presented in this work due to the complexity of such a task and poor understanding of ultrasonic induced material change and ultrasound dissipation in metal during impact. In this chapter, a simple impact FE model is introduced as an initial step toward the construction of a UIT FE model.

8.1 Mechanical properties improvement

High temperature tensile tests were performed with different peak temperatures and thermal cycles. The experimental arrangement is shown in Fig. 8-1. Thermal mechanical simulations were performed with a Gleeble 1500 physical simulator. The basis of thermal mechanical simulation is an electric current passing through the sample that provides the required heat input (Joule heating). The electrical signal is controlled by a thermocouple placed on the specimen to match the actual temperature with the desired temperature profile. Additionally, the force that the clamps transmit to the specimen can be controlled by a

hydraulic system, making it possible to control the strain under compression or tension, or to maintain a zero force by compensating for any strain.
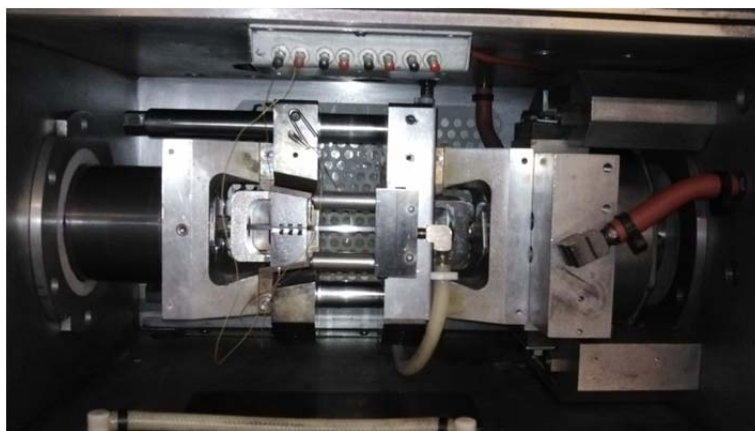
Fig. 8-1: Gleeble 1500 experimental arrangement.
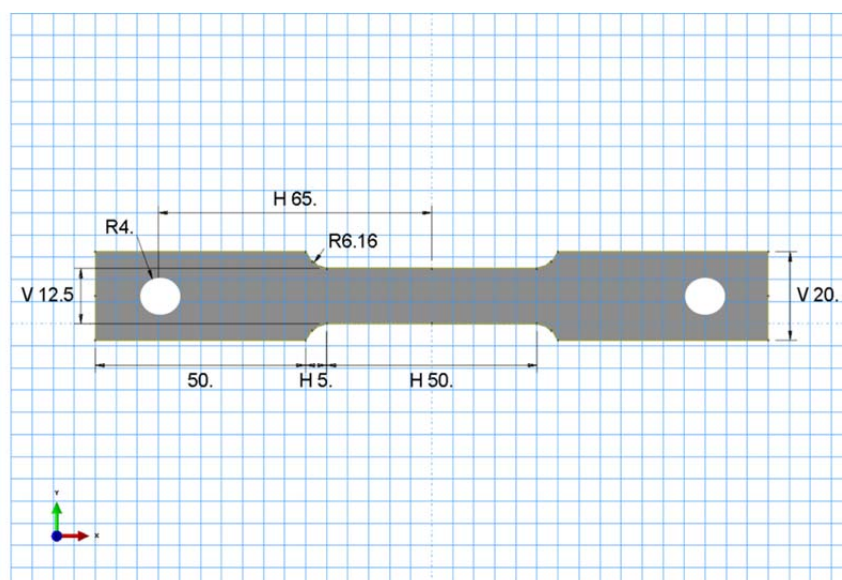
Fig. 8-2: Tensile sample dimension (unit: mm).

The sample was machined according to ASTM E8/E8M [141] as shown in Fig. 8-2. The overall length of the sample is 160 mm with a thickness of 4 mm. The grip section has a length of 50 mm and a width of 20 mm. Two holes with a diameter of 8 mm were drilled in the grip section, through which two cylindrical bars can be inserted to apply tensile forces. The length and width of the tensile section are 50 mm and 12.5 mm, respectively. In the middle of the sample, a K-type thermocouple was spot-welded to measure the temperature during the test. The sample was clamped by two serrated wedges and mounted in the Gleeble machine. All five high temperature tensile tests were carried out at 400 °C as indicated in Table 8-1.

The thermal cycles, force and displacement evolution, rescaled displacement

evolution and stress strain curves of sample 1 to 5 are shown in Fig. 8-3 to Fig. 8-6. The value of the stroke indicates the elongation of the sample in terms of displacement.

Table 8-1: Experimental arrangement for high temperature tensile tests.

Sample	Abbreviation	Description
1	H4	
2	HP10C4	H: Heat up
3	HP8C4	P: Peak temperature Number [$\times 10^2$ °C]
4	HP10C1.5H4	C: Cool down
5	HP10C1.5HP10C4	

In the heating stage, the heating rate was 10 K s^{-1}. Sample 1 was heated up to 400 °C, the reaction force on the sample was maintained at zero during the heating stage. The sample was free to expand and an increment of the stroke was observed. Immediately after the temperature reached 400 °C, the stroke reading was reset to zero and the sample was pulled by moving the stroke with a constant strain rate of 2×10^{-2} s^{-1}. The applied force started to increase, which was proportional to the stroke in the elastic range. During the tensile test the temperature was maintained at 400 °C. When the strain reached 12%, the stroke movement was stopped and the applied force was released. The temperature then gradually dropped to room temperature.

Sample 2 was heated up to 1000 °C. The Ac$_1$ and Ac$_3$ temperatures of this high strength steel are 720 °C and 850 °C, respectively. In the heating stage, the stroke kept increasing up to 720 °C. The volume reduction due to the austenitic transition occurred between 720 °C and 850 °C. Above 850 °C, the expansion followed that expected for austenite. The temperature was maintained at 1000 °C for 3 min for homogenisation. The sample was then quenched by air cooling until 400 °C. The cooling rate was about 30 K s^{-1}. The martensite start and finish temperature are 430 °C and 300 °C, respectively. During cooling, the stroke kept decreasing until 430 °C. The volume increase due to the martensitic transition was observed, but was not completely finished at 400 °C. Martensite and austenite were mixed and the stroke reading was reset to zero before the tensile test started. The test was stopped when the strain reached 12%, and the sample was released.

Sample 3 was heated up to 800 °C in the intercritical region and maintained at

this temperature for 3 min for homogenisation. The transition of the austenite was not completely finished, and the sample had a mixed phase of tempered martensite and austenite before cooling. During cooling, the martensitic transition had not yet started at 400 °C. The stroke reading was reset to zero and the tensile test started.

Sample 4 was heated up to 1000 °C and maintained for 3 min. The sample was then cooled to 150 °C, which is the inter-pass temperature during welding of this kind of steel. During cooling the martensitic transition was completely finished. The stroke kept decreasing according to the martensite expansion rate. The sample was then reheated to 400 °C. The stroke reading was reset to zero before the tensile test started.

Sample 5 followed the same routine as sample 4 in the first thermal cycle, and then the sample was heated up to 1000 °C again, kept for 3 min and cooled down to 400 °C. The sample experienced two cycles of full austenisition, one fully martensitic transition during the first thermal cycle and one partially martensitic transition in the second thermal cycle. The stroke reading was reset to zero before the tensile test started.

Based on the slope analyses of the stress strain curves, the yield points from sample 1 to 5 are 630, 574, 508, 610 and 570 MPa, respectively. The base material of the sample was quenched and tempered high strength steel with a yield strength of 830 MPa at room temperature. As all the tensile tests were carried out at 400 °C, it is reasonable that the yield points are reduced as the material becomes much softer compared to room temperature. However, attention has to be paid to the differences of the yield points experiencing different thermal cycles. When sample 1 was heated up to 400 °C, no phase change was expected. The tensile test was performed on a quenched and tempered martensitic sample; this can be regarded as a base line measurement. Sample 2 was first fully austenitised above Ac_3, and then quenched to 400 °C. The tensile test was performed on a sample with a mixture of martensite and austenite. As the strength of autstenite at the same temperature is weaker than martensite, the yield point of sample 2 is lower than that of sample 1. Sample 3 was heated up to 800 °C in the intercritical region. A mixture of tempered martensite and austenite co-existed before cooling. During cooling, the martensitic transition was not observed at 400 °C. The yield point of sample 3 is understandably lower than sample 1 due to the existence of austenite. The reason why the yield point of sample 3 is also lower than sample 2 are explained based on the fraction of phases.

Assuming the sample was 100% tempered martensite before the heat treatment. Sample 1 remained 100% tempered martensite. The yield strength of tempered martensite at 400 °C was obtained (630 MPa). In sample 2, 4 and 5, the peak temperature was above Ac_3, and the samples were fully austenitised before cooling. In sample 3, the peak temperature was 800 °C in the intercritical

region. Based on the linear lever rule, the austenite fraction at 800 °C is 61%, and the remaining tempered martensite fraction is 39%. During cooling, no volume change due to phase transition was observed. The tensile test was performed on the mixture of 61% austenite and 39% martensite. With the known yield strength of tempered martensite (690 MPa) and sample 3 (574 MPa), the yield strength of austenite at 400 °C can be calculated to be 430 MPa. For sample 2, with the known yield strength of martensite, austenite and sample 2, the fractions of austenite and martensite are 26% and 74%, respectively. The yield strength of sample 3 is lower than that of sample 2 due to a large fraction of austenite (61% compared to 26%). For sample 4, the final fractions of austenite and martensite are calculated to be 10% and 90%. After the first thermal cycle, the re-heating process to 400 °C does not change the phases, which indicates that the fraction of austenite and martensite are already 10% and 90% at the inter-pass temperature before reheating. It can be concluded that cooling from 1000 °C to 400 °C, 26% austenite and 74% martensite are formed. When cooling to 150 °C, although the martensitic finish temperature is passed, only 90% martensite is formed, while still 10% austenite remained. Due to the existence of 90% tempered martensite, the yield strength of sample 4 is slight lower than sample 1, while higher than sample 2 and 3. For sample 5, the fraction of austenite and martensite after the first thermal cycles are calculated to be 10% and 90%. However they are fully austenitised in the second heating stage. When the sample was cooled down to 400 °C, the final fraction of austenite and martensite are 30% and 70%, respectively. In principle, the fraction of the phases should be the same as in sample 2. This minor difference might be because sample 1 started with 100% tempered martensite, while sample 5 in the second thermal cycle started with 90% martensite and 10% retained austenite.
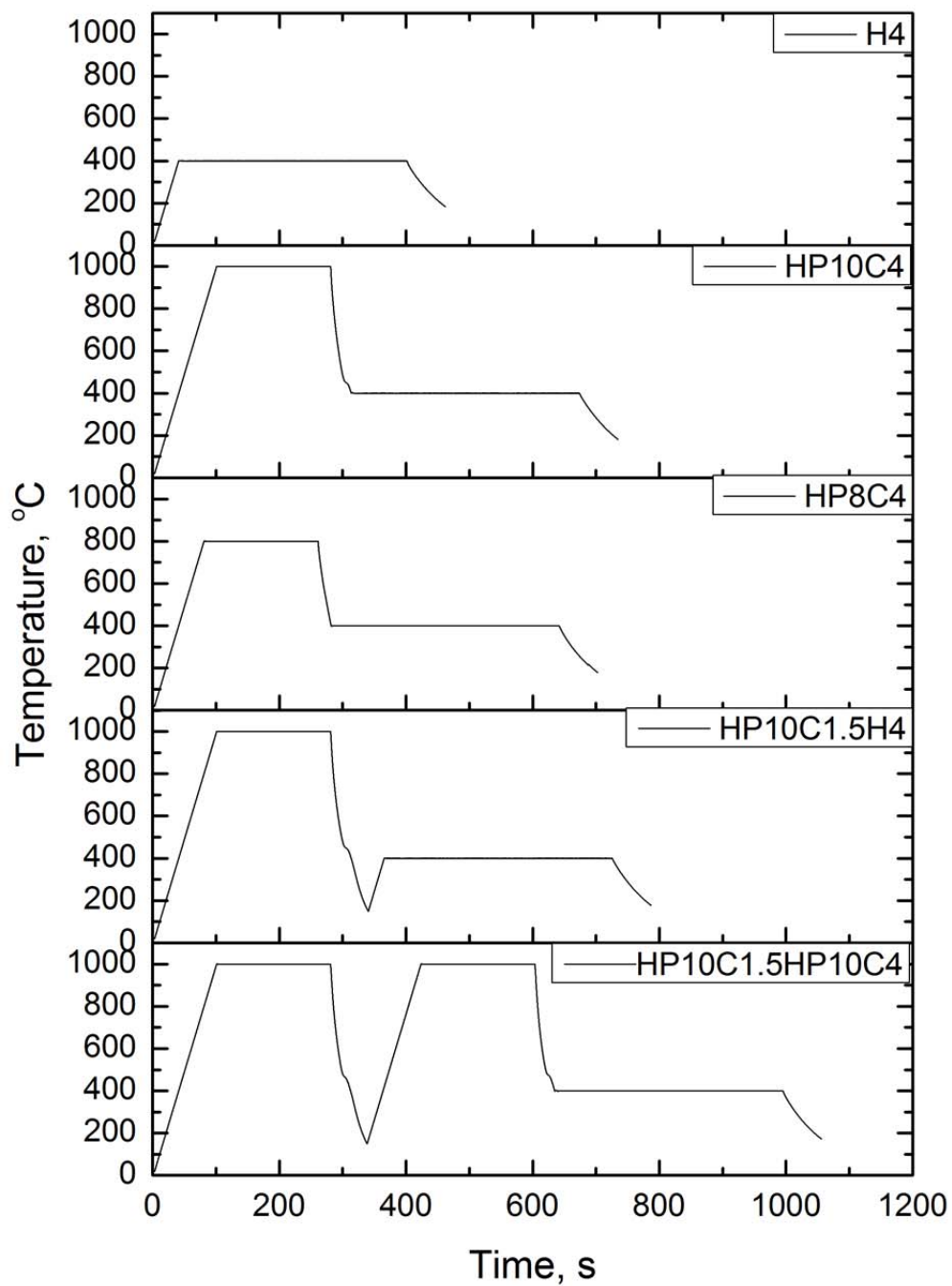
Fig. 8-3: Thermal cycles of sample 1 to 5.
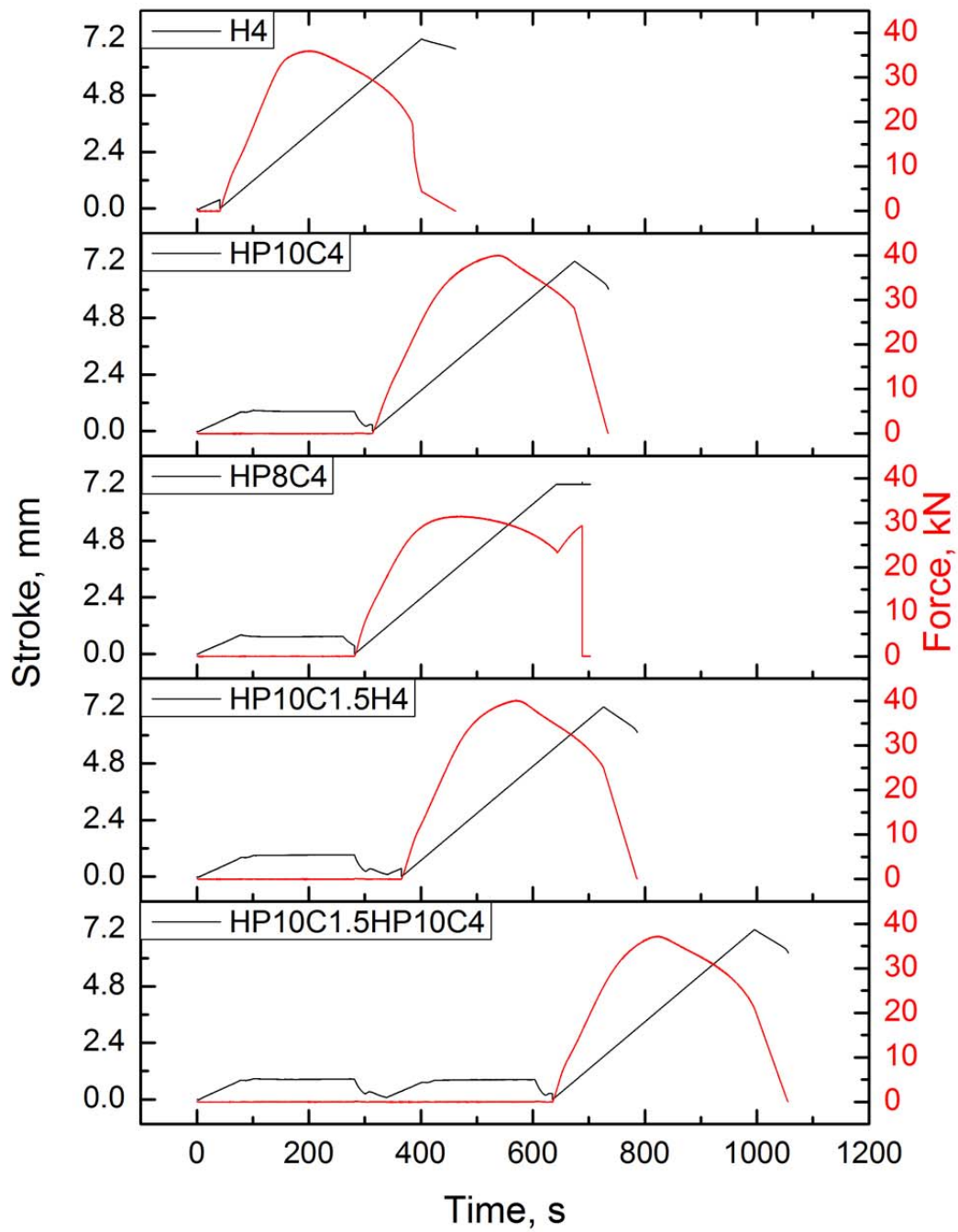
Fig. 8-4: Force and displacement evolution of sample 1 to 5.
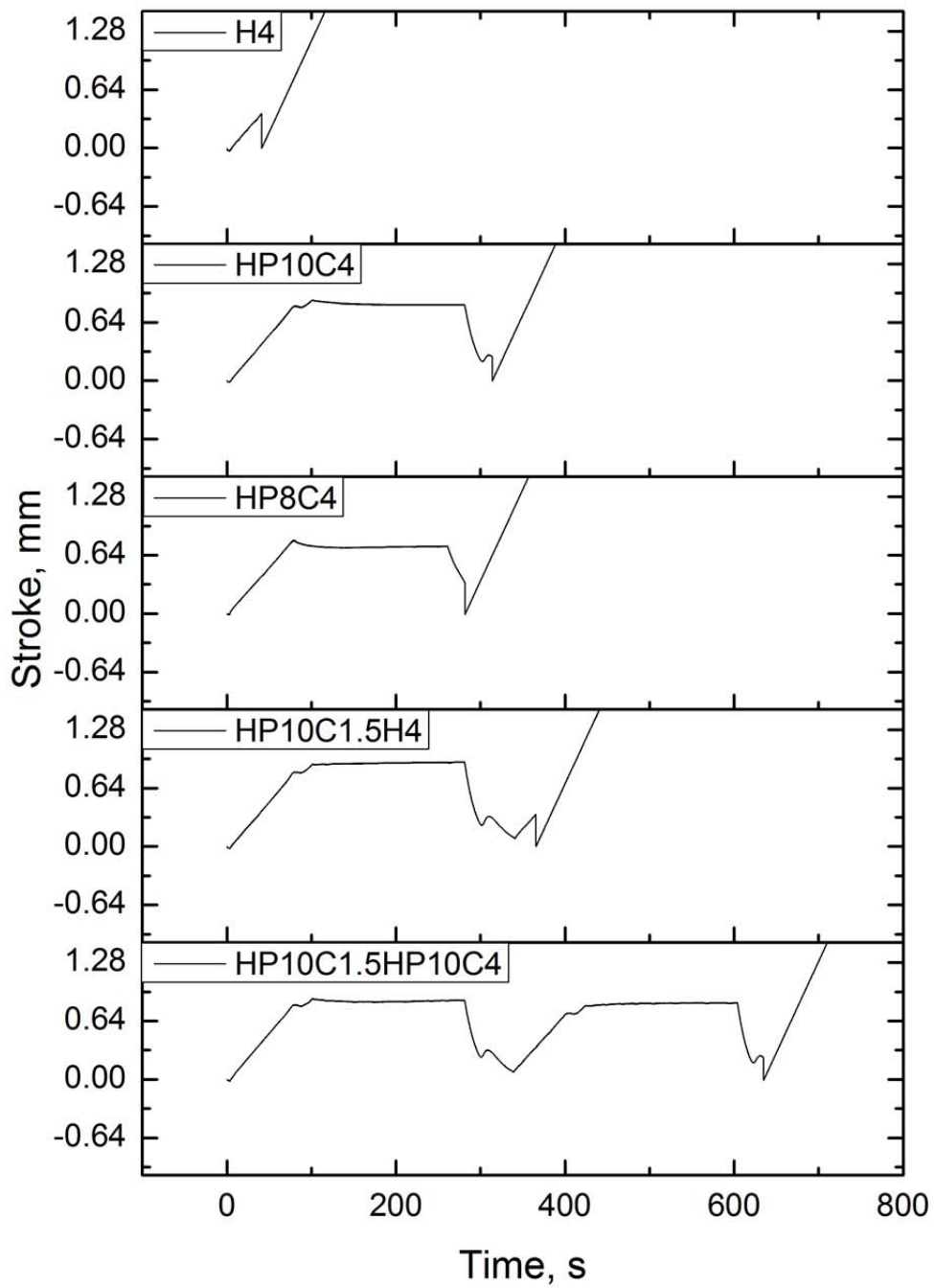
Fig. 8-5: Rescaled displacement of sample 1 to 5.
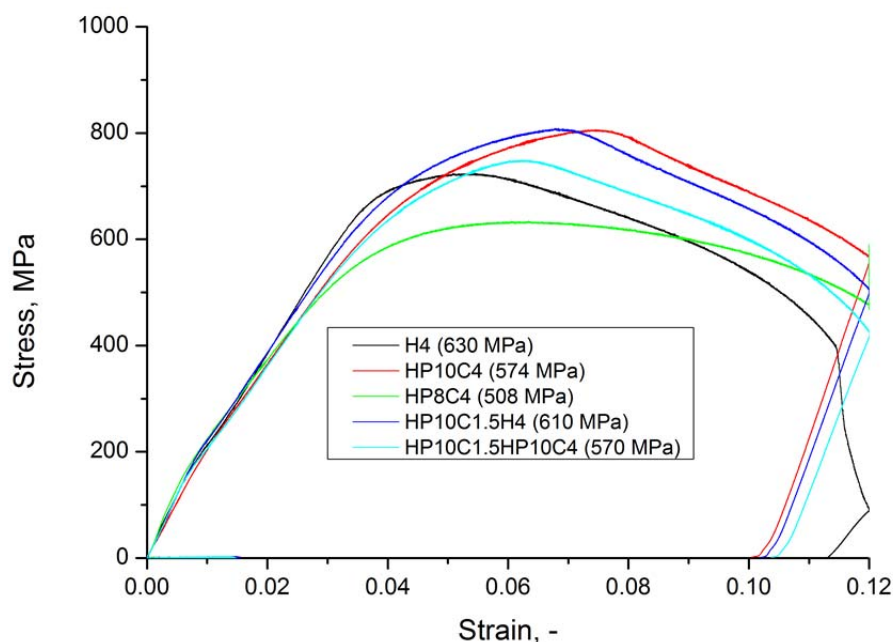
Fig. 8-6: Stress strain curves of sample 1 to 5.

Local heating during welding produces a heat flow in and around the welded area. The material will locally melt and after solidification a joint is created. The mechanical properties of the weld metal and the HAZ are related to their microstructures, and depend on the initial chemical composition of the material and the thermal history. Knowledge of the weld thermal cycle in the HAZ and in the weld pool can help to prevent problems concerning cracking. The peak temperature reached in a specific region in combination with the heating and cooling rates determine the microstructural development. In numerical models, if the same mechanical properties are used both in the heating and cooling stages, the final predicted stresses can deviate by approximately 20% in the weld metal and HAZ.

Results show that the temperature dependent mechanical properties are sensitive to prior thermal histories giving rise to phase transformations. However, a large number of experiments are required in order to obtain a comprehensive material database with respect to different peak temperatures, cooling rates and thermal cycles, which is recommended for future work.

8.2 Modelling of ultrasonic impact treatment

Based on the stress measurements, post weld ultrasonic impact treatment led to a stress relaxation in the six pass weld as introduced in chapter 7. The stresses in a six pass weld were validated with numerical models on a pass-by-pass

basis. Ultrasonic impact treatment includes two processes: a high frequency mechanical impact and ultrasound induced material changes. To construct a UIT FE model, the contact time and initial impact velocity are essential. The contact time during UIT is determined by the initial pressure of the indenter and the hardness of the treated material. For the impact velocity, it can be assumed that all the impacts occur at the same velocity and an average velocity is considered. This average velocity is taken to be the maximum initial velocity of the pins during contact [147, 148]. Considering that the sinusoidal harmonic signal delivered by the generator is

$$x(t) = A \sin wt \tag{8-1}$$

where A is the amplitude and w represents the angular frequency. The velocity is

$$\frac{dx}{dt} = Aw \cos wt \tag{8-2}$$

and the maximum initial velocity is

$$V_{ini\,max} = 2A\pi f \tag{8-3}$$

where f represents the impact frequency [149].

Observed from the high speed camera, the maximum amplitude of the pin is 3 mm, and the impact frequency is 50 Hz. The initial impact velocity calculated with these experimental parameters is 0.96 m s^{-1}. This value can be considered as the average velocity of the impacts during the process and used as an input in the simulations. The real impact velocity in UIT is difficult to estimate due to the complex kinematics of the impacts in the peening tool. A value of 0.96 m s^{-1} is in the order of velocities estimated by other authors, as Todaka *et al.* [150] indicated that the impact velocity in UIT is lower than 20 m s^{-1}. Pilé *et al.* [151] have established a model of the UIT process and obtained an impact mean speed of the order of 3 m s^{-1}.

The ultrasonic impacting process involves severe plastic deformation under the treated surface. The yield stress and ultimate stress of the material are altered depending on the applied strain rates. In this study, the Johnson-Cook model was used to calculate the material response due to high strain rate deformation [147]. The yield stress can be expressed as

$$\sigma = (A + B\overline{\varepsilon}^n)(1 + C \ln \dot{\varepsilon}^*)(1 - T^{*m}) \tag{8-4}$$

where $\overline{\varepsilon}$ is the equivalent plastic strain; $\dot{\varepsilon}^*$ is the dimensionless strain rate; T^* is a dimensionless temperature; A is the yield stress of the material; B and n are the strengthening parameters; C is a strain sensitivity parameter; m is a temperature softening parameter. As the temperature increase during the treatment is much smaller than the temperature needed for phase transformation,

material softening effects are ignored in this case. Table 8-2 provides the material properties and Johnson-Cook parameters.

Table 8-2: Material properties and Johnson-Cook parameters [147].

Elastic modulus (GPa)	Possion's ratio -	Density (kg m^{-3})	A (MPa)	B (MPa)	n -	C -	$\dot{\varepsilon}_0$ (s^{-1})
210	0.3	7930	830	1000	0.65	0.07	1.0

The hardness of the pin is much higher than the treated material. Therefore, no deformation of the pins is assumed and they are defined as rigid bodies. Due to the symmetry of the pin and workpiece, only a quarter of the impact zone is considered in the model. The workpiece is one fourth of a cylinder with a radius of 30 mm and a height of 6 mm. The diameter of the pin is 3 mm with a top radius of 1.5 mm. The element type is C3D8R (continuous 3 dimensional body with 8 nodes and reduced integration). The two edges of the workpiece are symmetrically constrained, and the bottom of the workpiece is constrained in the vertical direction. The impact model with explicit analysis is shown in Fig. 8-7. Table 8-3 shows different treating parameters for a sensitivity test of the impact model.
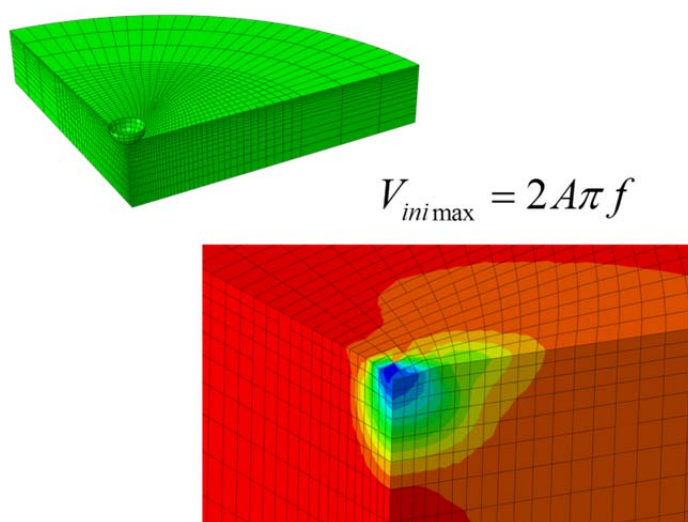
$$V_{ini\,max} = 2A\pi f$$

Fig. 8-7: Impact model with explicit analysis.

Table 8-3: Impact model with different treating parameters.

Case	Velocity (m s^{-1})	Friction coefficient	Contact time ($\times 10^{-3}$ s)
1	1	0	1
2	2	0.05	2
3	3	0.1	3

The residual stress along the thickness due to the impact velocity, friction coefficient, and contact time are shown in Fig. 8-8(a-c). Close to the treated surface, the residual stresses are compressive in nature. Below this compressive region, a transition of residual stress is observed from compression to tension followed by a gradual decrease to zero. In order to consider the effects of different impact velocities (1, 2 and 3 m s^{-1}), the friction and contact time are fixed as 0.05 and 2×10^{-3} s. The peak compressive stress of case 1 and 2 are similar, while case 3 shows the largest compressive peak stress. The stress penetration depth is increased from case 1 to 3. The effects of different friction coefficients (0, 0.05 and 0.1) are considered with the impact velocity and contact time fixed at 3 m s^{-1} and 2×10^{-3} s, respectively. The peak compressive stress at the surface is increased from case 1 to 3, while the stress penetration depth is not influenced by the friction coefficients. The effects of different contact time (1, 2 and 3×10^{-3} s) are considered with the impact velocity and friction coefficient fixed at 3 m s^{-1} and 0.05. The peak compressive stresses at the surface are similar, while the stress penetration depth is increased from case 1 to 3.
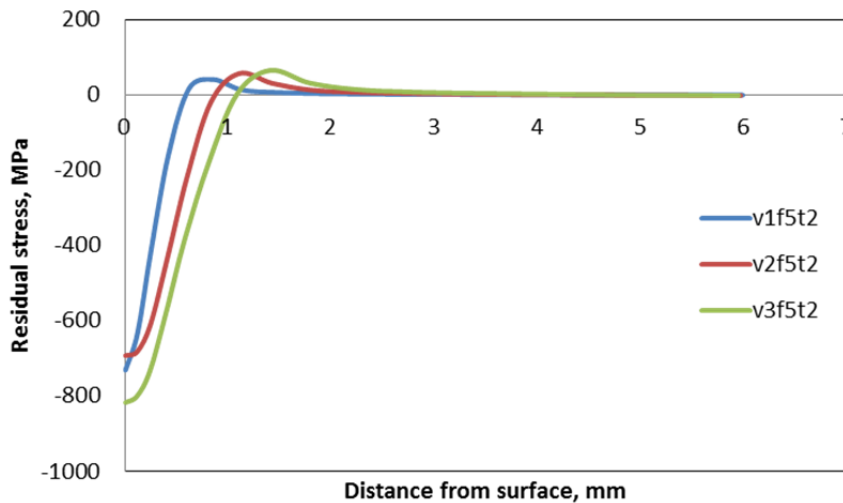
(a)
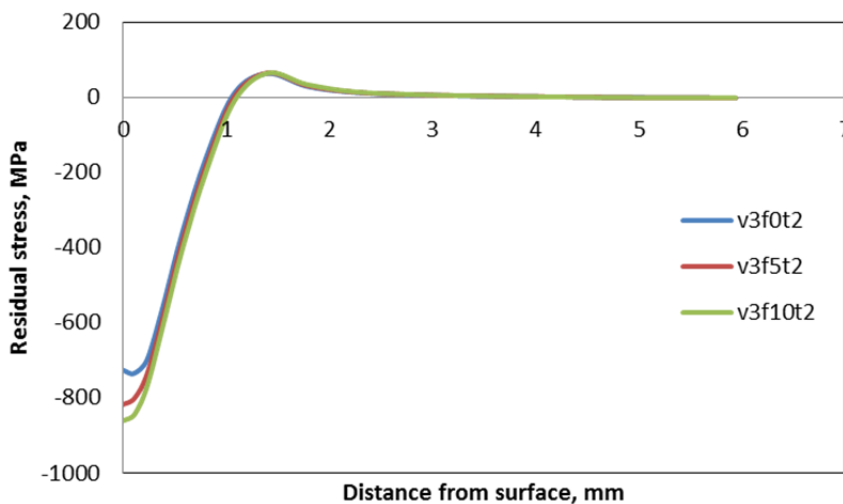
(b)
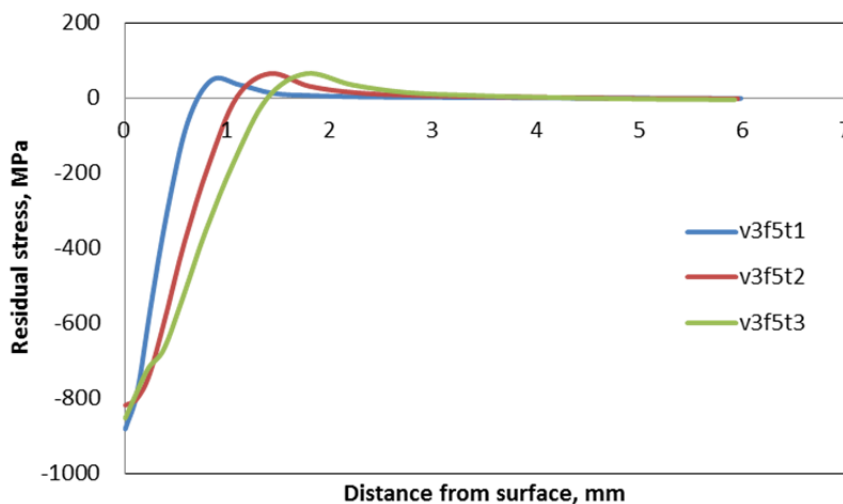
(c)

Fig. 8-8: Effects on through-thickness stress due to (a) impact velocity (v), (b) friction coefficient (f), (c) contact time (t).

The example above only represents a stationary UIT process. In the

147

experiments undertaken in this work, the peening tool is travelling along in the longitudinal direction. The time for travelling is in the order of minutes, while the time for impact is in the order of 10^{-3} seconds, *i.e.* orders of magnitude smaller. Thus, a 3D solid model will lead to an expensive computational time. Unlike welding, UIT is quite a dynamic process. It is difficult to quantify the contact time in a typical cross section, and a 2D shell model is therefore not applicable.

To give an indication on how the multi-pass weld is affected by the high frequency impact, a typical cross section was assumed to be treated by four impact cycles as there are four pins in a row during the treatment. The stress state after the six pass weld was imported as a pre-defined field. The indenter was modelled by a circle using an analytical rigid body. The centre of the circle was defined as the reference of motion. The constraints on the workpiece were the same as those employed for the six pass weld, and were removed after unclamping. The indenter has an initial impact velocity of 0.96 mm s^{-1}, which is given to the reference of the indenter in a pre-defined step. The contact time is 0.004 s and the friction coefficient of the surface is assumed to be 0.05.
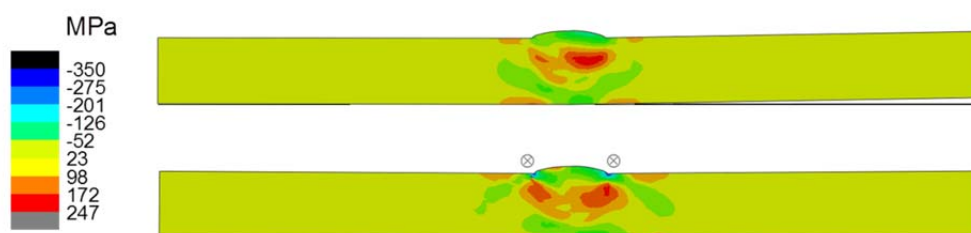
Fig. 8-9: Stress re-distribution due to post weld high speed impact.

The indentation was applied at the toes on both sides of the weld as previously indicated. Fig. 8-9 shows the simulated stress distribution after welding and due to post weld high speed impact. Compressive stresses are found (maximum 350 MPa) close to the surface at the weld toes, which is a slightly higher than that measured by hole drilling (290 MPa). As stated before, the contact time is assumed to be four impact cycles, which could be over-estimated. More contact time will lead to more compression at the surface. Tensile stresses through the thickness are re-distributed, which is not unexpected as the stresses have to be in equilibrium. However, the ultrasonic induced material softening was not included, and the stress relaxation measured from the experiment cannot be observed in the model. The distortion of the treated workpiece after unclamping is reasonably smaller than for the six pass weld due to the introduction of compressive stresses at the weld toes and re-distribution of tensile stresses in

the workpiece.

For the ultrasonic induced material change, Shalvandi [143] and Dutta [144] performed a series of tensile tests and found that ultrasonic waves induce material softening effects during deformation. The material becomes much softer when the intensity of the ultrasound is increased.

To have a reliable physical FE model representing the UIT process, apart from the high speed impact model, material properties at different ultrasonic intensities, *i.e.* Young's modulus and yield point, are firstly required. A precise description of how the impact energy is dissipated and as well as the distribution of ultrasonic energy, and how the ultrasound transports and dissipates in the workpiece as a function of time, are required.

9 Conclusion and recommendation

9.1 Conclusion

The primary aim of this project is to understand the mechanisms involved in post weld ultrasonic impact treatments and how these affect the residual stress states in the welded area.

Six pass welds were made on a 16 mm thick high strength steel section, followed by an ultrasonic impact treatment (UIT) with different treating conditions. These involved only ultrasound, various treating speeds, different numbers of treating passes, treating angles and plate temperatures prior to the treatment. Residual stresses were measured both on the six pass weld and the ultrasonic impact treated welds by means of synchrotron X-ray diffraction in combination with centre hole drilling. Fatigue tests were carried out on the specimen to access the effects of welding and UIT. The stress evolution in the weld heat-affected-zone (HAZ) was studied by means of electro-thermal mechanical testing. Sequentially coupled thermal mechanical finite element (FE) welding models were constructed for temperature and stress predictions.

Based on results of this work, the following conclusions can be drawn;

- Ultrasonic impact treatment is an effective method to introduce beneficial compressive stresses under the treated surface (measured by centre hole drilling method), and releases and re-distributes residual stresses through the thickness of the workpiece (measured by synchrotron XRD). Ultrasonic induced material softening is more pronounced when deformation takes place, which leads to a more uniform stress re-distribution in the weld (see chapter 7.2).

- After welding, diffraction peak broadening is observed under the weld toe due to the increase of lattice defects. Ultrasonic impact treatment significantly reduces the lattice defects, by more than 20% under the treated surface (see chapter 7.2).

- Lower travel speed and more treating passes contribute to the effectiveness of the stress relaxation. When applying UIT at the weld toe, stress relaxation is more effective with the pins at an angle from the normal and transverse directions, thereby simultaneously treating the weld metal and the heat-affected-zone. The tensile residual stresses in the weld are observed to be more uniformly re-distributed. When the workpiece is treated in a warm condition directly after welding, besides the stress relaxation in the subsurface, additional compressive stresses

151

are introduced under the weld toe (see chapter 7.2).

- Ultrasonic impact treatment is an effective way to extend the fatigue life of a workpiece. Grooves reduce the fatigue life of a component if the stress concentration factor is increased. An indentation groove created by UIT may reduce the fatigue life, however due to the beneficial compressive stresses introduced at the surface, the overall fatigue performance is improved (see chapter 7.3).

- The predicted thermal fields of single, two and six pass welds are in good agreement with the measured results (see chapter 4.4). The temperature in the HAZ varies from approximately 700 to 1400 °C. The temperature deviation between the experiments and model predictions is within 30 °C during the six thermal cycles. The 2D shell model is much more time efficient than the 3D solid model (30 times faster).

- Electro-thermal mechanical testing with appropriate thermal and mechanical boundary conditions can be used to represent the stress evolution in a weld, which helps to understand the influence of high temperature elasto-plastic behaviour and phase transformations occurring during welding (see chapter 5.4).

- The thermal expansion and phase evolution during the multiple thermal cycles can be well simulated. The mechanical material properties are very sensitive to the prior thermal histories, and thus the elasto-plastic input data should be carefully selected. If the same data is appointed to the model both in the heating and cooling stages, the predicted stresses could deviate up to 20% from the reality when the peak temperature in a certain thermal cycle is higher than the Ac_3 temperature (see chapter 8.1).

- Residual stress measurements on a pass-by-pass basis provide a better understanding of the stress development in multi-pass welding than measurements after completion of the entire weld. Tensile stresses are observed under the last weld bead and compressive stresses close to the weld root. After each weld pass, the stress field is re-distributed in response to the additional heating and cooling, and a new stress equilibrium is obtained (see chapter 6.4).

- Three FE models, *i.e.* a 2D shell plane strain (PS), a 2D shell generalised plane strain (GPS) and a 3D solid model were constructed for stress prediction and comparison. The PS model constrains the longitudinal expansion, which in turn overestimates the longitudinal stress. The GPS model releases the longitudinal expansion, and the longitudinal stress is the lowest. The 3D solid model predicts stresses in between those of the PS and GPS models. The final stress states predicted by all three models are within 70 MPa. The transverse stress of the three models shows

similar trends. The calculation time of the GPS model is 2.6 times more than the PS model, and the 3D solid model is 127 times more than the PS model (see chapter 6.3).

- The 2D shell GPS model was selected for pass-by-pass stress prediction/simulation of the six pass weld. The predicted stresses at the bottom face after each weld pass are in good agreement with the measured results. The peak stress alternation due to repositioning of the welding torch for subsequent passes can be well simulated. Comparing the simulated and measured stress maps after the final weld pass, the stresses under the last weld bead are under-estimated by 100 MPa (see chapter 6.4).

9.2 Recommendation

Results show that UIT is more effective for stress relaxation in a warm condition after welding. Application of UIT after each pass at inter-pass temperatures in multi-pass welds should be investigated.

Instead of using centre hole drilling and synchrotron XRD, deep hole drilling can be applied under the treated surface, and depth resolved stress measurement can be obtained in a single measurement with the same gauge length.

Tests to quantify the ultrasonic induced material softening can be extended and improved. It is suggested to integrate an ultrasonic transducer in a tensile machine to measure the ultrasonic induced elastic material changes. Ultrasonic intensity dependent material properties in combination with an appropriate definition of ultrasound distribution under the treated surface can be included into the impact model to simulate the ultrasonic impact treatment.

The temperature dependent material properties can be improved by additional tests, which can better represent the conditions encountered in welding, *i.e.* free dilatation and high temperature tensile testing at different peak temperatures, cooling rates and thermal cycles. The reliability of the welding FE model will be improved.

In-situ strain gauge or contour mapping tests during welding can provide the stress evolution at the surface, which helps with further development of the welding FE models.

3D welding FE models are time consuming when phase transformations and multiple thermal cycles are considered. Besides using advanced computers, construction of the model can also be improved by domain decomposition to save computational time. When modelling multi-pass welds (less than 6 passes), a 2D shell cross section model with a 3D moving heat source is suggested to

simplify the model. For welding of very thick sections with a large number of passes, a 2D shell cross section model with a stationary heat source can be considered.

Reference

1. Ermolaeva, N.S. and M.J.M. Hermans, *Research on post-weld impact treatments of high-strength steel.* Proceedings of the Twenty-fourth (2014) International Ocean and Polar Engineering Conference, Busan, Korea, 2014: p. 410-417.

2. Hassan, N., *Feasibility study on the application of UIT on welds to improve the fatigue lifetime of welded structures.* Master thesis, 2008. **TU Delft**.

3. Webster, G.A. and A.N. Ezeilo, *Residual stress distributions and their influence on fatigue lifetimes.* International Journal of Fatigue, 2001. **23**(SUPPL. 1): p. 375-383.

4. Harada, Y., K. Fukaura, and S. Haga, *Influence of microshot peening on surface layer characteristics of structural steel.* Journal of Materials Processing Technology, 2007. **191**(1-3): p. 297-301.

5. He, T.T., et al., *Mechanisms and characteristics of ultrasonic impact treatment on steel surface.* Advanced Materials Research, 2013. **834-836**: p. 649-653.

6. Kudryavtsev, Y., *Fatigue improvement of welded elements by ultrasonic impact treatment.* Conference Proceedings of the Society for Experimental Mechanics Series, 2011. **6**: p. 75-87.

7. Berezhnyts'ka, M.P., *Methods for determining residual welding stresses and their relief.* materials science, 2001. **37**(6): p. 933-939.

8. Cullity, B.D., *Elements of X-ray diffraction.* Prentice Hall, New Jersey, 2001.

9. Ohms, C., et al., *Residual stress measurements in thick structural weldments by means of neutron diffraction.* Materials Science Forum, 2000. **347**: p. 658-663.

10. Janssen, M., *Acoustoelastic stress evalution in metal plate.* PhD thesis, 1994. **TU Delft**.

11. Tanala, E., et al., *Determination of near surface residual stresses on welded joints using ultrasonic methods.* NDT and E International, 1995. **28**(2): p. 83-88.

12. Togasaki, Y., et al., *Effect of ultrasonic impact treatment on fatigue life in butt welded joints of austenitic stainless steel.* American Society of Mechanical Engineers, Pressure Vessels and Piping Division PVP, 2010. **6**: p. 503-508.

13. Pedersen, M.M., et al., *Comparison of post weld treatment of high strength steel welded joints in medium cycle fatigue.* IIW Document XIII-2272-09, 2009.

14. Kirkhope, K.J., et al., *Weld detail fatigue life improvement techniques.* Marine Structures, 1999. **12**: p. 477-496.

15. Polezhayeva, H., et al., *Effect of weld toe burr grinding on fatigue strength of transverse welded specimens made from DH36 steel.* 28th International Conference on Ocean, Offshore and Arctic Engineering, 2009. **6**: p. 69-73.

16. Hildebrand, J., *Numerical simulation of TIG-dressing of welded joints Joint.* International Conference on Computing and Decision Making in Civil and Building Engineering, 2006: p. 3406-3415.

17. Simoneau, R., D. Thibault, and J.L. Fihey, *A comparison of residual stress in*

155

hammer-peened, multi-pass steel welds - A514 (S690Q) and S41500. Welding in the World, 2009. **53**(5-6): p. 124-134.

18. Everett Jr, R.A., et al., *The effects of shot and laser peening on crack growth and fatigue life in 2024 aluminum alloy and 4340 steel.* NASA Technical Memorandum, 2001: p. 1-18.

19. Hatamleh, O., I.V. Rivero, and J. Lyons, *Evaluation of surface residual stresses in friction stir welds due to laser and shot peening.* Journal of Materials Engineering and Performance, 2007. **16**(5): p. 549-553.

20. Luh, G.C. and R.M. Hwang, *Evaluating the effectiveness of vibratory stress relief by a modified hole-drilling method.* The International Journal of Advanced Manufacturing Technology, 1998. **14**(11): p. 815-823.

21. Statnikov, E.S., *Physics and mechanism of ultrasonic impact treatment.* IIW Document XIII-2004-04, 2004.

22. Weich, I. and T. Ummenhofer, *Effects of high-frequency peening methods on the surface layers and the fatigue strength of welded details.* Materials and Manufacturing Processes, 2011. **26**(2): p. 288-293.

23. Statnikov, E.S., *Applications of operational ultrasonic impact treatment (UIT) technologies in production of welded joints.* IIW Document XIII-1667-97, 1997.

24. Haagensen, P.J., E.S. Statnikov, and L. Lopez-Martinez, *Introductory fatigue tests on welded joints in high strength steel and aluminium improved by various methods including ultrasonic impact treatment (UIT).* IIW Document XIII-1748-98, 1998.

25. Manteghi, S. and S.J. Maddox, *Methods for fatigue life improvement of welded joints in medium and high strength steels.* IIW Document XIII-2006-04, 2006.

26. Statnikov, E.S., V.O. Muktepavel, and V.N. Vityazev, *Comparison of the improvement in corrosion fatigue strength of weld repaired Marine Cu 3-grade bronze propellers by Ultrasonic Impact Treatment (UIT) or Heat Treatment.* IIW Document XIII-1964-03, 2003.

27. Galtier, A. and E.S. Statnikov, *The influence of ultrasonic impact treatment on fatigue behaviour of welded joints in high-strength steel.* IIW Document XIII-1976-03, 2003.

28. Statnikov, E.S. and V.O. Muktepavel, *Comparison of ultrasonic impact treatment (UIT) and other fatigue life improvement methods.* IIW Document XIII-1817-00, 2000.

29. Kudryavtsev, Y. and J. Kleiman, *Fatigue Life Improvement of Welded Elements by Ultrasonic Peening.* IIW Document XIII-2010-04, 2004.

30. Statnikov, E.S., *Esonix ultrasonic impact treatment versus ultrasonic peening.* IIW Document XIII-2050-05, 2005.

31. Kudryavtsev, Y. and J. Kleiman, *Application of ultrasonic peening for fatigue life improvement of automotive welded wheels.* IIW Document XIII-2075-05, 2005.

32. Kudryavtsev, Y. and J. Kleiman, *Rehabilitation and repair of welded elements and structures by ultrasonic peening.* IIW Document XIII-2076-05, 2005.

33. Statnikov, E.S., *Physics and mechanism of ultrasonic impact.* IIW Document XIII-2096-06, 2006.

34. Statnikov, E.S., *Development of Esonix ultrasonic impact treatment techniques.* IIW Document XIII-2098-06, 2006.

35. Kudryavtsev, Y. and J. Kleiman, *Fatigue life improvement of tubular welded joints by ultrasonic peening.* IIW Document XIII-2117-06, 2006.

36. Statnikov, E.S., *UIT application for angular distortion compensation in welded T-joints.* IIW Document XIII-2107-06, 2006.

37. Ohms, C., *Residual stresses in thick bi-metaliic fusion welds.* PhD thesis, 2013. **TU Delft**.

38. Withers, P.J. and H.K.D.H. Bhadeshia, *Overview - Residual stress part 2 - Nature and origins.* Materials Science and Technology, 2001. **17**(4): p. 366-375.

39. *Veqter residual stress workshop handouts.*

40. Lee, D.-W. and S.-S. Cho, *Comparison of X-ray residual stress measurements for rolled steels.* International Journal of Precision Engineering and Manufacturing, 2011. **12**(6): p. 1001-1008.

41. *Strain Gages and Instruments.* http://www.vishaypg.com/docs/11053/tn503.pdf

42. *ASTM Standard E837.* http://www.h-and-m-analytical.com/pdfs/residual_stress.pdf.

43. Beaney, E.M., *Accurate measurement of residual stress on any steel using the centre hole method.* Strain, 1976. **12**(3): p. 99-106.

44. Keil, S., *Experimental determination of residual stresses with the ring-core method and an on-line measuring system.* Exp. Tech, 1992. **6**(5): p. 17-24.

45. *Determining residual stresses by hole-drilling strain gauge method.* ASTM E 837-95.

46. Leggatt, R.H., et al., *Development and experimental validation of the Deep Hole method for residual stress measurement.* Journal of Strain Analysis for Engineering Design, 1996. **31**(3): p. 177-186.

47. Prime, M.B., *Cross-sectional mapping of residual stresses by measuring the surface contour after a cut.* Journal of Engineering Materials and Technology, Transactions of the ASME, 2001. **123**(2): p. 162-168.

48. Wang, Y., *Regularities of longitudinal residual stress in welded section members.* Department of Civil Engineering, Tongji University, Shanghai, China, 2010. **40**: p. 204-208.

49. *X-ray diffraction pattern.* camet-lab.com/retained_austenite.html.

50. Bragg, W.L., *The diffraction of short Electromagnetic waves by a Crystal.* Proceedings of the Cambridge Philosophical Society, 1913. **17**: p. 43-57.

51. Pearson, W.B., *A handbook of lattice spacings and structures of metals and alloys.* Pergamon Press, 1958.

52. Aa, E.M.v.d., *Local cooling during welding: Prediction and control of residual stresses and buckling distortion.* PhD thesis, 2007. **TU Delft**.

53. Steuwer, A., et al., *High-resolution strain mapping in bulk samples using full-profile analysis of energy dispersive synchrotron X-ray diffraction data.* Nuclear Instruments and Methods in Physics Research Section B: Beam Interactions with Materials and Atoms, 2005. **238**: p. 200-204.

54. Owen, R.A., R.V. Preston, and P.J. Withers, *Neutron and synchrotron measurements of residual strain in TIG welded aluminium alloy 2024.* Materials Science and Engineering A, 2003. **A346**: p. 159-167.

55. Oliver, E.C., et al., *Neutron diffraction study of stress-induced martensitic transformation and variant change in Fe-Pd.* Acta Materialia, 2003. **51**: p. 6453-6464.

56. Kang, H. and Y. Lee, *Effects of residual stress and heat treatment on fatigue strength of weldments.* Materials Science and Engineering, 2008. **497**: p. 37-43.

57. Kleber, X. and S.P. Barroso, *Investigation of shot-peened austenitic stainless steel 304L by means of magnetic Barkhausen noise.* Materials Science and Engineering A, 2010. **527**(21-22): p. 6046-6052.

58. Schröter, F., *Höherfeste Stähle für den Stahlbau – Auswahl und Anwendung.* Bauingenieur, 2003. **78**(9): p. 426-432.

59. Pors, W., *Special Hogesterktestaal.* Lastechniek, 2006. **11**: p. 4-15.

60. Pinto, H., et al., *Microstructure and residual stress formation in induction-assisted laser welding of the steel S690QL.* Steel Research International, 2009. **80**(1): p. 39-49.

61. http://www.masteel.co.uk/s690-ql.htm.

62. Dainelli, P. and F. Maltrud, *Management of welding operations with high strength steels.* Welding in the World, 2009. **53**(SPECIAL ISSUE): p. 589-594.

63. Francis, J.M. and J.A. Juston, *The application of thin layer x-ray fluorescence analysis to oxide composition studies on stainless steels.* Journal of Physics E: Scientific Instruments, 1968. **1**(7): p. 772-774.

64. Lewis, M.G. and E.H. Scott, *Method for analysis of total sulfur as SO3 in Portland cement and clinker using the LECO sulfur analyzer.* ASTM Special Technical Publication, 1988. **985**: p. 89-91.

65. Dutta, R.K., *High frequency post weld impact treatments of high strength steel* PhD thesis, 2014. **TU Delft**.

66. *AWS A5.28* http://www.techstreet.com/products/59.

67. *http://pnumbers.com/onlinePackages/fmc/csp-fmc-material.asp?classId=1554.*

68. Naito, T., H. Fujishiro, and Y. Yamada, *Thermal conductivity and thermal dilatation of commercial BSCCO (DI-BSCCO) tapes.* IEEE Transactions on Applied Superconductivity, 2009. **19**(3): p. 3034-3036.

69. Born, M., A. Seichter, and S. Starke, *Characterization of baking behaviour of carbonaceous materials by dilatation investigations.* Carbon, 1990. **28**(2-3): p. 281-285.

70. Jiang, W., et al., *Experimental to study the effect of multiple weld-repairs on microstructure, hardness and residual stress for a stainless steel clad plate.* Materials and Design, 2013. **51**: p. 1052-1059.

71. Chen, G., et al., *High-temperature short-term tensile test and creep rupture strength prediction of the T92/TP347H dissimilar steel weld joints.* Engineering Failure Analysis, 2012. **26**: p. 220-229.

72. Dutta, R.K., et al., *Kinetics of bainitic transformation and transformation plasticity in a high strength quenched and tempered structural steel.* Materials Science and Engineering: A, 2013. **559**: p. 86-95.

73. Saunders, N., et al., *Using JMatPro to model materials properties and behavior.* JOM, 2003. **55**(12): p. 60-65.

74. Bracke, L., et al., *S700MC/Grade 100 in heavy gauges: industrialisation at ArcelorMittal europe.* Revue de Métallurgie, 2011. **108**(6): p. 323-330.

75. *S700 Materials Sheet.* MCB Nederland B.V.

76. Mark, A.F., et al., *On the evolution of local material properties and residual stress in a three-pass SA508 steel weld.* Acta Materialia, 2012. **60**(8): p. 3268-3278.

77. Turski, M., et al., *Residual stress driven creep cracking in AISI Type 316 stainless steel.* Acta Materialia, 2008. **56**(14): p. 3598-3612.

78. Withers, P.J., *Residual stress and its role in failure.* Reports on Progress in Physics, 2007. **70**(12): p. 2211-2264.

79. Ouden, G.D. and M.J.M. Hermans, *Welding technology.* VSSD, 2009.

80. Craig, E., *Gas Metal Arc and Flux Cored Welding Parameters.* Chicago: Weldtrain, 1991. **ISBN 978-0-9753621-0-5**.

81. Chen, J., et al., *Predicting the influence of groove angle on heat transfer and fluid flow for new gas metal arc welding processes.* International Journal of Heat and Mass Transfer, 2011. **55**: p. 102-111.

82. Coules, H.E., et al., *Experimental measurement of biaxial thermal stress fields caused by arc welding.* Journal of Materials Processing Technology, 2012. **212**(4): p. 962-968.

83. Schenk, T., et al., *Influence of clamping support distance on distortion of welded T joints.* Science and Technology of Welding and Joining, 2010. **15**(7): p. 575-582.

84. Schenk, T. and C. Schwenk, *Material response of GMA welded 1 mm thick DP600 overlap joints.* Science and Technology of Welding and Joining, 2010. **15**(7): p. 567-574.

85. Willms, R., *High strength steel for steel constructions.* NSCC, 2009: p. 597-604.

86. Bachorski, A., et al., *Finite-element prediction of distortion during gas metal arc welding using the shrinkage volume approach.* Journal of Materials Processing Technology, 1999. **93**: p. 405-409.

87. Wu, C.S., et al., *Numerical analysis of double-electrode gas metal arc welding process.* Computational Materials Science, 2007. **39**(2): p. 416-423.

88. Goldak, J., A. Chakravarti, and M. Bibby, *A new finite element model for welding heat sources.* Metallurgical Transactions B-Process Metallurgy, 1984. **15**(2): p. 299-305.

89. Long, H., et al., *Prediction of welding distortion in butt joint of thin plates.* Materials & Design, 2009. **30**(10): p. 4126-4135.

90. Lindgren, L.E., *Computational welding mechanics: Thermomechanical andmicrostructural simulations.* Cambridge, 2007.

91. Hui, H., et al., *Finite element simulation of multi-pass welding process with rezoning technique.* Transactions of JWRI, 2010. **39**: p. 85-87.

92. Jiang, W., et al., *Finite element simulation of multipass welding: full three-dimensional versus generalized plane strain or axisymmetric models.* Journal of Strain Analysis for Engineering Design, 2005. **40**(6): p. 587-597.

93. Lee, C.-H. and K.-H. Chang, *Finite element simulation of the residual stresses in high strength carbon steel butt weld incorporating solid-state phase transformation.* Computational Materials Science, 2009. **46**(4): p. 1014-1022.

94. Kasuya, T. and N. Yurioka, *Prediction of welding thermal history by a comprehensive solution* Welding Research Supplement 1991: p. 107-115.

95. Wahab, M.A. and M.J. Painter, *Numerical models of gas metal arc welds using experimentally determined weld pool shapes as the representation.* International Journal of Pressure Vessels and Piping, 1997. **73**(2): p. 153-159.

96. Wang, S., et al., *Simulation on the thermal cycle of a welding process by space–time convection–diffusion finite element analysis.* International Journal of Thermal Sciences, 2009. **48**(5): p. 936-947.

97. Aa, E.M.V.d., et al., *Experimental study of the influence of a trailing heat sink on the welding residual stress distribution.* Materials Science Forum, 2006. **524-525**: p. 479-484.

98. Pazooki, A.M.A., M.J.M. Hermans, and I.M. Richardson, *Numerical investigation of the influence of microstructure on the residual stress distribution and distortion in DP600 welds.* Residual Stresses Viii, 2011. **681**: p. 79-84.

99. Pazooki, A.M.A., *Distorsion control during welding.* Phd thesis, 2014. **TU Delft**.

100. Dai, X.Y., T. Sabuwala, and G. Gioia, *Experiments on elastic polyether polyurethane foams under multiaxial loading: mechanical response and strain fields.* Journal of Applied Mechanics-Transactions of the Asme, 2011. **78**(3): p. 1-11.

101. Withers, P.J. and H.K.D.H. Bhadeshia, *Residual stress part 1 - Measurement techniques.* Materials Science and Technology, 2001. **17**(4): p. 355-365.

102. Wang, Y., et al., *Simulation and analysis of temperature field for in-service multi-pass welding of a sleeve fillet weld.* Computational Materials Science, 2013. **68**: p. 198-205.

103. Heinze, C., C. Schwenk, and M. Rethmeier, *Numerical calculation of residual stress development of multi-pass gas metal arc welding.* Journal of Constructional Steel Research, 2012. **72**: p. 12-19.

104. Chen, Z.Y., Y.L. Ma, and S.Q. Xing, *Effect of welding thermal cycle on microstructure and mechanical properties in multi-pass submerged-arc welding.* Adv. Manuf. Tech. , 2011. **314-316**: p. 1163-1166.

105. Deng, D. and H. Murakawa, *Prediction of welding residual stress in multi-pass butt-welded modified 9Cr–1Mo steel pipe considering phase transformation effects.* Computational Materials Science, 2006. **37**(3): p. 209-219.

106. Ye, J., et al., *Influence of welding passes on grain orientation - The example of a multi-pass V-weld.* International Journal of Pressure Vessels and Piping, 2012. **93-94**: p. 17-21.

107. Heinze, C., C. Schwenk, and M. Rethmeier, *Numerical calculation of residual stress development of multi-pass gas metal arc welding under high restraint conditions.* Materials & Design, 2012. **35**: p. 201-209.

108. Coules, H.E., et al., *Residual strain measurement for arc welding and localised high-pressure rolling using resistance strain gauges and neutron diffraction.* Journal of Strain Analysis for Engineering Design, 2012. **47**(8): p. 576-586.

109. De Strycker, M., et al., *Validation of welding simulations using thermal strains measured with DIC.* Adv. Exp. Mech. Viii, 2011. **70**: p. 129-134.

110. Flansbjer, M. and T. Sjogren, *Using digital image correlation techniques and finite element models for strain-field analysis of a welded aluminium structure.* Adv. Exp. Mech. Viii, 2011. **70**: p. 123-128.

111. Steuwer, A., et al., *High-resolution strain mapping in bulk samples using full-profile analysis of energy dispersive synchrotron X-ray diffraction data.* Nuclear Instruments & Methods in Physics Research Section B-Beam Interactions with Materials and Atoms, 2005. **238**(1-4): p. 200-204.

112. Steuwer, A., et al., *The evolution of crack-tip stresses during a fatigue overload event.* Acta Materialia, 2010. **58**(11): p. 4039-4052.

113. Satoh, K. and T. Ohnishi, *Transient thermal stress of weld heat-affected-zone by both-ends-fixed bar analogy.* Jap. Weld. Soc., 1969. **34**(4): p. 359-371.

114. Shirzadi, A.A. and H.K.D.H. Bhadeshia, *Accumulation of stress in constrained assemblies: novel Satoh test configuration.* Science and Technology of Welding and Joining, 2010. **15**(6): p. 497-499.

115. *Electro-thermal mechanical testing machine handbook.*

116. Gao, H., et al., *Simulation of multi-pass welding of high strength steel.* Mathematical modelling of weld phenomena 10, 2013: p. 167-184.

117. Chen, Y., et al., *Numerical simulation on temperature and stress field of multi-pass welding of thin stainless steel plate.* 2013. **302**: p. 258-262.

118. Satoh, K., *Transient thermal stresses of weld heat- affected zone by both- ends- fixed bar analogy.* Kovove Materialy, 1970. **8**(6): p. 569-587.

119. Gao, H., M.J.M. Hermans, and I.M. Richardson, *Simulation of transient force and strain during thermal mechanical testing relevant to the HAZ in multi-pass welds.* Science and Technology of Welding and Joining, 2013. **18**: p. 525-531.

120. Radaj, D. and S. Zhang, *Notch effect of welded joints subjected to antiplane shear loading.* Engineering Fracture Mechanics, 1992. **43**: p. 663-669.

121. Grong, O., *Metallurgical modelling of welding.* 1997, Cambridge: University Press.

122. Wolff, M. and M. Böhm, *On the singularity of the leblond model for TRIP and its influence on numerical calculations.* Journal of Materials Engineering and Performance, 2005. **14**(1): p. 119-122.

123. Deng, D., et al., *Prediction of the residual welding stress in 2.25Cr-1Mo steel by taking into account the effect of the solid-state phase transformations.* Acta Metallurgica Sinica (English Letters), 2013. **26**(3): p. 333-339.

124. Amirthalingam, M., *Microstrurctual development during welding of TRIP steels.* PhD thesis, 2010. **TU Delft**.

125. Steuwer, A., et al., *High-resolution strain mapping in bulk samples using full-profile analysis of energy-dispersive synchrotron X-ray diffraction data.* Journal of Applied Crystallography, 2004. **37**(6): p. 883-889.

126. Vashista, M. and S. Paul, *Correlation between full width at half maximum (FWHM) of XRD peak with residual stress on ground surfaces.* Philosophical Magazine, 2012. **92**(33): p. 4194-4204.

127. Dutta, R.K., et al., *In situ synchrotron diffraction studies on the temperature-dependent plane-specific elastic constants in a high-strength quenched and tempered structural steel.* Scripta Materialia, 2013. **69**: p. 187-190.

128. Brennan, F.P., P. Peleties, and A.K. Hellier, *Predicting weld toe stress concentration factors for T and skewed T-joint plate connections.* International Journal of Fatigue, 2000. **22**(7): p. 573-584.

129. Free, J.A. and R.F.D. Goff, *Predicting redidual stresses in multi-pass weldments with the finite element methods.* Computers and Structures, 1989. **32**(2): p. 365-378.

130. *Abaqus 6.10 Documentation*.

131. Webster, J.M., J.K. Hepworth, and C. Forno, *Strain in transition joints measured by high-resolution moiré photography.* Experimental Mechanics, 1981. **21**(5): p. 195-200.

132. Nishidate, Y. and G.P. Nikishkov, *Generalized plane strain deformation of multilayer structures with initial strains.* Journal of Applied Physics, 2006. **100**(11): p. 1-4.

133. Carmignani, C., R. Mares, and G. Toselli, *Transient finite element analysis of deep penetration laser welding process in a singlepass butt-welded thick steel plate.* Comput. Methods Appl. Mech. Engrg., 1999. **179**: p. 197-214.

134. Law, M. and V. Luzin, *Effect of spatial variation of stress-free lattice spacings on measured residual stresses.* J. Strain Analysis, 2011. **46**: p. 831-841.

135. Gao, H., et al., *Residual stress measurements in multi-pass welded high strength steel using energy dispersive synchrotron X-ray diffraction.* Advanced Materials Research, 2014. **922**: p. 177-182.

136. Yang, X., X. Ling, and J. Zhou, *Optimization of the fatigue resistance of AISI304 stainless steel by ultrasonic impact treatment.* International Journal of Fatigue, 2014. **61**: p. 28-38.

137. Ekstrom, T. and C. Charfield, *The use of X-ray diffraction peak broadening analysis to characterize ground Al2o3 powders.* Journal of Materials Science 1985. **20**: p. 1266-1274.

138. Von Mirbach, D., *Hole-drilling method for residual stress measurement - Consideration of elastic-plastic material properties.* Materials Science Forum, 2014. **768-769**: p. 174-181.

139. Von Mirbach, D., *Experimental validation of the calibration function of the hole drilling method and ring core method for residual stress measurement.* Materialpruefung/Materials Testing, 2014. **56**(3): p. 184-190.

140. Vishay, *Measurement of Residual Stresses by the Hole-Drilling Strain Gage Method.* Tech Note TN-503, 2010: p. 19-33.

141. *ASTM E8.* http://enterprise.astm.org/filtrexx40.cgi?+REDLINE_PAGES/E8E8M.htm.

142. DSI, *Series 3 digital control update for Gleeble 1500 systems: Product description and specifications*, ed. D.S. Inc. 2003: New York: DSI.

143. Shalvandi, M., et al., *Influence of ultrasonic stress relief on stainless steel 316 specimens: A comparison with thermal stress relief.* Materials & Design, 2013. **46**(0): p. 713-723.

144. Dutta, R.K., et al., *The effect of tensile deformation by in situ ultrasonic treatment on*

the microstructure of low-carbon steel. Acta Materialia, 2013. **61**(5): p. 1592-1602.

145. Gao, H., et al., *Stress measurements on ultrasonic impact treated multi-pass welds using synchrotron X-ray diffraction.* Thermal Forming and Welding Distortion, 2014: p. 71-82.

146. Murakami, Y. and K. Takahashi, *Crack Branching and Threshold Condition of Small Cracks in Biaxial Fatigue.* Biennial conference; 12th, Fracture: ECF 12, 1998: p. 67-72.

147. Li, J.Y., X. Ling, and J.X. Zhou, *Finite element simulation of residual stress field induced by ultrasonic impact treatment.* Hangkong Cailiao Xuebao/Journal of Aeronautical Materials, 2012. **32**(1): p. 84-88.

148. Chen, J., L. Lü, and K. Fang, *Numerical simulation of ultrasonic impact treatment on 6061 aluminum alloy welding residual stress.* Hanjie Xuebao/Transactions of the China Welding Institution, 2013. **34**(12): p. 88-92.

149. Chaise, T., et al., *Modelling of multiple impacts for the prediction of distortions and residual stresses induced by ultrasonic shot peening (USP).* Journal of Materials Processing Technology, 2012. **212**(10): p. 2080-2090.

150. Todaka, Y., M. Umemoto, and K. Tsuchiya, *Comparison of nanocrystalline surface layer in steels formed by air blast and ultrasonic shot peening.* Materials Transactions, 2004. **45**(2): p. 376-379.

151. Pilé, C., et al., *Modelling of the ultrasonic shot peening process.* 2005. **490-491**: p. 67-72.

Summary

Allseas Engineering bv is an engineering center of the Allseas group, a major player in the offshore pipe lay market and recently expanding the activities to the offshore heavy lift sector. Because of the necessity to design and build lifting structures and equipment of a tremendously high capacity, the demand for high-strength steels usage has been arisen. These steels are to be welded and used in a harsh offshore environment. Localized heating and melting of a workpiece during welding lead to the build-up of residual stresses. When distortion is prevented due to constraints in structures or due to clamping, stress levels will be high and may exceed the yield strength. Post weld treatments are often carried out to mitigate or re-distribute the residual stresses. Ultrasonic impact techniques make use of the combined effects of the high frequency impacts and ultrasonic oscillations in the treated material. Ultrasonic impact treatment (UIT) has been applied successfully to increase the fatigue life of parts and welded elements, to eliminate distortion caused by welding and other technological processes, to relieve residual stresses, and to increase the hardness of materials. Although reported results on fatigue life are very promising, the detailed changes induced in the treated material and the mechanisms by which such changes occur are still poorly understood.

In this research, the main objectives are to understand the stress build-up during multi-pass welding, and the mechanisms involved in post weld ultrasonic impact treatments, how these affect the residual stress state in the welded area. A summary of this work is given as follows:

a. Residual stress

Residual stresses can be considered as internal stresses that maintain a balance within the materials after external forces are removed. During the processing of the materials, such as casting, pressing, welding, cutting, heat treatment and assembly, different levels of residual stresses can be generated within the workpiece. Residual stress measurement techniques should be selected based on the requirement of the length scales involved (*e.g.* surface, through thickness, local or global). In this work, synchrotron XRD in combination with centre hole drilling was used to obtain through-thickness stresses due to multi-pass welding and post weld ultrasonic impact treatment.

b. Materials

High strength steels (HSS) have a high yield and tensile strength, and are therefore extensively used in high load bearing body structures, such as jacket

structures, bridges, buildings and cranes. High strength steel S690QL1 (Fe-0.16C-0.2Si-0.87Mn-0.33Cr-0.21Mo (wt.%)) was used in this study.

Temperature dependent thermal properties, such as density, thermal conductivity and specific heat, are mainly affected by the chemical composition of the materials. A decreasing tendency of these thermal properties is observed at elevated temperatures. The specific heat has a sudden increase during the solid to solid and solid to liquid phase transformations.

Temperature dependent mechanical properties, such as elastic modulus, Poisson's ratio, and yield stress, can be obtained from tensile testing at elevated temperatures. The material becomes softer at elevated temperature. Free dilatation testing is an effective method to measure the expansion coefficients, and volume changes due to phase transformation at different cooling rates. The material with faster cooling rate shows a higher hardness due to the formation of martensite.

c. Welding experiment

Multi-pass welds were performed on a 16 mm thick steel sections using gas metal arc welding. The first weld pass was made with a relatively low heat input to avoid burn-through. In subsequent weld passes, higher welding heat inputs were generally employed to maximise productivity. Each successive thermal cycle will introduce additional local re-melting, solid state phase transformations, grain growth, grain refinement, recrystallization and recovery.

Thermal analysis can be classified into three main parts: heat input, heat loss, and heat transportation. To apply finite element (FE) modelling using solid mechanics, an accurate simulation of the welding heat source is required to produce a reliable heat distribution. Heat conduction, convection and radiation can be defined *via* suitable initial and boundary conditions. Heat transportation is mainly affected by the temperature dependent material properties.

A step-by-step welding strategy was arranged: a thickness of 4 mm with single pass, and 8 mm with two passes 16 mm with six passes. Optimised welding parameters, such as welding voltage, wire feed rate, travel speed and repositioning of the torch, were obtained. Transient temperatures at several distances from the weld centre line were measured by thermocouples.

The thermal fields predicted from the FE model show a good agreement with the measured time-temperature profiles. The geometry of the weld pool was compared for further validation. Sensitivity of the thermal models with respect to the input parameters and model construction were described.

d. Electro-thermal mechanical testing

The use of electro-thermal mechanical testing (ETMT) permits simplification of the complex situation under welding conditions, as boundary conditions are well defined. Based on the temperature measurements during welding, two positions in the heat-affected-zone (10 mm at the top surface and 2 mm at the bottom surface from the weld centre line), which experience a peak temperature of approximately 1000 °C, were selected and applied to the ETM samples.

Three mechanical boundary conditions are considered: (i) free dilatation tests, which provide in-situ strain data, (ii) completely constrained, and (iii) combined tests of free dilatation in the heating stage and complete constraint in the cooling stage. These tests were performed to represent realistic welding conditions. The high temperature elasto-plastic behaviour and phase transformation in the HAZ were studied.

e. Welding induced stress

Residual stress measurement was performed on the six pass welds. Synchrotron X-ray diffraction is used to measure the strains in two orthogonal directions. Biaxial Hooke's law is selected to calculate the planar stresses using the diffraction elastic constant.

Three FE models, *i.e.* a 2D shell plane strain (PS), a 2D shell generalised plane strain (GPS) and a 3D solid model were constructed and compared. The 2D shell GPS assumption was used to construct a FE welding model with increased accuracy over the 2D PS model, but with increased calculation time. Thermal expansion, strain reset and phase transformations were considered for stress prediction.

Residual stress measurements on a pass-by-pass basis provide a better understanding of the stress development in multi-pass welding than measurements after completion of the entire weld. Tensile stresses are observed under the last weld bead and compressive stresses close to the weld root. After each weld pass, the stress field is re-distributed in response to the additional heating and cooling, and a new stress equilibrium is obtained.

f. Post weld treatment

Ultrasonic impact treatments (UIT) were applied to the weld toes of the six pass welds. Different treating conditions involving only ultrasound, various treating speeds, different numbers of treating passes, treating angles and plate temperatures prior to the treatment, were examined. Stress relaxation due to UIT was studied *via* synchrotron XRD stress measurement. Tensile residual stresses underneath the last weld bead are reduced. Compressive stresses close to the weld root are re-distributed to maintain the stress equilibrium. Close surface stresses were measured with the hole drilling method. Compressive

stresses are found under the treated surface, and stresses in the subsurface become more tensile in nature. Moreover, UIT reduces the lattice defects under the weld toe.

Lower travel speed and more treating passes contribute to the effectiveness of the stress relaxation. When applying UIT at the weld toe, stress relaxation is more effective with the pins at an angle from the normal and transverse directions, thereby simultaneously treating the weld metal and the heat-affected-zone. The tensile residual stresses in the weld are observed to be more uniformly re-distributed. When the workpiece is treated in a warm condition directly after welding, besides the stress relaxation in the subsurface, additional compressive stresses are introduced under the weld toe.

Ultrasonic impact treatment is an effective way to extend the fatigue life of a workpiece. Grooves reduce the fatigue life of a component if the stress concentration factor is increased. An indentation groove created by UIT may reduce the fatigue life, however due to the beneficial compressive stresses introduced at the surface, the overall fatigue performance is improved.

Samenvatting

Allseas Engineering B.V. is een engineering centrum van de Allseas group, een belangrijke speler in offshore pijpenlegmarkt, die recentelijk de activiteiten uitbreidt naar de offshore heavy lift sector. Vanwege de noodzaak tot het ontwerpen en bouwen van hijsconstructies en apparatuur met een enorm hoge capaciteit, is de vraag naar het gebruik van hogesterkte staal ontstaan. Deze staalsoorten moeten gelast worden en toegepast in de hardvochtige offshore omgeving. Het plaatselijke verwarmen en smelten van een werkstuk tijdens lassen introduceert inwendige spanningen. Als vervorming wordt verhinderd door beperkingen in de bewegingsvrijheid door de constructie of door klemmen, zal het spanningsniveau hoog zijn en kan de vloeigrens worden overschreden. Nabehandeling van lassen heeft ten doel het spanningsniveau te verlagen of de restspanningen te herverdelen. Ultrasone impact technieken maken gebruik van het gecombineerde effect van hoogfrequente impacts en ultrasone trillingen in het behandelde materiaal. Ultrasonic Impact Treatment (UIT) is met succes toegepast om de vermoeiingslevensduur van onderdelen en gelaste componenten te verhogen, vervormingen door lassen en andere technologische processen te elimineren, restspanningen te relaxeren en de hardheid van materialen te verhogen. Hoewel de gerapporteerde resultaten ten aanzien van de vermoeiingslevensduur veelbelovend zijn, zijn de gedetailleerde veranderingen in het behandelde materiaal en de mechanismen waardoor deze veranderingen optreden nog steeds niet volledig begrepen.

De belangrijkste doelstellingen in dit onderzoek zijn het krijgen van een beter begrip van de spanningsopbouw in een meerlagen las, het begrijpen van de mechanismen die werkzaam zijn tijdens de Ultrasonic Impact Treatment en hoe deze mechanismen de restspanningen in het gelaste gebied beïnvloeden. De bevindingen van dit onderzoek zijn hieronder samengevat.

a. Restspanningen

Restspanningen kunnen worden beschouwd als interne spanningen in het materiaal die in evenwicht zijn wanneer geen externe krachten op het onderdeel werkzaam zijn. Tijdens de verwerking van materialen, zoals gieten, persen, lassen, snijden, warmtebehandelingen en assemblage, worden verschillende niveaus van restspanningen gegenereerd in het werkstuk. De selectie van een geëigende techniek om restspanningen te meten hangt af van de lengteschaal waarover de spanning werkzaam is (bijvoorbeeld oppervlaktespanningen, spanningen in de dikterichting van het werkstuk, lokale of globale spanningen). Om de spanningen in de dikterichting van het gelaste werkstuk te verkrijgen is in dit onderzoek gebruik gemaakt van synchrotron Röntgendiffractiemetingen

gecombineerd met centraal gat boren. De spanningen zijn gemeten voor meerlagen lassen en lassen die behandeld zijn met de ultrasonic impact treatment.

b. Materiaal

Hogesterkte staalsoorten (HSS) hebben een hoge vloei- en treksterkte, en worden daarom op grote schaal toegepast in zwaar belaste constructies, zoals jacket constructies, bruggen, gebouwen en kranen. In deze studie is het hoge sterkte staal S690QL1 (Fe-0.16C-0.2Si-0.87Mn-0.33Cr-0.21Mo (gew.%)) gebruikt.

Temperatuurafhankelijke thermische eigenschappen, zoals dichtheid, thermische geleidbaarheid en soortelijke warmte, worden hoofdzakelijk beïnvloed door de chemische samenstelling van het materiaal. Deze thermische eigenschappen laten een dalende tendens zien bij verhoogde temperatuur. De soortelijke warmte heeft een plotselinge toename bij fase transformaties in de vaste stof en bij de overgang van de vaste naar de vloeibare toestand.

Temperatuurafhankelijke mechanische eigenschappen, zoals elasticiteitsmodulus, Poisson ratio en vloeispanning, zijn verkregen door trekproeven uit te voeren op verhoogde temperatuur. Op hogere temperatuur wordt het materiaal zachter. De vrije dilatatie test is een effectieve methode om de uitzettingscoëfficiënten en volumeveranderingen ten gevolge van fase transformaties bij verschillende afkoelsnelheden te meten. Bij hogere afkoelsnelheden wordt het staal harder door de vorming van martensiet.

c. Lasexperimenten

Meerlagen lassen in 16 mm dikke staal plaat zijn vervaardigd door middel van MAG lassen. Voor de eerste lasrups is een relatief lage warmte-inbreng toegepast om doorbranding te voorkomen. In de daaropvolgende lassen is een hogere warmte-inbreng gebruikt om de productiviteit te verhogen. Elke thermische cyclus resulteert in plaatselijk hersmelten, vaste stof fase transformaties, korrelgroei en korrelverfijning, rekristallisatie en herstel.

De thermische analyse van het lasproces bestaat uit drie delen: de warmte-inbreng, warmteverliezen en warmtetransport in het werkstuk. Bij het gebruik van eindige elementen (FE) modellering is een nauwkeurige simulatie van de warmtebron nodig om een betrouwbare warmtedistributie in het werstruk te verkrijgen. Warmtegeleiding, convectie en straling moeten gedefinieerd worden via passende begin- en randvoorwaarden. Warmtetransport wordt vooral beïnvloed door de temperatuur afhankelijke materiaaleigenschappen.

Er is gekozen om de complexiteit van de eindige elementen modellen stapsgewijs te vergroten door te starten met een enkelvoudige las in een 4 mm plaat, een tweevoudige las in een 8 mm werkstuk en een meervoudige las (6 rupsen) in een 16 mm dik werkstuk. De modellen zijn gevalideerd voor experimenten met geoptimaliseerde lasparameters, zoals lasspanning, draadaanvoersnelheid, voortloopsnelheid en de herpositionering van de lastoorts. Tijdens het lassen is het temperatuurverloop op verschillende afstanden van de lasmiddenlijn gemeten met behulp van thermokoppels.

De thermische velden voorspeldt door de FE-modellen tonen een goede overeenkomst met de gemeten tijd-temperatuur-profielen. Daarnaast geeft de geometrie van het lasbad en de positie van de smeltlijn verdere informatie over de geldigheid van de modellen. De gevoeligheid van de thermische modellen met betrekking tot de invoerparameters en constructie van de modellen is beschreven.

d. Elektro-thermische mechanische testen

Elektro-thermische mechanische testen (ETMT), waarbij randvoorwaarden goed gedefinieerd zijn, maken het mogelijk de complexe situatie tijdens het lassen te vereenvoudigen. ETMT proefstukken zijn onderworpen aan thermische cycli gebaseerd op de temperatuurmetingen tijdens het lassen. Hiervoor zijn twee posities in de warmte beïnvloede zone geselecteerd, 10 mm van de hartlijn van de las aan de bovenzijde en 2 mm van de hartlijn van de las aan het onderzijde van het werkstuk van de lasnaad hartlijn). De piektemperatuur op deze posities is ongeveer 1000 ° C.

Drie mechanische randvoorwaarden worden beschouwd: (i) vrij dilatatie testen waarbij de rek *in-situ* wordt gemeten, (ii) testen waarbij dilatatie volledig wordt verhinderd, en (iii) gecombineerde testen waarbij het werkstuk in eerste instantie vrij kan bewegen en vervolgens tijdens een afkoelfase volledig wordt vastgezet. Deze experimenten zijn uitgevoerd om realistische lascondities te benaderen. Het hoge temperatuur elastisch-plastisch gedrag en faseovergangen in de warmtebeïnvloede zone zijn hiermee bestudeerd.

e. Lassenspanningen

Restspanningsmetingen zijn uitgevoerd op de meerlagenlassen. De synchrotron röntgendiffractie techniek is gebruikt om de rekken in twee orthogonale richtingen te meten. Met behulp van de biaxiale wet van Hooke en diffractie elastische constanten is de vlakspanningstoestand berekenend.

Drie FE-modellen, te weten een 2D-shell vlakke rek model (PS), een 2D-shell gegeneraliseerde vlakke rek model (GPS) en een 3D solid model zijn geconstrueerd en de resultaten zijn vergeleken. De 2D shell GPS aanname is

gebruikt om een FE lasmodel met een grotere nauwkeurigheid te verkrijgen in vergelijking tot het 2D PS model. Hierbij neemt echter de rekentijd toe. Thermische uitzetting, het resetten van de rek op verhoogde temperatuur en fase transformaties werden beschouwd bij de voorspelling van de spanningstoestand.

Restspanningsmetingen zijn uitgevoerd na iedere las om een beter begrip te krijgen van de spanningsontwikkeling in meerlagenlassen. Trekspanningen worden waargenomen onder de laatste gelegde las en drukspanningen in de buurt van de laswortel. Door de thermische cyclus tijdens elke las herverdelen de spanningen zich en wordt een nieuw spanningsevenwicht verkregen.

f. Lasnabewerking

De lastenen van de meerlagenlas zijn behandeld met de Ultrasonic Impact Treatment. Verschillende procescondities zijn hierbij toegepast, te weten processnelheid, het aantal malen dat de behandeling wordt herhaald, de hoek waaronder het de lasteen wordt behandeld en de temperatuur van het werkstuk. Ook is het werkstuk onderworpen aan een behandeling waarbij alleen ultrasound is gebruikt en de impacts achterwege zijn gelaten. Spanningsrelaxatie ten gevolge van UIT is bestudeerd met behulp van synchrotron XRD. De residuele trekspanningen onder de laatste las verminderen. Drukspanningen nabij de laswortel worden herverdeeld om het spanningsevenwicht te handhaven. Spanningen aan het oppervlakte van het werkstuk zijn gemeten met het gat boormethode. Drukspanningen zijn te vinden net onder het behandelde oppervlak. Dit gaat geleidelijk over in trekspanningen met toenemende afstand van het oppervlak. Bovendien vermindert UIT roosterdefecten onder de lasteen.

Een lagere voortloopsnelheid en het herhalen van de behandeling draagt bij tot een efficiëntere spanningsrelaxatie. Dit is ook het geval als de pennen onder een hoek worden geplaatst ten opzichte van de normaal en transversale richtingen, waarbij gelijktijdig het lasmetaal en de warmtebeïnvloede zone worden behandeld. Het is waargenomen dat de residuele trekspanningen in de las gelijkmatiger worden herverdeeld. Wanneer het werkstuk wordt behandeld in warme toestand direct na het lassen, zullen naast de spanningrelaxatie onder het oppervlak extra drukspanningen worden ingebracht onder de lasteen.

De ultrasone impact behandeling is een effectieve manier om de vermoeiingslevensduur van een werkstuk te verlengen. Groeven in het werkstuk verlaagt de vermoeiingslevensduur, als de spanningsconcentratiefactor toeneemt. De groef ten gevolge van de indentatie van de UIT behandeling zou de vermoeiingslevensduur kunnen verlagen, door de ingebrachte drukspanningen aan het oppervlak wordt de totale vermoeiingslevensduur echter verlengd.

List of publications

Published

1. **H. Gao**, M. J. M. Hermans, and I. M. Richardson: 'Simulation of transient force and strain during thermal mechanical testing relevant to the HAZ in multi-pass welds', *Sci. Tech. Weld. Join.*, 2013, **18**, 525-531.

2. **H. Gao**, R. K. Dutta, R. M. Huizenga, M. Amirthalingam, M. J. M. Hermans, T. Buslaps, and I. M. Richardson: 'Pass-by-pass stress evolution in multi-pass weld', *Sci. Tech. Weld. Join.*, 2014, **19**, 256-264.

3. **H. Gao**, R. K. Dutta, R. M. Huizenga, M. Amirthalingam, M. J. M. Hermans, T. Buslaps, and I. M. Richardson: 'Stress relaxation due to ultrasonic impact treatment on multi-pass welds', *Sci. Tech. Weld. Join.*, 2014, **19**, 505-513.

4. **H. Gao**, R. K. Dutta, M. J. M. Hermans, and I. M. Richardson: 'Simulation of multi-pass welding of high strength steel', *Mathematical modelling of weld phenomena 10*, 2013, 167-184.

5. **H. Gao**, R. M. Huizenga, R. K. Dutta, M. Amirthalingam, M. J. M. Hermans, T. Buslaps, and I. M. Richardson: 'Residual stress measurements in multi-pass welded high strength steel using energy dispersive synchrotron X-ray diffraction', *Advanced Materials Research*, 2014, **922**, 177-182.

6. **H. Gao**, R. K. Dutta, R. M. Huizenga, M. Amirthalingam, M. J. M. Hermans, T. Buslaps, and I. M. Richardson: 'Stress measurements on ultrasonic impact treated multi-pass welds using synchrotron X-ray diffraction', *Thermal Forming and Welding Distortion*, 2014, 71-82.

7. R. K. Dutta, R. M. Huizenga, M. Amirthalingam, A. King, **H. Gao**, M. J. M. Hermans, and I. M. Richardson: 'In situ synchrotron diffraction studies on the temperature-dependent plane-specific elastic constants in a high-strength quenched and tempered structural steel', *Scripta Mater*, 2013, **69**, 187-190.

8. R. K. Dutta, R. M. Huizenga, M. Amirthalingam, A. King, **H. Gao**, M. J. M. Hermans, J. Sietsma, and I. M. Richardson: 'In-Situ Synchrotron Diffraction Studies on Transformation Strain Development in a High Strength Quenched and Tempered Structural Steel—Part I. Bainitic Transformation', *Metallurgical and Materials Transactions A*, 2014, **45**(1), 218-229.

9. R. K. Dutta, R. M. Huizenga, R. H. Petrov, M. Amirthalingam, A. King, **H. Gao**, M. J. M. Hermans, and I. M. Richardson: 'In-Situ Synchrotron Diffraction Studies on Transformation Strain Development in a

High-Strength Quenched and Tempered Structural Steel—Part II. Martensitic Transformation', *Metallurgical and Materials Transactions A*, 2014, **45**(1), 230-238.

10. R. K. Dutta, R. M. Huizenga, M. Amirthalingam, **H. Gao**, A. King, M. J. M. Hermans, and I. M. Richardson: 'Synchrotron diffraction studies on the transformation strain in a high strength quenched and tempered structural steel', *Materials Science Forum*, 2014, **777**, 231-236.

11. R. K. Dutta, R. M. Huizenga, M. Amirthalingam, **H. Gao**, A. King, M. J. M. Hermans, and I. M. Richardson: 'In-situ synchrotron diffraction studies on hot deformation of austenite in a high strength quenched and tempered structural steel', *Advanced Materials Research*, 2014, **922**, 126-131.

Accepted or Submitted

12. R. K. Dutta, R. M. Huizenga, **H. Gao**, M. Amirthalingam, A. King, M. J. M. Hermans and I. M. Richardson: 'Anisotropy in thermal expansion of bainitic ferrite', *Metallurgical and Materials Transactions A*, accepted (in print).

13. R. K. Dutta, L. Malet, **H. Gao**, M. J. M. Hermans S. Godet and I. M. Richardson: 'Formation of nanostructures in severely deformed high strength steel induced by high frequency ultrasonic impact treatment', *Metallurgical and Materials Transactions A*, submitted.

In preparation

14. **H. Gao**, J. Rodriguez, R. K. Dutta, M. Amirthalingam, M. J. M. Hermans, and I. M. Richardson: 'Stress relaxation and fatigue improvement due to post weld ultrasonic impact treatment', *Sci. Tech. Weld. Join.,* in preparation.

15. R. K. Dutta, M. Herbig, **H. Gao**, M. Amirthalingam, M. J. M. Hermans, P. Choi, D. Raabe and I. M. Richardson: 'Microstructural evolution in welded high strength steel subjected to severe plastic deformation: Experiments and analysis', *Acta Materialia*, in preparation.

Acknowledgements

Curriculum Vitae

He Gao was born on May 1st 1984 in Dalian, Liaoning, China. He received his primary education in Dalian, China. After finishing his secondary education in Dalian he started his college education at University of Science and Technology Beijing, China, where he received his Bachelor degree majoring Materials Chemistry in 2007. From 2007 to 2010, he did his Master study in Rheinisch Westfaelische Technische Hochschule (RWTH) Aachen, Germany, and majoring Metallurgical Engineering.

From July 2010, he was enrolled as a PhD employee by the Material Innovation Institute (M2i), the former Netherlands Institute for Metal Research (NIMR), and started his research in High-Frequency Post Weld Impact Treatments for High-Strength Steels under the supervision of Prof. Ian Richardson and Dr. Marcel Hermans at Delft University of Technology, the Netherlands.